

# **The use of polarimetric EMISAR for the mapping and characterization of the semi-natural environment**

Stefán Meulengracht Sørensen

Department of  
Informatics and Mathematical Modelling  
Technical University of Denmark

&

National Environmental Research Institute

Kongens Lyngby 2005  
IMM-PHD-2004-128

© Copyright 2005 by Stefán Meulengracht Sørensen

Technical University of Denmark  
Informatics and Mathematical Modelling  
Building 321, DK-2800 Kongens Lyngby, Denmark  
Phone +45 45253351, Fax +45 45882673  
[reception@imm.dtu.dk](mailto:reception@imm.dtu.dk)  
[www.imm.dtu.dk](http://www.imm.dtu.dk)

IMM-PHD: ISSN 0909-3192

# Preface

---

This thesis has been prepared at the Institute of Informatics and Mathematical Modelling (IMM), Technical University of Denmark (DTU), as partial fulfilment of the requirements for the degree of Ph.D. in engineering.

The general framework of the thesis is data analysis, multivariate statistics and digital image analysis. It is implied that the reader has a basic knowledge of these areas.

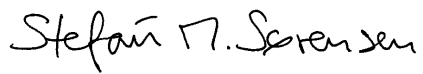
The work presented is a part of the multidisciplinary project named DANMAC (DANish Multisensor Airborne Campaign) and is split between Informatics and Mathematical Modelling (IMM) at the Technical University of Denmark (DTU) and the National Environmental Research Institute (NERI) departments of Freshwater Ecology at Silkeborg and Landscape Ecology (LAND) at Kalø. The purpose of the DANMAC project has been to achieve a better understanding of the physical conditions and processes at or near the surface and their influence on the signals registered by radar and optical, remote sensing sensors.

The DANMAC project (1994 – 1998) was led by Keith McCloy at the Danish Institute of Agricultural Sciences (DIAS). The project collaborated furthermore with the Danish Center for Remote Sensing (DCRS) at the Ørsted•DTU at DTU. Another research institution involved in the DANMAC project is the Institute of Geography (GI) at the University of Copenhagen.

A core aspect of this Ph.D. is the development and application of appropriate analysis methods, based upon advanced mathematical modelling, for the optimal

use of the Synthetic Aperture Radar (SAR) data in the characterization of semi-natural ecosystems in Denmark.

Kgs. Lyngby, June 2005

A handwritten signature in black ink, reading "Stefán M. Sørensen". The signature is written in a cursive style with a large, stylized 'S' at the beginning.

Stefán Meulengracht Sørensen

# Acknowledgements

---

The author is especially grateful to Professor Knut Conradsen of IMM for his guidance and encouragement and for granting me outstanding research facilities and flexibility.

I would also like to thank Dr. Allan Aasbjerg Nielsen of IMM for his excellent guidance and commentary and for introducing me to a lot useful software. Furthermore I would like to thank Dr. Henning Skriver of EMI for his highly valuable guidance and expert comments on remote sensing.

Special thanks must go to Dr. Carl Christian Hoffmann and Michael Stjernholm of NERI for their splendid commentary and guidance in collecting field data. Moreover I would like to gratefully acknowledge Dr. Geoff Groom of NERI for guidance and for providing many useful comments and references.

I wish to thank the people of the Sheffield Centre for Earth Observation Science (SCEOS) at the University of Sheffield for providing a pleasant and inspiring scientific and social environment during my stay at SCEOS. In particular I would like to thank Professor Shaun Quegan for his splendid hospitality and for inspiring discussions and to Dr. Maged Abdel Messeh for his invaluable help concerning computer issues.

I am also grateful to Dr. Jens Michael Carstensen of IMM for his expert comments on Markov random fields and to my colleagues of IMM and NERI for their enduring support. Moreover I wish to express my gratitude to the biologists Jakob Petersen and Torsten Krienke and to Nikolaj Visby Rasmussen for assisting me in the field collecting *in situ* data. I also enjoyed collabora-

ting with Dr. Hans Estrup Andersen of NERI in measuring up the topography and I acknowledge him for keeping up appearances in those moments when the temperature was below zero and the water well above our knees.

My deepest gratitude goes to my wife, Karen, for her patience, forbearance and support and to our three children Hans Kjartan, Signe Marie and Anne Kirstine. They make my life and work joyous.

This research was funded by the DANMAC project, which was supported by the research councils through the "ESA Følgeforskningsbevilling".

# Summary

---

Methods for segmentation and restoration of SAR data using Markov Random Fields (MRF) have been studied extensively by many researchers over the last two decades. What is of special interest is not only methods for segmentation and classification of SAR data for land cover labeling applications, but also methods for detail preservation, which have experienced a rapid growth over the past few years.

The main part of this thesis concerns the development of image restoration methods that facilitate the extraction of biotope relevant information from polarimetric SAR data. Because the semi-natural environments under study are very small, it is crucial for this investigation that the restoration methods are capable of restoring fine structures as well as preserving homogeneous areas.

The restorations are carried out in a signal adaptive mode using MRF in a Bayesian framework. Different *a priori* models are implemented in both the local optimizer Iterated Conditional Modes (ICM) and the global optimization technique Simulated Annealing (SA).

A new technique for algorithm optimization is presented, which relies on ratios of SAR data and their histograms. A quantitative evaluation of the restorations based on statistics derived from the ratio images is presented together with comparative analyses of restorations using ICM and SA.

The relation between the restored polarimetric SAR data and *in situ* data collected at two semi-natural wetland and grassland areas is investigated using multivariate techniques. The restored polarimetric SAR data are classified by

using a supervised and an unsupervised classifier and comparative analyses of their performances are carried out.



# Resumé

---

Metoder til segmentering og restaurering af SAR data ved anvendelse af Markov Random Fields (MRF) er blevet studeret intensivt af forskere i de sidste to årtier. Hvad der har speciel interesse, er ikke alene metoder til restaurering og klassifikation af landskabstyper, men også metoder til restaurering af små detaljer har været under kraftig udvikling de senere år.

Hoveddelen af denne afhandling omhandler udvikling og undersøgelse af metoder, der kan lette kortlægning og karakterisering af biotop relevant information i polarimetriske SAR data. Da de semi-naturlige økosystemer under betragtning er meget små, er det af afgørende betydning for resultatet af denne undersøgelse, at restaurerings metoderne evner at bevare fine strukturer og homogene områder.

Restaureringerne, der er tilpasset data, gør brug af Bayes regel og er foretaget inden for rammerne af MRF. Forskellige *a priori* modeller er implementeret i både den lokale optimerings algoritme Iterated Conditional Modes (ICM) og den globale optimerings algoritme Simulated Annealing (SA).

En ny teknik til algoritme optimering, der er baseret på ratioer af SAR billeder og deres histogrammer, er præsenteret. En kvantitativ evaluering af restaureringerne, baseret på statistiske parametre udledt af ratio billederne, er foretaget og sammenlignende analyser mellem ICM og SA er fremlagt.

Sammenhængen mellem de restaurerede polarimetriske SAR data og *in situ* data indsamlet i de to semi-naturlige våd- og engområder er undersøgt ved brug af multivariate teknikker. De restaurerede SAR data er klassificerede ved brug af en supervised og en unsupervised algoritme, og resultaterne er sammenlignet.



# Contents

---

<b>Preface</b>	<b>i</b>
<b>Acknowledgements</b>	<b>iii</b>
<b>Summary</b>	<b>v</b>
<b>Resumé</b>	<b>vii</b>
<b>Contents</b>	<b>ix</b>
<b>1 Introduction</b>	<b>1</b>
1.1 Ecosystems . . . . .	2
1.2 Polarimetric EMISAR . . . . .	3
1.3 Digital image processing . . . . .	6
1.4 Scope of the thesis . . . . .	9
1.5 Outline of the thesis . . . . .	10

---

<b>2 SAR theory</b>	<b>13</b>
2.1 Introduction . . . . .	13
2.2 Radar Theory . . . . .	15
2.3 Geometrical distortion . . . . .	17
2.4 Polarimetric SAR . . . . .	18
2.5 Speckle . . . . .	20
<b>3 Methodology</b>	<b>23</b>
3.1 Measurements <i>in situ</i> . . . . .	23
3.2 Kriging . . . . .	27
3.3 Geometric rectification . . . . .	32
3.4 Multiple regression analysis . . . . .	36
3.5 Orthogonal transformation . . . . .	38
3.6 Classification . . . . .	41
<b>4 Markov random fields</b>	<b>47</b>
4.1 Introduction . . . . .	48
4.2 Random fields . . . . .	48
4.3 Iterated conditional modes . . . . .	56
4.4 Simulated annealing . . . . .	58
<b>5 Restorations</b>	<b>65</b>
5.1 Introduction . . . . .	66
5.2 Optimization . . . . .	66

---

5.3	Gaussian <i>a priori</i> model . . . . .	69
5.4	Exponential <i>a priori</i> model . . . . .	77
5.5	LaPlace <i>a priori</i> model . . . . .	83
5.6	Gamma <i>a priori</i> models . . . . .	91
5.7	The Gamma sampler . . . . .	104
5.8	Discussion . . . . .	113
<b>6</b>	<b>Gjern</b> . . . . .	<b>117</b>
6.1	Description of test site . . . . .	118
6.2	Ladegaards Enge 1997 . . . . .	121
6.3	Ladegaards Enge 1998–99 . . . . .	133
6.4	Fusion of topography and $K_a$ . . . . .	142
6.5	Discussion . . . . .	148
<b>7</b>	<b>Mols Bjerge</b> . . . . .	<b>151</b>
7.1	Description of test sites . . . . .	152
7.2	Trehøje 1997 . . . . .	154
7.3	Stenhøje 1997 . . . . .	159
7.4	Benlighøj 1997 . . . . .	165
7.5	Discussion . . . . .	168
<b>8</b>	<b>EMISAR data versus Gjern</b> . . . . .	<b>171</b>
8.1	Principal components . . . . .	178
8.2	Synergy between <i>in situ</i> data and EMISAR data . . . . .	184

---

8.3	Supervised classification of EMISAR data . . . . .	191
8.4	Mapping $K_a$ from EMISAR data . . . . .	194
8.5	Unsupervised classification of EMISAR data . . . . .	200
8.6	Discussion . . . . .	205
<b>9</b>	<b>EMISAR data versus Mols Bjerge</b>	<b>209</b>
9.1	Principal components . . . . .	216
9.2	Synergy between <i>in situ</i> data and EMISAR data . . . . .	224
9.3	Supervised classification of EMISAR data . . . . .	229
9.4	Unsupervised classification of EMISAR data . . . . .	234
9.5	Discussion . . . . .	239
<b>10</b>	<b>Conclusion</b>	<b>243</b>
10.1	Summary . . . . .	243
10.2	Discussion . . . . .	245
<b>A</b>	<b>Synthetic SAR images</b>	<b>247</b>
<b>B</b>	<b>Large EMISAR scene</b>	<b>263</b>
<b>C</b>	<b>Vegetation list</b>	<b>275</b>
<b>D</b>	<b>Vegetation data Gjærn 1997</b>	<b>277</b>
<b>E</b>	<b>Programs</b>	<b>279</b>
	<b>References</b>	<b>281</b>

# Introduction

---

Ecosystems are of fundamental importance to society and to sustain life on Earth by providing a wide variety of goods and services. These goods and services that are critical to individuals and societies include e.g. food, fiber, shelter, energy, the purifying of water and air, the storing of carbon and nutrients and providing opportunities for recreation and tourism. Moreover, ecosystems are housing the Earth's entire reservoir of genetic and species diversity as well as providing cultural, religious and aesthetic benefits to society [85].

However, in recent years vulnerable ecosystems have been disturbed regionally and globally due to both anthropogenic and natural impact. The use of Earth-observing satellites in the monitoring of our planet has therefore become increasingly important. These spacecrafts are the world's chief eyes on critical issues such as how fast the ice caps are melting, the concentration of greenhouse gases in the atmosphere, the change of the ozone hole and the state of the ecosystems [70]. In order to help answering these and other important issues about the current variations in the climate the ENVISAT satellite was launched 1 March 2002. ENVISAT is a part of the European Space Agency's (ESA) ongoing Earth Observation Programme. Among the ten instruments onboard ENVISAT is the Advanced Synthetic Aperture Radar (ASAR).

Interferometric and polarimetric SAR represent some of the most sophisticated and up-to-date developments in SAR remote sensing, providing wide scope for

research and application development work. Interferometric SAR is a technique used to generate height difference information of the Earth's surface. As such interferometric SAR possesses a great potential in the monitoring of the natural environment e.g. the studying of glacier dynamics, dune dynamics and earthquake mapping. Polarimetric SAR can provide information of the geometrical structure and orientation of the constituents of a medium as well as its geophysical properties. As such polarimetric SAR has unique capabilities in e.g. sea ice mapping, flood monitoring, the mapping of forest and agricultural crops, in hydrology and in the characterization of ecosystems.

The general purpose of the DANMAC project was to achieve better understanding of the physical conditions at the surface of the Earth influencing the signal of both optical and radar sensors. This understanding is necessary to improve the interpretation, the parameter estimation, the monitoring and classification using present and future satellite sensors. The parameters are needed for applications within hydrology, atmospheric sciences, agricultural and environmental management, forestry, and eco-system managing [30], [49].

## 1.1 Ecosystems

Wetland regions are unique ecological resources that include saltwater marshes, coastal wetlands, estuaries, coral reefs, swamps, marshes and shallow waters. They are considered to be one of the most productive ecosystems on Earth and have an abundance in wildlife species and are a habitat for many different types of plants and animals. In addition wetlands play an important role in water purification by absorbing nutrients and help cycle them through the food chain. Finally, wetlands can counteract global warming by accumulating carbon from decaying plant and animal tissue rather than releasing it into the atmosphere as carbon dioxide. The existence of wetlands is vital to maintaining a balanced hydrological system and their geographical distribution is likely to be affected by changes in temperature and precipitation. Methods for characterizing and monitoring wetlands on local and global scales are therefore crucial because changes in these ecosystems could seriously affect freshwater supplies, fisheries and biodiversity [85].

Also methods for characterizing and monitoring the properties of vegetated surfaces e.g. agriculture, forests and grasslands on local and global scales are of paramount importance. Parameters such as tree height, crown width and vegetation structure are key factors that reflect biomass, growth dynamics and biodiversity. Biomass estimates are important for the estimation of surface energy balance, hydrology modelling and evaluation of the atmospheric carbon



dioxide concentrations.

Ecological systems are dynamic in the sense that they are constantly being affected by changes in the environment. The pressure that the ecosystems are exposed to is due not only to changes in the global climate but also to human activities such as agriculture, nutrient inputs, urban expansion, wastes from industry, extraction of groundwater and changes in land use or management. Quantifying geophysical and biophysical parameters such as soil moisture, soil roughness, biomass and vegetation characteristics retrieved from e.g. forests, agriculture, wetlands and landscape-ecology are therefore crucial in the understanding of how much pressure ecosystems can stand and what probable changes may occur. Furthermore, the geophysical and biophysical parameters are essential to the understanding and modelling of hydrology, the global carbon cycle and the effects of global warming.

Two types of terrestrial semi-natural ecosystems located in Denmark are the subject for this investigation. The selected areas include important representatives of physical, biological and land variation in Denmark. The first is a riparian wetland environment with dense vegetation located at Ladegaards Enge in the river valley of Gjern [2], [53]. The second comprises three dry moderately to heavily vegetated grassland environments located at Trehøje, Benlighøj and Stenhøje at Mols Bjerge [38]. The main focus in the test area at Gjern is the moisture content of the upper soil layers and the vegetation characteristics. The subject of interest at Mols Bjerge is the differences in biomass and vegetation characteristics between the three test areas. Each of the test areas is relatively small and flat and measures approximately 100 m × 100 m. Within the test sites small biotops exist characterized by different plant species and soil moisture contents. *In situ* data in terms of plant species, vegetation characteristics, TDR measurements, topography measurements, biomass and bulk densities of soil samples, were collected in the test sites simultaneously with the overflight by EMISAR.

## 1.2 Polarimetric EMISAR

The polarimetric SAR data to be used in this Ph.D. project are from EMISAR imaging missions over areas in Denmark. EMISAR is a fully polarimetric dual-frequency SAR developed and operated by the Danish Center for Remote Sensing (DCRS) at the Ørsted•DTU at DTU and carried on a Gulfstream G3 aircraft of the Royal Danish Air Force. The polarimetric SAR data were acquired by EMISAR on 3 and 4 June 1997 and cover the semi-natural ecosystems described in Section 1.1. These data comprise both C-(5.3 GHz) and L-(1.25 GHz)-band.

The image data to be used in this thesis are one-look, slant range, scattering matrix data. Data are motion compensated and calibrated. The scattering matrix is a 2-dimensional matrix, whose elements are complex numbers representing both magnitude and phase of the reflected microwaves from a resolution cell. An inherent feature of SAR imaging is a signal dependent noise known as *speckle*, which gives the SAR images a characteristic grainy appearance. This speckle phenomenon is a result of the coherent imaging process of SAR.

EMISAR transmits alternately in the horizontal (H) and the vertical (V) polarization and receives simultaneously in both the horizontal and the vertical polarization, with the resulting combinations VV (Vertical receive, Vertical transmit), VH, HV and HH. This gives the polarimetric EMISAR the capability of measuring the full polarimetric signatures of targets [82]. Throughout this thesis we will use amplitudes and phase differences of the elements in the scattering matrix, see Section 2.4. For example the notation LHH denotes the amplitude of the L-band HH polarized signal and  $\angle$ LHH-LVV denotes the L-band phase difference between HH and VV, unless otherwise mentioned.

Because EMISAR has the capability of measuring the full polarimetric signatures of targets, knowledge of the scattering matrix can provide unique information about the geometrical and dielectric properties of an area. This full polarimetric information is e.g. utilized by Schou and Skriver (2001), who proposed an algorithm for estimating the mean complex covariance matrix using Simulated Annealing (SA) [74]. Later Conradsen *et al.* (2003) have derived test statistics in the complex Wishart distribution for equality of two complex covariance matrices [20].

### 1.2.1 Vegetation and soil moisture

In vegetated areas the interaction between the polarized microwaves of SAR and a vegetation cover is highly complex. This is due to a number of factors, which affect the backscattering coefficient and the phase. These factors comprise: scattering mechanism, vegetation geometry, dielectric constant, wavelength and polarization of the microwave. Ozesmi and Bauer (2002) summarize the literature on satellite remote sensing of wetlands and Price *et al.* (2002) compare Landsat TM and ERS-2 SAR data for discrimination among grassland types in eastern Kansas [61], [66].

The vegetation geometry includes the size, orientation and distribution of e.g. leaves, ears, stems, twigs, branches and trunks. Because of the sensitivity of microwaves to structural characteristics, L-band is more likely to reflect from e.g. branches and trunks whereas at shorter wavelengths the backscatter is in-

fluenced by e.g. leaves, ears and stems. In Morrison *et al.* (2000) the scattering characteristics of wheat canopies are investigated using very high resolution polarimetric L, S, C and X-band 3D SAR imagery [51]. The depth of penetration increases with wavelength and vegetation is therefore more transparent to L-band than C-band. In case of double-bounce scattering from e.g. ground and vegetation a  $\pi$  phase shift is introduced between the HH and VV polarized signals [81].

The two cross-polarized combinations HV and VH are affected by very rough surfaces or by the orientations of the structural components in e.g. vegetation. This is due to depolarization of the transmitted wave, which occurs when e.g. a H-polarized wave undergoes multiple scattering in vegetation canopy and is then received by the antenna in a V-polarized state. The depolarized HV and VH backscatter are therefore particularly useful for separating areas with different vegetation geometries. This is utilized by Kouskoulas *et al.* (1999) for classification of short vegetation using multi-frequency SAR and by Dubois *et al.* (1995) where the cross-polarized L-band ratio HV/VV is used as a discriminator of biomass [44], [26].

In research done by Oh *et al.* (1992) it was concluded that the co-polarized ratio  $HH/VV \leq 1$  for all incidence angles, roughness conditions and moisture contents [57]. However, this is not always true. HH/VV can in general exceed 1 e.g. in situations where the vegetation geometry allows HH to be larger than VV. For heavily vegetated areas or very rough surfaces HH/VV approaches 1, whereas for areas with low vegetation or low surface roughness HH/VV decreases with increasing dielectric constant. This implies that areas with sparse vegetation cover, that is HV/VV less than -11 dB, HH/VV can be used for soil moisture retrieval [26], [37].

In this study the co-polarized and cross-polarized amplitude ratios LHH/LVV and LHV/LVV are selected in preference to LHH/LHV because of their higher sensitivity to soil moisture and vegetation biomass [26], [35]. The phase difference  $\angle LHH-LVV$  is selected in preference to  $\angle LHH-LHV$  and  $\angle LHV-LVV$  because of its sensitivity to double-bounce scattering from the ground and the vertically oriented stems, which are present in the Gjærn test site in particular. Because vegetation is more transparent at L-band than C-band LHH/LVV is less affected by backscatter due to vegetation than CHH/CVV and therefore more likely to represent backscatter due to soil moisture. The L-band amplitude ratio LHH/LVV is therefore selected in preference to CHH/CVV for soil moisture retrieval. Because vegetation is more transparent at L-band than C-band, the backscatter from LHV/LVV is more likely to represent multiple backscatter from the bottom to the top of the vegetation in areas with dense vegetation. Because of the dense vegetation in the test sites at Gjærn and Mols Bjerger the L-band amplitude ratio LHV/LVV is selected in preference to CHV/CVV as a

discriminator of biomass. The L-band phase difference  $\angle\text{LHH-LVV}$  is selected in preference to  $\angle\text{CHH-CHV}$  again due to the larger penetration for L-band. The  $\angle\text{LHH-LVV}$  is thereby more likely to represent backscatter due to double-bounce scattering from the ground and the vertically oriented stems than  $\angle\text{CHH-CHV}$ , which is likely to be affected by multiple scattering in the vegetation canopy. The polarized EMISAR data to be used in the analyses to follow then span CVV, CHV, CHH, LVV, LHV, LHH, LHV/LVV, LHH/LVV and  $\angle\text{LHH-LVV}$ .

### 1.3 Digital image processing

Since the advent of digital computers and the recent advances in hardware and software development, statistical computing has become increasingly important. Image processing is the manipulation of digital values contained in an image for subsequent processing and interpretation. For more general surveys the reader is referred to Andrews (1977) and Sonka (1999) [4], [77].

A digital image is simply the digital form of an image recorded by a sensing device. Examples of sensing devices are scanners, cameras, industrial radiographs, infrared sensors, multi-spectral remote sensing and radar remote sensing. A 2-dimensional plan can be partitioned in regular polygons in three ways. These partitionings are the regular square tessellation, the regular triangular tessellation and the regular hexagonal tessellation. By the term image is here meant 2-dimensional data, which constitute a series of square picture elements (pixels) arranged in a regular pattern of rows and columns. Such a partitioning is also called a square tessellation and the polygons correspond to pixels.

In case the data are obtained from e.g. an optical sensor the pixel has a digital value (grey-level) representing reflected light from the area, which the pixel covers. In radar remote sensing the pixel has a complex number representing both magnitude and phase of scattered microwaves from a resolution cell. In polarimetric SAR data a pixel may represent the complex scattering matrix. In case several values at each pixel are available the term multi-variate data or multi-dimensional image is used. In such a  $p$ -dimensional image each pixel has  $p$  values covering the same geographical area.

The computer vision process can be separated in three levels: low, intermediate and high. Low-level processing (or early vision) deals with raw pixel data and includes e.g. restoration, segmentation, edge detection, texture analysis and optical flow. Low-level processing is invariably data driven and nothing or little is known about the objects in the scene. The intermediate level of processing is concerning grouping the output from the low-level processing into e.g. lines.

High-level processing is object oriented and aims at extracting symbolic features such as the recognition of e.g. characters in a handwritten letter or wetlands in SAR data. Some knowledge about the objects in the scene is therefore required.

Because the test sites are relatively small compared to the pixel spacing it is crucial for this investigation that as much information as possible is preserved about the geophysical and biological properties of the test sites. Unfortunately, the price paid for moving from one level to the next is a loss of information. Since detail preservation in this work is of major concern the image processing in this thesis is therefore restricted to the low-level domain.

### 1.3.1 Contextual constraints

Textural information plays an essential role in human interpretation and analysis of visual data. Although no precise definition of texture exists texture can, according to Haralick (1979), be described as *something consisting of mutually related elements* [32]. Texture can therefore be perceived as a region that is spatially homogeneous in some sense. Within the context of remote sensing such texture regions could be e.g. cities, forests or grasslands.

The type of information or features that can be extracted from image data depends strongly on the scale at which the features are detected [48]. For example large object such as cities and forests are in satellite images observed at coarse scales, whereas smaller objects such as houses and trees are observed at finer scales.

This implies that at low level of detail (large scales) smaller objects are suppressed and likewise at high levels of detail (small scales) all information is retained. Because detail preservation is of great importance in this thesis the images are observed at the smallest scale possible corresponding to the resolution of the images. Here resolution refers to the size of the smallest objects that can be identified.

The presence of speckle considerably reduces the interpretability of the SAR images and consequently some kind of spatial filtering is used routinely to increase the signal-to-noise ratio. Some popular representatives of SAR speckle filters are the median, Lee, Frost and Kuan filters. In Dong *et al.* (2000) these speckle filters are examined in terms of texture preservation and in Rees and Satchell (1997) the effect of median filtering on SAR images is reviewed [24], [68]. Based on the Frost filter kernel a new method for SAR speckle reduction is proposed by Zhang *et al.* (2002) [89]. The simplest of these techniques is the median filter, which has edge-preserving properties but is unsuited for texture preser-

vation. The Lee, Frost and Kuan filters and the method proposed by Zhang *et al.* are on the whole efficient in speckle reduction but they have a tendency of slightly distorting the texture and oversmoothing fine details. Because detail preservation is of major concern in this thesis these filters do not seem suitable for speckle reduction in this investigation. More sophisticated techniques for speckle reduction are therefore applied.

As early as 1962 Chow proposed a method for using contextual information in pattern recognition [15]. Here the dependence between the pixels and their neighbours was used for character recognition. Chow utilized that neighbouring pixels tend to have similar intensities and such regularities are in a probabilistic framework conveniently described by MRF [34].

Markov Random Field (MRF) is an extension of the 1-dimensional Markov process to 2-dimensions and has attracted much attention in the image processing community. Hassner and Sklansky (1980) first proposed MRF as a statistical spatial interaction model for digital images [34]. One reason is that MRF provides a general and natural way of modeling spatially correlated image pixels. Another reason for using MRF is due to Hammersley and Clifford (1971) who established an equivalence between the local properties of MRF and the global properties of Gibbs distributions. This MRF–Gibbs equivalence gives an explicit formula for defining the joint distribution of MRFs through clique-potentials [6].

Most vision problems can be formulated in a general framework called *image labeling*. Here the task is to assign a label for a pixel, which in some sense is optimal. A label can belong to several categories depending on the problem we are trying to solve and a label set may be categorized as being continuous or discrete. For edge detection, for example, the label set is discrete containing the labels edge or non-edge, for image segmentation the label set is containing classes or regions and for image restoration it is containing grey-levels. In image segmentation the aim is to partition an image into homogeneous exclusive regions, where each region is assigned a unique label. Here the discrete label set could e.g. be grey-levels, colour or texture. For image restoration the aim is to estimate the true signal from a degraded or noise-corrupted image using knowledge about its nature [77]. Since the nature of the noise in SAR data is known in advance, the method to be used to search for the scene in the polarimetric EMISAR data that best describes the observed records is image restoration. The label set here includes both discrete and continuous grey-levels.

In a Bayesian framework the most successful criterion in optimization-based MRF modeling is the Maximum *A Posteriori* (MAP) estimate. The MRF-MAP framework for solving vision problems was formulated by Geman and Geman (1984) and later the subject is addressed by e.g. Besag (1986), Dubes and Jain (1989), Besag (1989) and Carstensen (1992) [29], [7], [25], [8], [11]. Our

approach in this investigation is probabilistic and we therefore wish to select the most probable labeling for a pixel in terms of the MAP estimate of the label field.

Unfortunately considerable computational cost is involved in solving a labeling problem. If we for example consider an image with  $150 \times 150$  pixels and only 2 possible labels, there exists a total number of  $2^{22500}$  labelings or configurations. It is obviously not practicable to find the optimum by computing all possible labelings and as the number of labels increases the number of configurations becomes astronomic.

Finding such an optimum requires a minimization of a non-convex energy function. This is not a trivial task and the use of classical gradient descent methods, such as Iterated Conditional Modes (ICM), is questionable because they are likely to get stuck in local minima [7]. A technique however, which is able to overcome this non-convexity and avoid being trapped in local minima is Simulated Annealing (SA) [43], [13].

## 1.4 Scope of the thesis

Due to the necessity to reduce the speckle in the polarimetric EMISAR data to facilitate the extraction of biotope relevant information the first and main part of this thesis concerns restoration in the framework of MRF-MAP. The contextual information in an image is embedded not only in the individual pixels but also in the spatial position of neighbouring pixel values. The potential of utilizing this relative position in the feature extraction is explored by taking the eight pair-site interactions in the local MRF into account.

In order to find the algorithm that best explains the structure underlying the observations, comparative analyses are carried out. These analyses comprise a comparison of various *a priori* models implemented in the two different optimization techniques ICM and SA.

The fact, that the speckle has a well defined statistical distribution for each pixel in the scene, is utilized in this thesis where one of our main results is a new method for algorithm optimization and a Multi-Temperature Annealing (MTA) schedule. Here the technique for algorithm optimization rely on ratios of SAR images and their histograms. The convergence of the MTA algorithm towards the global optimum is governed by a local temperature schedule where each clique has its own temperature. This has the great advantage for real-life applications that the optimized algorithms are completely data-driven.

The proposed models and algorithms are applied and evaluated on polarimetric EMISAR data and synthetic SAR data.

In the second part of this thesis exploratory analyses of the relations between the polarimetric EMISAR data and the semi-natural ecosystems are carried out. Here the multivariate image data to be used in the analyses comprise the restored C- and L-band polarizations VV, HV and HH, the restored L-band ratios HV/VV and HH/VV and the L-band phase difference between HH and VV.

The interaction between the collected *in situ* data and the polarized EMISAR data is investigated using multivariate techniques. These analyses are twofold. Firstly, the interactions between the *in situ* data and the polarized microwaves are analyzed and discussed using linear transforms of training data. Secondly, comparative analyses between a supervised and an unsupervised classification technique are performed. This will disclose to what extent the geographical distribution of classes predicted from training areas correspond to the geographical distribution of the natural grouping (clusters) and how possible differences relate to the *in situ* knowledge.

The results are encouraging but the work presented is by no means exhaustive. It is meant to explore the potential of using polarimetric SAR for monitoring semi-natural environments and hopefully improve the knowledge.

## 1.5 Outline of the thesis

Chapter 2 gives a short overview of the basic principles and aspects of SAR remote sensing. This includes a brief introduction to SAR theory, which is followed by a description of geometric distortion. The fundamental aspects of polarimetric SAR are presented and the speckle phenomenon is outlined.

Chapter 3 presents sample strategies for the collection of *in situ* data and relevant techniques and multivariate methods are reviewed. The sample strategies cover collection of biomass and soil samples. The techniques and methods comprise Time-Domain Reflectometry (TDR), geometrical rectification, Ordinary Kriging (OK), Multiple Regression Analysis (MRA), Principal Components Analysis (PCA), Canonical Discriminant Analysis (CDA), Multiple Discriminant Analysis (MDA) and Cluster Analysis (CA).

Chapter 4 deals with the framework of MRF-MAP and its theoretical foundation and the two optimization techniques ICM and SA are described.



Chapter 5 presents the technique of using ratios of SAR data for algorithm optimization. This technique is applied and evaluated on EMISAR data and synthetic SAR data for restoration purposes. The evaluation includes comparative analyses of different *a priori* models using both ICM and SA.

Chapters 6 and 7 contain a description of the test sites at Gjern and Mols Bjerger together with a presentation of performed fieldwork and collected *in situ* data. The presented and analyzed *in situ* data comprise plant species, vegetation characteristics, TDR measurements, topography measurements, biomass and fresh, dry and saturated bulk densities of soil samples.

Chapters 8 and 9 contain exploratory analyses of the relations between the *in situ* data and the polarimetric EMISAR data. The multivariate techniques used in these analyses comprise PCA, CDA, MDA, MRA and CA.

Appendix A contains a description of the synthetic SAR data together with a presentation of restored, segmented and filtered synthetic SAR data using different optimization techniques and algorithms. The restored, segmented and filtered synthetic SAR data are displayed together with their corresponding ratio images and histograms. Statistics and characteristic parameters derived from the histograms are tabled.

Appendix B contains the restored result of polarimetric EMISAR data covering the town Gjern and its surroundings. The restoration is carried out using the Gamma *pixel prior* through a SA algorithm and the large scene contains a wide range of human artefacts and cover types.

Appendix C shows the Danish and Latin names of plant species in biomass samples collected within the test sites at Gjern and Mols Bjerger.

Appendix D describes the coordinate system in which the vegetation in the test site at Gjern is mapped.

Appendix E contains a list of software developed during the course of this work.



# SAR theory

---

Since the origin of SAR in the 1950's SAR remote sensing technologies have gradually been refined and their applications extended. Of these new technologies and applications, one of the most interesting is polarimetry. Polarimetric SAR can reveal the underlying physical scattering mechanism for terrain type identification and geophysical parameter extraction. An example of such a development is the fully polarimetric EMISAR.

A comprehensive and detailed introduction to the techniques of remote sensing is found in Elachi, 1987 [27], and Ulaby & Elachi, 1986 [82]. For a thorough treatment of the fundamental properties of SAR images refer to Quegan and Oliver, 1998 [59].

## 2.1 Introduction

Synthetic Aperture Radar (SAR) is a side-looking imaging radar (RAdio Detection And Ranging). The SAR is mounted on an aircraft or a satellite, and is used to make high-resolution images of the surface of the Earth. A SAR possesses unique capabilities as an imaging tool, because it provides its own illumination in terms of the radar pulses. It can image at any time of day or

night regardless of sun illumination, and because the radar wavelengths are long the SAR can also penetrate cloudy conditions that visible and infrared instruments can not. The typical micro-wavelength used is in the range 1 cm to 1 m, which corresponds to a frequency range of about 300 MHz to 30 GHz. Other sensors used to image the Earth are e.g. optical sensors. Optical sensors mainly look straight down and commonly use wavelengths from 0.4  $\mu\text{m}$  to 1  $\mu\text{m}$ , which correspond to that of visible light and the near infrared region [27].

There are three basic scattering mechanisms between the microwave and a target. They involve single-bounce scattering, double-bounce scattering and volumetric or multiple scattering. In single-bounce scattering the pulse bounces off e.g. a surface only once before it is received by the antenna. In double-bounce scattering incoming pulses are able to bounce off e.g. buildings and then again bounce off the ground and is then received by the antenna. This types of scattering is also common in forested areas between e.g. vegetation and ground. In multiple scattering the pulse undergoes many bounces in e.g. vegetation before returning to the antenna.

The darker areas in a SAR image represent low *backscatter*, that is to say very little energy is reflected, and brighter areas represent high backscatter. The backscatter from a target that is received by the antenna is due to a number of factors. These comprise the look direction  $\chi$  of the sensor, the aspect angle  $\xi$ , the incidence angle  $\varphi$ , surface roughness, polarization, frequency, and the dielectric and geometrical properties of a target, see Figure 2.1. The aspect angle  $\xi$  will affect backscatter from very linear features such as urban areas, fences, rows of crops, ocean waves and fault lines. Also the incidence angle  $\varphi$  of the radar wave at the Earth's surface causes a variation in the backscatter. For smooth surfaces low  $\varphi$  will result in high backscatter and high  $\varphi$  will result in low backscatter. Rough surfaces are more independent of  $\varphi$  and the rougher the surface being imaged is, the higher the backscatter. For vegetated regions, however, low  $\varphi$  will result in low backscatter and high  $\varphi$  will result in high backscatter due to multiple scattering in e.g. the leaves and straws. Due to this multiple scattering the backscatter from vegetated areas is usually moderately high on the scale of most radar wavelengths. The vegetation therefore appears as grey or light grey in a SAR image.

The backscatter is furthermore often related to the size and orientation of an object. At specific transmit/receive polarizations objects with approximately the size of the wavelength have high backscatter whereas objects smaller than the wavelength have low backscatter. The dielectrical properties (and temperature) of a target also affect backscatter. Water in particular has a high dielectric constant and consequently areas with high moisture content or wet objects will appear bright, and drier targets will appear dark. The exception to this is a smooth body of water, which will act as a smooth surface and reflect incoming

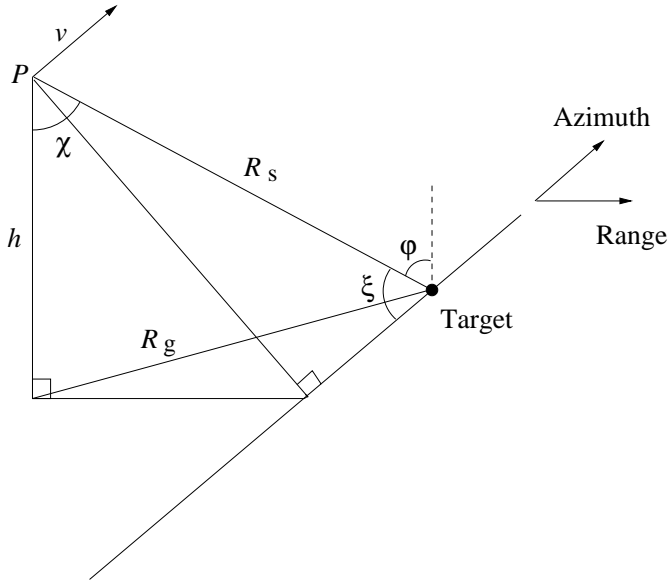


Figure 2.1: The imaging geometry of SAR. The SAR is positioned at the point  $P$  at the altitude  $h$  above ground surface. The velocity of the platform is  $v$ ,  $R_s$  is the slant range between the SAR and the target,  $R_g$  the ground range and  $R_0$  the shortest distance between the SAR and the target. The look angle is  $\chi$ ,  $\xi$  is the aspect angle and  $\phi$  the incidence angle.

pulses in a direction away from the antenna. Such a body will appear dark.

This chapter is organized as follows: In Section 2.2 the basic principles of SAR image formation are described and in Section 2.3 is given an overview of geometric distortion. Section 2.4 presents the fundamental aspects of a fully polarimetric SAR. In Section 2.5 the speckle and its statistical foundation are outlined.

## 2.2 Radar Theory

In Figure 2.1 is illustrated the imaging geometry of SAR for a flat Earth. The antenna is usually a planar array, which has its longest axis along the flight direction. The radar system measures the strength and the time delay of the microwave signal that is emitted by the radar antenna, reflected by a particular

target and received by the radar antenna. These echoes are converted to digital data and passed to a data recorder for later processing and display as an image. Where  $c$  is the speed of light and  $\tau$  is the duration of the pulse the resolution  $\Delta R$  in the range direction, or across-track direction, is given by

$$\Delta R_{range} = \frac{c\tau}{2},$$

where it is taken into account that the pulse travels both forward and backward.

Side-Looking Airborne Radar (SLAR) systems, also called Real Aperture Radar (RAR), is an early form of imaging radar, which generally have very long antennas in order to improve the azimuth resolution. The resolution in the azimuth direction, or along-track direction, is given by

$$\Delta R_{azimuth} = R_0 \frac{\lambda}{D},$$

where  $D$  is the length of the antenna,  $\lambda$  the wavelength of the pulses and  $R_0$  the shortest distance between the SAR and the target [12].

### 2.2.1 SAR

Synthetic Aperture Radar (SAR) refers to a technique used to synthesize a very long antenna by combining echoes received by the radar as it moves along its flight track. 'Aperture' means the opening used to collect the reflected energy that is used to form an image. In the case of a camera, this would be the shutter opening, which corresponds to the antenna for a radar. A synthetic aperture is constructed by moving a real aperture or antenna through a series of positions along the flight track.

As the radar moves, a pulse is transmitted at each position and the return echoes pass through the receiver and are recorded. Because the radar is moving relative to the target, the returned echoes are Doppler-shifted. By compensating for the Doppler-shift the returned signals are focused on a single point, effectively increasing the length of the antenna that is imaging that particular point. This focusing operation, commonly known as SAR processing, is now done digitally on fast computer systems.

The resolution in the azimuth direction for a SAR system is given by

$$\Delta R_{azimuth} = \frac{D}{2}.$$

Contrary to the SLAR system the resolution of the SAR is improved by reducing the length of the antenna [12].

## 2.3 Geometrical distortion

The characteristics of the SAR imaging system give rise to geometric and radiometric distortion in SAR images. The one-look, slant range, EMISAR data to be used have been radiometrically calibrated and since geocoding is of major concern in this project only geometric distortion will be addressed.

Geometric distortion occurs because SAR measures the slant range  $R_s$  rather than angle in the direction perpendicular to the line of flight. The conversion between the slant resolution and the ground resolution is given by

$$\Delta R_g = \frac{\Delta R_s}{\sin \varphi}. \quad (2.1)$$

Geometric distortion may be divided into three categories: shadowing, foreshortening and layover. Shadowing occurs when a radar is unable to receive signals from the backside of an object because the look angle  $\chi$  is too large. Due to the lack of signals, these regions will appear dark in a SAR image. The shadowing effect increases with increasing  $\chi$ . Foreshortening is an effect, which is common in mountainous areas. In this case the object reflects radar signals from all sides but because of the slopes facing the SAR the radiometric information in the foreslope areas will be compressed. Layover occurs in the extreme case where the top of e.g. a mountain has a smaller slant range than the bottom. In such a situation it appears as if the top of an object is closer to the radar than the bottom. This phenomenon is more pronounced for small incidence angles  $\varphi$ .

Due to the geometrical distortions SAR images have to be transformed to conform to a specific map projection system. In Section 3.3 is given a brief introduction to various techniques of geometric transformations.

## 2.4 Polarimetric SAR

Using the Backscatter Alignment (BSA) convention the transmitted electric field component  $E^t$  and the received field component  $E^r$  can be written as

$$\begin{aligned} E^t &= E_v^t \hat{\mathbf{v}}_t + E_h^t \hat{\mathbf{h}}_t \\ E^r &= E_v^r \hat{\mathbf{v}}_r + E_h^r \hat{\mathbf{h}}_r, \end{aligned}$$

where the horizontal and vertical unit vectors  $\hat{\mathbf{v}}$  and  $\hat{\mathbf{h}}$  are defined with respect to the direction of the propagation of the wave  $\hat{\mathbf{k}}$ . That is  $\hat{\mathbf{h}} = \hat{\mathbf{z}} \times \hat{\mathbf{k}} / |\hat{\mathbf{z}} \times \hat{\mathbf{k}}|$  and  $\hat{\mathbf{v}} = \hat{\mathbf{h}} \times \hat{\mathbf{k}}$ , where  $\hat{\mathbf{z}}$  is a unit vector normal to the Earth's surface.

For linearly polarized waves the components  $E^t$  and  $E^r$  are related through

$$\begin{pmatrix} E_v^r \\ E_h^r \end{pmatrix} = \frac{e^{i\frac{2\pi}{\lambda}R}}{R} \begin{pmatrix} S_{vv} & S_{vh} \\ S_{hv} & S_{hh} \end{pmatrix} \begin{pmatrix} E_v^t \\ E_h^t \end{pmatrix},$$

or

$$\mathbf{E}^r = \frac{e^{i\frac{2\pi}{\lambda}R}}{R} \mathbf{S} \mathbf{E}^t,$$

where  $\mathbf{S}$  is the *scattering matrix*,  $\lambda$  is the wavelength of the pulse and  $R$  the range between the antenna and the scatterer. Knowing the scattering matrix the response of a scatterer to any combination of transmitted and received polarizations can therefore be synthesized. The complex scattering amplitude  $S_{pq}$  is given by

$$S_{pq} = A_{pq} e^{i\phi_{pq}}, p, q = h, v,$$

where  $A_{pq}$  is the amplitude and  $\phi$  the phase angle [82].



Given the target vector

$$\mathbf{X} = \begin{pmatrix} S_{vv} \\ S_{vh} \\ S_{hv} \\ S_{hh} \end{pmatrix},$$

the covariance matrix  $\mathbf{C}$  is defined as

$$\mathbf{C} = \mathbf{X}\mathbf{X}^*.$$

For most naturally occurring scatterers

$$S_{hv} = S_{vh}, \quad (2.2)$$

and throughout this thesis we shall assume this reciprocity to be valid.

Taking (2.2) into account the calculated elements in  $\mathbf{C}$  are then reduced to the symmetrical matrix

$$\mathbf{C} = \begin{pmatrix} S_{vv}S_{vv}^* & S_{vv}S_{hv}^* & S_{vv}S_{hh}^* \\ S_{hv}S_{vv}^* & S_{hv}S_{hv}^* & S_{hv}S_{hh}^* \\ S_{hh}S_{vv}^* & S_{hh}S_{hv}^* & S_{hh}S_{hh}^* \end{pmatrix},$$

where \* indicates the conjugation. The diagonal backscattering coefficient  $\sigma_{pq}$  is given by

$$\sigma_{pq,pq} = \langle |S_{pq}|^2 \rangle, \quad p, q = h, v,$$

and the off-diagonal complex correlation coefficient  $\rho_{kl,pq}$  between  $S_{kl}$  and  $S_{pq}$  is defined as

$$\rho_{kl,pq} = \frac{\langle S_{kl}S_{pq}^* \rangle}{\sqrt{\sigma_{kl}\sigma_{pq}}}, \quad k, l, p, q = h, v,$$

where  $\langle \rangle$  indicates the ensemble average [59]. The three off-diagonal phase differences between  $S_{vv}$  and  $S_{hv}$ ,  $S_{vv}$  and  $S_{hh}$  and  $S_{hv}$  and  $S_{hh}$  are given by

$$\phi_{kl} - \phi_{pq} = \angle S_{kl}S_{pq}^*, \quad k, l, p, q = h, v.$$

Given the field polarization vector

$$\mathbf{P}^m = \frac{\mathbf{E}^m}{|\mathbf{E}^m|}, \quad m = r, t,$$

the backscattering coefficient  $\sigma^0$  can in terms of the scattering matrix be written as

$$\sigma_{pq}^0 = \frac{4\pi}{\mathcal{A}} \langle |\mathbf{P}^r \cdot \mathbf{S}\mathbf{P}^t|^2 \rangle, \quad p, q = h, v,$$

where  $\mathcal{A}$  is the illuminated area [82], [59].

Throughout this thesis we will use  $pq$  to denote the amplitude  $\sqrt{\sigma_{pq}^0}$ . For example the notation LHH is synonymous with the L-band  $\sqrt{\sigma_{hh}^0}$ . The  $\angle$ LHH-LVV is synonymous with the L-band phase difference  $\angle S_{hh} S_{vv}^*$ , where the complex element  $S_{hh} S_{vv}^*$  in the covariance matrix has been lowpass filtered before extracting the phase difference.

## 2.5 Speckle

The noise in a SAR image, which is called speckle, is a real electromagnetic phenomenon of interference. It originates from the interference of a large number  $N$  of discrete scatterers within a resolution cell. For a complex SAR image the signal measured from position  $(x, y)$  by the receiver is

$$g(x, r) = Ae^{i\theta} = X + iY$$

where

$$X = \sum_{i=1}^N A_i \cos \phi_i, \quad Y = \sum_{i=1}^N A_i \sin \phi_i.$$

Here  $X$  refers to the real part of the complex signal and  $Y$  the imaginary part,  $A_i$ 's and  $\phi_i$ 's are the amplitudes and phases of the individual scatterers within a resolution cell [75].

By making the assumptions:

1.  $\phi_i$  must be independent and uniformly distributed from 0 to  $2\pi$ .
2.  $A_i$  and  $\phi_i$  of the individual scatterers must be uncorrelated.
3.  $N$  must be large.
4.  $A_i$  must be identically distributed, or fulfil the weaker constraint that no term in the sum must predominate.

It can be shown *via* the Central Limit Theorem that  $X$  and  $Y$  are independent identically Gaussian distributed variables with

$$p(x) = \frac{1}{\sqrt{2\pi\sigma^2}} \exp\left(-\frac{x^2}{2\sigma^2}\right).$$

The observed power or intensity  $I = x^2 + y^2$  of the signal is exponentially distributed

$$p_I(I) = \frac{1}{2\sigma^2} \exp\left(-\frac{I}{2\sigma^2}\right), \quad I \geq 0.$$

An improved estimate of  $I$  can be provided by averaging  $L$  independent measurements also called  $L$  look. In terms of intensity data the  $L$  look average then is

$$\bar{I} = \frac{1}{L} \sum_{k=1}^L I_k.$$

The multi-look intensity data  $\bar{I}$  follow the Gamma distribution

$$p_I(\bar{I}) = \frac{\bar{I}^{L-1}}{\Gamma(L)\left(\frac{2\sigma^2}{L}\right)^L} \exp\left(-\frac{\bar{I}L}{2\sigma^2}\right), \quad \bar{I} \geq 0. \quad (2.3)$$

The amplitude  $A = \sqrt{I}$  of the observed signal will obey the Rayleigh distribution

$$p_A(A) = \frac{A}{\sigma^2} \exp\left(-\frac{A^2}{2\sigma^2}\right), \quad A \geq 0, \quad (2.4)$$

where the mean amplitude  $E(A)$  is

$$E(A) = \sigma \frac{\sqrt{2}}{2} \sqrt{\pi}, \quad (2.5)$$

and the variance  $\text{Var}(A)$  is given by

$$\text{Var}(A) = \sigma^2 \left(2 - \frac{\pi}{2}\right). \quad (2.6)$$

We can now derive the distribution for the multi-look amplitude data  $A = \sqrt{I}$  by utilizing (2.3) and the variable relation

$$p_A(A) = 2Ap_I(A^2),$$

resulting in the square root Gamma distribution

$$p_A(A) = \frac{2A^{2L-1}}{\Gamma(L)\left(\frac{2\sigma^2}{L}\right)^L} \exp\left(-\frac{A^2L}{2\sigma^2}\right), \quad A \geq 0.$$

Although the estimates of the intensity or amplitude at a particular pixel is improved by using  $L$ -look data the resolution is at the same time degraded by a factor  $L$ . Since the resolution is important in this study the SAR data to be used in the following are single-look data.

# Methodology

---

In this chapter central methods used in connection with the analyses of EMISAR data from Ladegaards Enge and Mols Bjerger are described. In the Sections 3.1.1 and 3.1.2 are the sampling strategies for collecting biomass- and soil samples outlined. A short introduction to Time-Domain Reflectometry (TDR) is given in Section 3.1.3. The interpolation technique Ordinary Kriging (OK) is introduced in Section 3.2. Section 3.3 deals with methods for geometric rectification. A short review of Multiple Regression Analysis (MRA) is provided in Section 3.4. Section 3.5.1 concerns Principal Component Analysis (PCA). Canonical Discriminant Analysis (CDA) is introduced in Section 3.5.2. In the Sections 3.6.1 and 3.6.2 are Multiple Discriminant Analysis (MDA) and Cluster Analyses (CA) briefly described.

## 3.1 Measurements *in situ*

In order to achieve relevant knowledge of the physical environment at the test sites *in situ* measurements were required. Relevant knowledge is in this context information about physical properties that affect the polarizations and frequencies used by EMISAR. The criteria for choosing the methods were their capability of providing information concerning hydrology and vegetation. The

geographical locations of the sampling points conform to the Universal Transverse Mercator (UTM) system, zone 32 ED(50).

### 3.1.1 Biomass samples

The above ground biomass in terms of vegetation and dead organic material has been collected at the test sites. The biomass samples collected are representative in terms of the distribution of species and the overall volumetric and geometric appearance within the areas that the samples represent. The location of each sample has either been chosen at random or at places that are typical for the area as a whole. An estimate of how much of the soil surface is covered by leaves and stems is made for each of the plant species. This implies that the total degree of cover can exceed 100 %.

At each location a frame with the dimensions 10 cm  $\times$  20 cm was placed on the ground. Subsequently all the biomass above the soil was harvested within the frame and a botanical determination carried out. The biomass was put in an airtight plastic bag and after the estimation of the fresh weight of the biomass the sample was dried at the temperature of 105° C for 24 hours [76]. Hereafter the dry weight and the water content in weight percent of the biomass samples were calculated.

The various species of vegetation are in the chapters specified by their Latin names. For the corresponding Danish names refer to appendix C.

### 3.1.2 Soil samples

Within each test site soil samples from the upper soil layer were collected. The soil samples were taken by pressing a metallic cylinder just below the surface of the ground. The cylinder filled up with soil of a volume  $V$  of approximately 88 cm<sup>3</sup>, was subsequently brought to the laboratory for further analyses.

After estimation of the fresh weight  $m_f$ , the samples were saturated with water by placing the fresh samples in a water bath for several days. The saturated weight  $m_s$  was then measured, after the surplus water had dripped off. After the saturation the soil samples were dried at a temperature of 105 °C and the dry weight  $m_d$  was determined. Finally, the organic content of the soil samples was estimated by using a method called *heat combustion in a muffle furnace*. Here the samples are dried at 550 °C until the organic matter disappears [76]. The fresh bulk density  $\rho_f$ , the saturated bulk density  $\rho_s$  and the dry bulk density

$\rho_d$  are then given by

$$\rho_f = \frac{m_f}{V}, \quad \rho_s = \frac{m_s}{V}, \quad \rho_d = \frac{m_d}{V}.$$

The porosity  $\theta_p$  is calculated using

$$\theta_p = \frac{m_s - m_d}{V \rho_p},$$

where  $\rho_p$  is the density of the fluids filling the pore space. The volumetric water content  $\theta_w$  of the fresh soil sample yields

$$\theta_w = \frac{m_f - m_d}{V \rho_p} \times 100\%,$$

and the relative volumetric water content  $\theta_r$  of the fresh soil sample is derived from

$$\theta_r = \frac{m_f - m_d}{(m_s - m_d)} \times 100\%.$$

In the case of Ladegaards Enge the fluids were ground water and we therefore make the approximation  $\rho_p \simeq 1$ . The loss in weight  $\Delta m_d$  of the sample represents the organic content  $m_o$ , which given in percent of the dried sample is

$$\Delta m_d = \frac{m_o}{m_d} \times 100\%.$$

### 3.1.3 Time-Domain Reflectometry

Time-Domain Reflectometry (TDR) and SAR are affected by the same physical property, namely the dielectric constant. Both methods are based on the principle of electromagnetic waves. But as the SAR makes remote measurements, TDR is here used for making measurements *in situ*.

The justification of using SAR as a tool for making remote measurements of the soil moisture relies on the backscattering coefficient, which is strongly affected by the complex dielectric constant  $\varepsilon$ . The complex dielectric constant of a material is

$$\varepsilon = \varepsilon' - i \left( \varepsilon'' + \frac{\sigma_{dc}}{2\pi f \varepsilon_0} \right),$$

where  $\varepsilon'$  is the real part and  $\varepsilon''$  the imaginary part. The zero-frequency conductivity is  $\sigma_{dc}$ ,  $f$  is the frequency of the electromagnetic wave and  $\varepsilon_0$  the free space permittivity [80]. The real part of the dielectric constant is rather invariant for most soil types ranging from sandy loam to silty clay in the frequency range from 1 MHz to 1 GHz. This is valid for temperatures above 5 °C and corresponds to the range of frequencies used by TDR [22]. Because  $\varepsilon'$  is about 30 times larger than  $\varepsilon''$  for a dry soil the imaginary part  $\varepsilon''$  can be neglected. The apparent dielectric constant  $K_a$  is therefore  $K_a = \varepsilon'$  [35].

The apparent dielectric constant of water is approximately 80 whereas the other main soil particles have a  $K_a$  value in the range of 2 - 4. A consequence of that is that even small changes in the volumetric water content  $\theta_w$  have a significant effect on  $K_a$  [56].

By taking the volume fractions of the soil components into account it is possible to establish an empirical relationship between  $K_a$  and the volumetric water content of the soil. Not surprisingly several calibration functions have been developed depending on the characteristics of the soil. The empirical calibration function most widely used is published by Topp *et al.* (1980) [80]. The third order polynomial relationship between  $K_a$  and  $\theta_w$  is

$$\theta_w = -0.053 + 0.0292K_a - 0.00055K_a^2 + 0.0000043K_a^3, \quad (3.1)$$

and is valid for four soils ranging from sandy loam to heavy clay soils.

The device used for making TDR measurements in this project was a portable TDR instrument (Tektronix model 1502 B/C cable tester). The probes to be used for vertical placement in the soil are made from 6 mm steel rods of length  $L_p = 10$  cm [79]. After the vertical placement in the soil the apparent probe length  $L_a$  is detected by the instrument and the apparent dielectric constant  $K_a$  is given by

$$K_a = \left( \frac{L_a}{L_p} \right)^2. \quad (3.2)$$



The penetration depth for frequencies larger than 1.4 GHz (L-band) is less than 10 cm. This is valid for loamy soils with a volumetric water content larger than 0.2 g/cm<sup>3</sup>.

## 3.2 Kriging

In the best of all worlds relevant data at every desired point would be available. However, that is not practically possible and interpolation is therefore used to predict unknown values from data at known locations. There exist numerous techniques for interpolating irregularly spaced data. Some of the commonly used methods are e.g. nearest neighbour interpolation, spline interpolation and weighted moving average methods.

Kriging is a weighted average method used in geostatistics and first introduced by the South African mining engineer E. Krige. This method uses a semi-variogram to express the spatial variation and it minimizes the error of the predicted values. In this section the most important elements of kriging are presented. This includes a description of ordinary kriging, which is a technique well suited for modelling the spatial irregularities we are facing in this project.

A detailed introduction to most geostatistical methods is provided in Isaaks and Srivastava (1989) [36] and Huijbregts (1978) [41]. Analysis of irregularly distributed points is given in Hartelius (1996) [33]. An explanatory introduction to geostatistics and kriging with applications is found in Nielsen (1999) [55] and for a thorough analysis of regularly and irregularly sampled spatial, multivariate, and multi-temporal data refer to Nielsen (1994) [54].

### 3.2.1 Geostatistics

The fundamental concept in geostatistics is *regionalized variables*. These variables have been introduced because the spatial variation of any continuous surface often is too irregular to be modeled by a simple mathematical function. Instead the variation can be described by a stochastic surface and the measurable quantity is then called a regionalized variable.

The regionalized variable theory states, that for each position  $\mathbf{x}$  in a domain  $\mathcal{D}$  there exists a measurable quantity  $z(\mathbf{x})$ . The quantity  $z(\mathbf{x})$  is called a regionalized variable and  $\mathcal{D}$  is typically a subset of  $\mathcal{R}^2$  or  $\mathcal{R}^3$ .  $z(\mathbf{x})$  is considered a particular realization of a random variable  $Z(\mathbf{x})$ . The set of random

variables  $\{Z(\mathbf{x})|\mathbf{x} \in \mathcal{D}\}$  constitutes a random function and  $Z(\mathbf{x})$  is often assumed to follow a normal or log-normal distribution.  $Z(\mathbf{x})$  has expectation value  $E\{Z(\mathbf{x})\} = \mu$  and covariance  $\text{Cov}\{Z(\mathbf{x}), Z(\mathbf{x} + \mathbf{h})\} = C(\mathbf{x}, \mathbf{h})$ . Here  $z(\mathbf{x})$  and  $z(\mathbf{x} + \mathbf{h})$  are quantities measured at two points in space  $\mathbf{x}$  and  $\mathbf{x} + \mathbf{h}$  and separated by  $\mathbf{h}$ . If  $\mu$  is constant over  $\mathcal{D}$ ,  $Z$  is said to be first order stationary. If the covariance is constant over  $\mathcal{D}$  also, i.e.  $C(\mathbf{x}, \mathbf{h}) = C(\mathbf{h})$ ,  $Z$  is second order stationary.

### 3.2.2 Semivariogram

The autocovariance function between  $Z(\mathbf{x})$  and  $Z(\mathbf{x} + \mathbf{h})$  is

$$C(\mathbf{x}, \mathbf{h}) = E\{[Z(\mathbf{x}) - \mu][Z(\mathbf{x} + \mathbf{h}) - \mu]\}.$$

The variability in space is also described by the semivariance, which is defined

$$\gamma(\mathbf{x}, \mathbf{h}) = \frac{1}{2}E\{[Z(\mathbf{x}) - Z(\mathbf{x} + \mathbf{h})]^2\}.$$

The *intrinsic hypothesis* states that the semivariogram is a function of the displacement vector  $\mathbf{h}$  and not of the position  $\mathbf{x}$ , that is

$$\gamma(\mathbf{x}, \mathbf{h}) = \gamma(\mathbf{h}).$$

The intrinsic hypothesis is less restrictive than second order stationarity. For the intrinsic hypothesis second order stationarity is not assumed for  $Z(\mathbf{x})$ , but rather the first order differences  $Z(\mathbf{x} + \mathbf{h}) - Z(\mathbf{x})$ . Second order stationarity for  $Z(\mathbf{x})$  implies the intrinsic hypothesis but not *vice versa*. If second order stationarity is assumed or imposed the relation between the semivariogram and the autocovariance is

$$\gamma(\mathbf{h}) = C(\mathbf{0}) - C(\mathbf{h}),$$

where  $C(\mathbf{0}) = \sigma^2$ .

The *experimental semivariogram* can be estimated using

$$\hat{\gamma}(\mathbf{x}, \mathbf{h}) = \frac{1}{2N(\mathbf{h})} \sum_{k=1}^{N(\mathbf{h})} [z(\mathbf{x}_k) - z(\mathbf{x}_k + \mathbf{h})]^2, \quad (3.3)$$

where  $N(\mathbf{h})$  is the number of point pairs separated by  $\mathbf{h}$ .

In order to characterize the experimental semivariogram a number of models can be fitted. A frequently used model, which is also applied in this project, is the spherical model  $\gamma^*(\mathbf{h})$  with nugget effect. A reason for this is the easy interpretability of the parameters. By setting  $|\mathbf{h}| = h$  we assume isotropy and get

$$\gamma^*(\mathbf{h}) = \begin{cases} 0 & \text{if } h = 0 \\ C_0 + C_1 \left[ \frac{3}{2} \frac{h}{R} - \frac{1}{2} \left( \frac{h}{R} \right)^3 \right] & \text{if } 0 < h < R \\ C_0 + C_1 & \text{if } h \geq R. \end{cases}$$

The constant  $C_0$  is the *nugget effect*, which is a discontinuity at  $\mathbf{h} = 0$  due to measurements errors and short range spatial variations. The quantity  $C_0/(C_0 + C_1)$  is the *relative nugget effect* where  $C_0 + C_1$  is the maximum level of semivariance also called the *sill* ( $= \sigma^2$ ). The range of influence is  $R$  corresponding to the maximum semivariance. Other models used are e.g. the cubic, exponential, Gaussian and the linear model.

### 3.2.3 Ordinary kriging

At the unsampled location  $\mathbf{x}_0$  we consider a value  $\hat{z}_0$ , which we wish to estimate as a weighted average of the values  $z_i$  sampled at locations around it. The unbiased linear estimator is given by

$$\begin{aligned} \hat{z}_0 &= w_0 + \sum_{i=1}^N w_i z_i = w_0 + \mathbf{w}^T \mathbf{z} \\ E(Z_0 - \hat{Z}_0) &= 0, \end{aligned}$$

where  $w_i$  are the weights,  $w_0$  is a constant and  $N$  refers to the number of neighbours to  $\hat{z}_0$ . The expected error of estimation is

$$\begin{aligned} E(Z_0 - \hat{Z}_0) &= E(Z_0 - w_0 - \mathbf{w}^T \mathbf{Z}) \\ &= \mu_0 - w_0 - \mathbf{w}^T \boldsymbol{\mu}, \end{aligned} \quad (3.4)$$

and this unbiasedness gives

$$\mu_0 - w_0 - \mathbf{w}^T \boldsymbol{\mu} = 0. \quad (3.5)$$

The *kriging variance*, or the minimum mean square error  $\sigma_E^2$ , is

$$\begin{aligned} \sigma_E^2 &= E(Z_0 - \hat{Z}_0)^2 \\ &= \sigma^2 + \mathbf{w}^T (\mathbf{C}\mathbf{w} - 2\text{Cov}(Z_0, \mathbf{Z})), \end{aligned} \quad (3.6)$$

where  $\mathbf{C}$  is the dispersion matrix of  $\mathbf{z}$ .

In *ordinary kriging* (OK) we suppose that  $E(Z_i) = \mu_0$  for the  $N$  neighbours and by combining (3.4) and (3.5) it follows that

$$E(Z_0 - \hat{Z}_0) = \mu_0(1 - \mathbf{w}^T \mathbf{1}) - w_0 = 0.$$

This implies that  $w_0 = 0$  and  $\mathbf{w}^T \mathbf{1} = 1$ . In the case of *simple kriging* (SK) the mean  $\mu_0$  is known and the constraint  $\sum_{i=1}^N w_i = 1$  is ignored.

The minimum variance of error is obtained by minimizing (3.6) under the constraint  $\sum_{i=1}^N w_i = 1$ . This can be done using the Lagrangian multiplier  $\lambda$  and solving the equations  $\partial[\sigma_E^2 + 2\lambda(\mathbf{w}^T \mathbf{1} - 1)]/\partial w_i = 0$  and  $\partial[\sigma_E^2 + 2\lambda(\mathbf{w}^T \mathbf{1} - 1)]/\partial \lambda = 0$ . This leads to the ordinary kriging system

$$\mathbf{C}\mathbf{w} + \lambda \mathbf{1} = \text{Cov}(Z_0, \mathbf{Z}) \quad (3.7)$$

$$\mathbf{1}^T \mathbf{w} = 1.$$

or

$$\begin{bmatrix} C_{11} & \cdots & C_{1N} & 1 \\ \vdots & \ddots & \vdots & \vdots \\ C_{N1} & \cdots & C_{NN} & 1 \\ 1 & \cdots & 1 & 0 \end{bmatrix} \begin{bmatrix} w_1 \\ \vdots \\ w_N \\ \lambda \end{bmatrix} = \begin{bmatrix} C_{01} \\ \vdots \\ C_{0N} \\ 1 \end{bmatrix},$$

where the covariances  $C_{ij}$ ,  $i, j = 1, \dots, N$  and  $C_{0j}$ ,  $j = 1, \dots, N$  are estimated from the semivariogram. Using (3.6) and (3.7) the estimated kriging variance is

$$\sigma_{OK}^2 = \sigma^2 - \mathbf{w}^T \text{Cov}(Z_0, \mathbf{Z}) - \lambda.$$

A variety of other kriging techniques has been developed. Of these are e.g. simple kriging, universal kriging, co-kriging. In simple kriging the mean is known and second order stationarity is assumed. *Universal kriging* is a technique where a drift polynomial is used to model a non-stationary trend surface. In case the original variables have been undersampled, the covariation between different variables can be taken into account in the reducing of the estimation variance. This is referred to as *co-kriging*. Ordinary kriging is well suited for interpolating surfaces where  $\mu_0$  is not constant i.e. the lack of first order stationarity. Hence the ordinary kriging technique described above is applied in this project.

Some very important advantages of kriging:

- Kriging is exact and it is the Best Linear Unbiased Estimator (BLUE). If a value at a location that has been sampled is estimated, the kriging system will return the sample value as the estimator and a kriging variance zero.
- The kriging system has a unique solution if and only if the covariance matrix  $C$  is positive definite, this also ensures a non-negative kriging variance.
- The kriging system and the kriging variance depend only on the covariance function (semivariogram) and on the spatial lay-out of the sampled supports and not on the actual data values. If a covariance function is known or assumed this has important potential for minimizing the estimation variance in experimental design (i.e. in the planning phase of the spatial lay-out of the sampling scheme).

The programs used to compute semi-variograms and to do the ordinary kriging (OK) is a part of GSLIB which is a library of geostatistical programs [23].

### 3.3 Geometric rectification

Raw sensor data often contain too many distortions to be used as a map. The process of correcting these errors is known as geometric correction. One of the key subjects of this thesis is the fusion between the *in situ* measurements performed at the test sites and the polarimetric dual frequency EMISAR data. In order to match these remotely sensed data with the *in situ* data the exact geographical position of a particular pixel in the SAR image has to be known. However, as explained in Section 2.3 the EMISAR data to be used are geometrical distorted and a geometric correction is therefore required.

#### 3.3.1 Introduction

The image to be geometrically rectified or warped is called the input image and the rectified result is called the output image. In this context the transformation is done by aligning the input image with another image called the reference image. The geometric rectification of the input image is performed using Ground Control Points (GCP's), which are features identified in both the input and the reference images.

The geometric rectification involves two steps described in the sections below. In Section 3.3.2 is the use of first order polynomials as deformation models reviewed and in Section 3.3.3 the bilinear resampling technique is outlined. The techniques of geometric transformations are described in e.g. Sonka (1993) [77] and Niblack (1985) [52].

#### 3.3.2 Deformation models

The deformation is often described by polynomials of up to third and fourth orders. It is these polynomials that connect the geometrical relationship between the input and the output image, or alternatively the output and the input image.

The output-to-input transformation of first order given by

$$\begin{aligned}x &= a_0 + a_1\hat{x} + a_2\hat{y} \\y &= b_0 + b_1\hat{x} + b_2\hat{y},\end{aligned}$$

maps the point  $(\hat{x}, \hat{y})$  in the output image to the point  $(x, y)$  in the input image, see Figure 3.1. The coefficients of the polynomials  $a_0, a_1, a_2, b_0, b_1, b_2$  are derived through the GCP's in the two coordinate systems. Although only three point pairs are necessary as a minimum for estimating the  $a$  and  $b$  coefficients of the first order polynomial, additional point pairs are often used. This will ensure a better estimation of the coefficients in a least squares sense and a quality measure of how well the transformation fits the points.

The  $a$ -coefficients for a transformation of first order is given by

$$\begin{bmatrix} x_1 \\ \vdots \\ x_N \end{bmatrix} = \begin{bmatrix} 1 & \hat{x}_1 & \hat{y}_1 \\ \vdots & \vdots & \vdots \\ 1 & \hat{x}_N & \hat{y}_N \end{bmatrix} \begin{bmatrix} a_0 \\ a_1 \\ a_2 \end{bmatrix} + \begin{bmatrix} \varepsilon_1 \\ \vdots \\ \varepsilon_N \end{bmatrix},$$

or

$$\mathbf{x} = \mathbf{A}\boldsymbol{\theta} + \boldsymbol{\varepsilon},$$

where  $N$  is the number of point pairs,  $\mathbf{A}$  is the design matrix for the model,  $\boldsymbol{\theta}$  is a vector containing the coefficients and  $\boldsymbol{\varepsilon}$  is the residual vector. The vector containing the coefficients is estimated from

$$\hat{\boldsymbol{\theta}} = (\mathbf{A}^T \mathbf{A})^{-1} \mathbf{A}^T \mathbf{x},$$

assuming that the measurement error is zero. The estimate of the observed geometric error  $\hat{\sigma}_o^2$  for the  $x$  coordinates is

$$\hat{\sigma}_o^2 = \frac{\|\mathbf{x} - \mathbf{A}\hat{\boldsymbol{\theta}}\|^2}{N - \text{rg}(\mathbf{A})}, \quad (3.8)$$

where  $\|\cdot\|$  is the Euclidean norm and  $\text{rg}(\mathbf{A})$  is the rank of matrix  $\mathbf{A}$ . The  $b$ -coefficients and  $\hat{\sigma}_o^2$  for the  $y$  coordinates are derived in a similar manner.

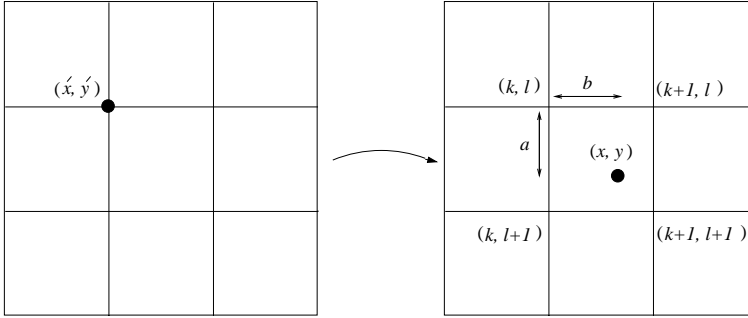


Figure 3.1: Illustration of the bilinear resampling. The point  $(\hat{x}, \hat{y})$  in the output image is mapped to the point  $(x, y)$  in the input image. The neighbours to  $(x, y)$  are located at  $(k, l)$ ,  $(k + 1, l)$ ,  $(k, l + 1)$  and  $(k + 1, l + 1)$ .

In practical applications polynomials of up to third and fourth orders are used. In the case of second order transformation we have

$$\begin{aligned} x &= a_0 + a_1\hat{x} + a_2\hat{y} + a_3\hat{x}^2 + a_4\hat{y}^2 + a_5\hat{x}\hat{y} \\ y &= b_0 + b_1\hat{x} + b_2\hat{y} + b_3\hat{x}^2 + b_4\hat{y}^2 + b_5\hat{x}\hat{y}, \end{aligned}$$

and here at least 6 point pairs are needed.

### 3.3.3 Resampling

After establishing an appropriate transformation each pixel in the output image is assigned a value. However, the position  $(x, y)$  of the pixels in the input image does typically not fit the integer coordinates  $(\hat{x}, \hat{y})$  of the output image. This is because the collections of transformed points give the samples of the output image with non-integer coordinates. However, values on the integer output grid are needed and it is therefore necessary to interpolate between the non-integer points in the input image. This process is called resampling.

The methods that most frequently are used for resampling are nearest neighbour (NN), bilinear and cubic convolution. The simplest method for assigning a value for the output image is the nearest neighbour, which chooses the pixel value in the input image that has its centre closest to the position  $(x, y)$  determined by the transformation. This method has the disadvantage of introducing a position error of at most half a pixel. On the other hand, the method preserves



the original values and the method is therefore preferred in situations where a classification is the intention or the preservation of the radiometric information is needed.

The bilinear resampling makes use of the four pixel values that surround the calculated position  $(x, y)$  in the input image. The interpolated pixel value  $\hat{p}$ , which is assigned the position  $(\hat{x}, \hat{y})$  in the output image is a weighted average between the calculated position and its four neighbours. With reference to Figure 3.1 the bilinear interpolation is given by the equation

$$\begin{aligned} \hat{p}(\hat{x}, \hat{y}) = & (1 - b)(1 - a)p(k, l) + b(1 - a)p(k + 1, l) \\ & + (1 - b)ap(k, l + 1) + abp(k + 1, l + 1). \end{aligned}$$

Due to the averaging nature of the bilinear interpolation the resampling will cause a small decrease in resolution as well as blurring of the output image. However, the problem of the step-like boundaries using nearest neighbour resampling is reduced.

In the cubic convolution or bicubic interpolation the fifteen neighbouring points are used in the resampling. The interpolation copes with the bilinear blurring as well as the step-like boundary problem of the nearest neighbour interpolation. Furthermore it is superior in terms of preserving fine details. The cubic convolution can be performed in many ways, but the result is also a weighted average that is assigned the position  $(\hat{x}, \hat{y})$  in the output image.

The test areas at Gjern and Mols Bjerger are relatively flat and very small and consequently the local incidence angle  $\varphi$  can be considered constant within each area. Using (2.1) this again implies that the ground resolution  $\Delta R_g$  can be considered constant within each area. A polynomial of first order is therefore used in the geometric rectification of the polarimetric EMISAR data covering the test sites.

Due to the varying topography of the areas surrounding the test sites the GCP's have been manually collected within or as close as possible to the test sites. Here the reference images are UTM rectified ortho-photos from 1995 and as input we use the EMISAR data. Due to the speckled nature of these EMISAR data it has been difficult to identify features in both the reference and the input images. The number of GCP's for each test site is therefore only 5 to 8. However, in spite of this small number of GCP's the affine transformation has proved to be quite accurate in terms of how well the transformation fits the points in the areas of the test sites, see page 172 and 210.

The resampling of the restored EMISAR data is performed using the bilinear

interpolation. This method is suitable because the restored regions to be rectified are coherent and homogeneous and without large discontinuities between them. The blurring effect of the bilinear resampling is therefore not significant. The cubic resampling could be used as well, however, there are no distinct fine details in the restored samples containing the test sites and consequently not much is gained. Concerning the nearest neighbour (NN) interpolation we are not interested in preserving the radiometric content in particular but rather the gap between mean amplitude levels. In addition the NN interpolation will cause a geometrical distortion, which is unwanted given the small size of the test areas.

### 3.4 Multiple regression analysis

The main goal of multiple regression is to learn about the association between a dependent variable  $Y_i$  and several independent variables  $x_i$ . This is done by determining the values of parameters for a model that causes the model to best fit a set of data or observations. Here the model in form of a parametric equation can range from simple linear to non-linear models such as polynomials and exponential functions. In this project a linear relationship between the apparent dielectric constant  $K_a$  and the restored EMISAR data is investigated using Multiple Regression Analysis (MRA). For an introduction to MRA refer to Anderson (2003) [3].

#### 3.4.1 Introduction

Consider the  $k$  dimensional stochastic variable  $\mathbf{Y} \in N(\boldsymbol{\mu}, \sigma^2 \boldsymbol{\Sigma})$ , where  $\sigma^2$  is the measure of how well the model as a whole accounts for the variation in the dependent variables and  $\boldsymbol{\Sigma}$  is the dispersion of the  $N$  observations  $\mathbf{x}_1, \mathbf{x}_2, \dots, \mathbf{x}_N$ . In linear regression, the dependent variable or response variable  $Y_i$  is modeled as a linear function of the independent variables or regressors  $x_{i1}, x_{i2}, \dots, x_{ik}$ .

The linear multiple regression model is then

$$y_i = \alpha + \beta_1 x_{i1} + \beta_2 x_{i2} + \dots + \beta_k x_{ik} + \varepsilon_i,$$

where  $\alpha, \beta_1, \dots, \beta_k$  are known as the regression coefficients. The residual is  $\varepsilon_i$  where  $\text{Cor}(\varepsilon_i, \varepsilon_j) = 0, \forall i \neq j$  and  $E(\varepsilon_i) = 0$ . This may also be written in a

matrix form as

$$\begin{bmatrix} Y_1 \\ \vdots \\ Y_N \end{bmatrix} = \begin{bmatrix} 1 & x_{11} & \cdots & y_{1k} \\ \vdots & \vdots & \ddots & \vdots \\ 1 & x_{N1} & \cdots & y_{Nk} \end{bmatrix} \begin{bmatrix} \alpha \\ \beta_1 \\ \vdots \\ \beta_k \end{bmatrix} + \begin{bmatrix} \varepsilon_1 \\ \vdots \\ \varepsilon_N \end{bmatrix},$$

or

$$\mathbf{Y} = \mathbf{x}\boldsymbol{\beta} + \boldsymbol{\varepsilon}.$$

The estimate of the vector  $\boldsymbol{\beta}$  containing the coefficients is

$$\hat{\boldsymbol{\beta}} = (\mathbf{x}^T \boldsymbol{\Sigma}^{-1} \mathbf{x})^{-1} \mathbf{x}^T \boldsymbol{\Sigma}^{-1} \mathbf{Y}.$$

This estimate is BLUE and is derived by minimizing the sum of squared residuals  $\sum_{i=1}^N \varepsilon_i^2$ .

The quantity  $\sigma^2$  is unknown but can be estimated using

$$\hat{\sigma}^2 = \frac{\|\mathbf{Y} - \mathbf{x}\hat{\boldsymbol{\beta}}\|^2}{N - \text{rg}(\mathbf{x})}. \quad (3.9)$$

The measure of how much variation in the dependent variable that can be explained by the model is  $R^2$  given by

$$R^2 = \frac{\|\mathbf{Y} - \bar{\mathbf{Y}}\|^2 - \|\mathbf{Y} - \mathbf{x}\hat{\boldsymbol{\beta}}\|^2}{\|\mathbf{Y} - \bar{\mathbf{Y}}\|^2}. \quad (3.10)$$

The range of  $R^2$  is from 0 to 1 and in general the larger the value the better the model fit. Some reservation should be taken in the interpretation of  $R^2$  because it is affected by the number of regressors in the model. That is  $R^2$  increases with an increasing number of regressors.

The observations to be used in this project are assumed to be multivariate normal and the computations have been performed with PROC GLM from the SAS package [73].

## 3.5 Orthogonal transformation

There is often a high correlation between the different channels or bands in multidimensional data. It has therefore proven useful to generate orthogonal linear transformations of the original bands when analyzing multivariate images. Such a linear method of projection is Principal Components, which is a well known and widely used technique for dimensionality reduction in multivariate image data. Other very successful linear methods for analyzing multivariate images are factor analysis, min/max autocorrelation factors, canonical variables and canonical discriminant functions.

The linear transforms to be focused upon in this thesis are principal components and canonical discriminant functions, which are described in the Sections 3.5.1 and 3.5.2 below. An instructive overview of orthogonal transformations of multichannel image data is given in Conradsen and Ersbøll (1991) and Windfeld (1992) [19], [87].

### 3.5.1 Principal components analysis

Principal Components (PC) reduces the dimensionality within the data and creates linear combinations of the original variables with maximal variance. This classical technique in stochastic multivariate data analysis was originated by Pearson (1901) [63] and later developed by Hotelling (1933). In this project PC are used to detect linear relationships in the restored multivariate EMISAR data and to evaluate the linear dependencies among variables.

#### 3.5.1.1 Introduction

Consider the stochastic vector  $\mathbf{X}^T = (X_1, X_2, \dots, X_p)$  where the variables e.g. are  $p$  dimensional image data. The dispersion matrix of  $\mathbf{X}$  is  $\Sigma$  and without loss of generality we assume  $E(\mathbf{X}) = \mathbf{0}$ . The eigenvalues to  $\Sigma$  are ordered  $\lambda_1 \geq \dots \geq \lambda_i \geq \dots \geq \lambda_p$  and the corresponding orthonormal eigenvectors are  $\mathbf{p}_1, \dots, \mathbf{p}_i, \dots, \mathbf{p}_p$ .

The principal components are then given as

$$\mathbf{Y}_i = \mathbf{a}_i^T \mathbf{X}, \quad i = 1, \dots, p,$$

where the unit vector  $\mathbf{a}_i$  has the property

$$\text{Var}(\mathbf{Y}_i) = \sup_{\mathbf{a} \in M_i} \frac{\text{Var}(\mathbf{a}^T \mathbf{X})}{\mathbf{a}^T \mathbf{a}} = \sup_{\mathbf{a} \in M_i} \frac{\mathbf{a}^T \boldsymbol{\Sigma} \mathbf{a}}{\mathbf{a}^T \mathbf{a}} = \lambda_i$$

where

$$M_i = \{\mathbf{a} | \mathbf{a}^T \mathbf{p}_1 = \cdots = \mathbf{a}^T \mathbf{p}_{i-1} = 0\}.$$

From the above we see that the first principal component  $\mathbf{Y}_1$  is the linear combination of the original variables that accounts for the greatest possible variance  $\lambda_1$ . The  $i$ 'th principal component  $\mathbf{Y}_i$  is the linear combination of the original variables that has the greatest possible variance  $\lambda_i$  and is uncorrelated with the first  $i - 1$  principal components.

Principal component analysis reduces the dimensionality of a set of data while preserving the structure. Furthermore, since the variance is maximized in the PC the first components are often more interpretable than the original data (images). The fraction of the total variation that is explained by the first  $i$  principal components is therefore given by

$$\frac{\lambda_1 + \cdots + \lambda_i}{\lambda_1 + \cdots + \lambda_i + \cdots + \lambda_p}.$$

A drawback of PC is that it does not take the spatial context into account. This has the consequence that the transformation is invariant to all permutations of the pixels in the image. A linear method of projection, which is able to cope with this problem and incorporate the spatial context in images is the Minimum/Maximum Autocorrelation Factor (MAF) transformation.

Unfortunately PC depend critically on the units in which the original variables are measured. If the PC transformation is performed on the standardized variables e.g. the correlation matrix instead of the dispersion matrix  $\boldsymbol{\Sigma}$ , this problem is eliminated. The PC analyses to follow have been performed with PROC PRINCOMP from the SAS package [73].

### 3.5.2 Canonical discriminant analysis

In Canonical Discriminant Analysis (CDA) differences between sets of observations are maximized, see Conradsen and Ersbøll (1991) [19]. CDA is in this thesis used to generate linear combinations of the variables in the restored EMISAR data with the highest possible between-group correlations.

#### 3.5.2.1 Introduction

Consider the  $k$ -classes or populations  $\pi_1, \dots, \pi_k$  with  $n_1, \dots, n_k$  observations (pixels), where each observation is a  $p$  dimensional vector  $\mathbf{x}^T = (x_1, x_2, \dots, x_p)$ . The group means are

$$\bar{\mathbf{x}}_i = \frac{1}{n_i} \sum_{j=1}^{n_i} \mathbf{x}_{ij}, i = 1, \dots, k,$$

and the overall mean is

$$\bar{\mathbf{x}} = \frac{1}{N} \sum_{i=1}^k \sum_{j=1}^{n_i} \mathbf{x}_{ij},$$

where  $N = \sum n_i$  is the total number of observations. The among-groups variation is then

$$\mathbf{A} = \sum_{i=1}^k n_i (\bar{\mathbf{x}}_i - \bar{\mathbf{x}})(\bar{\mathbf{x}}_i - \bar{\mathbf{x}})',$$

and the within-groups variation

$$\mathbf{W} = \sum_{i=1}^k \sum_{j=1}^{n_i} (\mathbf{x}_{ij} - \bar{\mathbf{x}}_i)(\mathbf{x}_{ij} - \bar{\mathbf{x}}_i)'$$

The Rayleigh coefficient is

$$\phi(\mathbf{d}) = \frac{\mathbf{d}' \mathbf{A} \mathbf{d}}{\mathbf{d}' \mathbf{W} \mathbf{d}},$$

and maximizing  $\phi(\mathbf{d})$  gives the direction  $\mathbf{d}_1$  with the maximum variation between group means relative to within-group variation. Here  $\mathbf{d}_1$  is the eigenvector corresponding to the largest eigenvalue of  $\mathbf{A}$  with respect to  $\mathbf{W}$ . The first canonical discriminant function is  $\mathbf{d}'_1\mathbf{x}$  and further discriminant functions can be found by maximizing  $\phi(\mathbf{d})$  under the constraint that  $\mathbf{d}'_i\mathbf{x}$  is uncorrelated with the previous variables. This process of computing linear combinations can be continued until the number of canonical discriminant functions equals

$$\min(k - 1, p).$$

CDA is robust to mild deviations from normality, which is implicitly assumed. However, nonlinearity or clustering of the observations can degrade the performance.

In this project it is assumed that the observations are mutually independent and that the distribution within each class is multivariate normal. The CDA computations have been performed with PROC CANDISC from the SAS package [72].

## 3.6 Classification

Classification is the process of sorting observations e.g. pixels into a finite number of individual categories based on a set of criteria. If a pixel satisfies one of those criteria the pixel is assigned a certain class label. There are basically two types of classification algorithms, namely, the supervised and the unsupervised classifier.

The supervised classifier Multiple Discriminant Analysis (MDA) and the unsupervised classifier Cluster Analysis (CA) is described below in the Sections 3.6.1 and 3.6.2. In this thesis these two types of classifiers are applied in the analyses of the multivariate restored EMISAR data and their performances are compared.

### 3.6.1 Multiple discriminant analysis

In Discriminant Analysis (DA) the classes are determined beforehand in terms of training samples or areas. The objective is here to determine the combination of variables that best discriminates between two or more classes. In case of more than two classes the classification is often referred to as Multiple Discriminant Analysis (MDA). DA is used for several purposes e.g. to investigate differences among classes or discard variables which are little related to group distinctions.

		Choice			
		$\pi_1$	$\pi_2$	$\cdots$	$\pi_k$
Population	$\pi_1$	0	$L(1, 2)$	$\cdots$	$L(1, k)$
	$\pi_2$	$L(2, 1)$	0	$\cdots$	$L(2, k)$
	$\vdots$	$\vdots$	$\vdots$	$\ddots$	$\vdots$
	$\pi_k$	$L(k, 1)$	$L(k, 2)$	$\cdots$	0

Table 3.1: Loss function

In this context MDA is performed on the multivariate restored EMISAR data using training areas. The training areas are here taken to represent different physical properties in the test sites such as variations in biomass, vegetation characteristics and soil moisture contents. For an introduction to DA refer to Anderson (2003) [3]. A Danish introduction to DA and related topics can be found in Conradsen (1984) [17].

### 3.6.1.1 Introduction

The problem of classification is to classify the observation

$$\mathbf{x} = \begin{pmatrix} x_1 \\ x_2 \\ \vdots \\ x_p \end{pmatrix}$$

into one of the predetermined populations or classes  $\pi_1, \pi_2, \dots, \pi_k$ . Here  $\mathbf{x}$  is a vector of  $p$  measured or derived features characterizing the observation.

The conditional density function

$$f_i(\mathbf{x}) = p(\mathbf{x}|\pi_i), \quad i = 0, 1, \dots, k$$

specifies the probability that the observation  $\mathbf{x}$  belongs to the class variable  $\pi_i$ . In situations where prior experience or belief of the class variable  $\pi_i$  is available the *a priori* probability of class  $\pi_i$  is denoted

$$p(\pi_i) = p_i, \quad i = 0, 1, \dots, k.$$



Through Bayes's theorem it now is possible to express the *a posteriori* probability

$$\begin{aligned} p(\pi_i|\mathbf{x}) &= \frac{p(\mathbf{x}|\pi_i)p(\pi_i)}{\sum_{j=1}^k p(\mathbf{x}|\pi_j)p(\pi_j)} \\ &= \frac{p_i f_i(\mathbf{x})}{h(\mathbf{x})}, \end{aligned}$$

which denotes the probability that the class is  $\pi_i$  given observation  $\mathbf{x}$ . The denominator  $h(\mathbf{x})$  serves as a normalization factor that ensures that the *a posteriori* probabilities sum to unity. The importance of Bayes's theorem is that it is possible to make optimal decisions based on the knowledge of the conditional density function  $f_i(\mathbf{x})$  and the prior probability  $p_i$ .

In many applications there may be serious consequences if a wrong classification is made e.g. classifying an image of a tumour as normal. We therefore define a loss function  $L(j, i)$ ,  $i \neq j$  as shown in Table 3.1. Here it appears that no loss is expected when the right choice is made, whereas a penalty term is associated with wrong decisions.

Using the loss function in Table 3.1 the expected loss  $E_{\mathbf{x}}\{L(j, i)\}$  for choosing class  $\pi_i$  is given by

$$\begin{aligned} E_{\mathbf{x}}\{L(j, i)\} &= L(1, i)p(\pi_1|\mathbf{x}) + L(2, i)p(\pi_2|\mathbf{x}) + \dots + L(k, i)p(\pi_k|\mathbf{x}) \\ &= -\frac{1}{h(\mathbf{x})}S_i^*, \end{aligned}$$

where the discriminant score  $S_i^*$  is

$$S_i^* = -L(1, i)p_1 f_1(\mathbf{x}) - L(2, i)p_2 f_2(\mathbf{x}) - \dots - L(k, i)p_k f_k(\mathbf{x}).$$

The Bayes solution of the classification problem is to choose the class  $\pi_i$  that minimizes the expected loss  $E_{\mathbf{x}}[L(j, i)]$  which is equivalent to maximizing  $S_i^*$ . In other words we choose  $\pi_\nu$  if

$$S_\nu^* \geq S_i^*, \quad \forall i.$$

If all losses  $L(j, i)$ ,  $i \neq j$  are equal then the discriminant score  $S_i^*$  can be simpli-

fied to

$$S'_i = p_i f_i(\mathbf{x}),$$

which corresponds to choosing the class with the maximum *a posteriori* probability.

Supported by the *central limit theorem* and due to its analytical simplicity the multivariate normal distribution

$$f_i(\mathbf{x}) = \frac{1}{\sqrt{2\pi^p}} \frac{1}{\sqrt{\det \boldsymbol{\Sigma}_i}} \exp\left(-\frac{1}{2}(\mathbf{x} - \boldsymbol{\mu}_i)^T \boldsymbol{\Sigma}_i^{-1}(\mathbf{x} - \boldsymbol{\mu}_i)\right), \quad (3.11)$$

is a common choice for expressing the class conditional density function of the feature vector  $\mathbf{x}$ . When equal losses and known priors are considered we therefore can apply the logarithm to the discriminant score  $S'_i$ , which leads to the quadratic discriminant function of the form

$$S_i = -\frac{1}{2} \log(\det \boldsymbol{\Sigma}_i) - \frac{1}{2}(\mathbf{x} - \boldsymbol{\mu}_i)^T \boldsymbol{\Sigma}_i^{-1}(\mathbf{x} - \boldsymbol{\mu}_i) + \log p_i,$$

where the common factor  $2\pi^{-p/2}$  is neglected. In the case of equal covariance matrices ( $\boldsymbol{\Sigma}_i = \boldsymbol{\Sigma}$ ) the discriminant function is linear. The decision boundaries for classification are given by the regions where the discriminant functions are equal.

In many applications a rejection threshold is introduced in the classification procedure. Hereby it is possible to exclude observations that are too uncertain i.e. too far from known classes. In image analysis this is useful in situations where one extrapolates from the training areas to the rest of the image. This is conveniently done using the *Mahalanobis* distance

$$D_i = (\mathbf{x} - \boldsymbol{\mu}_i)^T \boldsymbol{\Sigma}_i^{-1}(\mathbf{x} - \boldsymbol{\mu}_i),$$

which is the distance from observation  $\mathbf{x}$  to the class mean  $\boldsymbol{\mu}_i$  with respect to  $\boldsymbol{\Sigma}_i^{-1}$ . Surfaces of constant probability in (3.11) are hyper-ellipsoids on which  $D_i$  is constant.

In this thesis the individual within-group covariance matrices  $\boldsymbol{\Sigma}_i$  are estimated from training data. It is here assumed that the observations are mutually independent and that the distribution within each class is multivariate normal. The

discriminant function to be used is quadratic with equal prior probabilities and losses. Furthermore the rejection threshold is set to the commonly used p value 0.05. The supervised classification is carried out using PROC DISCRIM from the SAS package [72].

### 3.6.2 Cluster analysis

It is usually expected that observations that are far apart belong to different classes or clusters, while observations that are close to each other are assigned to the same cluster. In Cluster Analysis (CA) the clusters are not predetermined and the aim is therefore to determine the best way of grouping data.

The clustering method to be focused upon in this thesis is MacQueen's non-hierarchical clustering algorithm *k-means* [47]. The k-means algorithm is chosen because we wish to study the natural grouping of the multivariate restored EMISAR data using different number of clusters.

In Baggesen, Nielsen and Larsen (2001) initial exploratory analysis of multivariate image data is carried out using a SMAF transformation and a fuzzy k-means algorithm [5]. For a thorough treatment of CA refer to Anderberg (1973) [1].

#### 3.6.2.1 Introduction

The MacQueen's *k-means* algorithm, which is a nearest centroid sorting method, can be described as follows: A number of clusters  $k$  is chosen in advance and a set of points called *cluster seeds* is selected. In order to form temporary clusters each observation is assigned to the nearest seed. Next, the new seed points are generated by replacing the old seed points by the mean vectors (centroids) of the temporary clusters. This procedure is repeated until no further grouping of the data occurs.

If a given seed point is chosen as the mean vector  $\bar{\mathbf{x}}_j$  of a cluster  $j$  then the sum of squared deviations between the seed point and the  $N_j$  data units in the cluster will be a unique minimum. Naturally, the algorithm therefore seeks to partition the data points into  $k$  disjoint subsets in such a way that the total within group sum of squares

$$E = \sum_{j=1}^k \sum_{i=1}^{N_j} \|\mathbf{x}_{ij} - \bar{\mathbf{x}}_j\|^2,$$

is minimized. The mean vector  $\bar{\mathbf{x}}_j$  is

$$\bar{\mathbf{x}}_j = \frac{1}{N_j} \sum_{i=1}^{N_j} \mathbf{x}_{ij},$$

and we note that it is the Euclidean distances between the centroid of cluster  $j$  and its  $N_j$  data units that are used.

It can be shown that the total number of different ways a set of  $N$  data units can be partitioned into  $k$  clusters is a finite number given by

$$\mathcal{S} = \frac{1}{k!} \sum_{i=0}^{i=k} (-1)^{k-i} \binom{k}{i} i^N,$$

which is a Stirling number of the second kind. The algorithm therefore is guaranteed to reach the global minimum if the  $\mathcal{S}$  partitions are generated [1]. We see that  $\mathcal{S}$  becomes very large for large data sets and algorithms such as simulated annealing and gradient descent methods are consequently often used in the process of searching for the global minimum.

The software used in our application for disjoint clustering of restored EMISAR data is PROC FASTCLUS developed by SAS [72]. This procedure is chosen because of its ability of finding good clusters of very large data sets with only a few passes over the data. The program uses the nearest centroid sorting method introduced by Anderberg (1973) and described above. Here the analysis is based on Euclidean distances and each observation is assigned to one and only one cluster. The FASTCLUS procedure combines an effective method for finding initial clusters with a standard iterative algorithm for minimizing the sum of squared distances from the cluster means.

# Markov random fields

---

Many of the tasks in computer vision can be regarded as optimization problems with respect to a function depending on one or more variables. The function which is often referred to as the cost or objective function of the problem serves as a heuristic guide in the search for the optimal solution.

Unfortunately these optimization problems are not easy to solve in terms of finding the optimal solution. Firstly, an exhaustive search is not feasible due to the often very large search space. Secondly, the objective function cannot be expressed in a closed form. However, the optimal solution can be located by resorting to numerical optimization techniques.

The optimization problem in relation with image restoration can be formulated as the minimization of an energy function. In this case the energy function corresponds to the cost or objective function of the problem. The energy function is typically non-convex having a large number of local minima. Normally these local minima are due to artifacts and noise in the image and are therefore viewed as sub-optimal solutions. The ultimate goal, however, is to retrieve the global energy minimum which corresponds to the optimal solution.

## 4.1 Introduction

In this chapter two different optimization schemes based upon Markov Random Field (MRF) are described. The optimization schemes presented are in Chapter 5 applied on synthetic SAR data and EMISAR data using various *a priori* models.

The first technique is the local optimizer Iterated Conditional Modes (ICM) suggested by Besag (1986) [7]. It is a quick deterministic algorithm, which based on a down-hill strategy unfortunately is likely to track a sub-optimal solution. The second optimization scheme is Simulated Annealing (SA). SA is a stochastic method proposed independently by Kirkpatrick (1983) and Cerny (1985) for global optimization [43], [13]. SA also relies on a down-hill strategy but instead of performing gradient descent the successful applications of SA rely on random search methods such as Metropolis algorithm or Gibbs sampler [50], [29]. In contrast to ICM SA is therefore able to escape local minima and thereby finally reach the global minimum.

In Section 4.2 the theory of Markov random fields and Gibbs random fields are reviewed. The definition of cliques is given and Bayes rule is outlined. Section 4.3 contains a description of Iterated conditional modes (ICM) and in Section 4.4 the concepts of Simulated Annealing (SA) are outlined.

## 4.2 Random fields

Let  $\mathbf{X} = X_1, \dots, X_n$  be a family of random variables defined on the (two-dimensional) region  $S$ , which has been partitioned into  $n$  pixels. Assume further that  $\Lambda$  denotes the corresponding state space i.e. the set of all possible values  $x_i$  which the random variable  $X_i$  can take. The family  $\mathbf{X}$  is called a random field. We use the notation  $X_i = x_i$  to denote the event that  $X_i$  takes the value or label  $x_i$  and the notation  $X_1 = x_1, \dots, X_n = x_n$  to denote the joint event. For simplicity, a joint event is abbreviated as  $\mathbf{X} = \mathbf{x}$  where  $\mathbf{x} = \{x_1, \dots, x_n\}$  is a configuration of  $\mathbf{X}$ , corresponding to a realization of the field. The set of all possible configurations on  $S$  is called  $\Omega$ . For a discrete label set  $\Lambda$ , the probability that random variable  $X_i$  takes the label  $x_i$  is denoted  $P(X_i = x_i)$  abbreviated as  $P(x_i)$  unless there is a need to elaborate the expressions, and the joint probability is denoted  $P(\mathbf{X} = \mathbf{x}) = P(X_1 = x_1, \dots, X_n = x_n)$  and abbreviated  $P(\mathbf{x})$ . For a continuous  $\Lambda$ , we have probability density functions (pdf's),  $p(X_i = x_i)$  and  $p(\mathbf{X} = \mathbf{x})$ .

5	4	3	4	5
4	2	1	2	4
3	1		1	3
4	2	1	2	4
5	4	3	4	5

Figure 4.1: Ordering of neighbours on a regular lattice.

### 4.2.1 Markov random fields

$\mathbf{X}$  is said to be a Markov Random Field (MRF) on  $S$  with respect to a neighbourhood system  $N$  if and only if the following two conditions are satisfied [29].

**Definition 4.1** Let  $S = \{s_0, s_1, \dots, s_{n-1}\}$  be a set of sites. A neighbourhood system  $N = \{N_s, s \in S\}$  is a collection of subsets of  $S$  for which

1.  $s \notin N_s$
2.  $r \in N_s \Leftrightarrow s \in N_r$ .

**Definition 4.2** A random field  $\mathbf{X}$  is a Markov Random Field (MRF) with respect to the neighbourhood system  $N = \{N_s, s \in S\}$  iff

1.  $P(\mathbf{X} = \mathbf{x}) > 0, \forall \mathbf{x} \in \Omega$
2.  $P(X_s = x_s | X_r = x_r, r \neq s) = P(X_s = x_s | X_r = x_r, r \in N_s), \forall s \in S \wedge \mathbf{x} \in \Omega$ .

The first *positivity* condition denotes that none of the possible random field realizations should have zero probability. This is a technical assumption that usually is satisfied in practice. The second condition is the Markov property that states that the probability of  $x_s$  given the values of all other sites depends only on the values of the sites in the neighbourhood of  $s$  [6].

### 4.2.2 Cliques

A graph on the finite lattice  $S$  is denoted  $\mathcal{G} = (\mathcal{V}, \mathcal{E})$  where  $\mathcal{V}$  is the set of neighbours that are connected with an edge  $\mathcal{E}$ .

**Definition 4.3** A clique  $c$  for  $(\mathcal{V}, \mathcal{E})$  is a subset of  $S$  for which every pair of sites are neighbours.

Individual sites are, by definition, cliques. The usual neighbourhood system for a square grid in image analysis defines the first-order neighbours of a pixel as the four pixels sharing a side with the given pixel, see Figure 4.1. The single-site, horizontal and vertical pair-site cliques corresponding to a first-order neighbourhood configuration are shown in Figure 4.2 (a). Second-order neighbours are the four pixels sharing a corner and Figure 4.2 (a)–(b) illustrates the clique types that exist when the neighbourhood is restricted to  $2nd$  order. Higher order neighbours are defined in an analogous manner as illustrated in Figure 4.1 [46].

The clique types for a  $2nd$  order neighbourhood include not only those in Figure 4.2 (a) but also diagonal pair-site cliques, triple-site and quadruple-site cliques, which are shown in Figure 4.2 (b). The set of all cliques for  $(\mathcal{V}, \mathcal{E})$  is

$$C = C_1 \cup C_2 \cup C_3 \cup \dots \cup C_n,$$

where  $C_1, C_2$  and  $C_3$  denote the collection of single-site, pair-site cliques, triple-site and quadruple-site cliques [42].

Together with the pair-site clique types in Figure 4.2 are shown their corresponding weights. These weights, and other parameters, are empirically derived using an optimization scheme presented in Section 5.2.

In the context of feature extraction the clique structure is vital because position information is very important to determine the value of the centre pixel  $x_i$ , see Park and Kurz (1996) [62]. In order to take full advantage of the information embedded in the relative spatial positions of pixels, all clique types involved in a  $2nd$  order neighbourhood system should be taken into account, see Figure 4.2. In Figure 4.3 is shown the 25 interactions involved in a  $2nd$  order neighbourhood system when all teen clique types in Figure 4.2 are used.



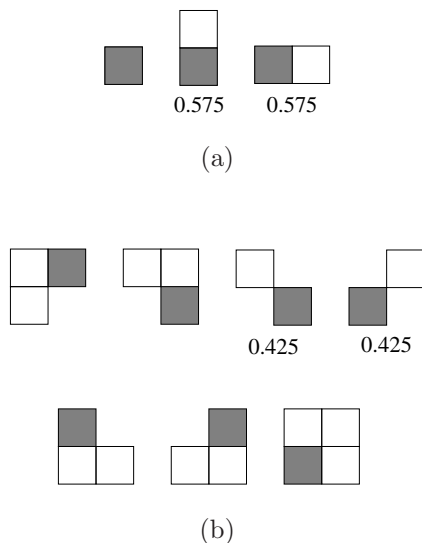


Figure 4.2: (a) cliques for a 1. order neighbourhood and (b) additional cliques for a 2nd order neighbourhood configuration. Associated with the pair-site cliques are their empirically derived weights.

### 4.2.3 Gibbs random fields

Markov random fields described in the terms of Gibbs distribution are known as Gibbs Random Fields (GRF). Hammersley-Clifford stated the following theorem:

**Theorem 4.4** (*Hammersley-Clifford*). *A random field  $\mathbf{X}$  is a Gibbs random field with respect to the neighbourhood system  $N$  if and only if  $\mathbf{X}$  is a Markov random field with respect to  $N$ .*

The Gibbs distribution is an exponential distribution that expresses certain desired structural properties. A Gibbs random field describes the global properties of an image in terms of a joint probability distribution function (pdf) for all the random variables in the considered field. A set of random variables is said to be a Gibbs Random Field (GRF) on  $S$  with respect to  $N$  if and only if its configurations obey a Gibbs distribution. MRFs are expressed in terms of local conditional pdfs through the clique potentials.

The Gibbs distribution is based on the principle of thermodynamics, where the probability that a molecule is at a specific state of energy  $E$  is governed by the

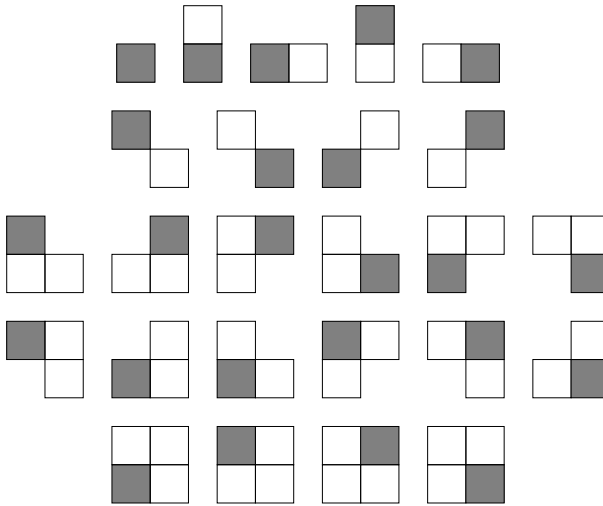


Figure 4.3: All 25 interactions involved in a  $2nd$  order neighbourhood system.

Boltzmann distribution

$$p(E) = \frac{1}{Z(T)} \exp\left(-\frac{E}{kT}\right), \quad (4.1)$$

where the partition function  $Z(T)$  is a normalizing constant,  $T$  the temperature and  $k$  Boltzmann's constant. The quantity  $kT$  equals energy and it will be substituted by  $T$  in the succeeding.

The Gibbs distribution now takes the form

$$p(\mathbf{X} = \mathbf{x}) = \frac{1}{Z(T)} \exp\left(-\frac{U(\mathbf{x})}{T}\right), \quad (4.2)$$

where

$$Z(T) = \sum_{\mathbf{x} \in \Omega} \exp\left(-\frac{U(\mathbf{x})}{T}\right).$$

$T$  controls the peak of the distribution and  $U(\mathbf{x})$  is the energy function. For  $T \rightarrow \infty$  (4.2) is a uniform distribution on  $\Omega$  i.e. all configurations have equal

probabilities. In the limit  $T \rightarrow 0$  (4.2) is concentrated only on configurations with global minimal energy [83]. One of the most studied models in statistical mechanics, which makes use of MRF is the Ising model (1925). It is a simplified model for describing ferromagnetism. Later the use of MRF in image processing became mostly inspired by Geman and Geman (1984) [29].

An interesting property of Gibbs measure is that it maximizes the entropy

$$-\sum_{\mathbf{x} \in \Omega} p(\mathbf{x}) \ln p(\mathbf{x}),$$

for a given energy, which makes it possible to assign a probability to an event [40].

The *positivity* condition in definition 4.2 ensures that an entire realization of zeros is possible and the relative probability measure  $Q(\mathbf{x})$  may be defined

$$Q(\mathbf{x}) \equiv \ln \frac{p(\mathbf{x})}{p(\mathbf{0})}.$$

It can be shown that the local characteristics is determined by  $Q(\mathbf{x})$  which has the following form [6]:

$$\begin{aligned} Q(\mathbf{x}) = & \sum_{1 \leq i \leq n} x_i G_i(x_i) + \sum_{1 \leq i < j \leq n} x_i x_j G_{i,j}(x_i, x_j) + \\ & \sum_{1 \leq i < j < k \leq n} x_i x_j x_k G_{i,j,k}(x_i, x_j, x_k) + \dots \\ & + x_1 x_2 \dots x_n G_{1,2,\dots,n}(x_1, x_2, \dots, x_n). \end{aligned}$$

Because of the Markov condition all cliques that do not include  $x_i$  will be cancelled out and the energy function  $U(\mathbf{x})$  becomes

$$Q(\mathbf{x}) - Q(x_i) = \sum_{c \in C} V_c(\mathbf{x}),$$

where the potential function  $V_c$  depends only on  $x_s, s \in C$ .

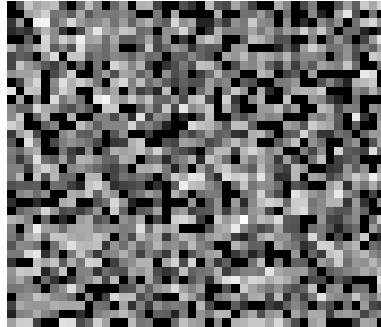


Figure 4.4: The C-band HH polarized EMISAR amplitude data covering a relatively homogeneous grassland area at Mols Bjerge. The data are stretched linearly between their mean  $\pm 3$  std

In the following only pair-site cliques are used to derive the potential  $V_c$ . As illustrated in Figure 4.2 the empirically derived weights for the horizontal and the vertical cliques are 0.575 and the weights for the diagonal cliques are 0.425. This has the implication that the four pixels sharing a side with the centre pixel  $x_i$ , have a larger impact on the restored results than the four pixels sharing a corner. The use of larger weights for horizontal and vertical cliques is natural in the sense, that the Euclidian distance between the centre of pixel  $x_i$  and the center of the pixels sharing a side is smaller than the Euclidian distance between the centre of pixel  $x_i$  and the center of the pixels sharing a corner.

#### 4.2.4 Bayes rule

When performing the unsupervised restoration of the SAR data, the discrete grey values (amplitudes) themselves represent the labels e.g. classes.

The true pixel labeling is denoted  $\mathbf{x}^* = \{x_1^*, x_2^*, \dots, x_n^*\}$  and the set of observable random variables is denoted  $\mathbf{y} = \{y_1, y_2, \dots, y_n\}$ , where  $y_i$  is the feature vector associated with the  $i$ th pixel.

The key subject is to find the *a priori* model  $\{H_i\}$  that best describes the data. By using Bayes' rule

$$p(\mathbf{x}|\mathbf{y}, H_i) = \frac{p(\mathbf{y}|\mathbf{x}, H_i)p(\mathbf{x}|H_i)}{p(\mathbf{y}|H_i)} \quad (4.3)$$

1	4	1	4	1	4
3	2	3	2	3	2
1	4	1	4	1	4
3	2	3	2	3	2
1	4	1	4	1	4
3	2	3	2	3	2

Figure 4.5: Coding pattern for a  $2nd$  order neighbourhood where pixels with the same number are members of the same coding pattern.

the MAP (Maximum *A Posteriori*) estimate is obtained by choosing the estimate  $\hat{\mathbf{x}}$  and the *a priori* model  $\{H_i\}$  that maximizes (4.3) [21].

In the ideal case when the  $y_1, y_2, \dots, y_n$  are conditionally independent, then

$$p(\mathbf{y}|\mathbf{x}) = \prod_{i=1}^n p(y_i|x_i) \quad (4.4)$$

is valid where all the  $y_i$  have the conditional density function  $p(y_i|x_i)$  depending on  $x_i$  only. Unfortunately, due to a *point spread function*, this is not quite true for the single-look SAR data [59]. Although there are some natural clutter these correlations will in the following be considered so small that they can be neglected. We furthermore assume, that the true scene  $\mathbf{x}^*$  is a realization of a locally dependent MRF with the *a priori* distribution  $p(\mathbf{x})$ .

In Figure 4.4 is shown a small sample of C-band HH polarized EMISAR amplitude data from a relatively homogeneous grassland at Mols Bjerge. The estimated empirical autocorrelation at lag 1 in the azimuth direction is 0.18, which is significant but not too high. The empirical autocorrelation at lag 1 in the range direction is 0.05 and thereby negligible. Here it should be noted that some correlation is to be expected due to possible variations in the physical environment within the grassland.

By using the local property of MRFs and the Gibbs distribution (4.2) only pixels in the neighbourhood of pixel  $i$  need be considered. We can therefore write

$$p(x_i|x_j, i \neq j) \equiv p_i(x_i|x_j, j \in N_i), \quad (4.5)$$

where  $p_i$  is specific to pixel  $i$  [7]. Actually (4.4) also defines  $\mathbf{Y}$  given  $\mathbf{X}$  as a MRF although with an empty neighbourhood. Both  $p(\mathbf{x})$  and  $p(\mathbf{y}|\mathbf{x})$  are according to Theorem 4.4 therefore Gibbs distributions and being a product of those functions the *a posteriori* distribution will inherit this property. By combining Bayes' theorem with (4.4) and (4.5) it now follows that

$$p(x_i|\mathbf{y}, \hat{x}_j, i \neq j) \propto p(y_i|x_i)p_i(x_i|x_j, j \in N_i). \quad (4.6)$$

The conditional density function  $p(y_i|x_i)$  to be used in this context is

$$p(y_i|x_i) \propto \exp\left\{-\frac{\alpha(y_i - \mu)^2}{2\sigma_i^2}\right\}, \quad (4.7)$$

where the selected mean level  $\mu$  and the variance  $\sigma_i$  is estimated from the local statistics. The weighting factor  $\alpha$  is a shape parameter which controls the edge preserving properties of the restoration. A small value will give a smooth restoration whereas a high value preserves details.

In order to prevent artifacts in the restored images the pixels are partitioned into a disjoint set of pixels called a coding pattern [6]. This will ensure that no two pixels, which are neighbours, are visited in the same coding pattern. Pixels belonging to the same coding pattern are conditionally independent and for a  $2nd$  order neighbourhood one iteration consists of four coding patterns called sweeps. Figure 4.5 illustrates the procedure to be used in the restoration process. Here pixels with the same number are members of the same coding pattern.

### 4.3 Iterated conditional modes

Consider the case where the final model of the previous image is propagated to the current image and the changes between these two image sequences are sufficiently small. Then it will be possible to track the global energy minimum through a local optimization technique.

Iterated Conditional Modes (ICM) is a deterministic relaxation technique with the properties of a local optimizer and proposed by Besag 1986 [7]. Because deterministic relaxation only makes changes which improve the current configuration it is faster than stochastic relaxation methods which makes changes at

random. It should be noted that as the ICM algorithm is regarded as a local optimization technique rather than a global one the quality of the final result is very dependent on the initial estimate [71].

Setting  $T = 1$  in (4.2) the basic idea of ICM is that an estimate of  $\mathbf{x}$  may possibly be enhanced by replacing the current estimate  $\hat{x}_i$  with the one that maximizes (4.6). This principle for estimating pixel labels by ICM is implemented as follows:

1. Choose a MRF model for the true label  $\mathbf{x}^*$ .
2. Initialize  $\hat{\mathbf{x}}$  by choosing  $x_i$  as the value  $\hat{x}_i$  that maximizes  $p(y_i|x_i)$  for each pixel  $i$ .
3. For  $i$  from 1 to  $n$  update  $\hat{x}_i$  by the value of  $x_i$  that maximizes

$$p(y_i|x_i)p(x_i|\hat{x}_j, j \in N_i)$$

4. Repeat (3)  $N_{iter}$  times or until no changes occur.

The convergence is assured by

$$p(\mathbf{x}|\mathbf{y}) = p(x_i|\mathbf{x}, \hat{x}_j, i \neq j)p(x_j|\mathbf{y})$$

so that  $p(\hat{\mathbf{x}}|\mathbf{y})$  never decreases [7]. The algorithm will normally converge within 6–10 iterations to the final estimate of  $\mathbf{x}^*$ .

In our context the selected number of equally spaced grey-levels or classes for the unsupervised restoration of the SAR data is 1000. Strictly speaking we then are performing a segmentation but due to the high number of grey-levels it is safe to view the reconstruction as a restoration.

It should be noted that in the case where the parameters  $\theta$  and  $\phi$  are unknown it is possible to obtain estimated values  $\hat{\theta}$  and  $\hat{\phi}$  which maximize  $p(\mathbf{x};\theta)$  and  $p(\mathbf{y}|\mathbf{x};\phi)$ . This can be done either by using relevant training data alone or if no training data are available the parameter estimation can be carried out simultaneously with the algorithm optimization [6].

## 4.4 Simulated annealing

Simulated Annealing (SA) is a stochastic relaxation technique based on the principles of thermodynamics. Metropolis *et al.* (1953) presented the algorithm as a method to simulate the equilibrium states of thermodynamic processes [50]. The idea of using SA to approximate the solution of very large combinatorial optimization problems was first introduced by Kirkpatrick *et al.* (1983). They used the technique for the optimization of the traveling salesman problem [43].

Since then the algorithm has been widely used for various types of optimization problems. Geman and Geman (1984) first applied the SA algorithm to image restoration and later Lakshmanan and Derin (1989) and Vandermeulen *et al.* (1994) used the algorithm in image segmentation [45], [84]. Oliver *et al.* (1996) [58] used the algorithm for segmentation of SAR data. For a general description of SA the reader is referred to Laarhoven and Aarts (1987) [83] and Otten and van Ginneken (1989) [60], which covers a wide range of the aspects.

Annealing or *heat bath* refers to the fundamental process in which a solid material is first melted, i.e. the molecules can move freely, and then allowed to cool by slowly reducing the temperature. Provided that the temperature is gradually lowered in stages and under the constraint that at each stage the thermal quasi-equilibrium is reached the molecules will attempt to arrange themselves in low energy states. By carefully continuing the process the molecules will finally form a crystal reflecting that the energy of the material has reached a global minimum.

The collective energy states of the ensemble of particles can be considered the configuration of the material. The probability that a particle is at any energy level can be calculated by use of the Boltzmann distribution (4.1). As the temperature of the material decreases, the Boltzmann distribution tends toward the particle configuration that has the lowest energy.

By applying the basic concepts of the physical annealing process to numerical optimization problems it is possible to develop algorithms which in theory are capable of reaching the global minimum of a given energy function.

### 4.4.1 Mathematical model

The simulated annealing algorithm generates a Markov chain, which at the state of thermal equilibrium approximates the Gibbs distribution. A Markov chain describes a series of trials where the outcome of each trial depends only on the



outcome of the previous one. In our context the previous outcome is the current configuration.

The conditional probability  $P_{ij}(k-1, k)$  denotes the probability that the outcome of the  $k$ 'th trial is  $j$  given that the outcome of the  $(k-1)$ 'th trial is  $i$ . This probability is also called the *transition probability*, which denotes the probability of obtaining configuration  $j$  given configuration  $i$  after the  $k$ 'th transition. If we let  $a_i(k)$  denote the probability of outcome  $i$  at the  $k$ 'th trial then  $a_i(k)$  is defined by the recursion

$$a_i(k) = \sum_l a_l(k-1)P_{li}(k-1, k),$$

where  $l$  is all possible outcomes. Given the initial state  $i$  the probability of reaching  $j$  after  $n$  transitions is  $P_{ij}^n$ . In the case where the conditional probabilities do not depend on  $k$  the Markov chain is called *homogeneous* otherwise it is called *inhomogeneous* [83].

Assuming a homogeneous Markov chain a stationary distribution is given by

**Theorem 4.5** *The stationary distribution  $\mathbf{q}$  of a finite homogeneous Markov chain exists if the Markov chain is irreducible and aperiodic. Furthermore the vector  $\mathbf{q}$  is uniquely determined by the equations:*

$$\begin{aligned} \forall i : \mathbf{q}_i > 0, \sum_i \mathbf{q}_i &= 1, \\ \forall i : \mathbf{q}_i &= \sum_j \mathbf{q}_j P_{ji}. \end{aligned}$$

**Definition 4.6** A Markov chain is irreducible if for all pair of states  $(j, k)$  there is a positive probability of reaching  $k$  from  $j$  in a finite number of transitions:

$$\forall j, k \exists n : P_{jk}^n > 0.$$

**Definition 4.7** A Markov chain is aperiodic if for all states  $i$ , the greatest common divisor of all integers  $n \geq 1$ , such that

$$P_{ii}^n > 0$$

is equal to 1.

The ergodic properties of an inhomogeneous Markov chain are

**Definition 4.8** An inhomogeneous Markov chain is weakly ergodic if for all  $m \geq 1, i, j \in R$

$$\lim_{n \rightarrow \infty} (P_{ik}(m, n) - P_{jk}(m, n)) = 0.$$

**Definition 4.9** An inhomogeneous Markov chain is strongly ergodic if there exists a vector  $\pi$ , satisfying

$$\sum_i \pi_i = 1, \forall i : \pi_i > 0,$$

such that for all  $m \geq 1, i, j \in R$

$$\lim_{n \rightarrow \infty} P_{ij}(m, n) = \pi_j.$$

In SA the homogeneous Markov chain is generated at a fixed temperature until thermal equilibrium is reached. Subsequently, the temperature is decreased, which results in a new homogeneous sequence. The inhomogeneous algorithm generates a single inhomogeneous Markov chain where the temperature is decreased in between each transition.

The convergence properties of the two types of Markov chains have been extensively discussed in Laarhoven (1987) [83]. They both approach the global energy minimum provided that the following relation is satisfied:

$$P(\mathbf{X}(k) \in \mathcal{R}_{opt}) = 1,$$

where  $\mathbf{X}(k)$  denotes the realization of the  $k$ 'th trial as  $k$  approaches infinity and  $\mathcal{R}_{opt}$  is the set of globally minimal configurations. In practice, however, these asymptotic values have to be approximated.

In the following two important methods of sampling are presented. They are known as the Metropolis algorithm and the Gibbs sampler and they both lead to equivalent results.

### 4.4.2 The Metropolis sampler

Metropolis *et al.* first realized that the thermal equilibrium process could be simulated for a fixed temperature by Monte Carlo methods to generate sequences of energy states [50]. These energy states, that can be referred to as a Markov chain, approximate the Gibbs distribution.

The algorithm given below illustrates the general principles of the Metropolis sampler.

1. Choose an initial temperature  $T$ .
2. Make a random change to the current configuration. Let

$$\Delta E = E_{old} - E_{new}, \quad (4.8)$$

be the differences in energy.

3. If  $\Delta E > 0$  then replace the old configuration by the new one; else accept the new configuration with probability  $e^{\Delta E/T}$ .
4. Repeat (2)-(3)  $N_{inner}$  times until thermal equilibrium.
5. Replace  $T$  by a lower temperature.
6. Repeat (2)-(5) until frozen.

As it appears we are looking for the configuration that minimizes a certain energy function  $E$ . In order to achieve this the system is perturbed to yield a new configuration by making a local random change. Here the random change is implemented by choosing a new value from a uniform distribution over the set of possible values.

The energy difference before perturbation  $E_{old}$  and after perturbation  $E_{new}$  is

$$\Delta E = E_{old} - E_{new}$$

If the change in cost function is positive that is  $\Delta E > 0$  the transition is unconditionally accepted.

If on the other hand  $\Delta E \leq 0$  the new perturbed configuration is accepted with a probability of acceptance that depends exponentially on the temperature. This acceptance probability is referred to as the *Metropolis criterion* [50].

Following this criterion to the state of thermal equilibrium at a fixed temperature the system will eventually approach Gibbs distribution. This temperature is then gradually lowered starting at a high value where almost every proposed transition is accepted to a freezing temperature, where no further changes occur.

### 4.4.3 The Gibbs sampler

The Gibbs sampler generates a Markov chain by sampling from the local characteristics of Gibbs distribution. Or in other words the values are sampled from the conditional distribution of a given pixel  $x_i$  given its neighbours. The Gibbs sampler was first introduced by Geman and Geman (1984) and contrary to the Metropolis sampler a new configuration is always accepted. Using this sampling technique the configuration will eventually reach its equilibrium.

### 4.4.4 The cooling schedule

The schedule by which the temperature  $T(k)$  is reduced is called the cooling schedule and is critical to the success of SA. The important parameters that govern the schedule are the initial temperature, the number transitions for each temperature, temperature decrement between successive stages and the stop criterion. Unfortunately a selection of the exact parameters to be used in an annealing scheme requires a detailed knowledge about the energy space. Not surprisingly there therefore in the literature exists a vast number of different heuristics for selecting the parameters.

The selection of the initial temperature should reflect that the system is just melted and is therefore crucial to the ability of SA to find the global minimum. Although the temperature is strongly dependent on the measured data and the initial image the following empirical rule has been proposed: The initial temperature should be chosen so that 80% of all the proposed transitions are accepted [83]. Selecting the initial temperature too high has the effect of smoothing out the features in a configuration whereas a low temperature leads the algorithm to track a local energy minimum.

The length  $l(T)$  of the homogeneous Markov chain, which is generated by the algorithm at a fixed temperature  $T(k)$ , depends heavily on the sampling technique. This length defines the time required to reach the thermal equilibrium at each stage. An informed sampling technique like the Gibbs sampler will normally reach the stage of thermal equilibrium faster than an uninformed sampling strategy. It therefore can be justified to use a Markov chain of length  $l = 1$  in the choice of the Gibbs sampler. In the choice of an uninformed sampling strategy like the Metropolis sampler a larger number is often required in order to achieve thermal equilibrium.

The decrement of the temperature has a major effect on the final result and should be chosen in such a fashion that small Markov chains can re-establish thermal equilibrium after the temperature decrement. The most widely used decrement rule is

$$T(k) = \alpha T(k - 1), \quad (4.9)$$

where  $\alpha$  is the cooling factor in the range of  $0.5 - 0.99$ . Although the rule can lead to good results it is not guaranteed of reaching the global energy minimum and the schedule is referred to as simulated quenching.

If the temperature is decreased under the condition

$$T(k) \geq \frac{c}{\ln(1 + k)}, \quad (4.10)$$

the convergence of the algorithm towards the global energy minimum is ensured as demonstrated by Geman and Geman (1984) [29]. The success of the convergence, however, is relying on the choice of the problem specific constant  $c$ . It has been demonstrated by Hajek (1988) that a sufficient condition for  $c$  is that it has to be larger than the deepest local minimum in the energy space [31].

Concerning the stop criterion the cooling stops when the configuration is frozen or the number of accepted transitions is sufficiently low.



# Restorations

---

The concepts of digital image restoration include the detail preservation and interpretation of information in an image. Image restoration requires some knowledge concerning the noise or degradation mechanism if the objective is an inversion of the process. This knowledge may e.g. include *a priori* information from training data or knowledge regarding the degradation process or physical sensing system.

A successful method for image restoration is the use of MRF in a Bayesian framework. Here the key question is how to design algorithms and energy functions for finding the optimal solution to a vision problem. However, the design of energy functions and optimization algorithms are highly problem specific and consequently no simple answers are given. Many useful models and algorithms have therefore been proposed through the years. They include multi-temporal, multi-scale and hierarchical algorithms and successful MRF models for modeling the energy function are e.g. coupled, compound, binary, binomial and Gaussian MRFs. Various aspects of MRF models and applications may be found in Kindermann (1980), Laarhoven (1987), Chellappa (1993) and Li (1995) [42], [83], [14], [46]. Methods for restoring and segmenting polarized SAR data using MRF are extensively investigated. Numerous algorithms have been proposed and among them are e.g. White (1994), Oliver (1996), Schou and Skriver (2001) and Xu *et al.* (2003) [86], [58], [74], [88].

## 5.1 Introduction

This chapter concerns the development and analyses of algorithms and techniques for restoring single-look SAR amplitude data in the framework of MRF-MAP, see Chapter 4. According to the test site description in Section 1.1 the algorithms must be capable of restoring details, homogeneous regions and edges at very small scales.

The unsupervised restorations are carried out in a signal adaptive mode using a new optimization principle, which makes use of ratios of synthetic SAR data. The *a priori* models to be used in the analyses comprise Gaussian, LaPlace, exponential, Gamma *mean prior* and Gamma *pixel prior* models all representing different shapes of the energy function. These models are implemented in the ICM algorithm and their performances are evaluated using an optimization criterion. The Gamma *pixel prior* is then implemented in a SA algorithm using a specially designed Multi-Temperature Annealing (MTA) schedule. A comparative analysis between ICM and SA using the Gamma *pixel prior* is finally carried out and the algorithm that best explains the structures underlying the EMISAR data covering the test sites at Gjærn and Mols Bjerger is selected. The proposed models and algorithms are applied and evaluated on  $150 \times 150$  single-look C-band VV-polarized EMISAR data and synthetic SAR data.

In Section 5.2 the optimization principle using ratios of SAR data is outlined. Sections 5.3, 5.4 and 5.5 contain a description of the Gaussian *a priori* model, the exponential *a priori* model and the LaPlace *a priori* model. In Section 5.6 the two new models the Gamma *mean a priori* and the Gamma *pixel a priori* are presented. Section 5.7 contains a description of the Gamma sampler and Section 5.8 is discussion.

## 5.2 Optimization

The ratio  $z$  between the SAR data and its restored equivalent is a good measure of how well the restored data describes the true scene. This has been utilized by Oliver and Quegan (1998) who used ratios of SAR data as a quality measure of various reconstructions and segmentations [59]. As it appears from the following the ratio image  $z$  will be pure speckle with mean  $\bar{z} = 1$  and variance  $S^2(z) = 4/\pi - 1$  everywhere, provided that the restoration is perfect and the amplitude data are correctly described by the Rayleigh distribution (2.4). Hence, following those criteria the ratio image will show no features [59]. We get



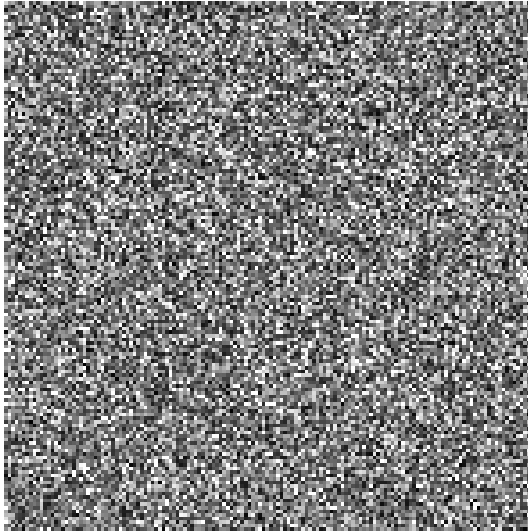
$$\begin{aligned}
\bar{z} &= \frac{1}{N} \sum_{i=1}^k \sum_{j=1}^{n_i} z_{ij} = \frac{1}{N} \sum_{i=1}^k \sum_{j=1}^{n_i} \frac{x_{ij}}{\hat{x}_i} \\
&= \frac{1}{\sum_{i=1}^k n_i} \sum_{i=1}^k n_i \frac{\hat{x}_i}{\hat{x}_i} = \frac{1}{\sum_{i=1}^k n_i} \sum_{i=1}^k n_i \times 1 = 1, \\
S^2(z) &= \frac{1}{N-k} \sum_{i=1}^k \sum_{j=1}^{n_i} (z_{ij} - \bar{z})^2 = \frac{1}{N-k} \sum_{i=1}^k \sum_{j=1}^{n_i} \left( \frac{x_{ij}}{\hat{x}_i} - 1 \right)^2 \\
&= \frac{1}{N-k} \sum_{i=1}^k (n_i - 1) S^2\left(\frac{x_i}{\hat{x}_i}\right) = \frac{\sum_{i=1}^k (n_i - 1)}{N-k} S^2\left(\frac{x_i}{\hat{x}_i}\right) \\
&= S^2\left(\frac{x_i}{\hat{x}_i}\right) = \frac{S^2(x_i)}{\hat{x}_i^2},
\end{aligned}$$

where  $N$  is the total number pixels,  $k$  is number classes or segments and  $n_i$  number pixels within the  $i$ 'th class.

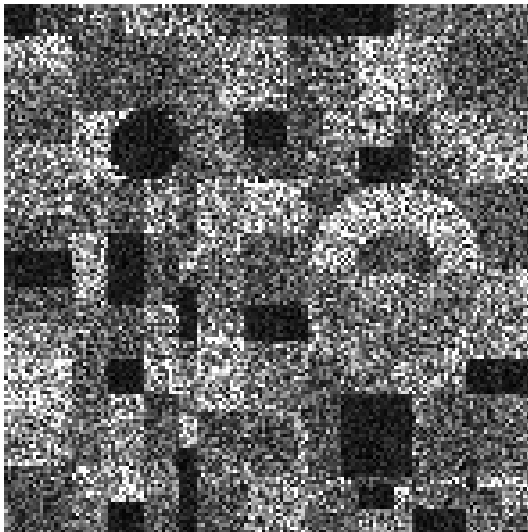
The fact that the statistics of the ratio image are well defined, given that the restoration is perfect, makes it possible in a unique way to compare model performances. This is done by carefully selecting the parameters in the succeeding *a priori* models and optimization techniques. That is to say the optimal parameters are chosen under the constraints that  $\bar{z}$  and  $S^2(z)$  of the observed ratio images are as close as possible to the ideal parameters  $\mu = 1$  and  $\sigma^2(z) = 4/\pi - 1$  or approximately 0.2732.

The  $\chi^2(f)$ -*Goodness of Fit test* with  $f$  degrees of freedom and histograms of the observed frequency data from the ratio image are used to evaluate the *null hypothesis*  $H_0$  that the observed frequency data from the ratio image do match the expected Rayleigh distribution. The commonly used standard for accepting  $H_0$  is if the  $p$  value for the calculated  $\chi^2$  is larger than the significance level of 0.05. Here  $p$  denotes the probability that the deviation of the observed from the expected is due to chance alone.

The fine tuning of the *a priori* models and algorithms is performed on ratios based on the synthetic one grey-level independent and identically-distributed SAR data presented in Figure 5.1 (a). This is done to ensure that homogeneous regions are fully restored without the disturbing effect discontinuities might have on the optimal parameters. With this a common basis for comparing the different models and algorithms is provided. It is furthermore illustrated and analyzed



(a)



(b)

Figure 5.1: (a) Homogeneous synthetic one grey-level SAR data and (b) synthetic five grey-levels SAR data. The original synthetic five grey-levels image is shown in Figure A.1. The data are stretched linearly between their mean  $\pm 3$  std.

to what extent discontinuities interfere with the statistics of the ratio images. This is done by applying the optimal parameter settings, derived from the homogeneous synthetic one grey-level SAR data, on the synthetic five grey-levels SAR data in Figure 5.1 (b). Here  $\beta$  is a factor that governs the correlation between neighbouring pixels. The weighting factor  $w_c$  depends on the orientation of the clique  $c$ , see Figure 4.2. The GRF is said to be isotropic if  $w_c = 1$  [46]. Finally, in order to evaluate the model performances on real SAR data, the optimal parameter settings are applied on the C-band VV polarized EMISAR data in Figure 5.2.

A description of the synthetic SAR data and tabled statistics derived from the ratio images is given in Appendix A.

### 5.3 Gaussian *a priori* model

The anisotropic Gauss-Markov Random Field (GMRF) model

$$p(x_i|x_j, j \in N_i) = \frac{1}{\sqrt{2\pi\sigma^2}} \exp\left\{-\frac{1}{2\sigma^2}U(x_i)\right\}, \quad (5.1)$$

where

$$U(x_i) = \left\{x_i - \mu - \beta \sum_{c \in C} \omega_c(x_j - \mu)\right\}^2,$$

and

$$\mu = \frac{1}{N_c} \sum_{i=1}^{N_c} x_i,$$

where  $N_c$  is the 9 pixels involved in the configuration.

The model (5.1) is a simple choice in terms of describing continuous phenomena in a  $2nd$  order neighbourhood system. The model (5.1), here involving the eight pair-site interactions, is known as a conditional autoregressive (CAR) model. The energy function is  $U(x_i)$  and  $\sigma^2$  is the variance of the conditional distribution given by the neighbours of  $x_i$ . The mean value is  $\mu$  and  $C$  denotes in this

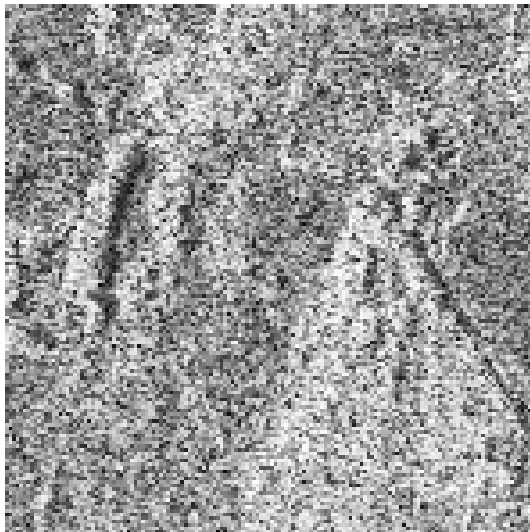
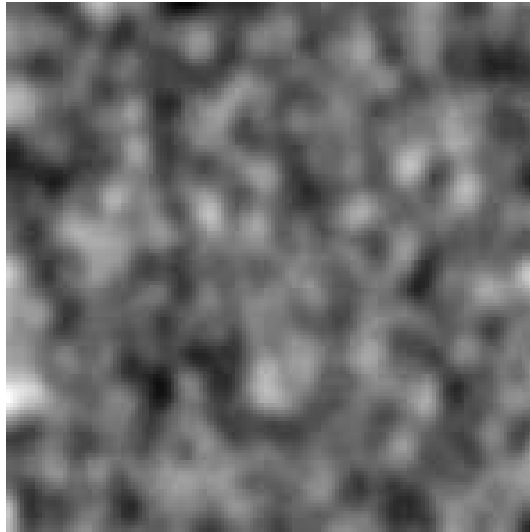


Figure 5.2: The C-band VV-polarized EMISAR amplitude data covering Lade-gaards Enge 3 June 1997. The data are histogram equalized using the beta distribution with the parameters 3 and 2.

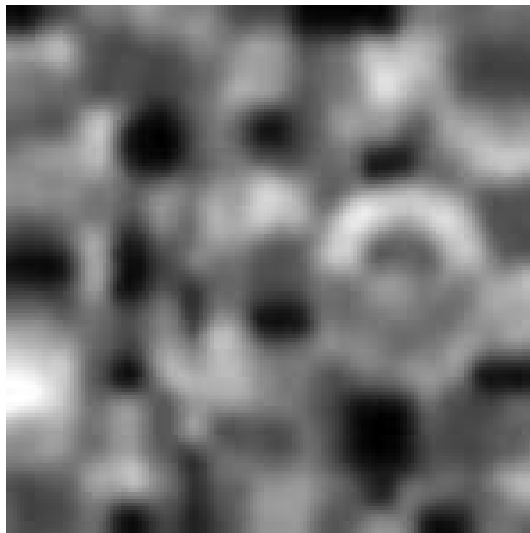
context the set of the pair-site cliques [6]. The quantity  $\beta$  is a factor that controls the dependence between  $x_i$  and its neighbours. The weights of the clique potentials as they appear in Figure 4.2 are  $\omega_c$ .

The distribution (5.1) is symmetrical while the amplitude data to be used are Rayleigh distributed. Because of the positive skewness the mode of the Rayleigh distribution is not at the mean. Unfortunately this skewness has the effect that (5.1) performs badly in terms of preserving mean levels in amplitude data. In other words the restored mean levels will be smaller than the true mean levels. This again implies that the mean value  $\bar{z}$  of the ratio between the SAR data and the restored data becomes larger than 1.

According to the concept of the Boltzmann distribution (4.1) and the principles of thermodynamics, particles attempt to arrange themselves towards a configuration that has the lowest energy. Consequently we are searching for a  $\hat{x}_i = \arg \max_{x_i} p(x_i | x_j, j \in N_i)$  that reflects that the neighbourhood configuration is in a minimum state of energy, that is e.g. to say the sum of absolute differences between the centre pixel  $x_i$  and its neighbours has reached a minimum. However, this is not always the case with the Gaussian model where (5.1) has the disadvantage of sometimes choosing estimates of  $\mu$  in the opposite direction

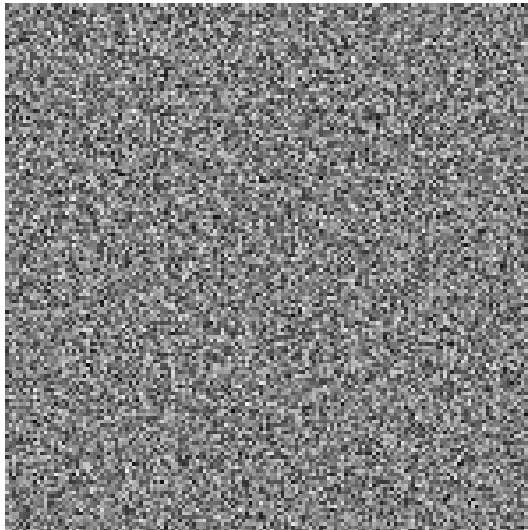


(a)

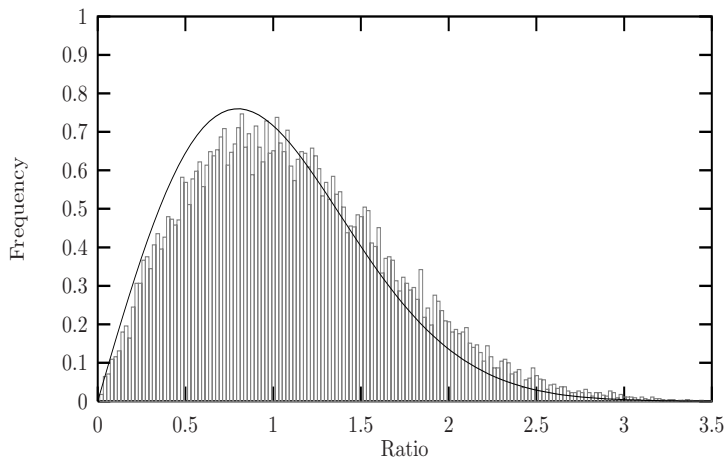


(b)

Figure 5.3: (a) The restored homogeneous synthetic one grey-level SAR data in Figure 5.1(a) and (b) the restored synthetic five grey-levels SAR data in Figure 5.1(b). The restorations are performed using the Gauss prior and ICM with the optimized parameters  $\alpha = 2, \beta = 3, n = 9$ . The data are stretched linearly between their mean  $\pm 3$  std.

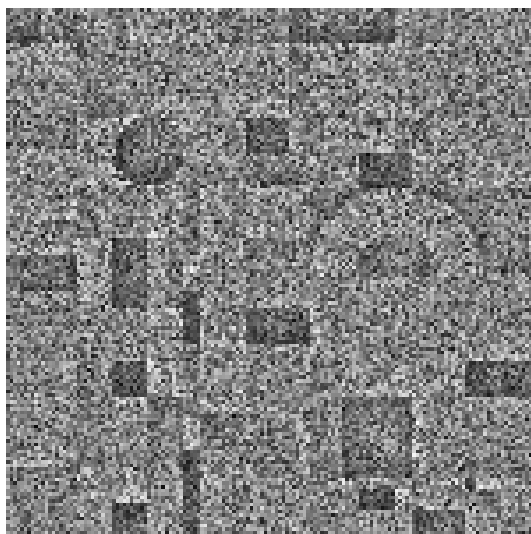


(a)

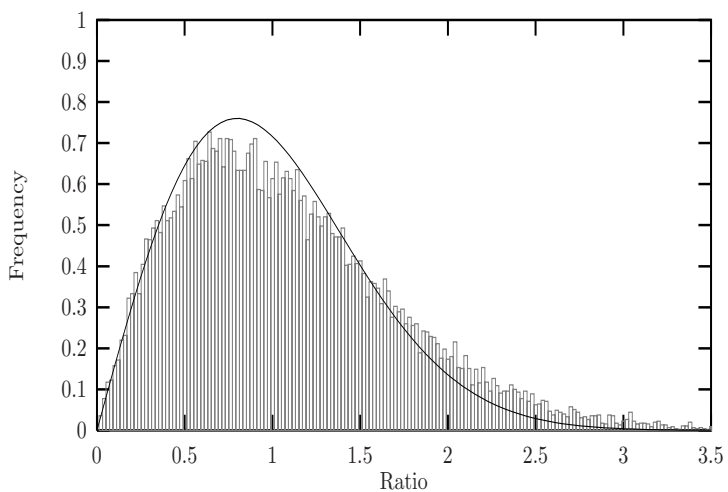


(b)

Figure 5.4: (a) The ratio between the homogeneous synthetic one grey-level SAR data in Figure 5.1 (a) and the restored SAR data in Figure 5.3 (a) using the Gaussian prior and the ICM algorithm and (b) a comparison of the histogram of the ratio image and the theoretical Rayleigh distribution.



(a)



(b)

Figure 5.5: (a) The ratio between the synthetic five grey-levels SAR data in Figure 5.1(b) and the restored data in Figure 5.3 (b) using the Gauss prior and ICM. In (b) is the histogram of the ratio image shown together with the theoretical Rayleigh distribution.



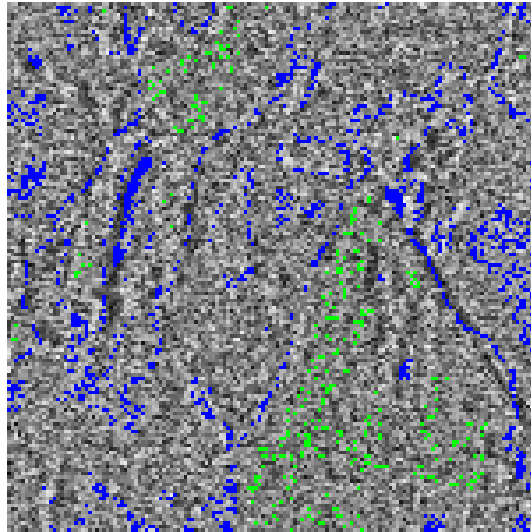
Figure 5.6: Restored C-band VV-polarized EMISAR data in Figure 5.2 after 9 iterations using a Gaussian prior and ICM with  $\alpha = 2$ , and  $\beta = 3$ . The data are histogram equalized using the beta distribution with the parameters 3 and 2.

of what is to be expected given the neighbours of pixel  $x_i$ . This occurs when the mean of the neighbourhood is larger than  $x_i$  and is a consequence of the fact that it is not the sum of the absolute values of the differences between  $x_i$  and its neighbours that enter the energy function in (5.1).

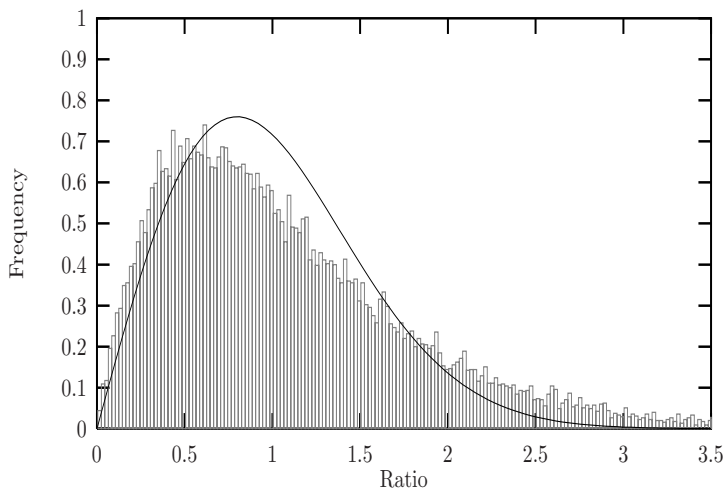
The Gaussian prior in the choice of (5.1) compensates by choosing an estimate  $\hat{x}_i < \mu$ , which is inconsistent with the principles of thermodynamics. This bias is significant for  $\beta < 0.2$  and small  $n$ . For large  $\beta$  and  $n$  the effect is negligible. Another disadvantage of (5.1) is that too much weight is put upon pixels that diverge. That is specific features in a neighbourhood configuration such as e.g. edges are not easily preserved. Or the opposite case where an outlier severely can change the local characteristics. It therefore follows that discontinuities in the restored data will have a smooth appearance in the choice of (5.1).

An unfavorable side effect of the previously mentioned problem concerning diverging pixels in a neighbourhood configuration is that mean values of areas close to discontinuities will be affected too. That is to say the areas with small amplitudes will increase their mean value whereas areas with large amplitudes will decrease their mean value. This side effect, which is amplified by the iterating nature of the ICM-algorithm, gets more pronounced as the iterations proceed





(a)



(b)

Figure 5.7: (a) Ratio of the C-band VV-polarized EMISAR data in Figure 5.2 to the restored data in Figure 5.6 using the Gaussian prior and ICM and (b) a comparison of the observed and the theoretical ratio distributions. The blue and green areas in (a) correspond to the pixels in the range 0–0.6 and 1.8–3.5 in (b) that exceed the theoretical curve.

and for  $n \rightarrow \infty$  all discontinuities eventually will be smeared out leaving a single grey-level image. On the other hand the property of (5.1) of smearing out discontinuities makes (5.1) a good *a priori* model in terms of reproducing homogeneous areas.

Figure 5.3 (a) shows the optimal restoration of the synthetic one grey-level SAR data in Figure 5.1 (a) using  $\alpha = 2$ ,  $\beta = 3$  and  $n = 9$ . The characteristic parameters from the restoration are listed in Table A.1(a). The mean value  $\bar{z}$  of the ratio between the synthetic one grey-level test data and the restored data is 1.108 and its variance  $S^2(z) = 0.331$ . As we see  $\bar{z} > 1$  which is in perfect agreement with the above mentioned inconsistency between (5.1) and the Rayleigh distribution. The chi-square statistics  $\chi^2(75)$  is 1216. Since we are interested in a significance level of 0.05 we may reject the *null hypothesis*  $H_0$ . In other words there is a significant difference between the expected and the observed results which is evident examining the histogram in Figure 5.4(b). It is therefore safe to say that (5.1) fails in terms of preserving the level of homogeneous regions.

In Figure 5.3 (b) is presented the restoration of the synthetic five grey-levels SAR data shown in Figure 5.1 (b). With reference to Table A.1(b)  $\bar{z} = 1.091$ ,  $S^2(z) = 0.406$  and the chi-square statistics  $\chi^2(77)$  is 5496 which means that the  $H_0$  hypothesis is rejected. This supposition is also supported by the ratio image in Figure 5.5(a), which does not look homogeneous, and the corresponding histogram in Figure 5.5(b). Obviously the observed histogram and the theoretical curve are not coincident as one would expect given the restoration was perfect. The frequencies causing the observed histogram to exceed the theoretical curve are in the range 0.3–0.4 and 1.6–3.5.

After the restoration and as expected the image appears blurred with a smooth transition from areas with small amplitudes to areas with large amplitudes. The previously mentioned tendency of (5.1) to pick low estimates of  $\mu$  has not proven to have any significant effect on the restored data in Figure 5.3 (b). All discontinuities in Figure 5.1 (b) are badly preserved. Areas with small amplitudes close to areas with larger amplitudes in Figure 5.1 (b) correspond to frequencies concentrated in the range 0.3–0.4 in Figure 5.5(b). These outlier frequencies are caused by the former mentioned tendency that areas with small amplitudes close to a discontinuity will increase their mean values during the iterations and therefore the ratio will be smaller than 1. Subsequently pixels or areas with large amplitudes in the immediate neighbourhood of areas with smaller amplitudes will decrease their mean values by the same amount but the ratio will now be larger than 1. These pixels are reflected in frequencies in the range 1.6–3.5 in Figure 5.5(b).

Finally, the optimal setting from the synthetic one grey-level SAR data is applied upon the EMISAR data illustrated in Figure 5.2. Figure 5.6 shows the

restored data. The statistical parameters derived from the ratio between the C-band VV-polarized EMISAR data and the restored data, which is illustrated in Figure 5.7(a), are  $\bar{z} = 1.101$ ,  $S^2(z) = 0.5953$  and the chi-square statistics  $\chi^2(52)$  is calculated to  $> 10^7$ . We therefore can reject the  $H_0$  hypothesis. The corresponding histogram in Figure 5.7(b) displays a considerable bias between the observed and the theoretical distribution. Here the frequencies causing the disturbance are located in the intervals 0–0.6 and 1.8–3.5 and the pixels causing the observed histogram to exceed the theoretical curve are indicated with blue and green colours in Figure 5.7(a).

The mechanism causing the smooth and blurred appearance of the Figures 5.3 (a), (b) and Figure 5.6 is the same. However, according to their respective histograms there are differences. This is due to the expected majority of classes and discontinuities in the real EMISAR data compared with the synthetic five grey-levels data. The overall performance of the restoration is decreasing with increasing number of discontinuities as reflected in the  $\chi^2$  test statistics. The restored homogeneous one grey-level data in Figure 5.3 (a), however, does not appear as a one grey-level image. This is partly due to the natural clutter in Figure 5.1 (a), which the algorithm (5.1) attempts to model, and partly due to the nature of the ICM algorithm in terms of being trapped in local minima.

## 5.4 Exponential *a priori* model

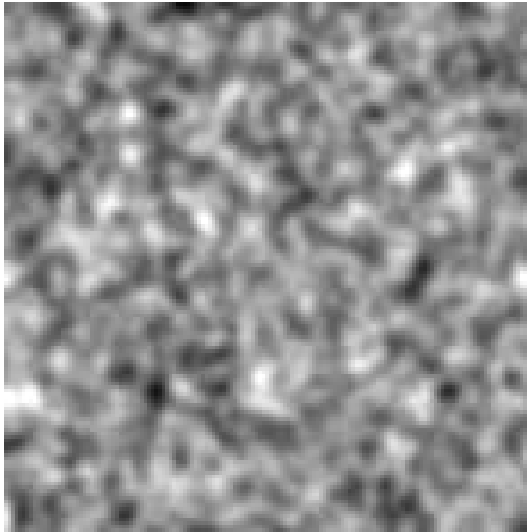
The anisotropic exponential *a priori* model is

$$p(x_i|x_j, j \in N_i) \propto \frac{1}{\mu} \exp\{-U(x_i)\}, \quad (5.2)$$

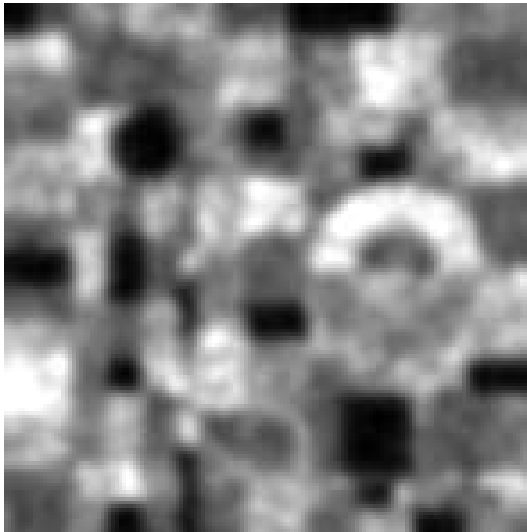
where the energy function  $U(x_i)$  is of the form

$$U(x_i) = \frac{x_i + \beta \sum_{c \in C} \omega_c(x_i + x_j)}{\mu(1 + \beta \sum_{c \in C} \omega_c)}.$$

The model involves the set of the eight pair-site interactions, which is denoted  $C$ . The quantity  $\omega_c$  corresponds to the weights of the clique potentials in Figure 4.2. The model (5.2) is not quite proper in the sense of directly minimizing the energy gap between  $x_i$  and its neighbours. Instead (5.2) is attempting to level the local differences in mean values within a given region. A high energy system is in this

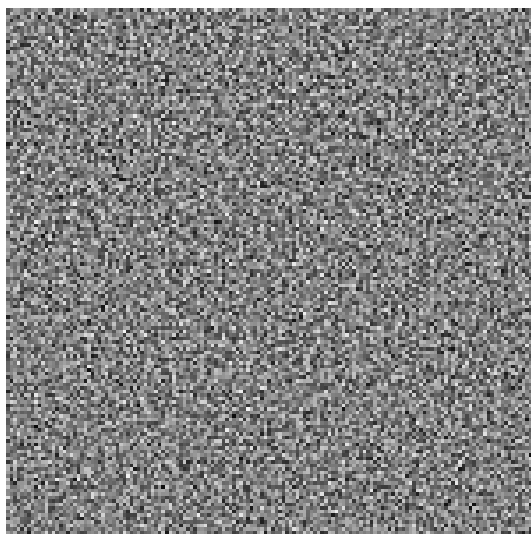


(a)

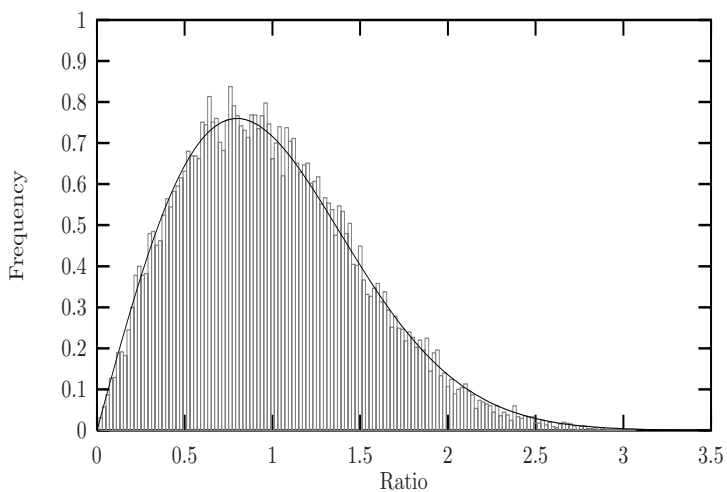


(b)

Figure 5.8: (a) The restored homogeneous synthetic one grey-level SAR data in Figure 5.1(a) and (b) the restored synthetic five grey-levels SAR data in Figure 5.1(b). The restorations are performed using the exponential prior and ICM with the optimized parameters  $\alpha = 2, \beta = 5, n = 9$ . The data are stretched linearly between their mean  $\pm 3$  std.

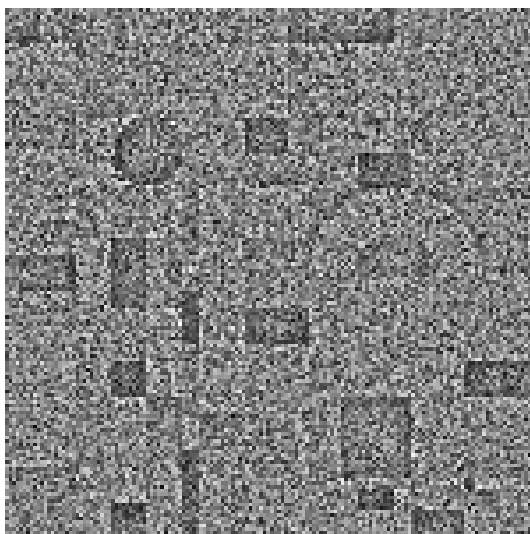


(a)

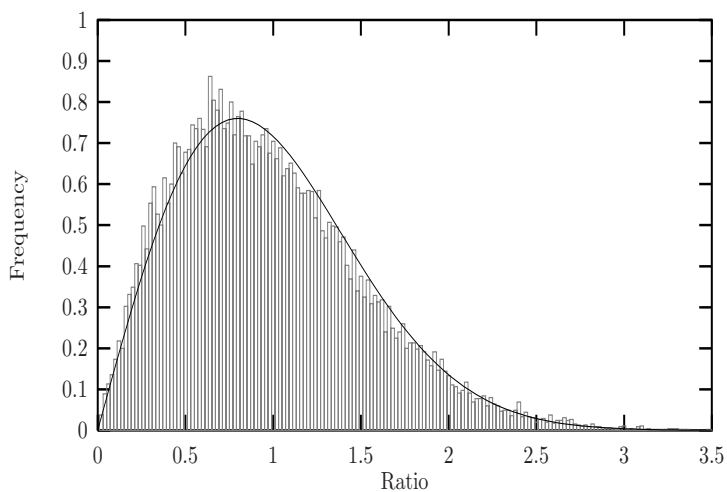


(b)

Figure 5.9: (a) The ratio between the homogeneous synthetic one grey-level SAR data in Figure 5.1 (a) and the restored data in Figure 5.8 (a) using the exponential prior and ICM and (b) a comparison of the histogram of the ratio image and the theoretical Rayleigh distribution.



(a)



(b)

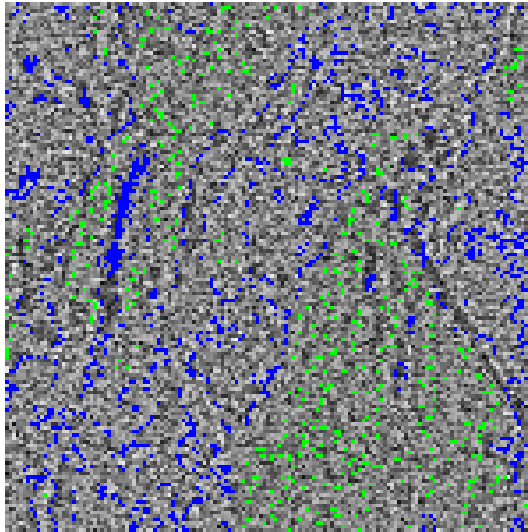
Figure 5.10: (a) The ratio between the synthetic five grey-levels SAR data in Figure 5.1(b) and the restored data in Figure 5.8 (b) using the exponential prior and ICM. In (b) is the histogram of the ratio image shown together with the theoretical Rayleigh distribution



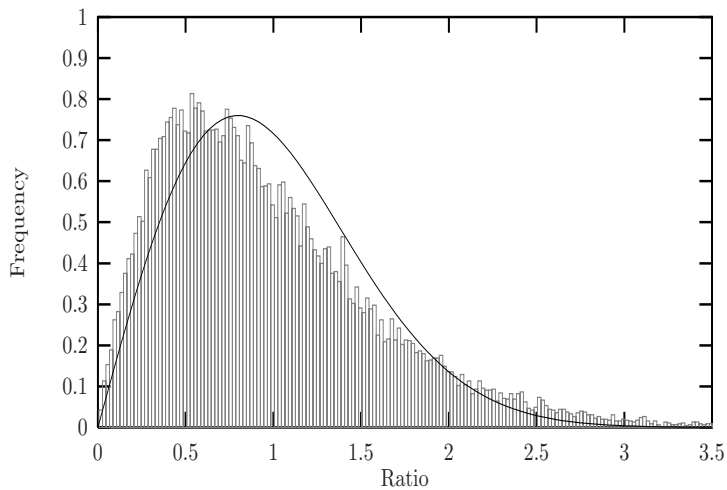
Figure 5.11: The restored C-band VV-polarized EMISAR data in Figure 5.2 after 9 iterations using the exponential prior and ICM with the optimized parameters  $\alpha = 2$  and  $\beta = 5$ . The data are histogram equalized using the beta distribution with the parameters 3 and 2.

context therefore equivalent with high local differences in mean values within a homogeneous area where  $E(U(x_i)) = 1$ . Notice, that  $U(x_i) \rightarrow 1$  while the energy gap between pixels decreases as the iterations proceed. The energy function in (5.2) is a relative measure between the pixels involved in a neighbourhood configuration and the true mean of the pixels. As a consequence, (5.2) has the advantage of not being as sensitive towards the presence of discontinuities as (5.1). Furthermore, because (5.2) is estimating the mean of the pixels involved in a neighbourhood configuration it is, contrary to (5.1), excellent in terms of preserving mean levels. Still, mean values of areas close to discontinuities are not left unaffected as the iterations proceed. For a more detailed description refer to Section 5.3.

Using the parameters  $\alpha = 2$ ,  $\beta = 5$  and  $n = 9$  the restored synthetic one grey-level SAR data are shown in Figure 5.8 (a). Referring to Table A.1(a) the statistics of the ratio between the synthetic one grey-level SAR and the restored data are as follows:  $\bar{z} = 0.9957$ ,  $S^2(z) = 0.2571$  and  $\chi^2(78) = 97$ . This is within the range of acceptable deviation and we can conclude that the observed histogram in Figure 5.9(b) matches the theoretical Rayleigh distribution.



(a)



(b)

Figure 5.12: (a) The ratio between the C-band VV-polarized EMISAR data in Figure 5.2 and the restored data in Figure 5.11 using the exponential prior and ICM and (b) a comparison of the histogram of the ratio image and the theoretical Rayleigh distribution. The blue and green coloured pixels indicate frequencies in the ranges 0 to 0.6 and 2 to 3.5.



The second test image to be used is the synthetic five grey-levels SAR data in Figure 5.1 (b). Using the parameters from above we get the restored data in Figure 5.8 (b). According to the information given in Table A.1(b) the mean of the ratio image  $\bar{z}$  is 0.9757,  $S^2(z) = 0.2892$  and  $\chi^2(81)$  is 214. The  $H_0$  hypothesis is thereby rejected and we conclude that some factor other than chance is operating for the deviation. Due to the unfavourable influence by the discontinuities there is a smooth transition between edges in Figure 5.8 (b). The mechanism behind this behaviour is explained in Section 5.3. The frequencies causing the observed histogram in Figure 5.10(b) to exceed the expected distribution are in the ranges 0–0.7 and 2.5–3.5. The location of the corresponding pixels is displayed in Figure 5.10(a) in the shape of the unwanted structure.

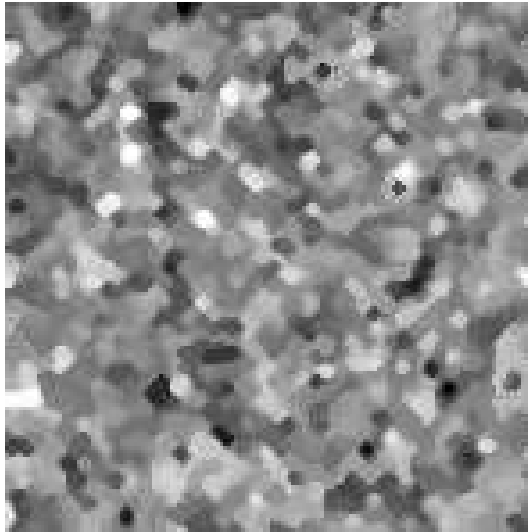
The restored example of the C-band VV-polarized EMISAR data are presented in Figure 5.11 and the data prior to the restoration are shown in Figure 5.2. The ratio of the EMISAR data to the restored data is illustrated in Figure 5.12(a), where  $\bar{z} = 0.9754$ ,  $S^2(z) = 0.4077$  and  $\chi^2(56)$  is calculated to 7348. These values are far from the ideal parameters that were derived in Section 4.3 and by this we reject the  $H_0$  hypothesis. The frequencies responsible for the bias between the observed and the theoretical distribution are located in the intervals 0–0.6 and 2–3.5 in Figure 5.12(b). The corresponding pixels which accounts for the structure in Figure 5.12(a) are indicated with blue and green colours. A comparison between the Figures 5.10 and 5.12 discloses not surprisingly that (5.2) fails in terms of reproducing regions with much structure. Nevertheless, the overall performance of (5.2) is slightly better than (5.1) due to the reduced sensitivity to discontinuities.

It is immediately striking that the restored data in Figure 5.8 (a) have such a blurred appearance. Again this is due to the natural dark and light clutter in Figure 5.1 (a), which are restored too as a part of the restoration. Furthermore artifacts must be expected due to the nature of the ICM algorithm. This suggests that a significant amount of the structure observed in Figure 5.11 is due to chance alone.

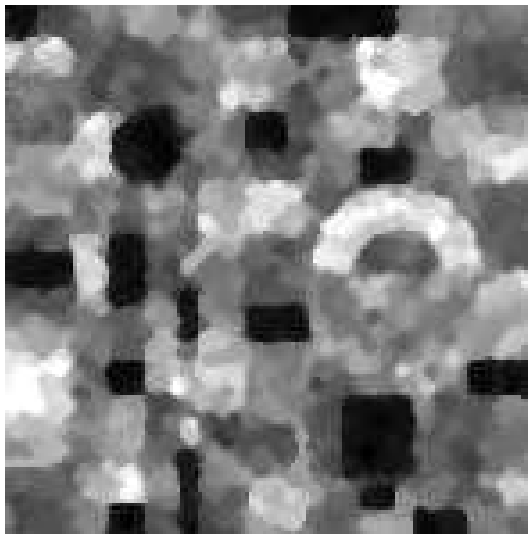
## 5.5 LaPlace *a priori* model

The anisotropic LaPlace *a priori* model involving the eight pair-site cliques has the form

$$p(x_i|x_j, j \in N_i) \propto \exp \left\{ -\frac{1}{\kappa} U(x_i) \right\}, \quad (5.3)$$

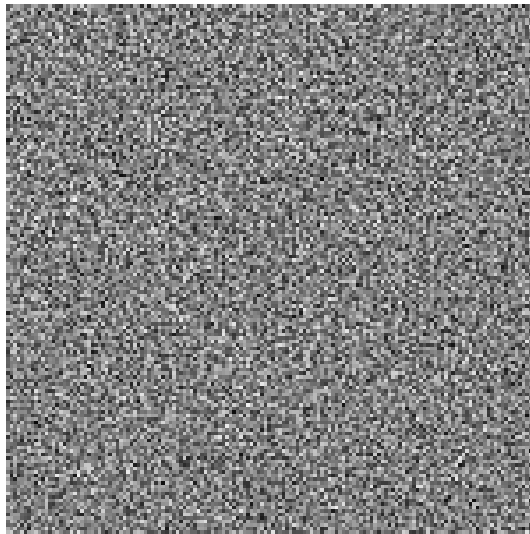


(a)

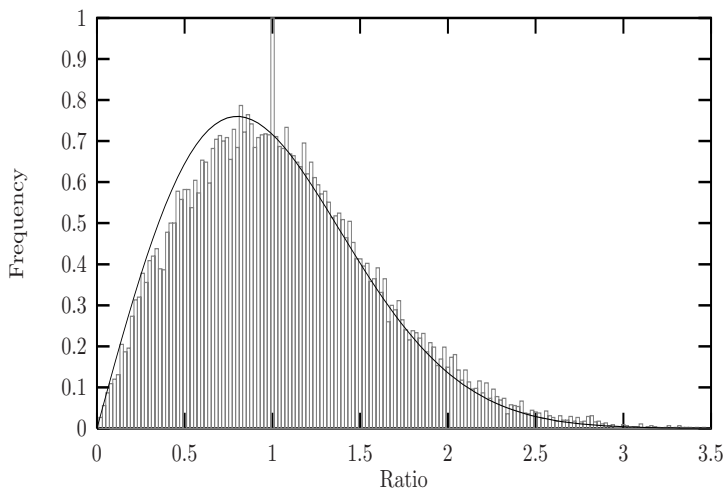


(b)

Figure 5.13: (a) The restored homogeneous synthetic one grey-level SAR data in Figure 5.1(a) and (b) the restored synthetic five grey-levels SAR data in Figure 5.1(b). The restorations are performed using the LaPlace prior and ICM with the optimized parameters  $\alpha = 2, \beta = 3, n = 9$ . The data are stretched linearly between their mean  $\pm 3$  std.

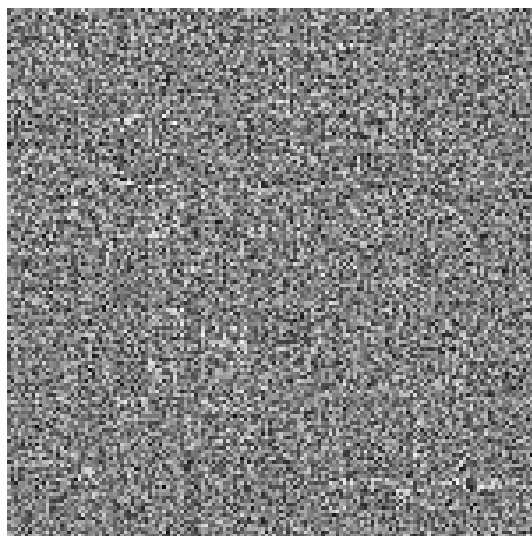


(a)

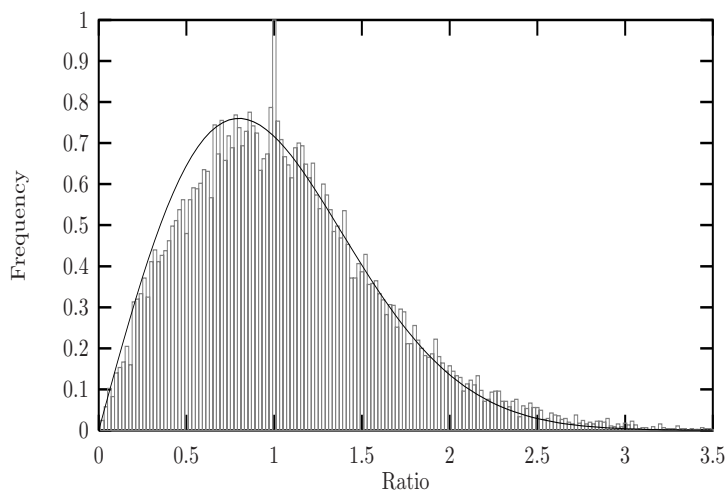


(b)

Figure 5.14: (a) The ratio between the homogeneous synthetic one grey-level SAR data in Figure 5.1 (a) and the restored data in Figure 5.13 (a) using the LaPlace prior and ICM. In (b) is the histogram of the ratio image shown together with the theoretical Rayleigh distribution.



(a)



(b)

Figure 5.15: a) The ratio between the synthetic five grey-levels SAR data in Figure 5.1(b) and the restored data in Figure 5.13 (b) using the LaPlace prior and ICM. In (b) is the histogram of the ratio image shown together with the theoretical Rayleigh distribution.

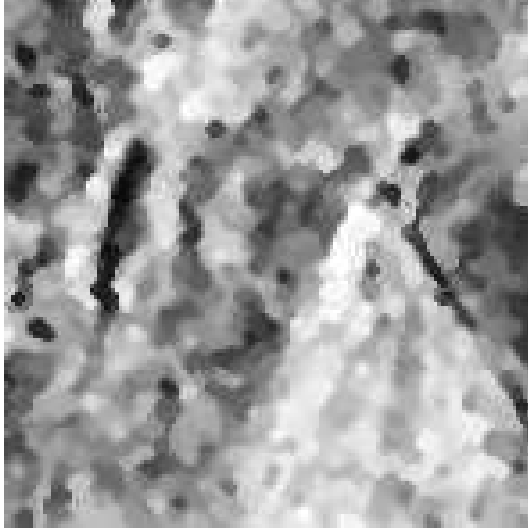


Figure 5.16: The restored C-band VV-polarized EMISAR data in Figure 5.2 after 9 iterations using the LaPlace prior and ICM. The optimized parameters are  $\alpha = 2$  and  $\beta = 3$ . The data are histogram equalized using the beta distribution with the parameters 3 and 2.

where  $\kappa$  is a positive scale parameter [18]. The energy function is

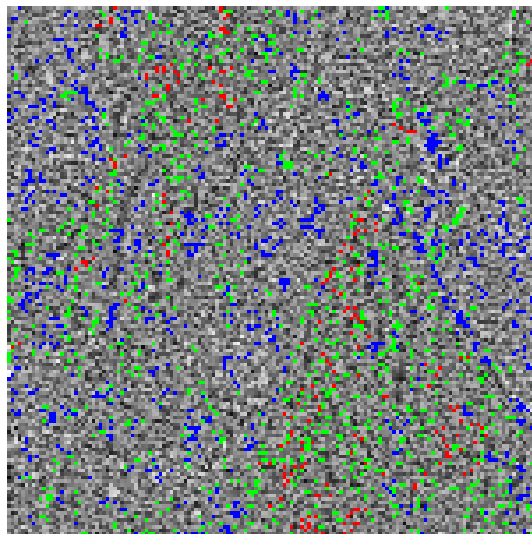
$$U(x_i) = |x_i - \mu| + \beta \sum_{c \in C} \omega_c |x_j - \mu|,$$

where

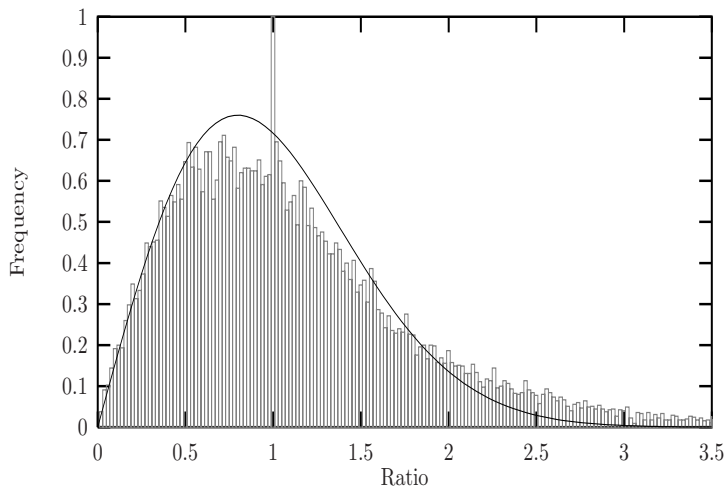
$$\mu = \frac{1}{N_c} \sum_{i=1}^{N_c} x_i,$$

and  $N_c$  is the 9 pixels involved in the configuration. Again  $C$  is the eight pair-site interactions in the 2nd order neighbourhood system. Referring to Figure 4.2  $\omega_c$  corresponds to the weights of the clique potentials.

Because (5.3) has its mode at the median rather than at the mean of the neighbours of  $x_i$  the model is also known as the median prior [8]. As was the case



(a)



(b)

Figure 5.17: (a) The ratio between the C-band VV-polarized EMISAR data in Figure 5.2 and the restored data in Figure 5.16 using the LaPlace prior and ICM and (b) a comparison of the histogram of the observed ratio image and the theoretical Rayleigh distribution. The blue, green and red areas in (a) illustrate the pixels in the intervals 0–0.5, 0.95–1.05 and 1.8–3.5 in (b) that exceed the theoretical curve.

with the Gaussian *a priori* model, (5.3) is symmetrical while the amplitude data to be used are skewed. While (5.3) at the same time has its mode at the median rather than at the mean the LaPlace model is even worse compared to the Gaussian model when it comes to preserving mean levels and consequently we again have  $\bar{z} > 1$ . On the other hand, contrary to the Gaussian *a priori* model, (5.3) is always reflecting that the neighbourhood configuration is in its minimum state of energy when  $\hat{x}_i = \arg \max_{x_i} p(x_i|x_j, j \in N_i)$ .

The optimized parameters are  $\alpha = 2$ ,  $\beta = 3$  and  $n = 9$ , which applied on the synthetic one grey-level SAR data in Figure 5.1 (a) results in the restored data in Figure 5.13 (a). Using Table A.1(a) we find the values reflecting the statistics of the corresponding ratio data to be  $\bar{z} = 1.0554$ ,  $S^2(z) = 0.2920$  and the  $\chi^2(77) = 545$ . The *null hypothesis* is therefore rejected and as we see from Figure 5.14(b) the observed frequency data do not match the theoretical Rayleigh distribution. As previously mentioned the combination of the skewed amplitude data and (5.3) enforce the ratio  $\bar{z}$  to become larger than 1. The rejected *null hypothesis* and the observed high mean value  $\bar{z} = 1.0554$  derived from the one grey-level ratio image are therefore not suspicious.

Next we use the synthetic five grey-levels SAR data in Figure 5.1 (b) in our investigation and the restored result is illustrated in Figure 5.13 (b). In Table A.1(b) are listed some statistics derived from the ratio between the synthetic five grey-levels SAR data and the restored data, namely,  $\bar{z} = 1.0587$ ,  $S^2(z) = 0.3122$  and  $\chi^2(68) = 1206$ . Based on the high  $\chi^2$  test value the  $H_0$  hypothesis is rejected. The rejection of the *null hypothesis* is supported by the structure in the ratio image in Figure 5.15(a) and the corresponding frequencies are displayed in Figure 5.15(b).

An examination of the Figures 5.15(a)–(b) indicates, that the LaPlace *a priori* model is sharing the same weakness as (5.1) and (5.2), namely, that specific features in a neighbourhood configuration are either badly preserved e.g. edges or given too much weight e.g. outliers. As described in Section 5.3 this has the consequence that mean values of areas close to discontinuities are affected too as the iterations proceed. However, the disadvantages of (5.3) as described above are not as pronounced as for (5.1) and (5.2), because (5.3) has its mode closer to the median. In fact the capabilities of (5.3) in terms of preserving discontinuities can for certain very high outliers result in ratios close to one. This phenomenon is visualized by the peak in the histogram in Figure 5.15(b)

In Figure 5.16 is shown the isotropic LaPlace *a priori* model applied on the C-band VV-polarized EMISAR data in Figure 5.2. The ratio between the EMISAR data and the restored data is illustrated in Figure 5.17(a). Based on the ratio image the  $\chi^2(52) > 10^5$ ,  $\bar{z} = 1.125$  and the variance  $S^2(z) = 0.5446$ . Thus, the  $H_0$  is not accepted. This substantial bias indicated by the  $\chi^2$  *Good-*

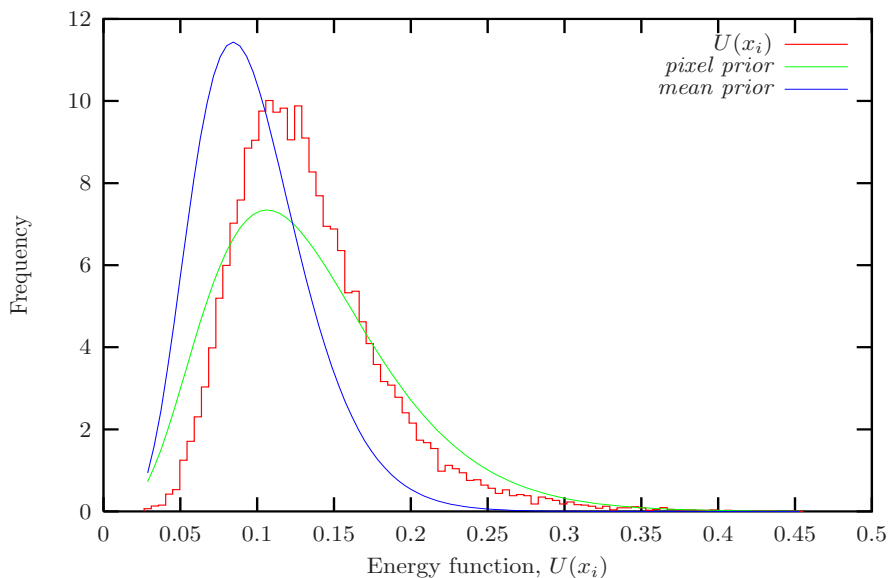


Figure 5.18: The histogram of the observed energy function  $U(x_i)$  using (5.4) and the pdf's for the optimized Gamma *pixel prior* and the Gamma *mean prior*. The histogram is derived on basis of the synthetic one grey-level SAR data in Figure 5.1 (a).

*ness of Fit test* is visualized in Figure 5.17(a) in term of the unwanted structure. This bias is also clear when examining Figure 5.17(b) that illustrates the theoretical distribution and the observed histogram of the ratio image. Here the frequencies causing this disturbance are located in the intervals 0–0.5, 0.95–1.05 and 1.8–3.5 and the spatial distribution of the corresponding pixels are indicated by blue, red and green colours in Figure 5.17(a).

As one would expect (5.3) performs better than (5.1) and (5.2) in terms of preserving e.g. edges because less weight is put upon diverging pixels. However, as mentioned before, (5.3) is insufficient when it comes to restoring mean values. This is evident in Figure 5.17(b) where the frequencies causing the disturbance dominate in the tail of the distribution. Again there is reason to believe that the restored data in Figure 5.16 has artifacts caused by the tendency of the ICM algorithm to become trapped in local minima. Again the unwanted natural dark and light clutter, which are generated by the statistics, are restored by the algorithm.



## 5.6 Gamma *a priori* models

Except for the exponential prior the *a priori* models described so far have been symmetrical. However, as mentioned earlier, the conditional distribution of the observed amplitude data is the Rayleigh distribution, which is asymmetric. In the need of *a priori* models that model the skewed distribution of the data a new model is presented. This model utilizes the Gamma distribution, which provides a good basis for modeling the SAR amplitude data.

The Gamma *a priori* model has the form

$$p(x_i|x_j, j \in N_i) \propto \frac{U(x_i)^{k-1}}{\Gamma(k)(\nu_i/k)^k} \exp\left\{-\frac{kU(x_i)}{\nu_i}\right\}, \quad (5.4)$$

where  $\Gamma$  is the Gamma function and

$$U(x_i) = |p_i - x_i| + \beta \sum_{c \in C} \omega_c |p_i - x_j|,$$

where  $p_i$  is the perturbed value.

The constant  $k$  governs the peak of the distribution and  $U(x_i)$  is the energy function involving the single-site clique  $x_i$  and the eight pair-site interactions in the configuration. The constant  $k$  is estimated so that (5.4) models the actual distribution of  $U(x_i)$ . The set of the eight pair-site interactions in the 2nd order neighbourhood configuration is denoted  $C$ . The quantity  $w_c$  is a weighting factor between the centre pixel  $x_i$  and its neighbours  $x_j$  depending on the clique is horizontal, vertical or diagonal, see Figure 4.2.

As demonstrated earlier (5.3) is more convincing in terms of preserving discontinuities than (5.1) and (5.2), because it has its mode closer to the median than to the mean of the neighbourhood configuration. In order to utilize that advantage the energy function of (5.3) is implemented in (5.4).

The value  $\nu_i$  represents the energy  $U(x_i)$  in accordance to a predefined mean level of the local configuration. This is a crucial step in the development of the algorithm because  $\nu_i$  governs the shape of the energy function. Hence, using  $\beta = 0.5$ , two versions of the Gamma *a priori* model are proposed.

### 5.6.1 Gamma *mean a priori* model

The first version we denote the Gamma *mean a priori* and here the estimate of the local energy level  $\nu_i$  is defined as the estimated mean  $\bar{m}$  of the pixels involved in the neighbourhood configuration. Let  $\nu_i$  be given by

$$\nu_i = |x_i - \bar{m}| + \beta \sum_{c \in C} w_c |\bar{m} - x_j|, \quad (5.5)$$

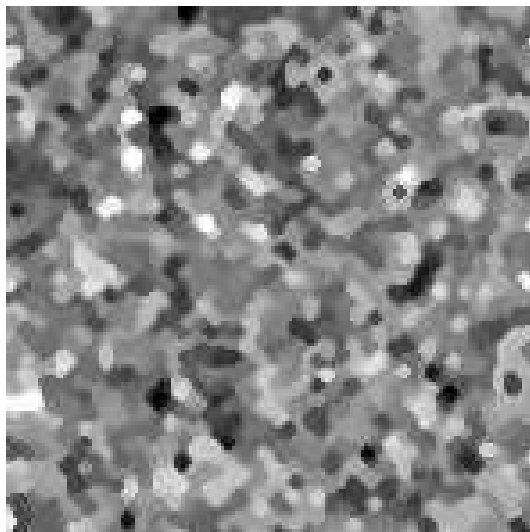
then

$$\bar{m} = \frac{1}{N_c} \sum_{i=1}^{N_c} x_i,$$

where  $N_c$  is the 9 pixels involved in the configuration. As was the case with the previous *a priori* models (5.5) has the disadvantage of not being satisfactory in terms of reconstructing e.g. edges and discontinuities. For a more detailed description of that phenomenon refer to Section 5.5.

In Figure 5.18 is illustrated to what extent (5.5) approximates  $U(x_i)$  in the initial state of the restoration of the synthetic SAR data in Figure 5.1 (a). In Figure 5.18 the observed histogram of  $U(x_i)$  is shown together with the pdf of the optimized *mean a priori* using the parameters  $\alpha = 2$ ,  $\beta = 0.5$ ,  $n = 9$  and  $k = 7$ . Although the mode of (5.5) is not coincident with the mode of observed histogram, its pdf possesses a positive skewness like the observed frequencies of  $U(x_i)$ .

The restoration of the synthetic one grey-level SAR data in Figure 5.1 (a), using (5.5) and the optimal parameter setting above, is illustrated in Figure 5.19. Statistics derived from the ratio between the synthetic one grey-level SAR data and the restored data are listed in Table A.1(a). Reading from the table we find  $\bar{z} = 1.0554$ ,  $S^2(z) = 0.2901$  and the test statistics  $\chi^2(74)$  is estimated to 797. Since  $p < 0.05$   $H_0$  is rejected. The structure in the ratio image in Figure 5.20(a) is not evident, however, according to the histogram in Figure 5.20(b) the observed frequencies in the range 0.95–1.05 and 1.05–3.5 are exceeding the theoretical distribution. The bias in the interval 1.05–3.5 is due to the same conditions accounted for in Section 5.5, namely that (5.5) has its mode closer to the median than to the mean and consequently  $\bar{z} > 1$ . The mechanism causing the small peak in the interval 0.95–1.05 is also explained in Section 5.5.

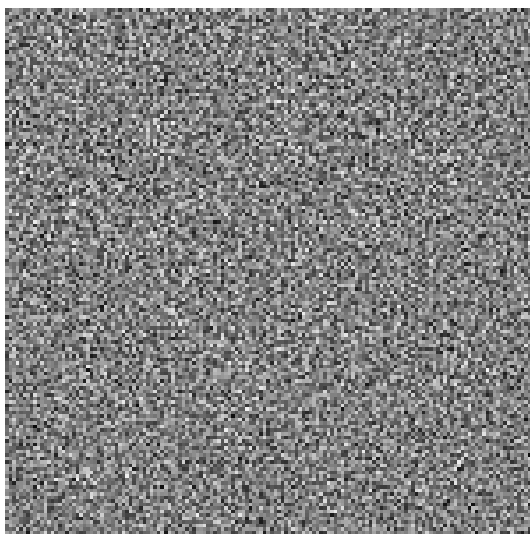


(a)

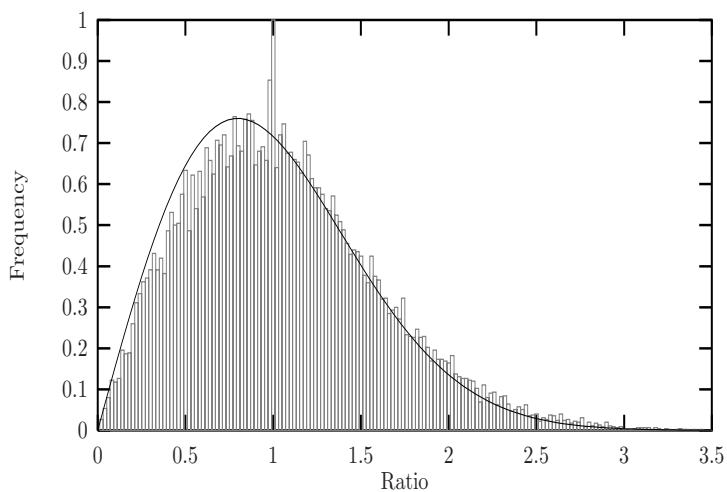


(b)

Figure 5.19: (a) The restored homogeneous synthetic one grey-level SAR data in Figure 5.1(a) and (b) the restored synthetic five grey-levels SAR data in Figure 5.1(b). The restorations are performed using the Gamma *mean prior* and ICM with the optimized parameters  $\alpha = 2$ ,  $k = 7$ ,  $\beta = 0.5$  and  $n = 9$ . The data are stretched linearly between their mean  $\pm 3$  std.

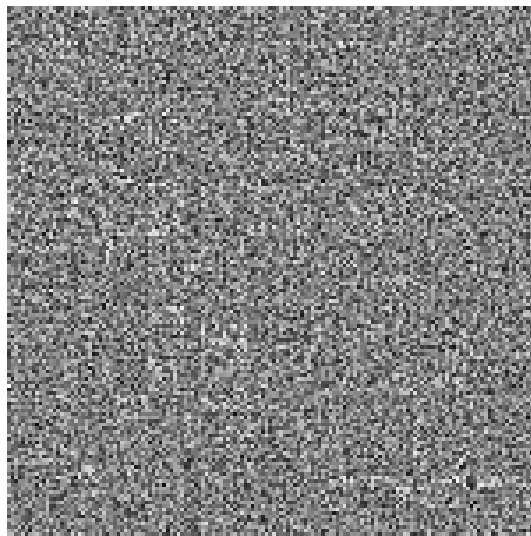


(a)

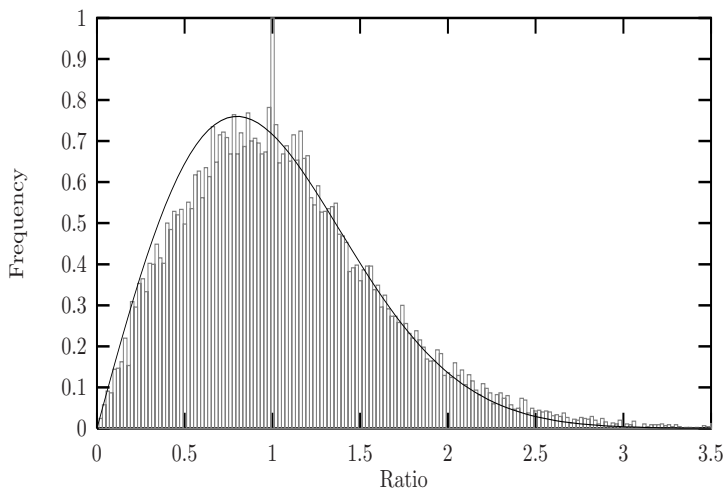


(b)

Figure 5.20: (a) The ratio between the homogeneous synthetic one grey-level SAR data in Figure 5.1 (a) and the restored SAR data in Figure 5.3 (a) using the Gamma *mean prior* and ICM. In (b) is the histogram of the ratio image shown together with the theoretical Rayleigh distribution.



(a)



(b)

Figure 5.21: (a) The ratio between the synthetic five grey-levels SAR data in Figure 5.1(b) and the restored data in Figure 5.19 (b) using the Gamma *mean prior* and ICM. In (b) is the histogram of the ratio image shown together with the theoretical Rayleigh distribution.

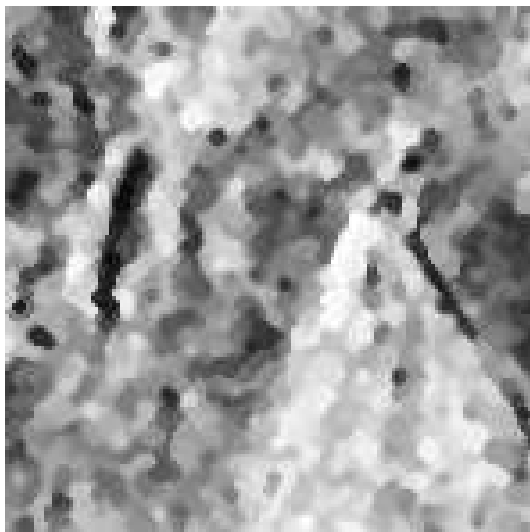
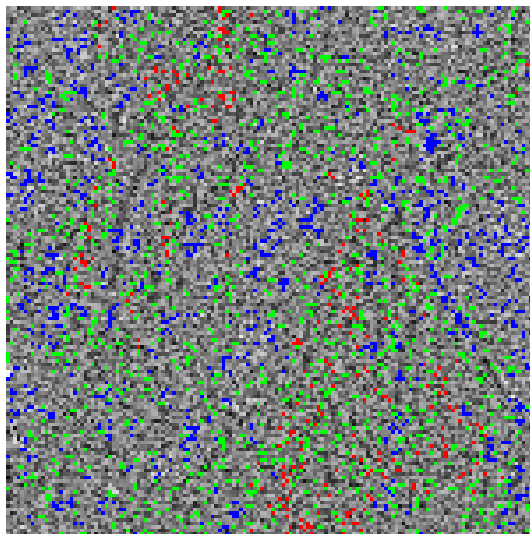


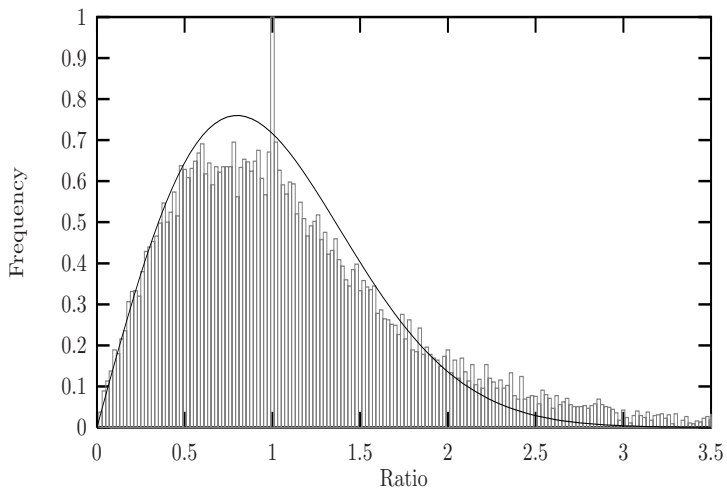
Figure 5.22: The restored C-band VV-polarized EMISAR data in Figure 5.2 after 9 iterations using the Gamma *mean prior* and ICM with the optimized parameters  $\alpha = 2$ ,  $\beta = 0.5$  and  $k = 7$ . The data are histogram equalized using the beta distribution with the parameters 3 and 2.

In Figure 5.19 (b) is shown the restoration of the synthetic five grey-levels SAR data in Figure 5.1 (b). With reference to Table A.1(b) the statistics of the corresponding ratio image in Figure 5.21(a) are  $\bar{z} = 1.0598$ ,  $S^2(z) = 0.311$  and  $\chi^2(54) = 1404$ . Again  $H_0$  is rejected, which is in perfect accordance with the unwanted structure in Figure 5.21(a). It is striking that the histograms derived from the one grey-level and five grey-levels SAR data in the Figures 5.20(b) and 5.21(b) seem very similar. This implies that (5.5) is well suited for preserving structure.

The restored C-band VV-polarized EMISAR data are presented in Figure 5.22 and the data prior to the restoration are shown in Figure 5.2. The ratio of the EMISAR data to the restored data is illustrated in Figure 5.23(a), where  $\bar{z} = 1.1250$ ,  $S^2(z) = 0.5375$  and  $\chi^2(54)$  is  $> 5 \times 10^5$ . These values are far from the parameters for the ideal ratio image derived in Section 4.3 and naturally  $H_0$  is rejected. The frequencies responsible for the bias between the observed and the theoretical distribution are located in the intervals 0–0.6, 0.95–1.05 and 2–3.5 in Figure 5.23(b). The corresponding pixels, which account for the structure, are indicated with blue, red and green colours in Figure 5.23(a). The bias is due to the same reasons given above, which caused the disturbances in the ratio



(a)



(b)

Figure 5.23: (a) The ratio between the C-band VV-polarized EMISAR data in Figure 5.2 and the restored data in Figure 5.22 using the Gamma *mean prior* and ICM and (b) a comparison of the histogram of the ratio image and the theoretical Rayleigh distribution. The red, blue and green areas in (a) indicate pixels located in the intervals 0.95–1.05, 0–0.6 and 2–3.5.

images in the Figures 5.20(a) and 5.21(a).

## 5.6.2 Gamma *pixel a prior* model

The second version we call the Gamma *pixel prior* and here the estimated energy level  $\nu_i$  simply is defined as

$$\nu_i = \beta \sum_{c \in \mathcal{C}} w_c |\bar{m} - x_j|. \quad (5.6)$$

where

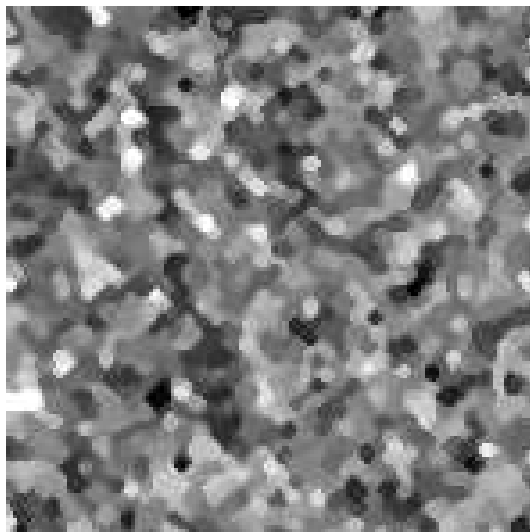
$$\bar{m} = x_i.$$

In other words the value of the centre pixel  $x_i$  itself is taken to represent the mean of the neighbourhood configuration. The approximation to  $U(x_i)$  using (5.6) is shown in Figure 5.18. Again the synthetic one grey-level SAR data in Figure 5.1 (a) are used in the process of deriving the observed histogram of  $U(x_i)$  in the initial state of the restoration. As it appears the mode and the long tail of the observed  $U(x_i)$  are well represented by (5.6) using the optimized parameters  $\alpha = 2$ ,  $\beta = 0.5$ ,  $n = 9$  and  $k = 5$ .

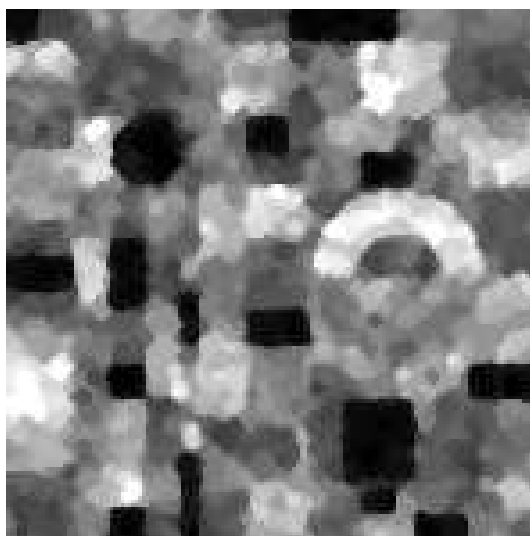
These parameters from the fine tuning of (5.6) are also used in the restoration of the synthetic one grey-level SAR data in Figure 5.1 (a) shown in Figure 5.24. Referring to Table A.1(a) the statistics of the corresponding ratio between the synthetic one grey-level SAR data and the restored data are  $\bar{z} = 1.0440$ ,  $S^2(z) = 0.2813$  and  $\chi^2(76) = 573$ . This is far from within the range of acceptable deviation and we conclude that  $H_0$  is rejected. The rejection of  $H_0$  is supported by the histogram in Figure 5.25(b) where the observed frequencies do not match the theoretical Rayleigh distribution. Here the frequencies exceeding the Rayleigh distribution are located in the intervals 0.95–1.05 and 1.05–3.5. This bias is due to the same condition as explained above concerning the *mean prior* (5.5). However, in the choice of (5.6) these effects are less pronounced because the reference level  $\bar{m}$  now is  $x_i$  instead of the mean of the pixels in the neighbourhood configuration.

We now turn to the synthetic five grey-levels SAR data in Figure 5.1 (b), which restored equivalent is illustrated in Figure 5.24 (b). Referring to the information provided in Table A.1(b) the mean  $\bar{z}$  of the corresponding ratio image is 1.0450,



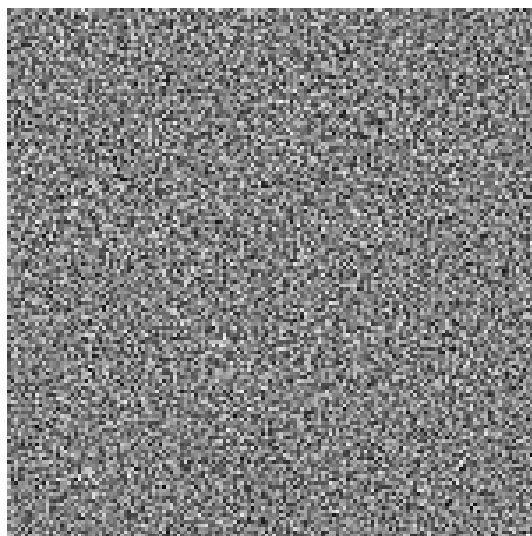


(a)

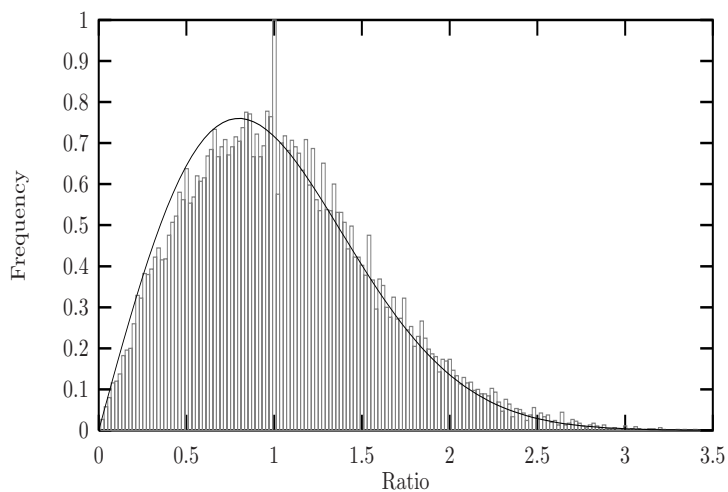


(b)

Figure 5.24: (a) The restored homogeneous synthetic one grey-level SAR data in Figure 5.1(a) and (b) the restored synthetic five grey-levels SAR data in Figure 5.1(b). The restorations are performed using the Gamma *pixel prior* and ICM with the optimized parameters  $\alpha = 2$ ,  $k = 5$ ,  $\beta = 0.5$  and  $n = 9$ . The data are stretched linearly between their mean  $\pm 3$  std.

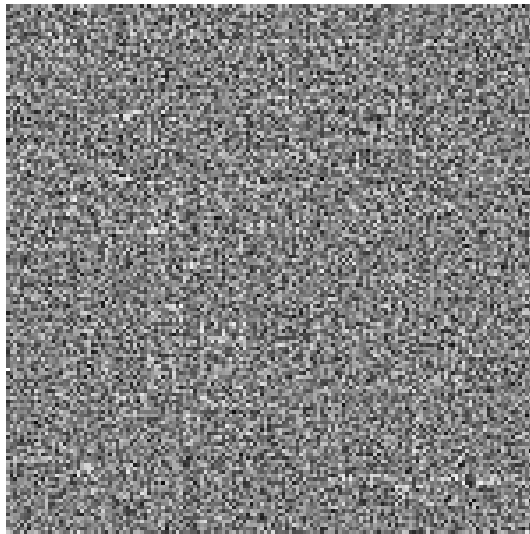


(a)

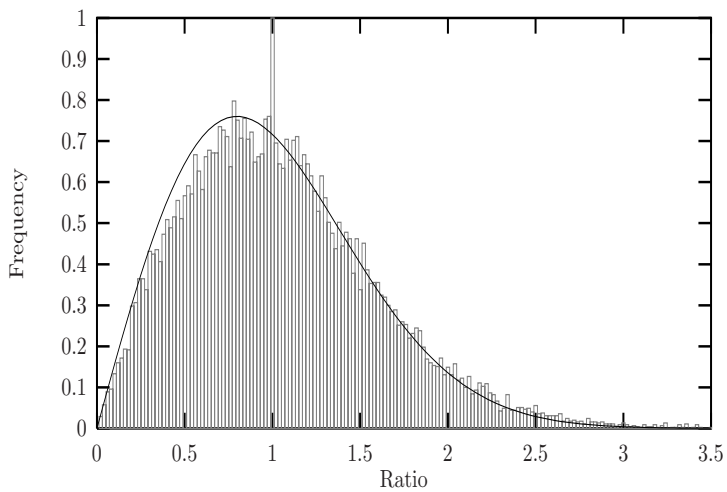


(b)

Figure 5.25: (a) The ratio between the homogeneous synthetic one grey-level SAR data in Figure 5.1 (a) and the restored SAR data in Figure 5.24 (a) using the Gamma *pixel prior* and ICM. In (b) is the histogram of the ratio image shown together with the theoretical Rayleigh distribution.



(a)



(b)

Figure 5.26: (a) The ratio between the synthetic five grey-levels SAR data in Figure 5.1(b) and the restored data in Figure 5.24 (b) using the Gamma *pixel prior* and ICM. In (b) is the histogram of the ratio image shown together with the theoretical Rayleigh distribution.

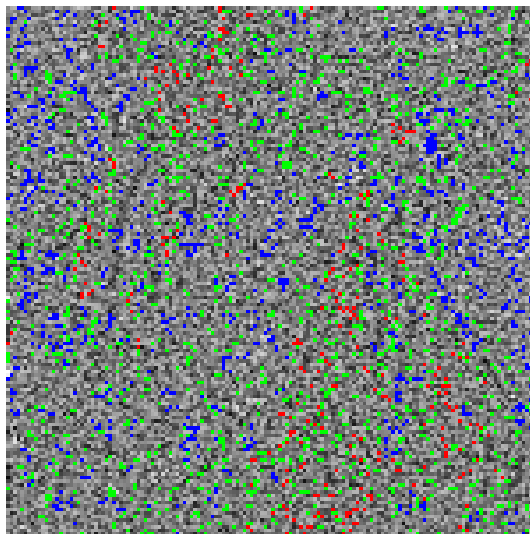


Figure 5.27: The restored C-band VV-polarized EMISAR data in Figure 5.2 after 9 iterations using the Gamma *pixel prior* and ICM with the optimized parameters  $\alpha = 2$ ,  $\beta = 0.5$  and  $k = 5$ . The data are histogram equalized using the beta distribution with the parameters 3 and 2.

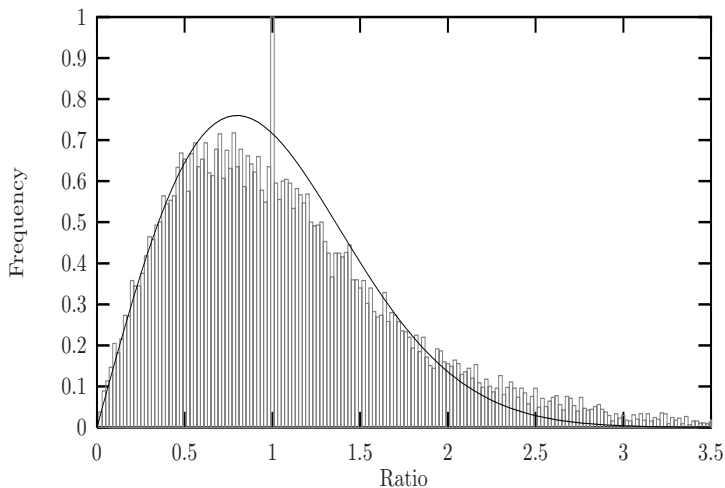
$S^2(z) = 0.2970$  and  $\chi^2(55)$  is 748. Hereby  $H_0$  is rejected and we conclude that some factor other than chance is operating for the deviation. The frequencies which account for the bias are located in the intervals 0.95–1.05 and 1.05–3.5 according to the histogram in Figure 5.26(b). This bias is due to the same conditions that caused the bias in the histogram for the one grey-level ratio image in Figure 5.25(b). The small differences between the ratio images and the histograms of the synthetic one grey-level SAR data and the five grey-levels SAR data in the Figures 5.25(a)–(b) and Figures 5.26(a)–(b) indicate, that edges and discontinuities are well preserved using (5.6).

Figure 5.27 illustrates the restoration of the C-band VV-polarized EMISAR data in Figure 5.2 using (5.6). The ratio of the EMISAR data to the restored data is illustrated in Figure 5.28(a) and the corresponding statistics are  $\bar{z} = 1.1037$ ,  $S^2(z) = 0.5092$ , and  $\chi^2(54) > 1.7 \times 10^5$ . This rejects  $H_0$ , which is supported by the histogram in Figure 5.28(b).

A comparison of the statistics in the Tables A.1(a)–(b) suggests that the exponential *a priori* model (5.2) using ICM has the best over-all performance. This



(a)



(b)

Figure 5.28: (a) The ratio between the C-band VV-polarized EMISAR data in Figure 5.2 and the restored data in Figure 5.27 using the Gamma *pixel prior* and ICM and (b) a comparison of the histogram of the ratio image and the theoretical Rayleigh distribution. The red, blue and green areas in (a) indicate pixels located in the intervals 0.95–1.05, 0–0.6 and 2–3.5.

is due to the energy function, which makes (5.2) superior in terms of preserving mean levels of homogeneous regions. Unfortunately, as Figure 5.8 (b) indicates, (5.2) is less convincing when it comes to preserving discontinuities. According to Figure 5.24 (b) and the Tables A.1(a)–(b) the Gamma *pixel prior* (5.6) is superior when it comes to the preservation of structure and sharp transitions but less satisfactory in terms of preserving mean levels of homogeneous regions.

## 5.7 The Gamma sampler

In Section 5.6 two Gamma *a priori* models were introduced. They were implemented in an ICM algorithm and designed to model the skewed distribution of SAR amplitude data. As mentioned previously a core aspect of this thesis is the development of a model that is superior in terms of preserving both discontinuities and homogeneous areas.

In that sense the Gamma *pixel a priori* model (5.6) turned out to be well suited, although it fails in terms of preserving homogeneous areas. This insufficiency in terms of restoring homogeneous areas is ascribed to ICM because it is likely to get trapped in local minima. Simulated Annealing (SA), however, is a technique able to escape these local minima and finally reach the global minimum, see Section 4.4. In order to improve the restoration of homogeneous regions a promising choice is therefore to implement the Gamma *pixel prior* in the SA algorithm.

Using (4.1) and (5.4) the Gamma *pixel prior* now takes the form

$$p(x_i|x_j, j \in N_i) \propto \frac{U(x_i)^{\frac{k-1+T}{T}-1}}{\Gamma(\frac{k-1+T}{T})(T\nu_i/k)^{\frac{k-1+T}{T}}} \exp\left\{-\frac{kU(x_i)}{T\nu_i}\right\}, \quad (5.7)$$

where  $\Gamma$  is the Gamma function,  $T$  the temperature and  $k$  a constant. The variance is

$$S^2 = (k-1+T) \frac{T\nu_i^2}{k^2}$$

and the energy function  $U(x_i)$  is

$$U(x_i) = |p_i - x_i| + \beta \sum_{c \in C} \omega_c |p_i - x_j|,$$

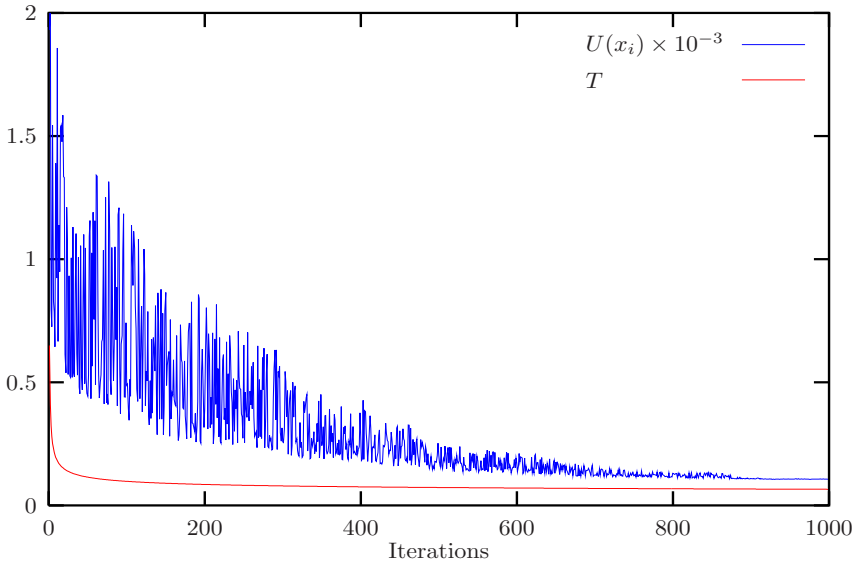


Figure 5.29: The evolution of the energy function  $U(x_i)$  and the temperature  $T$  for the Gamma *pixel prior* and SA during the annealing process. The cooling schedule used is logarithmic.

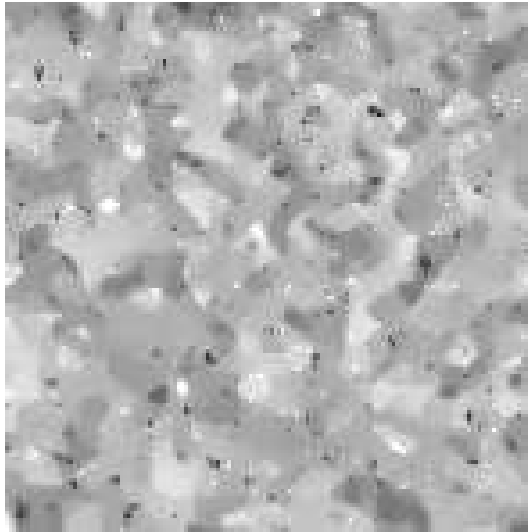
where  $p_i$  is the perturbed value and

$$\nu_i = \beta \sum_{c \in C} w_c |\bar{m} - x_j|.$$

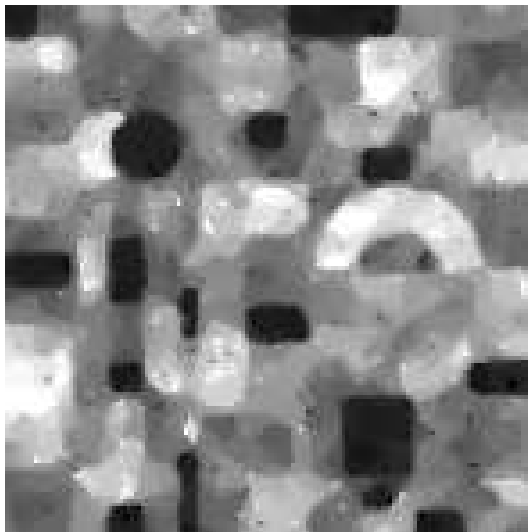
The eight pair-site interactions in the neighbourhood configuration are involved and the quantity  $\nu_i$  again denotes the local energy of  $U(x_i)$  where

$$\bar{m} = x_i.$$

The set of all pair-site cliques in a second order neighbourhood configuration is  $C$ . The weighting factor  $w_c$  depends on the clique  $c$  is horizontal, vertical or diagonal, see Figure 4.2.



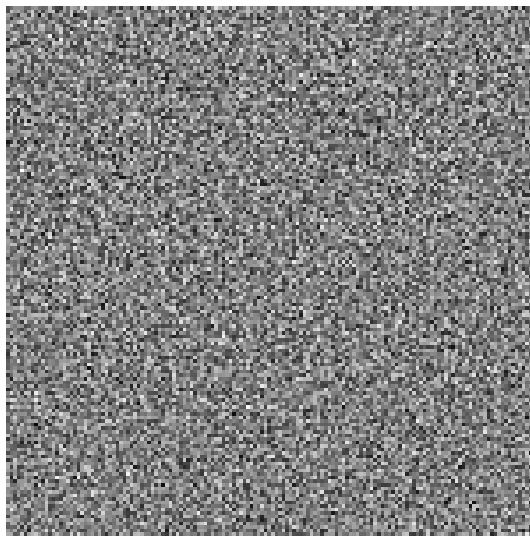
(a)



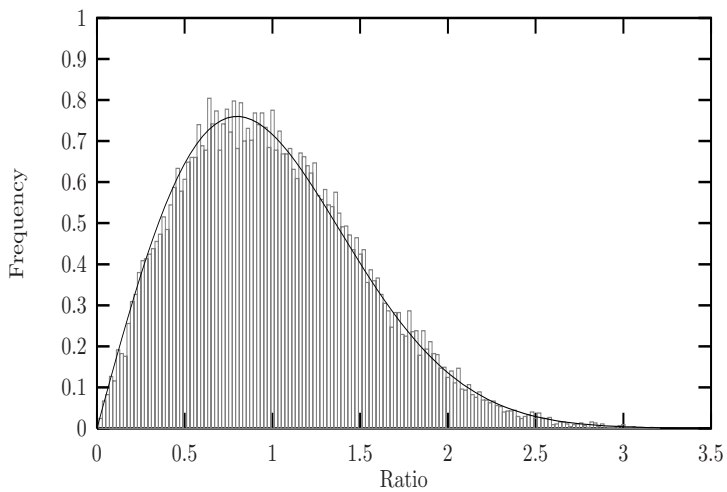
(b)

Figure 5.30: (a) The restored homogeneous synthetic one grey-level SAR data in Figure 5.1(a) and (b) the restored synthetic five grey-levels SAR data in Figure 5.1(b). The restorations are performed using the Gamma *pixel prior* and SA. The Markov chain is inhomogeneous and the cooling schedule used is logarithmic. The data are stretched linearly between their mean  $\pm 3$  std.



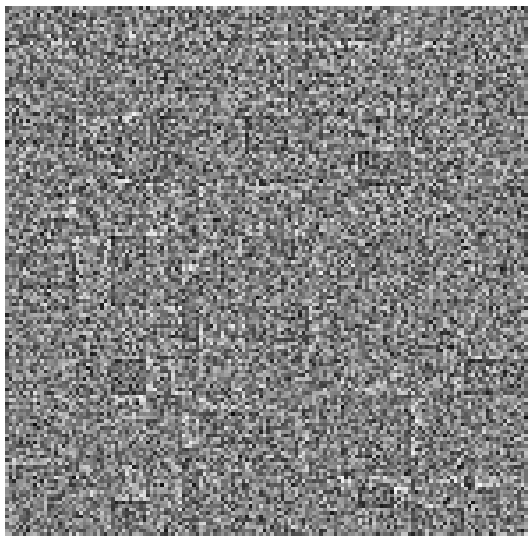


(a)

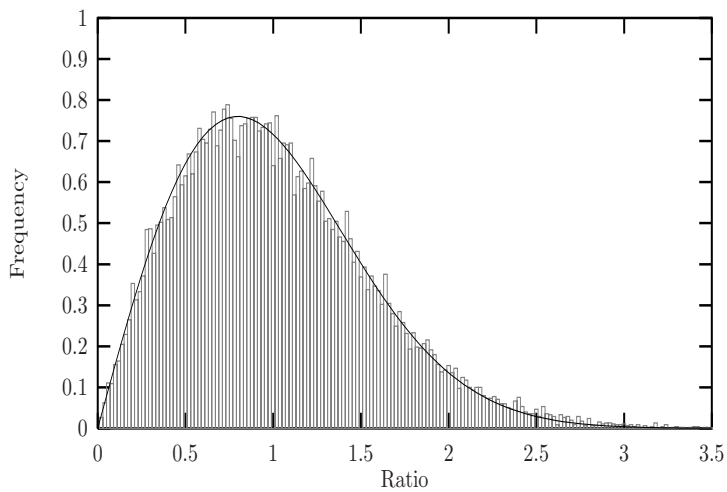


(b)

Figure 5.31: (a) The ratio between the homogeneous synthetic one grey-level SAR data in Figure 5.1 (a) and the restored data in Figure 5.30 (a) using the Gamma *pixel prior* and SA. In (b) is the histogram of the ratio image shown together with the theoretical Rayleigh distribution.



(a)



(b)

Figure 5.32: (a) The ratio between the synthetic five grey-levels SAR data in Figure 5.1 (b) and the restored data in Figure 5.30 (b) using the Gamma *pixel prior* and SA. In (b) is the histogram of the ratio image shown together with the theoretical Rayleigh distribution.

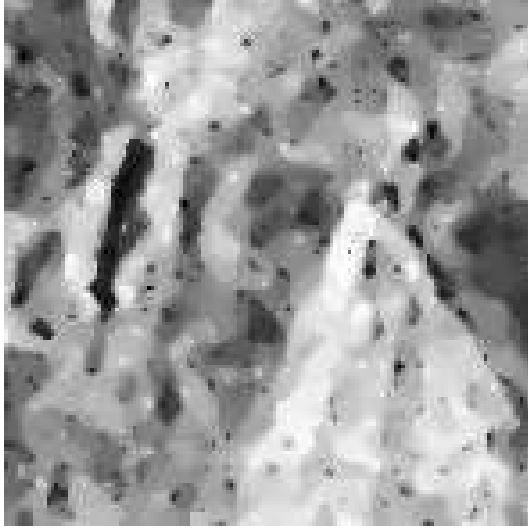


Figure 5.33: The restored C-band VV-polarized EMISAR data in Figure 5.2 using the Gamma *pixel prior* and SA. The cooling schedule is logarithmic with an inhomogeneous Markov chain. The data are histogram equalized using the beta distribution with the parameters 3 and 2.

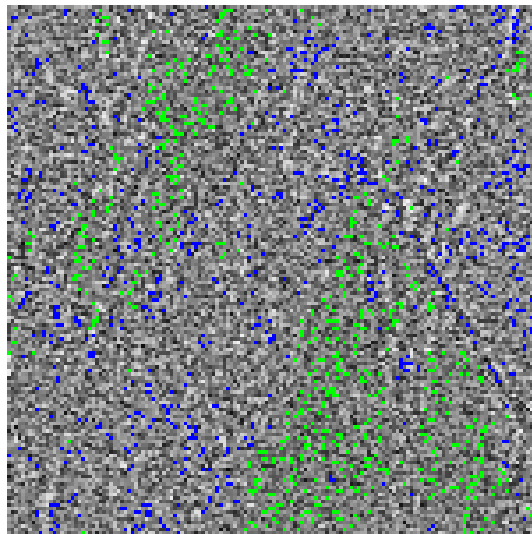
A modified version of the Gamma *pixel prior*, which is implemented in the annealing algorithm is

$$p(x_i|x_j, j \in N_i) \propto \frac{U(x_i)^{k/T-1}}{\Gamma(\frac{k}{T})(T\nu_i/k)^{k/T}} \exp\left\{-\frac{kU(x_i)}{T\nu_i}\right\}. \quad (5.8)$$

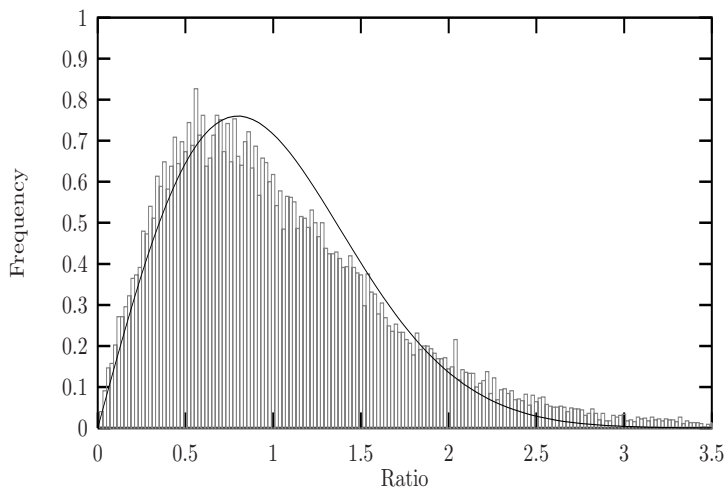
It is important to emphasize, that (5.8) is not converging towards a uniform distribution when the temperature is raised. The proposed (5.8) is therefore inconsistent with (4.1) and the fundamental thermodynamic principle that the energy distribution must converge towards a uniform distribution for  $T \rightarrow \infty$ . We recall that the estimated variance  $S^2$  of (5.8) is given by

$$S^2 = \frac{T\nu_i^2}{k}. \quad (5.9)$$

As mentioned in Section 4.4.4 the decrement rule is of paramount importance



(a)



(b)

Figure 5.34: (a) The ratio between the C-band VV-polarized EMISAR data in Figure 5.2 and the restored data in Figure 5.33 using the Gamma *pixel prior* and SA and (b) a comparison of the corresponding histogram and the theoretical Rayleigh distribution. The cooling schedule is logarithmic with an inhomogeneous Markov chain.

for the quality of the final result. Although the decrements of  $T$  quickly become very small using the logarithmic cooling (4.10) our experiments show that it is more convincing in restoring single-look SAR amplitude data than the exponential schedule (4.9). The logarithmic cooling schedule (4.10) is therefore applied in the SA algorithm. The stochastic sampling scheme used is the Metropolis algorithm and here the random variable used to perturb the system is sampled from a uniform distribution. In order to keep the system close to its thermal equilibrium the random variable is sampled within a range close to the mean of the local neighbourhood configuration.

A short homogeneous Markov chain is with that sufficient to obtain stages between temperature decrements which are close to equilibrium. In addition the temperature decrements quickly become very small using (4.10) as illustrated in Figure 5.29. As the iterations proceed the thermal equilibrium is therefore considered re-established after each decrement using a short Markov chain. In the SA algorithm presented a short Markov chain of length  $l = 1$  is applied. This inhomogeneous Markov chain is chosen in order to prevent too much smoothing between sharp transitions and smaller objects.

Due to the Rayleigh distribution the variance of SAR amplitude data is proportional to the squared mean amplitude level, see (A.1). Since the variance again reflects the thermal energy of the system, different types of e.g. grassland areas may be represented by different temperatures. A common temperature  $T$  for regions with different variances is therefore not appropriate. In order to overcome this problem a Multiple Temperature Annealing (MTA) schedule is introduced. Here  $S^2$ , which according to (5.9) is proportional to  $T$ , is re-estimated from the characteristics of the local neighbourhood configuration for each iteration. Furthermore by using the logarithmic cooling schedule (4.10) the variance of the restored EMISAR data is strongly reduced as the annealing proceeds but it never reaches zero. Because of the MTA-schedule and the fact that the variance never reaches zero the variance of the restored EMISAR data is larger in regions with large mean amplitude levels than in regions with small mean amplitude levels. It should be noted, that by using (5.8) instead of (5.7)  $S^2$  is proportional to  $T$  and not  $(k - 1 + T)T$ . This has the implication for the restored result, that the smoothing effect of (5.8) is larger than the smoothing effect of (5.7).

Using the uninformed sampling strategy above the SA-MTA algorithm quickly converges towards the global energy minimum. This is demonstrated in Figure 5.29 where the thermal energy  $U(x_i)$  and its fluctuations have diminished considerably after only 1000 iterations. The cooling stops when no significant improvements of the statistics of the ratio image are found. Experiments show that this stop criterion is met after 1000 iterations.

The restored result of the synthetic one grey-level SAR data in Figure 5.1 (a)

using (5.8) after the fine tuning, is shown in Figure 5.30 (a). The corresponding tuned parameters are  $\alpha = 2$ ,  $k = 3.75$  and  $T_0 = 0.65$ . In Table A.2(a) is listed a number of statistics derived from the ratio between the synthetic one grey-level SAR data and the restored data. Reading from the Table A.2(a) we find  $\bar{z} = 1.010$ ,  $S^2(z) = 0.267$  and the test statistics  $\chi^2(78)$  is estimated to 91. Since  $p > 0.05$  the  $H_0$  hypothesis is accepted. The absent structure in the ratio image in Figure 5.31(a) is therefore expected as well as the perfect match between the observed frequencies and the theoretical Rayleigh distribution in Figure 5.31(b).

In Figure 5.30 (b) is shown the restoration of the synthetic five grey-levels SAR data in Figure 5.1 (b). In the restored result the transitions between homogeneous regions are relatively sharp, the homogeneous regions appear uniform and there is a high degree of detail preservation, which gives the first impression that the restoration is good. This is supported in the ratio image in Figure 5.32(a), where there is only faint evidence of structure and in the corresponding histogram in Figure 5.32(b), where the observed frequencies are almost Rayleigh distributed. However, with reference to the statistics  $\bar{z} = 1.023$ ,  $S^2(z) = 0.310$  and  $\chi^2(53) = 156$  derived from the ratio image in Table A.2(b), the  $H_0$  hypothesis is rejected.

Figure 5.33 illustrates the restoration of the C-band VV-polarized EMISAR data in Figure 5.2 using (5.8). Again the transitions between homogeneous regions are relatively sharp and homogeneous areas have a smooth appearance. The statistics of the corresponding ratio image in Figure 5.34(a) are  $\bar{z} = 1.0556$ ,  $S^2(z) = 0.4781$  and  $\chi^2(63)$  is estimated to 38855.  $H_0$  is hereby rejected and the bias between the observed histogram and the theoretical Rayleigh distribution is visualized in Figure 5.34(b). The pixels causing this disturbance are located in the intervals 0–0.6 and 2–3.5 and indicated with blue and green colours in Figure 5.34(a). Obviously the test statistics based on ratios of the C-band VV-polarized EMISAR data are worse than statistics based on ratios of the synthetic five-grey-levels SAR data above. This is due to the high number of discontinuities in the C-band VV-polarized EMISAR data. For a description of how discontinuities affect the restorations refer to Section 5.3.

A characteristic feature in the Figures 5.30, 5.30 (b) and 5.33 is the clutter. This clutter is not due to artifacts, but is reflecting the original structure in the SAR data, which is preserved by the annealing algorithm. Another characteristic feature is the salt-and-pepper like appearance caused by single pixels. Some of these single pixels are frozen artifacts generated by the algorithm. This is due to the inhomogeneous Markov chain, which is too short to ensure thermal equilibrium between temperature decrements. Others of these single pixels were originally outliers that are preserved as such by the annealing. This is partly due to an inaccuracy in the optimized parameters, partly due to (5.8), which is not perfect in terms of modeling the actual shape of  $U(x_i)$ . Finally, a number

of the single pixels in Figure 5.33 represent real measurements caused by the interaction between the polarized microwaves and e.g. trees.

## 5.8 Discussion

In this chapter a new approach for restoring SAR data in the framework of MRF-MAP has been presented. This approach relies on ratio images for algorithm optimization. The optimization techniques under study are Iterated Conditional Modes (ICM) and Simulated Annealing (SA).

The Gaussian *a priori* model and ICM in Section 5.3 turned out to be well suited for reproducing homogeneous regions in SAR data. However, when it comes to the preservation of discontinuities and mean amplitude levels, the Gaussian prior performs badly. The performance of the LaPlace *a priori* model, as described in Section 5.5, is better than the Gaussian *a priori* model in terms of reproducing discontinuities and mean levels of amplitudes. However, the preservation of homogeneous areas is worse.

In a need for modeling the positive skewness of the SAR amplitude data, the exponential *a priori* model was selected. The exponential *a priori* model in Section 5.4 proved to be good in terms of preserving mean levels of amplitudes. But again discontinuities are not reproduced satisfactorily. The Gamma distribution provides a good model for the skewed distributed SAR amplitude data. This is utilized in the Gamma *mean prior* in Section 5.6.1 and in the Gamma *pixel prior* in Section 5.6.2 where the energy function is specially designed to preserve discontinuities and homogeneous regions in SAR data. While the performance of the Gamma *mean prior* was quite similar to the LaPlace *a priori* model, the Gamma *pixel prior* turned out to be more convincing when it comes to preserving discontinuities and mean amplitude levels.

Unfortunately the price paid for the high speed of the ICM algorithm is that ICM easily gets trapped in local energy minima. As we have demonstrated this makes the use of ICM for preserving homogeneous areas and details in SAR data doubtful. The other optimization technique, which makes successful use of MRF, is SA. It has the advantage, in preference to ICM, that it is capable of escaping these local energy minima. In order to avoid the artifacts created by ICM the Gamma *pixel prior* is therefore implemented in the SA algorithm. A characteristic property of SAR amplitude data is that the standard deviation is proportional to the mean amplitude value. This is utilized by introducing a MTA schedule, where the temperature is proportional to the variance of the local energy distribution.

Also the 8 pair-site interactions where  $w_c = w$  are implemented in the Gamma *pixel prior* using the SA algorithm. The corresponding restored examples of the synthetic one grey-level and five grey-levels SAR data are displayed in the Figures A.3(a)–(b). A comparison of Figure 5.30 (b) and Figure A.3(b) shows a small improvement in the preservation of edges and details using  $w_c = w$  instead of pair-site interactions with different weights. This is supported by the corresponding statistics in Table A.2, which also indicate that, in terms of preserving mean amplitude level, there is no significant improvement in using the selected weights of the cliques.

The synthetic noise in Figure 5.1 (a) is independent identically-distributed SAR speckle and one therefore could expect the restored equivalent to be a uniform image. However, the restored one grey-level synthetic SAR data in Figure 5.30 do not look homogeneous but have a lot of clutter. This clutter is not due to artifacts, but is due to the natural micro-structure in Figure 5.1 (a), which the SA-MTA algorithm is capable of preserving. In the cases where the clutter is a problem for the restored result one has to e.g. reduce the image by a factor 2 in order to remove the correlation between neighbouring pixels. In this context where the preservation of details in the test sites in Gjern and Mols Bjerger is of paramount importance no reduction or filtering of the EMISAR data is performed prior to the restoration.

The median filter, i.e. the 50% quantile, is known to be better than the mean filter at preserving discontinuities and sharp edges. This is because single unrepresentative pixels in a neighbourhood configuration do not affect the median significantly. For that reason it could be interesting to see how the median filter performs in terms of preserving features in the speckled SAR data. Research done by Rees and Satchell (1997) has pointed out, that although the median filter does have edge-preserving properties, it can introduce significant bias and is not suited for preserving small details in SAR data [68]. However, the MAP estimate (4.3) of the local neighbourhood configurations, which is used in the presented algorithms, is at the mode of the energy distribution corresponding to the 40% quantile in the Rayleigh distribution. Instead of the median filter it therefore seems more appropriate to use the 40% quantile filter. The filtered result is presented in Figure A.6 and the statistics derived from the corresponding ratio image are listed in Table A.2. A comparison between the statistics in the Tables A.1 and A.2 shows, that the MRF-MAP framework is better suited for preserving edges and discontinuities in the impulsive noise environment of SAR speckle than the 40% quantile filter. Note that because the SAR amplitude data are Rayleigh distributed, and thereby positively skewed, the 40% quantile is lower than the mean level. This explains the high  $\bar{z}$  value using the 40% quantile filter in Table A.2.

In Figures A.9 (a)-(b) are presented the segmented results of the synthetic SAR



data in Figures 5.1 (a) and 5.1 (b) using the licensed SA program *segann*. The *segann* algorithm was kindly offered at my disposal by Shaun Quegan of the Sheffield Centre for Earth Observation Science (SCEOS). Even though there is a fundamental difference between a restoration and a segmentation, it is possible to compare their qualitative performances through the statistics of the respective ratio images. Given the specific parameter settings in the two algorithms, the statistics in Table A.2 suggest the qualitative performances of the *segann* algorithm and the Gamma *pixel prior* to be quite similar. That is to say the *segann* algorithm is on the large-scale slightly better in terms of preserving discontinuities and mean amplitude levels whereas the Gamma *pixel prior* is more convincing in terms of preserving small-scale structures and homogeneous regions in SAR data.

A comparison between the test statistics in the Tables A.1 and A.2 shows that the Gamma *pixel prior* implemented in the SA algorithm is superior in terms of preserving discontinuities as well as homogeneous regions in SAR data. It is therefore concluded that the *a priori* model and optimization technique that best fulfills the objective of this study is the Gamma *pixel prior* and the SA-MTA schedule.



## CHAPTER 6

# Gjern

---

In this chapter fieldwork performed within the semi-natural wetland environment at Ladegaards Enge in the river valley of Gjern is presented. The collected *in situ* data are used in Chapter 8 where a possible correlation between the physical properties of the wetland and the restored EMISAR data is investigated.

The fieldwork was initiated at the date of the EMISAR acquisitions 3 and 4 June 1997. In order to support the investigation, supplementary fieldwork was carried out in the autumn of 1998 and in July 1999. The fieldwork comprises a description of vegetation cover, estimation of biomass, soil samples and TDR-measurements. In Sections 3.1.1, 3.1.2 and 3.1.3 is given a brief description of sampling methodologies of *in situ* data.

The area in Ladegaards Enge has been subject to a vast amount of research due to its unique properties for studying e.g. ground-water flow and seepage to surface-water in a catchment. For a thorough investigation within these areas refer to Rasmussen (1996) [16] and Andersen E. (2001) [2].

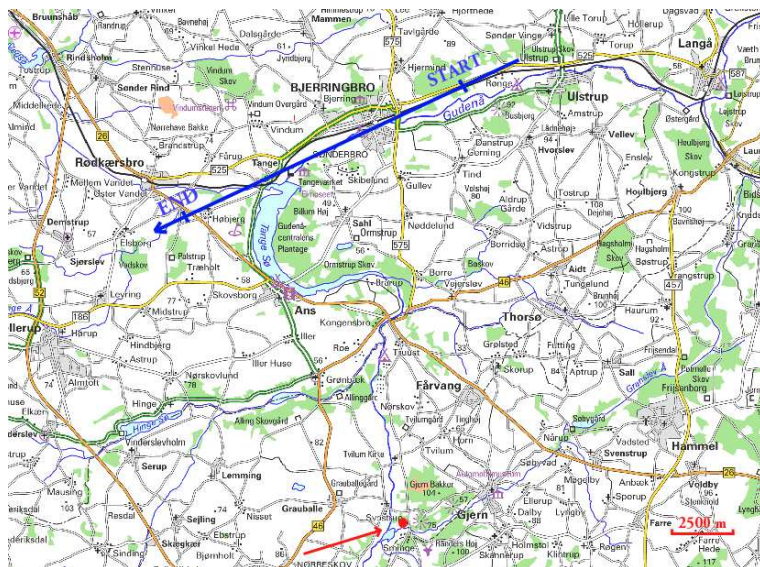


Figure 6.1: Map displaying the geographical placement of the Gjern area. The blue arrow shows the flightline of the EMISAR where the acquisitions are made within the start and end points on 3 June 1997. The EMISAR is looking to the left and the red spot indicates the test site at Ladegaards Enge. (Map material from the Danish Kort- og Matrikelstyrelsen (KMS) is reproduced according to agreement G18/1997 between NERI and KMS.)

## 6.1 Description of test site

The test site at Ladegaards Enge is located in the river valley of Gjern, which is a part of the Gjern catchment in Eastern Jutland in Denmark. The catchment area for the test site is 114 km<sup>2</sup> and the land use is 77% cultivated, 14% forest, 4.5% wetland and riparian meadows and 3% urban areas and roads [16]. The geological history of the catchment starts in the late Oligocene and since then several geological events such as glacial activities have formed the landscape.

For a geographical placement of the area refer to Figure 6.1, where the red spot indicates the test site. In Figure 6.2 the test area is marked within the red crosses on an aerial ortho-photo covering Ladegaards Enge. The ortho-photos in the succeeding are from 1995 and are originally geometrically rectified according to system 34 for Jutland. However, the coordinate system used in the following is Universal Transverse Mercator (UTM), zone 32, datum ED50.



Figure 6.2: An orthophoto from 1995 displaying an aerial view of the test site at Ladegaards Enge. The test area is located within the red crosses. (Ortho-photos are copyright Kampsax 1995.)

The test site is a riparian wet meadow due to a high level of ground-water and during the winter the area is flooded by a stream and in the summer period the conditions are less humid [53]. This particular site has been selected because of its homogeneity. The area can be divided into the three sub-areas I, II and III and within each sub-area the vegetation cover and soil moisture are relatively homogeneous. The wettest part of the test site is sub-area I, which is a swampy area with standing water. This area is numbered 1, 2, 4, 5, 6, 10, 16 in Figure 6.3. Sub-area II, which is intermediate in terms of soil moisture, constitutes number 14 and the third and driest sub-area III is represented by the numbers 3 and 13.

The water table generally follows, with a more subdued form, the contours of the surface topography. In the case of Ladegaards Enge the ground water is near the surface and the 'outcrops' of the water table are typically the river bed. This implies that the soil moisture of the upper layers in the floodplain during periods of low precipitation mainly is a function of the discharge in the river and the local topography.

The sediment in the test area, or floodplain, is sand and silt which is deposited as the river meanders back and forth. As the river overflows its banks, it rapidly decreases in velocity away from the channel and drops most of its sediment. The

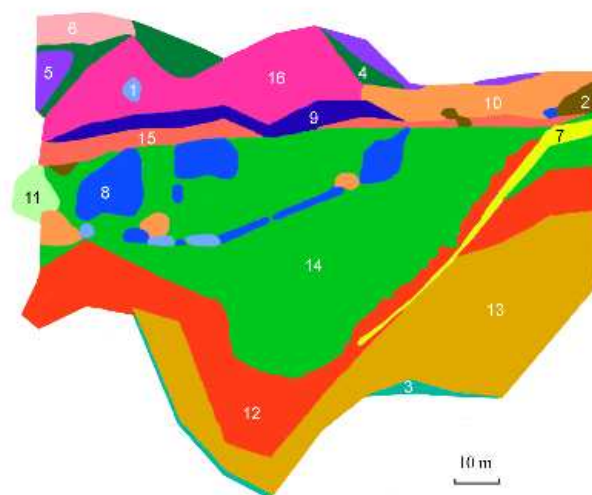


Figure 6.3: Vegetation map illustrating the distribution of the dominant species within the test site at Ladegaards Enge June 1997. (1) *Phalaris arundinacea*, (2) *Carex acuta*, (3) vegetation at the cliff of the river which is a mixture of *Glyceria maxima*, *Deschampsia caespitosa* and *Phalaris arundinacea*, (4) *Glyceria maxima* and *Rumex hydrolapathum*, (5) *Glyceria maxima* and *Typha angustifolia*, (6) *Potentilla palustris*, (7) mixture of *Phalaris arundinacea*, *Glyceria maxima* and *Deschampsia caespitosa*, (8) *Glyceria fluitans*, (9) *Filipendula ulmaria*, (10) *Glyceria maxima* and *Filipendula ulmaria*, (11) *Poa trivialis* and *Carex elata* All., (12) mixture of *Alopecurus pratensis* and *Deschampsia caespitosa*, (13) *Alopecurus pratensis*, (14) *Deschampsia caespitosa*, (15) *Juncus effusus*, (16) mixture of *Glyceria maxima* and *Carex acuta*

coarser fraction of sediments is deposited at the levee or near the channel and the finer fraction of sediments such as silt, clay and organic matter, is layered over most of the floodplain. In this way successive floods have build up natural levees and the plain gradually falls away from the levees for about 100 m [2], [64].

The levee is at the surface a sandy loam and the whole levee profile is classified a Gleyic Fluvisol. The central part of the floodplain is in the upper 8 cm a fibric to hemic peat which is overlaying a clay loam. The wettest part of the test site is a marsh which is a hemic peat at the surface and the classification is Histic/Fibric Histosol [2].

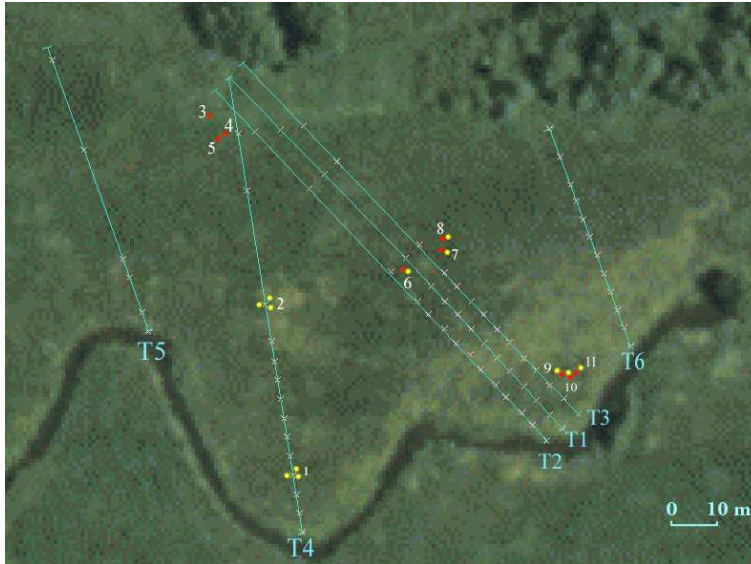


Figure 6.4: Fieldwork performed in Ladegaards Enge on 3 June 1997. The blue lines represent the 6 transects T1 – T6 used for TDR measurements starting at the cliff of the river. The location for the TDR measurements is shown with a pink cross. Biomass samples are collected at the red circles and soil samples are collected at the yellow circles. (Ortho-photos are copyright Kampsax 1995.)

In Figure 6.4 the setup for the fieldwork in 1997 is illustrated. To the south the area is limited by the stream and to the west and east the area is limited by transect T5 and T6. Facing the north the test site is limited by the endpoints of the transects. The six transects in the figure are uniformly distributed within the test site each crossing the three zones of different geomorphological, hydrological and vegetation characteristics.

## 6.2 Ladegaards Enge 1997

The *in situ* data collected during the field campaign 3 and 4 June 1997 comprise biomass and soil samples, estimation of vegetation cover and TDR-measurements. The fieldwork was carried out simultaneously with EMISAR acquisitions in both C-(5.3 Ghz) and L-(1.25 Ghz) band. In Figure 6.1 the flightline of the EMISAR is shown together with the start and end points of the acquisitions. The EMISAR

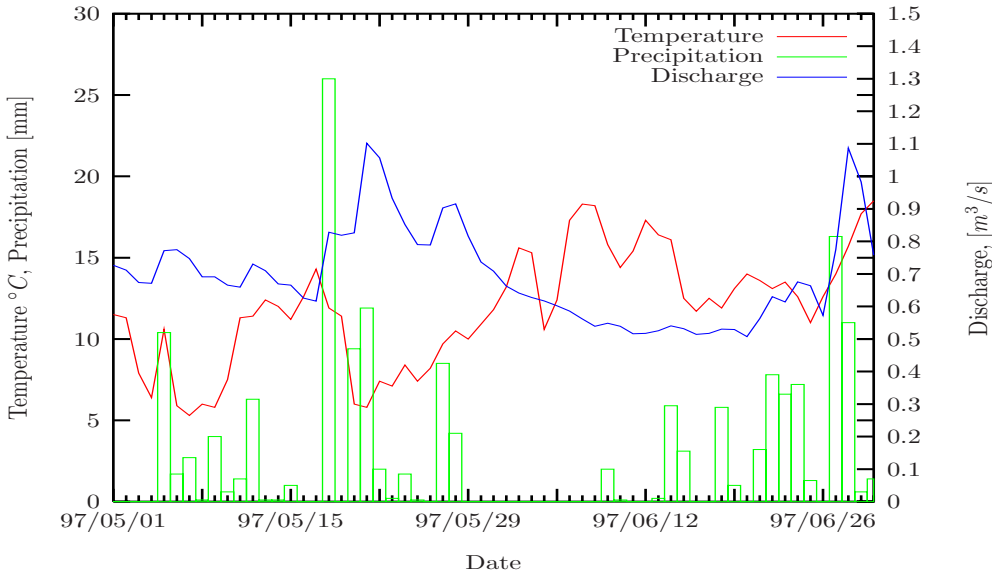


Figure 6.5: Discharge, temperature and precipitation in Ladegaards Enge from 1 May 1997 to 30 June 1997. The fieldwork was performed 3 June 1997. The river discharge is measured at the gauging station in Ladegaards Enge and the temperature and precipitation is averaged over 24 hours within an area of  $40 \text{ km} \times 40 \text{ km}$ . (Copyright Danish Institute of Agricultural Sciences. The hydrometric data are from NERI's gauging station at Sminge Vad).

is looking to the left and the test area at Ladegaards Enge is indicated with the red spot. At the test area the local incidence angle  $\varphi$  is  $50^\circ$ .

During the campaign the weather was hot and dry as it had been some weeks prior to the fieldwork. Furthermore it was calm so wind did not have any significant affect on the interaction between the EMISAR and the vegetation. The general weather conditions within the Gjern area in terms of the temperature and precipitation are illustrated in the Figures 6.5. Here the temperature and precipitation are averaged over 24 hours within an area of  $40 \text{ km} \times 40 \text{ km}$ .

### 6.2.1 Vegetation cover

In June 1997 a botanical determination and registration of the vegetation at Ladegaards Enge was performed by botanist J. Petersen. The vegetation was





Figure 6.6: The boundaries between the dominant species of vegetation within the test site at Ladegaards Enge June 1997 projected upon an orthophoto. (Ortho-photos are copyright Kampsax 1995.)

registered along 13 transects according to a coordinate system with its origin in the centre of the test area and its axes going south–north and east–west. Besides, the vegetation was evaluated along the 6 transects illustrated in Figure 6.4.

For a description of how the botanical determination was carried out refer to appendix D. Based upon the various vegetation data in appendix D maps covering the dominant species and their boundaries are presented in the Figures 6.3 and 6.6.

### 6.2.2 Biomass samples

At the test site at Ladegaards Enge 9 biomass samples were collected 3 June 1997. The samples were grouped in three with each group located within each of the three sub-areas. The positions of the centres of the groups were selected at



(a)



(b)

Figure 6.7: (a) Photo taken 3 June 1997 showing the test-site at Ladegaards Enge. In the foreground is the intermediate sub-area II dominated by *Deschampsia caespitosa* and in the background it is possible to catch a glimpse of the driest part of the site, sub-area III, dominated *Alopecurus pratensis*. Sub-area III dominated by the long vertical straws of *Alopecurus pratensis* is also shown in (b).



(a)



(b)

Figure 6.8: (a) A typical scene from the intermediate sub-area II within Ladegaards Enge dominated by *Deschampsia caespitosa* and (b) shows *Glyceria maxima* and *Carex elata* All. which are pre-dominating in sub-area I, which is the wettest part of the test site. The photos were taken 3 June 1997.

Sub-area	Nr.:	Fresh weight kg/m <sup>2</sup>	Dry weight kg/m <sup>2</sup>	Water weight %
I	$B_3$	6.02	1.14	81.00
	$B_4$	5.54	0.88	84.00
	$B_5$	6.13	0.88	85.70
II	$B_6$	4.69	1.13	75.80
	$B_7$	4.66	0.96	79.30
	$B_8$	7.64	1.32	82.80
III	$B_9$	3.15	0.73	77.00
	$B_{10}$	4.37	1.00	77.10
	$B_{11}$	2.90	0.70	75.90

Table 6.1: Biomass samples collected at Ladegaards Enge 3 June 1997. The index is referring to the numbers of the red circles in Figure 6.4.

random on a map. The positions of the biomass samples within each group were chosen at the points where a thrown object landed. In Figure 6.4 is shown with red circles how the biomass samples are distributed within the test site. Each sample is numbered as it appears from the figure and these numbers correspond to the index numbers in Table 6.1. In Section 3.1.1 is described how the samples were collected and analyzed.

The samples  $B_9$ – $B_{11}$  in Table 6.1 are collected in the sub-area III. This sub-area has the lowest soil moisture content and the ground has a firm appearance. The area was dominated by *Alopecurus pratensis* with a 100% degree of cover and an estimated height of 1.1 m, see Figure 6.7 (b). Due to the long stems the dominating geometrical structure of *Alopecurus pratensis* is vertical, in particular in the eastern part of sub-area III. Although *Alopecurus pratensis* is prevailing *Poa pratensis* and *Phalaris arundinacea* are frequent downstream in the western part of sub-area III.

The distribution of the various species in sample  $B_9$  was *Alopecurus pratensis* 100%, *Festuca rubra* 20%, *Deschampsia caespitosa* 10% and *Rumex acetosa* 2%. In  $B_{10}$  the distribution was 60% for *Deschampsia caespitosa*, *Holcus lanatus* 30%, *Alopecurus pratensis* 30%, *Rumex acetosa* 10% and *Cardamine pratensis* 5%. The contents of  $B_{11}$  are *Alopecurus pratensis* 100% and *Holcus lanatus* 10%.

The biomass samples  $B_6$ – $B_8$  were collected in the intermediate sub-area II in terms of soil moisture content. Here the ground was soft and saturated with water. In this area *Deschampsia caespitosa* was dominating with an estimated degree of cover of 100%. Figures 6.7 (a) and 6.8 (a) show a view over the sub-

area and a close up of *Deschampsia caespitosa*. The height was 0.20 m and the tussocks were growing close together. The stems from the fresh vegetation were mainly ranging from oblique to vertical and below the fresh vegetation the prevailing direction of the withered material was horizontal. From the surface of the soil the approximate length of the fresh stems was 20 cm.

The content of sample  $B_6$  was 100% *Deschampsia caespitosa*. In  $B_7$  *Deschampsia caespitosa* again was dominating with 100% and *Ranunculus repens* 2%. For  $B_8$  the estimate was 100% for *Deschampsia caespitosa*.

In the wettest sub-area I the samples  $B_3$ – $B_5$  have been collected. This area, which is a mixture of fresh and withered material, is pre-dominated by *Glyceria maxima* and *Carex elata* All. that grow in water, see Figure 6.8 (b). The fresh vegetation is randomly orientated whereas the withered material to a large extent is horizontal. The estimated height is 0.5 m. The biomass sample  $B_3$  contains 20% *Carex elata* All. and 80% *Glyceria maxima*. In  $B_4$  the distribution was 80% *Glyceria maxima* and 20% *Carex elata* All. and finally  $B_5$ , which contains 30% *Glyceria maxima* and 20% *Carex elata* All.

Although the number of biomass samples is very small evidence suggests that the fresh and dry weight of the samples in Table 6.1 increases with increasing soil moisture content. This is not surprising viewed in the light that the higher soil moisture content enables a more dense and vigorous vegetation. Besides additional water from the environment might affect the estimates too. This is in particular the case concerning the samples  $B_3$ – $B_5$ , which explains the higher content of water in the leaves in weight percent.

### 6.2.3 Soil samples

During the fieldwork 3 June 1997 at Ladegaards Enge 12 soil samples were collected. These samples were distributed all over the test site within the two sub-areas II and III. Due to the standing water no soil samples were collected in the swampy sub-area I. For a description concerning the methodology in terms of collecting and analyzing the samples refer to Section 3.1.2. In Figure 6.4 the yellow circles show the locations for the collection of these soil samples. The numbers at the circles correspond to the index numbers of the soil samples in Table 6.2.

In Table 6.2 the soil samples  $S_9$ – $S_{11}$  were collected in the sub-area III with the lowest soil moisture content. Soil sample  $S_9$  was sampled at the same location as  $B_9$ ,  $S_{10}$  under  $B_{10}$  and likewise  $S_{11}$  under  $B_{11}$ . For a description of the vegetation refer to Section 6.2.2.

Sub-area	Nr.:	$\rho_f$ g/cm <sup>3</sup>	$\rho_d$ g/cm <sup>3</sup>	$\rho_s$ g/cm <sup>3</sup>	$\theta_p$	$\theta_w$ vol. %	$\theta_r$ vol. %	$\Delta m_d$ weight %
II	$S_{1a}$	0.980	0.48	2.27	0.73	49.85	68	17.5
	$S_{1b}$	1.37	0.76	2.22	0.73	60.07	83	14.1
	$S_{1c}$	1.15	0.63	2.34	0.71	51.21	72	13.5
	$S_{2a}$	0.88	0.14	1.29	0.91	73.81	81	70.0
	$S_{2b}$	1.04	0.21	1.16	0.91	83.45	92	52.9
	$S_{2c}$	1.01	0.18	1.13	0.91	83.20	92	57.8
	$S_6$	0.67	0.12	1.41	0.77	55.04	71	69.2
	$S_7$	0.81	0.11	1.23	0.84	69.21	83	79.1
	$S_8$	1.02	0.23	1.14	0.78	79.16	101	44.8
III	$S_9$	0.77	0.42	3.17	0.83	35.29	42	25.2
	$S_{10}$	0.79	0.34	2.14	0.79	45.47	58	31.8
	$S_{11}$	0.98	0.47	2.25	0.81	50.76	63	22.8

Table 6.2: Soil samples collected at Ladegaards Enge 3 June 1997. The fresh-, dry- and the saturated bulk densities of the soil samples are referred to as  $\rho_f$ ,  $\rho_d$  and  $\rho_s$ . The porosity of the samples is  $\theta_p$ , the volumetric water content is  $\theta_w$  and the relative water content  $\theta_r$ . The organic content given in percent of the dried soil sample is  $\Delta m_d$ . The index of numbers of the samples is referring to the numbers of the yellow circles in Figure 6.4.

The soil samples  $S_{1a}$ ,  $S_{1b}$  and  $S_{1c}$  were collected at transect T4 12 m from the river. This corresponds to the intermediate sub-area II area in terms of soil moisture. The vegetation at that location was characterized by *Phalaris arundinacea* 80%, *Poa trivialis* 30% and *Alopecurus pratensis* 10%.

Also the samples  $S_6$ – $S_8$  were collected in the sub-area II. Here sample  $S_6$  was collected under  $B_6$ ,  $S_7$  under  $B_7$  and finally  $S_8$  under  $B_8$ . The soil appeared wet and soft and again refer to Section 6.2.2 for a description of the vegetation.

Samples  $S_{2a}$ ,  $S_{2b}$  and  $S_{2c}$  in Figure 6.4 and Table 6.2 were from transect T4 collected 48 m from the river. Here the distribution of the various species was: *Deschampsia caespitosa* 80%, *Ranunculus repens* 20% and *Poa pratensis* < 5%.

Roughly speaking the gathered samples can be divided into two groups. One group is collected in sub-area III close to the levee and the other is collected in sub-area II in the floodplain. This is also reflected in Table 6.2 where the samples  $S_9$ – $S_{11}$ , which were collected in sub-area III, have a lower volumetric water content  $\theta_w$  compared to the samples  $S_{1a}$ ,  $S_{1b}$ ,  $S_{1c}$  and  $S_{2a}$ ,  $S_{2b}$ ,  $S_{2c}$  and  $S_6$ – $S_8$ , which were collected in the wetter sub-area II.

However, it is noticeable from Table 6.2 that within sub-area II variations in moisture content also exists. This is the case when addressing the central part of sub-area II where  $S_{2a}$ ,  $S_{2b}$  and  $S_{2c}$  have a higher  $\theta_w$  compared to the samples  $S_6$ – $S_8$ . In other words the general soil moisture content in the floodplain is increasing downstream, which possibly reflects the falling terrain.

Concerning the organic content in weight percent  $\Delta m_d$  it is evident from Table 6.2 that there is a significant difference between whether the samples are gathered at the relatively dry levee or in the wetter floodplain. The high organic content in the floodplain is caused by the fibric to hemic peat whereas the organic content at the levee is lower due to the sandy loam.

### 6.2.4 Time-Domain Reflectometry

The fieldwork 3 June 1997 also included preliminary TDR measurements. The purpose of these measurements was to evaluate the spatial distribution of the apparent dielectric constant  $K_a$  within the test site and the autocorrelation between points of measuring. This is relevant because  $K_a$  is strongly affected by the soil moisture content. For a brief introduction to the TDR device and the fundamental theory refer to Section 3.1.3.

The TDR measurements were performed along the six transects T1–T6 shown in Figure 6.4. These transects were distributed to cover the whole test area. The transects are all crossing the three sub-areas of different soil moisture content and vegetation characteristics and the spacing between the transects is at least 4 m. The measurements start on the levee of the river and the spacing between the points of measurement along the transects is 4 m. The measuring points are shown with pink crosses in Figure 6.4. At each location 3–5 TDR measurements were made within an area of approximately 80 cm  $\times$  80 cm.

At each point of measuring the average apparent probe length  $\bar{L}_a$  is estimated. Figure 6.9 illustrates the graphical variation of  $\bar{L}_a$  and the estimated volumetric water content  $\theta_w$  along the transects T1–T6. Here the  $\theta_w$  is estimated using (3.2) and the third-order polynomial relationship (3.1) published by Topp *et al.* (1980) [80]. Topp's relation is valid for four soils ranging from sandy loam to heavy clay soils. As it appears from Figure 6.9 there is an almost linear relationship between  $\bar{L}_a$  and the volumetric water content within the first 40 m of the transects using (3.1) and (3.2).

As previously mentioned the spacing between neighbouring points of measurements within Ladegaards Enge is at least 4 m. This is too much for our purpose and interpolation between the points and transects is therefore of paramount

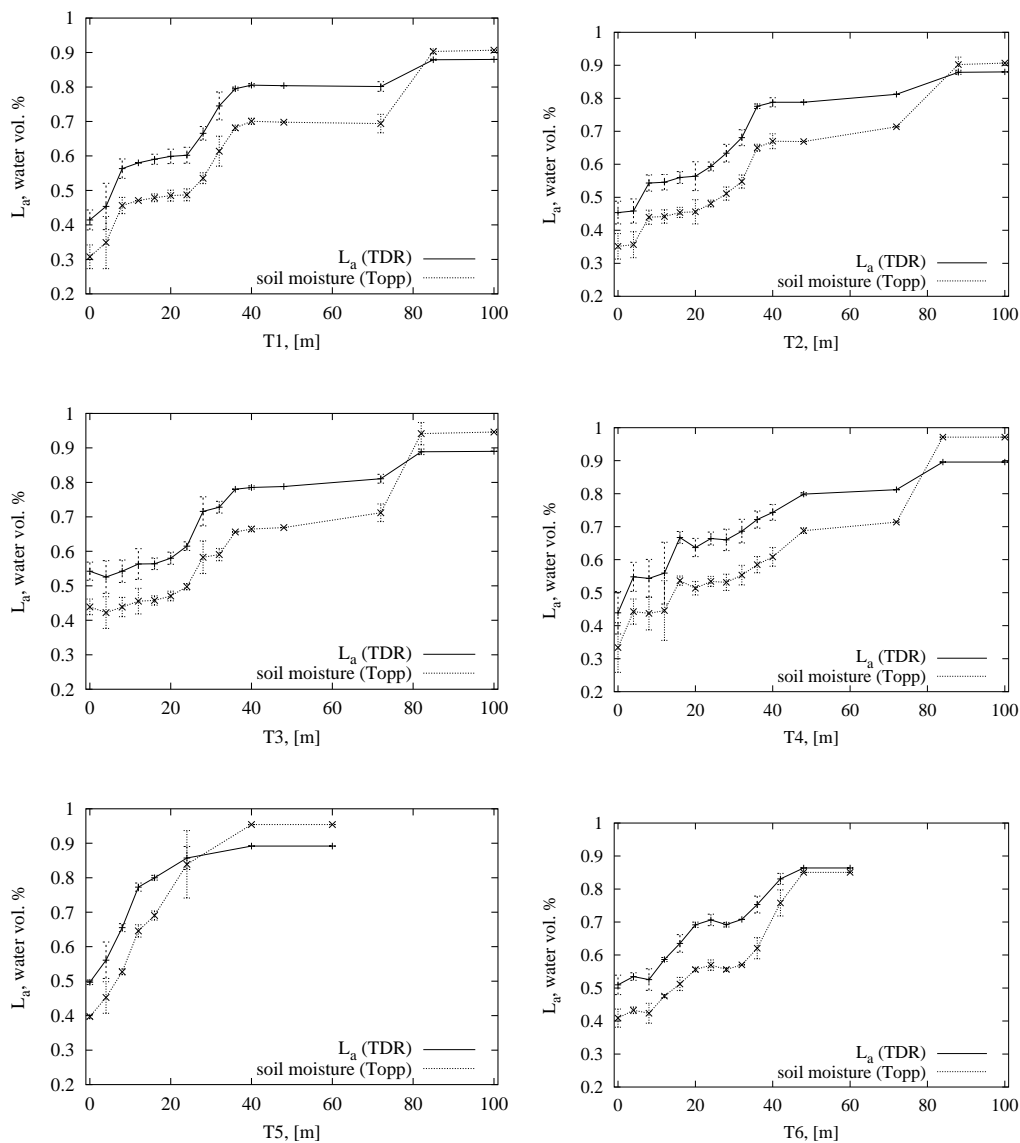


Figure 6.9: Graphic plot illustrating the variation of the apparent probe length  $\bar{L}_a$  in metres and the volumetric water content in percent along the transects T1–T6 at Ladegaards Enge in Gjern 3 June 1997. The volumetric water content is estimated from a third-order polynomial relationship published by Topp *et al.* (1980). The errorbars indicate the standard deviation of the measurements.



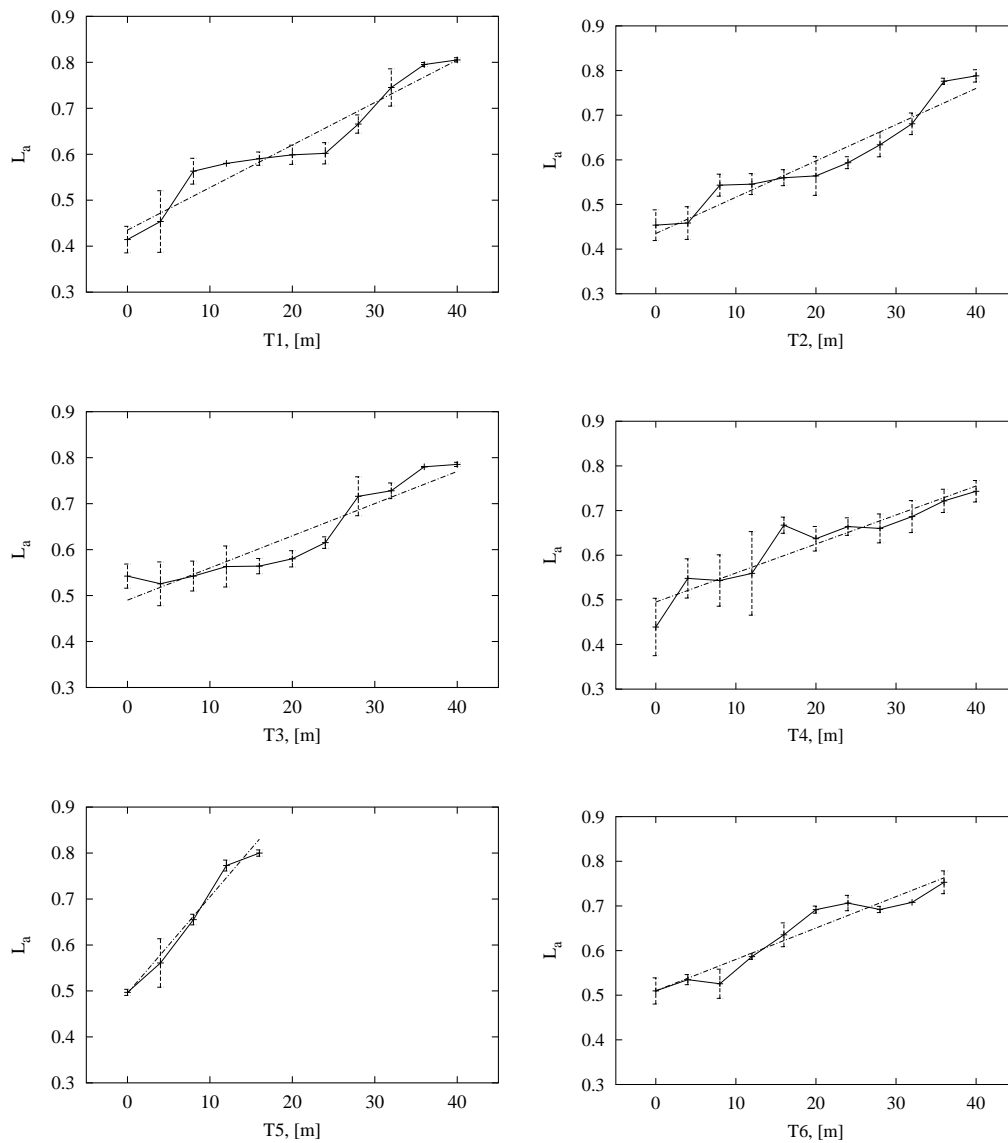


Figure 6.10: Plot illustrating the variation in the apparent probe length  $\bar{L}_a$  in metres along the first 40 m of the transects T1–T6 at Ladegaards Enge in Gjern 3 June 1997. The straight line represents the best linear fit in a least squares sense.

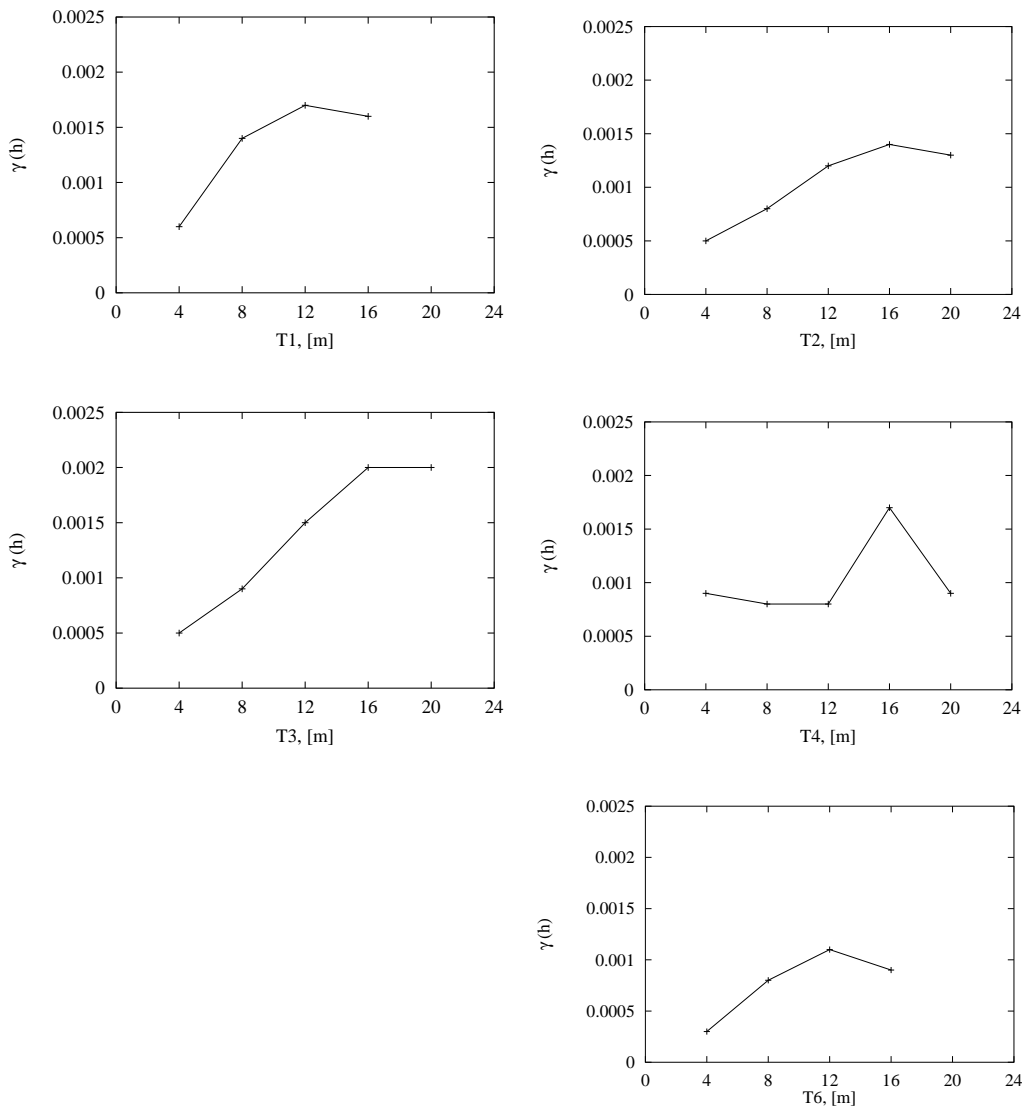


Figure 6.11: Experimental semivariograms of the apparent probe length  $\bar{L}_a$  along the transects T1–T4 and T6 at Ladegaards Enge in Gjern 3 June 1997. Due to the small number of measurements the semivariogram concerning T5 is left out.

importance in order to generate an interpolated map to be used in further analyses with other *in situ* data. The interpolation is provided by the "optimal prediction" method kriging described in Section 3.2, which requires spatial correlations between neighbouring points.

As it appears from the various plots in Figure 6.9 there is a trend in the data due to the increasing moisture content. In order to calculate the autocorrelation this trend has to be subtracted. By assuming a linear trend within the first 40 m of the transects we have estimated the best linear fit using a linear least squares regression. In Figure 6.10 the variation in  $\bar{L}_a$  along the first 40 m of the transects T1–T6 is displayed. The straight line represents the best linear fit in a least squares sense. After subtracting the trend the spatial autocorrelation is estimated using semi-variograms. Based on (3.3) the experimental semi-variograms are calculated for each of the transects T1–T6 and shown in Figure 6.11.

Unfortunately none of the semi-variograms in Figure 6.11 are suitable in terms of evaluating the nugget effect, sill and range of influence. This circumstance is due to the number of point pairs  $N(h)$  in (3.3), which is too small to obtain a significant semi-variogram. It is therefore not possible to use kriging for interpolating between points of TDR-measurements performed 3 June 1997. However, the plots in Figure 6.10 suggest that TDR-measurements that are 4 m or less apart are correlated.

In order to construct a low resolution map covering  $K_a$  at Ladegaards Enge 3 June 1997 we therefore in the following apply an alternative approach.

## 6.3 Ladegaards Enge 1998–99

In order to support the fieldwork performed in June 1997 in Ladegaards Enge supplementary fieldwork was required. The additional fieldwork took place in the autumn of 1998 and in July 1999 and was split between an estimation of the micro-topography, additional soil samples and TDR measurements.

### 6.3.1 Micro-topography

In collaboration with agronomist H. E. Andersen additional fieldwork was performed in Ladegaards Enge during the fall of 1998 with the purpose of measuring topography. The topography is measured according to the Danish National Ver-

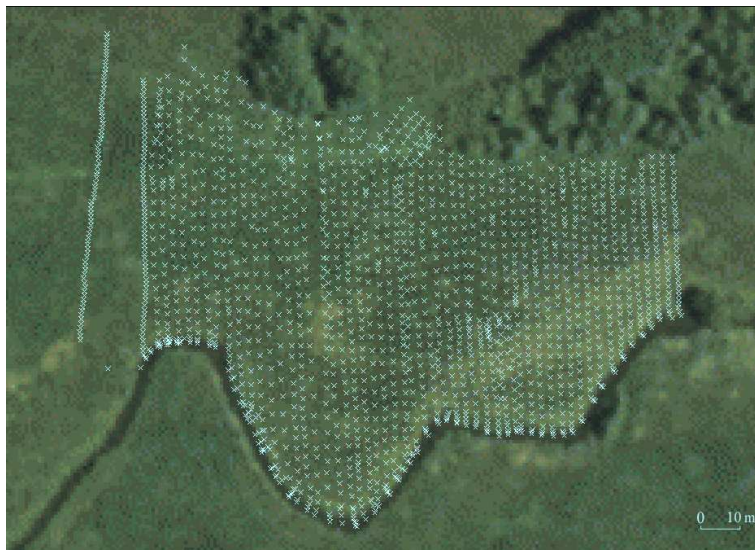


Figure 6.12: A map illustrating the points of topography measurements performed in the autumn of 1998 at the test site in Ladegaards Enge. The points are displayed on an ortho-photo from 1995 covering the area. (Ortho-photos are copyright Kampsax 1995.)

tical Reference system called Dansk Normal Nul (DNN), which is height above sea level. These measurements were carried out because the volumetric water content in the upper soil layer is strongly governed by the micro-topography in this area. Or in other words the micro-topography reflects the soil moisture content. The device to be used for surveying was a Theodolite which is a level and electronic distance measuring instrument.

The micro-topography in Ladegaards Enge is estimated with the purpose of covering spatial variations within the range of 2 m. Therefore the sampling is very dense in order to ensure that neighbouring points are correlated. The layout for the fieldwork is illustrated in Figure 6.12 where the measurements of the topography were made at the crosses.

The points of measurement are irregularly distributed over the test site and the average distance between the points is 2 m. At each point one measurement is made. Subsequently the coordinates of the points have been converted to UTM, zone 32, ED50 and the level to metres above sea level. Figure 6.13 shows a contour map over Ladegaards Enge based on the measurements. The contours of the micro topography are drawn using a smooth cubic spline interpolation. The distance between the isolines is 10 cm and as expected the level is highest

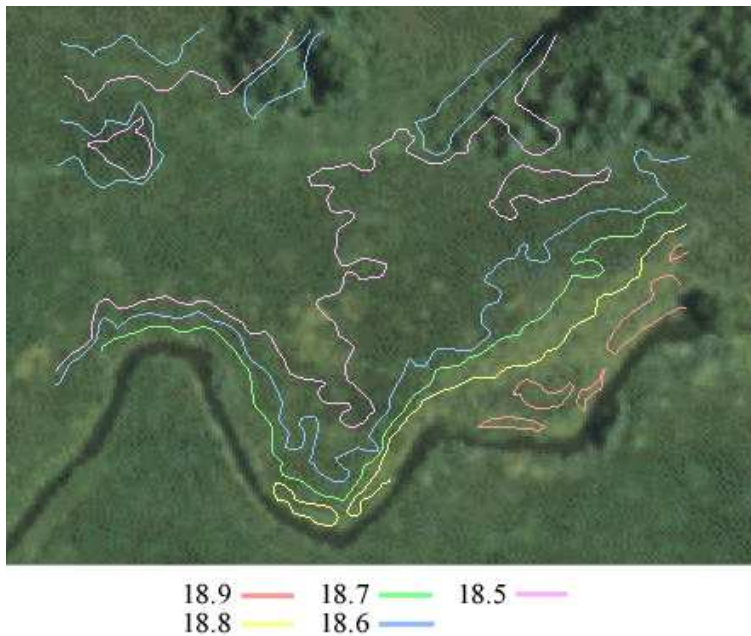
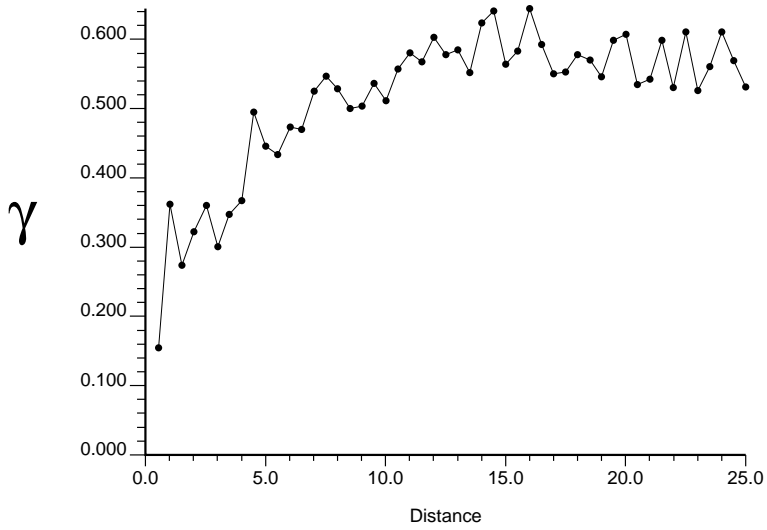


Figure 6.13: A map illustrating the contours of the micro topography [m] in the autumn of 1998 in the test site at Ladegaards Enge. The level is highest at the levee and is then gradually falling towards the north. The contours are based upon the topography measurements in Figure 6.12. (Ortho-photos are copyright Kampsax 1995.)

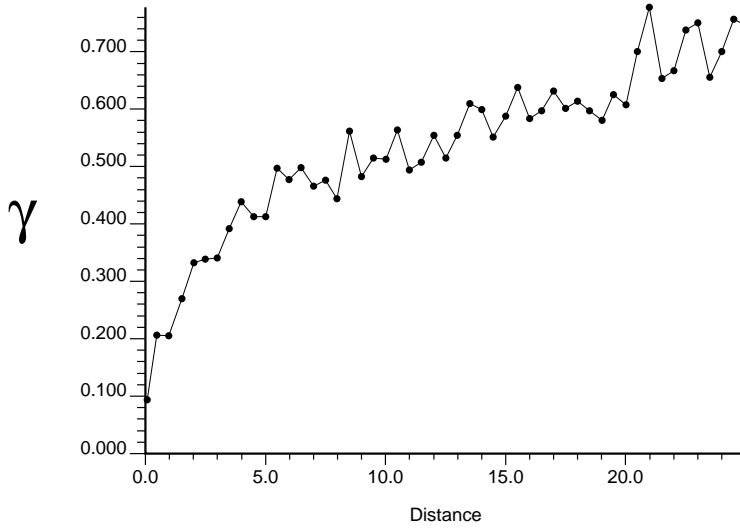
at the levees and is then gradually falling towards the north.

In order to combine topography data at every desired point with the other *in situ* data available, spatial interpolation is applied. The method used for interpolating the topography data is kriging because it e.g. handles spatial autocorrelation and is the best linear unbiased estimator. For a brief description of the technique refer to Section 3.2.

Due to a trend in the topography in the area close to the levee the experimental semi-variogram (3.3) is performed on sample data from the floodplain, which is



(a)



(b)

Figure 6.14: Experimental semi-variogram based on topography data from Lade-gaards Enge. In (a) the direction for the semi-variogram is north-south and in (b) the direction for the semi-variogram is east-west.

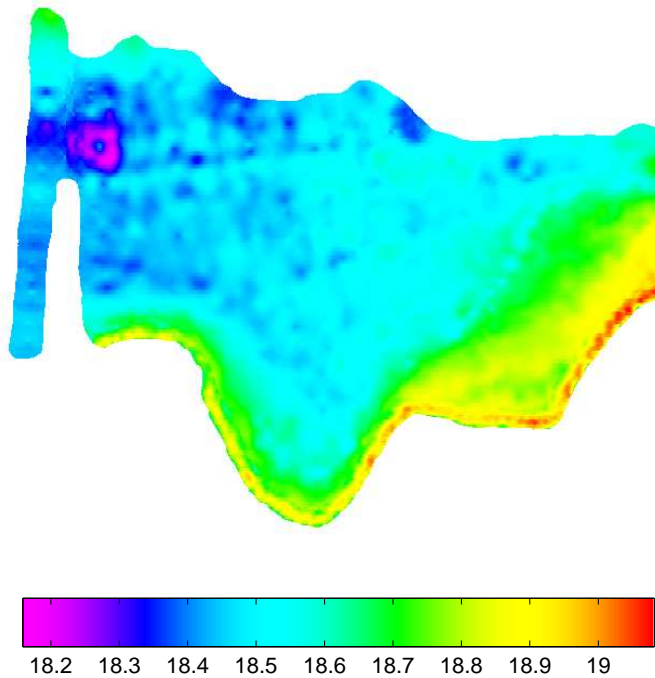


Figure 6.15: Kriged map of the topography [m] at Ladegaards Enge. A spherical structure is used with 5 m as the range of influence and the nugget effect 0.14. The spacing of grid nodes is 0.25 m and the coordinate system is UTM zone 32 (ED50).

the flattest part of the test site. This can be justified because the scale of the autocovariance structure to be modeled has a range of 5 m. This is much less than the scale of the autocovariance structure that the levee is a part of, which is approximately 20 m.

In order to analyze whether or not anisotropy exists in the autocovariance function the experimental semi-variogram is made in two directions, one in the north-south direction and one in the east-west direction. The two semi-variograms are shown in Figure 6.14. Due to the similarity in the semi-variograms we assume the autocovariance structure to be isotropic and therefore the average nugget effect is  $0.14 \text{ m}^2$ , range of influence 5 m and sill  $0.45 \text{ m}^2$ . As it appears from the figures the covariation between measurements are not zero for measurements taken further apart from the range of influence. This is due to the different autocovariance structures at different scales.

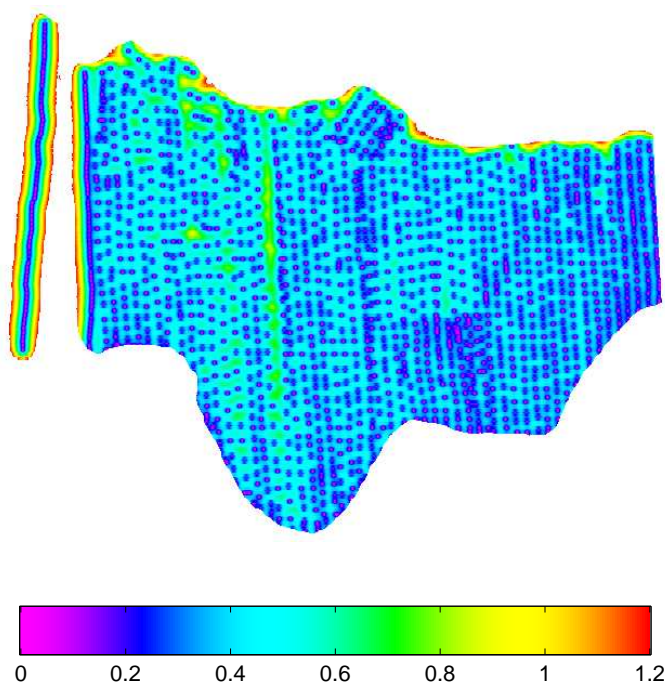


Figure 6.16: The estimated krigingvariance [ $m^2$ ] corresponding to the kriged map in Figure 6.15 of the micro topography in the test site at Ladegaards Enge. The coordinate system is UTM zone 32 (ED50).

In Figure 6.15 is shown the interpolated map of the topography in Ladegaards Enge using ordinary kriging (OK). The interpolation is based on the isotropic spherical model for the experimental semi-variogram (3.3), which is shown in the Figure 6.14. The spacing of grid nodes is 0.25 m, the search radius used for kriging is 6 m and the minimum and maximum number of data points is 2 and 80. In Figure 6.16 is the corresponding krigingvariance shown and we note that the variance is small close to the points of measurements.

### 6.3.2 Time-Domain Reflectometry

The TDR measurements performed in June 1997 turned out not to be sufficient in terms of evaluating the apparent dielectric constant  $K_a$  of the top soil layers at Ladegaards Enge. Therefore additional TDR-measurements were performed



12 July 1999 in order to study the spatial variation of  $K_a$ . For a brief description of the TDR-measurements refer to Section 3.1.3.

The TDR measurements constitute a regular grid as illustrated in Figure 6.17 and are carried out along transects which are parallel with transect T1 in Figure 6.4. Thereby the transects cuts through the three zones of different soil moisture and vegetation characteristics. In Section 6.3.1 it was shown that the autocovariance structure of the topography has a range of 5 m. If the soil moisture, and thereby  $K_a$ , follows the topography we can assume that the autocovariance structure of  $K_a$  also has a range of 5 m. The spacing between the transects is therefore 4 m and the interval between points of measurements is alternately 4 m and 8 m along the transects.

In order to reduce the variance 4–6 TDR readings are made within an area of 80 cm  $\times$  80 cm at each point of measurement and subsequently the readings are averaged. The TDR measurements are performed within the first 20–40 m of the transects starting at the levee of the river. Beyond the point of the 20–40 m the soil was saturated and consequently no significant changes in  $K_a$  occurred.

Based on the TDR measurements and a cubic spline interpolation a preliminary contour map showing  $K_a$  is presented in Figure 6.18. Here the isolines show similarities with the isolines in Figure 6.13, which indicates that  $K_a$ , and thereby the soil moisture, is affected by the topography. In order to evaluate the temporal variation of  $K_a$  the TDR measurements performed in June 1997 at T1 were repeated in July 1999. This enables a comparison between measured  $K_a$  values in 1997 and in 1999 at T1. The variation of  $K_a$  along T1 in 1997 and 1999 is illustrated in Figure 6.19. As the figure shows the conditions were generally drier in 1997 than 1999 within the test site. However, beyond the point of 35 m at T1 the soil moisture conditions were the same.

### 6.3.3 Soil samples

As a part of the additional fieldwork 3  $\times$  10 soil samples were collected 12 July 1999. For a description concerning the methodology in terms of collecting and analyzing the samples refer to Section 3.1.2. These soil samples are collected along T1 in Figure 6.4 and sampled at the yellow circles in Figure 6.17. This strategy is chosen because T1 cuts through the three sub-areas in places that are representative in terms of soil moisture and vegetation characteristics. The spacing between sampling points is 4 m, which as the succeeding sections will show, is sufficient to ensure correlation between soil moisture content and possibly organic matter.

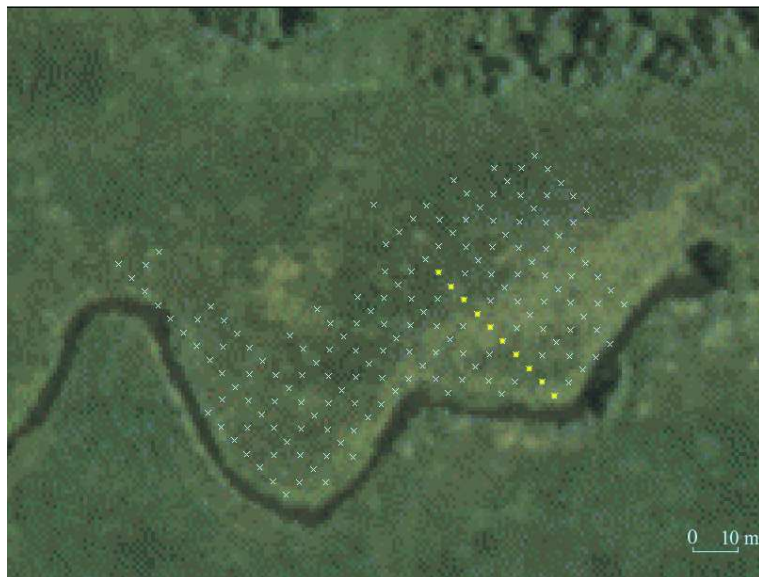


Figure 6.17: The location for TDR measurements and soil samples for the additional fieldwork performed on 12 July 1999. The points for TDR measurements are marked with a blue cross and the location for the collection of soil samples are indicated by yellow circles. The locations of the TDR measurements and the soil samples are coincident with transect T1 in Figure 6.4. (Ortho-photos are copyright Kampsax 1995.)

Three samples were collected within an area of  $30\text{ cm} \times 30\text{ cm}$  at each location starting at the levee of the river. The soil samples were collected within the first 36 m of transect T1. Samples beyond the point of 36 m were not necessary due to the saturated soil. In order to ensure a small estimation variance the derived soil characteristics of the three samples at each location are averaged and listed in Table 6.3.

The essence of Table 6.3 is as expected that the derived volumetric water content  $\theta_w$  is increasing away from the river. This is illustrated graphically in Figure 6.19 where the variation of  $\theta_w$  along T1 is shown. The figure again indicates that there exists a relationship between  $\theta_w$  and the topography.

In terms of the organic content one would expect there to be variations too due to the sandy loam at the levee and the organic fibric to hemic peat in the central parts of the floodplain. Indeed, this is also the case as reflected in Table 6.3 where there is an increase in  $\Delta m_d$  away from the levee. Furthermore  $\rho_d$  and  $\rho_s$  are decreasing away from the river as the porosity  $\theta_p$  is increasing which also

T1 m	$\rho_f$ g/cm <sup>3</sup>	$S^2(\rho_f)$ g <sup>2</sup> /cm <sup>6</sup>	$\rho_d$ g/cm <sup>3</sup>	$\rho_s$ g/cm <sup>3</sup>	$\theta_p$	$\theta_w$ vol. %	$\theta_r$ vol. %	$\Delta m_d$ weight %
0	1.52	0.01	1.05	1.64	0.59	47.47	79.67	8.6
4	1.28	0.0009	0.60	1.37	0.77	67.84	88.37	18.5
8	1.29	0.0001	0.62	1.39	0.77	67.63	87.57	19.4
12	1.40	0.0036	0.76	1.45	0.70	64.60	92.93	13.8
16	1.32	0.0169	0.67	1.42	0.74	64.63	86.90	18.1
20	1.41	0.0004	0.74	1.48	0.74	67.22	90.43	16.5
24	1.43	0.0036	0.78	1.50	0.71	64.74	90.39	13.7
28	1.21	0.0001	0.41	1.26	0.85	79.23	93.45	26.3
32	1.15	0.0009	0.32	1.20	0.88	82.97	94.35	32.5
36	1.15	0.0016	0.32	1.17	0.84	82.40	97.90	33.4

Table 6.3: Soil samples collected at Ladegaards Enge July 1999. The fresh, dry and saturated bulk densities of the soil samples are referred to as  $\rho_f$ ,  $\rho_d$  and  $\rho_s$ . The porosity of the samples is  $\theta_p$ , the volumetric water content is  $\theta_w$  and the relative water content  $\theta_r$ . The organic content given in percent of the dried soil sample is  $\Delta m_d$ . The variance of the bulk density of the fresh soil samples is  $S^2(\rho_f)$ . The samples are collected along transect T1 in Figure 6.4 starting at the cliff of the river. The sites of collection are shown in Figure 6.17 with yellow circles. The distance between the sites is 4 m and at each site 3 samples were collected. The calculated characteristics in the Table are based upon an average of the 3 samples at each site.

indicates an increase in the organic content.

The soil samples were collected at the locations of the TDR measurements and immediately after that the TDR measurements were made. By doing so it is possible to analyze to what extent the variations in  $K_a$ , the organic matter and  $\theta_w$  are coincident. Here the  $K_a$  values were calculated from the TDR measurements and  $\theta_w$  and the organic matter were derived from the soil samples. By examining Figure 6.19 it is striking that there exists an almost linear relationship between  $K_a(1999)$  and  $\theta_w$  derived from the soil samples. This indicates that  $K_a$  reflects the soil moisture conditions within Ladegaards Enge.

The estimated  $\theta_w$  along T1 using  $K_a(1999)$  and Topp's relation (3.1) is also shown in Figure 6.19. Here the estimated  $\theta_w$  derived from the soil samples is diverging compared to the estimated  $\theta_w$  based on Topp's relation. This deviation is also obvious in Figure 6.20 where our empirical relationship between  $K_a$  and  $\theta_w$  at T1 in Ladegaards Enge is shown together with the relationship by Topp. Here it should be noted that our calibration curve is improper in the sense that it is based on soil samples collected in two sub-areas with two different soil types.

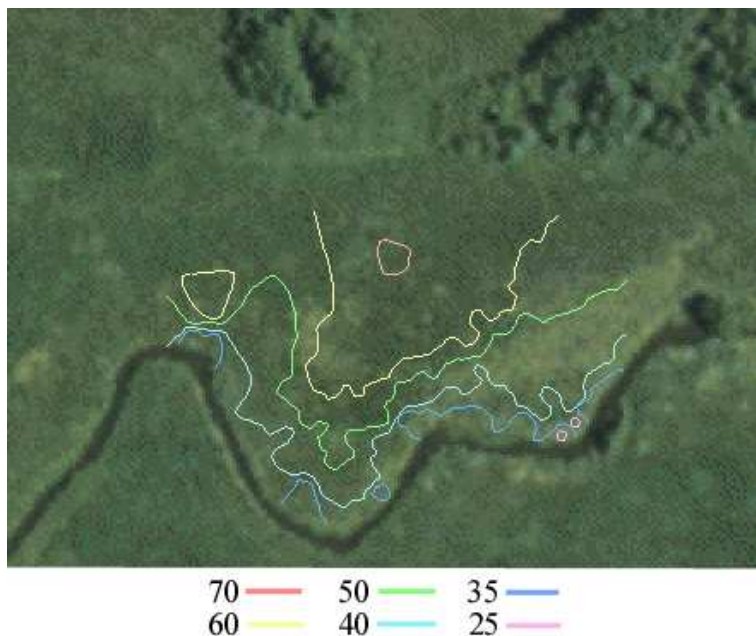


Figure 6.18: A map illustrating  $K_a$  in the test site at Ladegaards Enge 12 July 1999. The contours are based upon TDR readings shown in Figure 6.17. (Ortho-photos are copyright Kampsax 1995.)

However, the bias between the two soil types does not affect the conclusion that Topp's calibration function is unsuitable for the organic soil types at Ladegaards Enge.

## 6.4 Fusion of topography and $K_a$

In Sections 6.3.3 and 6.3.2 it was indicated that a relationship between the volumetric water content of the upper soil layer and the topography exists. In this section this relationship is further analyzed and  $K_a$  within Ladegaards Enge 3 June 1997 is reconstructed. In addition a possible connection between the volumetric water content of the upper soil layer in Ladegaards Enge and the discharge in the river during periods of low precipitation is investigated.

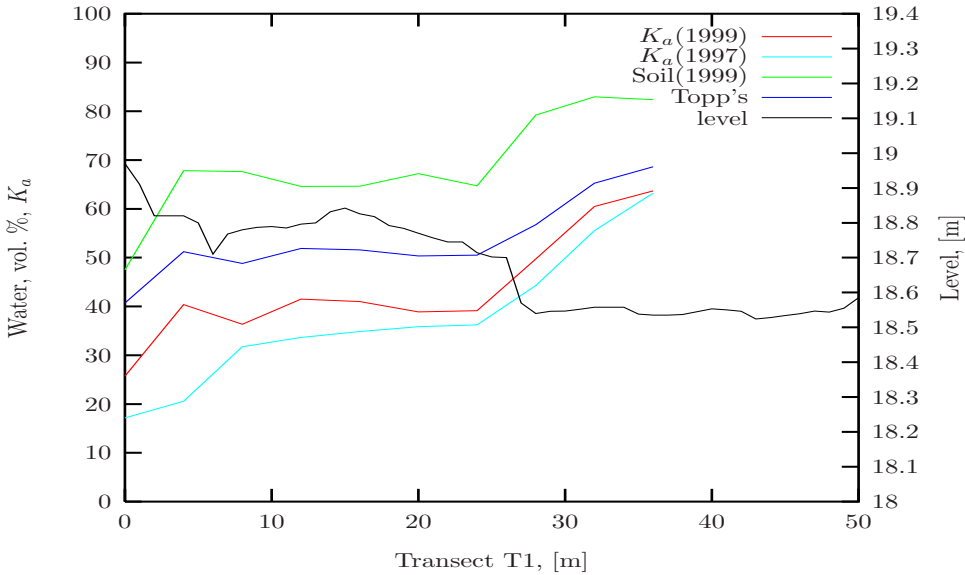


Figure 6.19: Variations in  $K_a$ , the volumetric water content and the level along transect T1 at Ladegaards Enge.  $K_a$  is based on TDR measurements from June 1997 and July 1999. The estimated volumetric water content is derived from soil samples from 1999 and based on  $K_a$  from 1999 derived from Topp *et al* (1980). The level corresponds to the height above sea level.

#### 6.4.1 Ladegaards Enge 1997

In Figure 6.19 a relation between the topography and the volumetric water content  $\theta_w$  along transect T1 is evident. Here  $\theta_w$  is derived from soil samples gathered 12 July 1999 and listed in Table 6.3.

In order to test the strength of the monotonic association between  $\theta_w$  and the topography we apply Spearman's rank order correlation test. This is a distribution free test that determines whether or not a monotonic relation exists between two variables. Because linear relations very often will be unrealistic in practical situations Spearman's test is more appropriate in this context than Pearson's correlation test.

Spearman's rank order correlation coefficient  $r_s$  is given by

$$r_s = 1 - \frac{6D}{n^3 - n}, \quad (6.1)$$

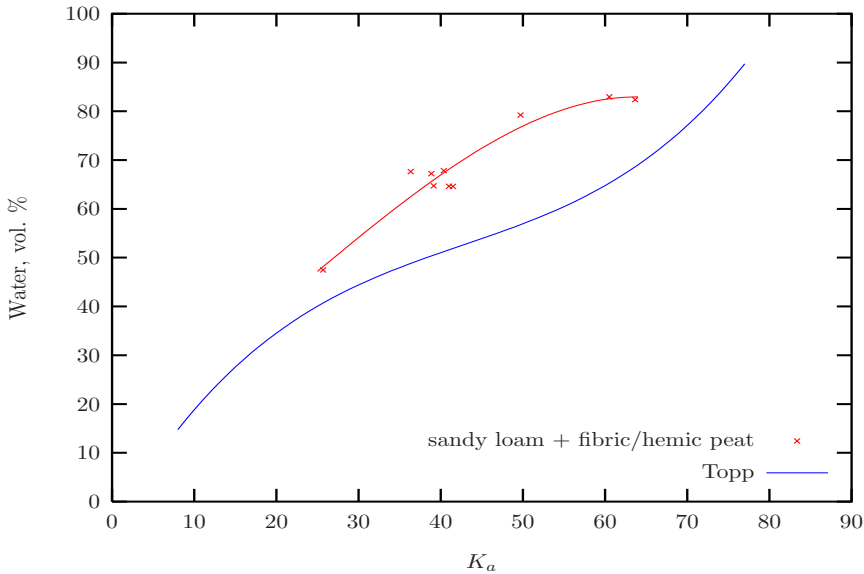


Figure 6.20: Correlation between the estimates of the volumetric water content  $\theta_w$  in the soil samples and the estimates of the corresponding  $K_a$  values from 12 July 1999 in Ladegaards Enge. The samples are collected along transect T1. The solid black curve is a least squares fit using a third-order polynomial. The solid grey curve shows the relation by Topp *et al.* (1980).

where  $D$  is the sum of the squared differences in rank order constants and  $n$  is number of observations. The distribution of  $D$  is symmetrical around  $(n^3 - n)/6$ , it is only defined for even numbers and  $0 \leq D \leq \frac{1}{3}(n^3 - n)$ . The distribution is given under the constraint that no correlation exists, which is our  $H_0$  hypothesis.

Using (6.1) the correlation coefficient  $r_s$  between  $\theta_w$  and the topography is  $-0.77$  for  $n = 10$  and  $D = 292$ . We therefore have  $1 - P(D \geq 292) = 0.0063$  which implies that  $H_0$  is rejected using the significance level 0.05. In other words we may conclude that  $\theta_w$  and the topography are correlated.

In Figure 6.19 there also is an almost linear relationship between the apparent dielectric constant  $K_a(1999)$  and  $\theta_w$  derived from the soil samples. In Figure 6.20 these values are plotted against each other and the third-order polynomial relationship is estimated using a least squares fit. This plot again suggests a relationship and it would therefore be relevant to test to what extent  $K_a(1999)$  values and  $\theta_w$  are correlated.

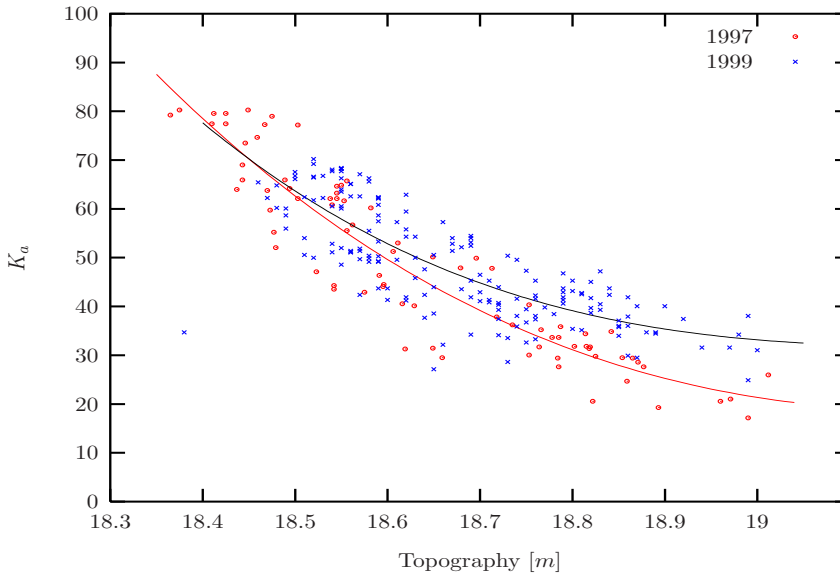


Figure 6.21: Scatter-plot of the kriged topography in Figure 6.15 against the estimated  $K_a$  derived from the TDR-measurements performed 3 June 1997 and 12 July 1999 at Ladegaards Enge. The height is metres above sea level and the solid lines are the best fitted third-order polynomials in a least squares sense.

We again use (6.1) to estimate the correlation coefficient and get  $r_s = 0.64$   $D = 60$  and  $n = 10$ . This results in  $P(D \leq 60) = 0.0272$  which means that it is unlikely that no correlation exists. Based on that we conclude that  $\theta_w$  and  $K_a$  are associated.

Given the correlations and test statistics above strong evidence suggests that the topography and  $K_a$  at T1 3 June 1997 are correlated. It therefore seems relevant to test the correlation between the topography and  $K_a$  values derived from TDR-measurements performed 3 June 1997. This is possible due to the kriged topography in Figure 6.15, which enables estimates of the topography at every location where TDR-measurements are performed. The constraint that the topography has not changed in the period from 3 June 1997 until the measurements of the topography in the fall of 1998 is fulfilled.

In Figure 6.21 the kriged topography at Ladegaards Enge is plotted against the  $K_a$  estimates from 3 June 1997. Applying Spearman's rank order correlation test (6.1) we get  $D = 165670$ ,  $n = 81$  and  $r_s = -0.87$ . Because  $n$  is high,  $D$  is approximately Gaussian distributed and the test statistic is therefore

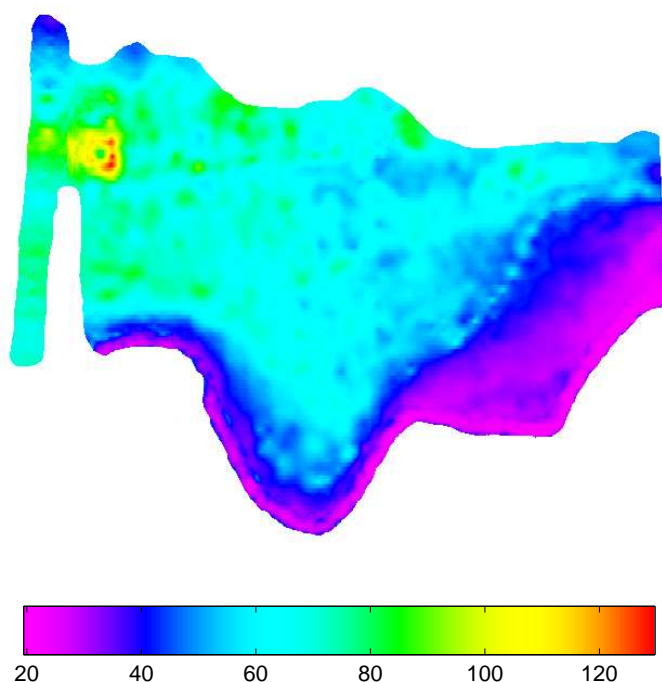


Figure 6.22: A map showing the kriged  $K_a$  in the test site at Ladegaards Enge 3 June 1997. The resolution is 0.25 m.

$1 - \Phi(7.8) < 0.00003$ . This rejects the  $H_0$  hypothesis and we conclude that  $K_a$  is correlated with the topography.

In order to establish a relation between the topography and the  $K_a$  estimates a third-order polynomial in a least squares sense is fitted to the points in the scatter-plot in Figure 6.21. The polynomial relationship is

$$K_a = 274305.04 - 41581.42h + 2099.20h^2 - 35.289h^3, \quad (6.2)$$

where  $h$  is the height above sea level. The polynomial relationship between the topography and  $K_a$  is only valid for the test area at Ladegaards Enge 3 June 1997. Based on (6.2) and the kriged topography in Figure 6.15 a 2-D representation of the variation of  $K_a$  3 June 1997 is constructed and illustrated in Figure 6.22.



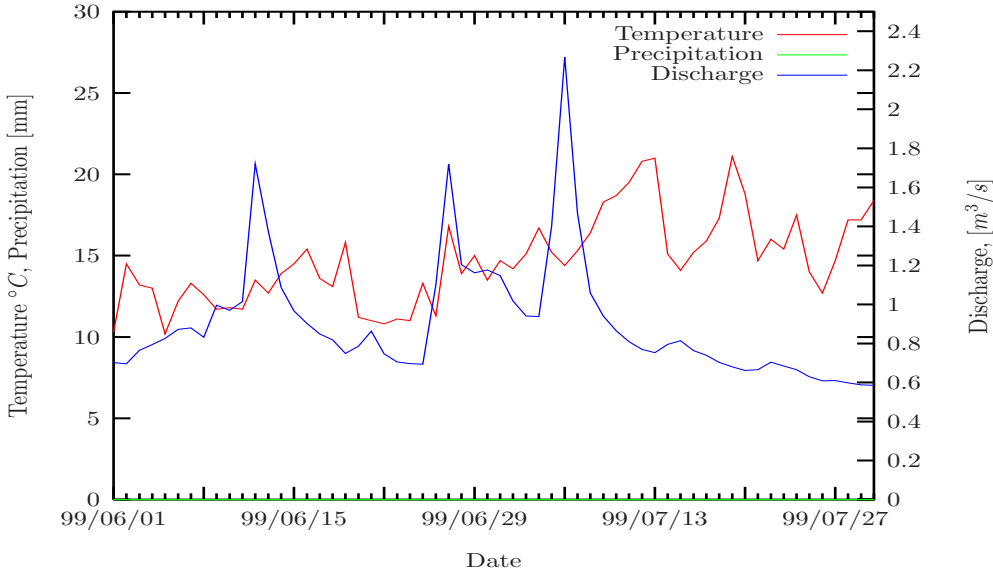


Figure 6.23: Discharge and temperature in Ladegaards Enge from 1 June 1999 to 30 July 1999. The precipitation in the period is negligible. The additional fieldwork was performed 12 July 1999. The river discharge is measured at the gauging station in Ladegaards Enge and the temperature and precipitation are averaged over 24 hours within an area of  $20 \text{ km} \times 20 \text{ km}$ . (Copyright Danish Institute of Agricultural Science. The hydrometric data are from NERI's gauging station at Sminge Vad).

### 6.4.2 Ladegaards Enge 1999

In Section 6.4.1 it was shown that the topography and  $K_a$  were correlated 3 June 1997 at Ladegaards Enge. It therefore would be interesting to explore to what extent  $K_a$  in general is governed by the topography and to what extent  $K_a$  is affected by the discharge in the river.

In this section we therefore will test the strength of the monotonic association between the topography and the  $K_a$  estimates derived from the TDR-measurements performed 12 July 1999. Figure 6.21 illustrates the plot of the topography against  $K_a$  and the solid curve represents a least squares fit using a third-order polynomial. The fitted third-order polynomial in the least squares

sense is

$$K_a = 487163.93 - 75812.97h + 3932.97h^2 - 68.01h^3, \quad (6.3)$$

where  $h$  is the height above sea level. This relationship is valid for the test area in Ladegaards Enge 12 July 1999.

Spearman's rank order correlation test (6.1) is again applied and the calculated statistics are  $n = 175$ ,  $D = 1574235$  and  $r_s = -0.76$ . Thereby  $H_0$  is rejected and  $K_a$  is again correlated with the topography.

When comparing the two plots in Figure 6.21 it is obvious that  $K_a$ , and thereby  $\theta_w$ , is lower 3 June 1997 than 12 July 1999 within the upper soil layer. This is also in perfect accordance with the Figures 6.5 and 6.23 that state that the discharge in the river 3 June 1997 was  $0.6273 \text{ m}^3/\text{s}$  and 12 July 1999  $0.77 \text{ m}^3/\text{s}$ . The assertion that the volumetric water content during periods of low precipitation is related to the discharge in the river and the topography is thereby supported.

## 6.5 Discussion

The test site in Ladegaards Enge is a part of the Gjern catchment in the Eastern Jutland. It is a riparian wetland where the water table is high and approximately intersecting the ground surface at the river bed.

Within the area the various plant communities are strongly correlated with the soil moisture content. In the drier part of the test site corresponding to sub-area III *Alopecurus pratensis* is prevailing and in the more humid sub-area II *Deschampsia caespitosa* is widely distributed. Ellenberg (1992) has classified the plant species on a scale from 1–12 in accordance to their preference for humidity [28]. Here *Alopecurus pratensis* scores 6 and *Deschampsia caespitosa* 7, which supports our experiences from the field that soil moisture and plant communities are related.

The deposits in the upper 8 cm in the floodplain is fibric to hemic peat, which is overlaying a cleyic loam. The coarser fraction of sandy loam is deposited at or near the levee. These deposits originate from overflows and the meandering of the river. It is therefore natural that the organic content and fine-textured soil particles increase away from the river as Table 6.3 indicates.

Fine-textured soil particles such as clay and organic matter bind the water molecules, which results in a lower  $K_a$  than if the soil had been coarse textured [39]. According to Table 6.3 the organic content increases along T1 away from the river and as a consequence one might expect the estimated  $K_a$  within Ladegaards Enge to be affected by the variability of the organic content. However, according to Figure 6.19 the increase in the organic content along T1 does not seem to affect the estimated  $K_a$ . This is because the microwave frequencies are strongly sensitive to water compared to the soil particles. Here the  $K_a$  value for water is approximately 80 whereas it is only 2–4 for the other soil constituents [56]. Because the general conditions were quite humid 12 July 1999, especially in the area where the organic content was high, the contribution from the fine textured soil and organic content was negligible. The soil moisture conditions were also high 3 June 1997 and it is therefore assumed that the derived  $K_a$  from the fieldwork 3 June 1997 is unaffected by the organic content within Ladegaards Enge.

In Section 6.4.1 and 6.4.2 it was shown that  $K_a$  is strongly correlated with the topography within Ladegaards Enge. This was in Section 6.4.1 utilized in the making of the map in Figure 6.22, which covers  $K_a$  3 June 1997. When examining the plots in Figure 6.21 it is obvious that the spatial distribution of  $K_a$  3 June 1997 and 12 July 1999 within the test site is different. The general level of  $K_a$  at the test site 12 July 1999 is higher than 3 June 1997 and the variability of  $K_a$  12 July 1999 less than 3 June 1997. This suggests that the best fitted line in the figures approaches the level of 80, which is the  $K_a$  value for water at 20°C, as the general soil moisture increases within the test site [35]. It is therefore necessary to have some prior knowledge of  $K_a$  in order to utilize the topography for estimating  $K_a$  within the test site at a given time.



## CHAPTER 7

# Mols Bjerge

---

Fieldwork was performed at Mols Bjerge 4 June 1997 at three test sites in order to enable the study of the synergy between semi-natural grasslands and the restored polarimetric EMISAR data in Chapter 9.

The test areas of investigation are located at Trehøje, Benlighøj and Stenhøje and the *in situ* data collected comprise an evaluation of the vegetation characteristics, estimation of biomass, soil samples and TDR-measurements. These *in situ* data represent factors that are all known to affect the polarizations and frequencies used by EMISAR. For a brief description of the sampling methodologies and the interaction between the *in situ* data and EMISAR refer to the Sections 3.1.1, 3.1.2 and 3.1.3. In this chapter the sampling strategy at each test site is outlined and the *in situ* data are presented and analyzed.

A lot of research has earlier been performed on grasslands at Mols Bjerge. For a study of the spectral identification of plant communities for mapping of semi-natural grasslands refer to Jacobsen (2000) [38].

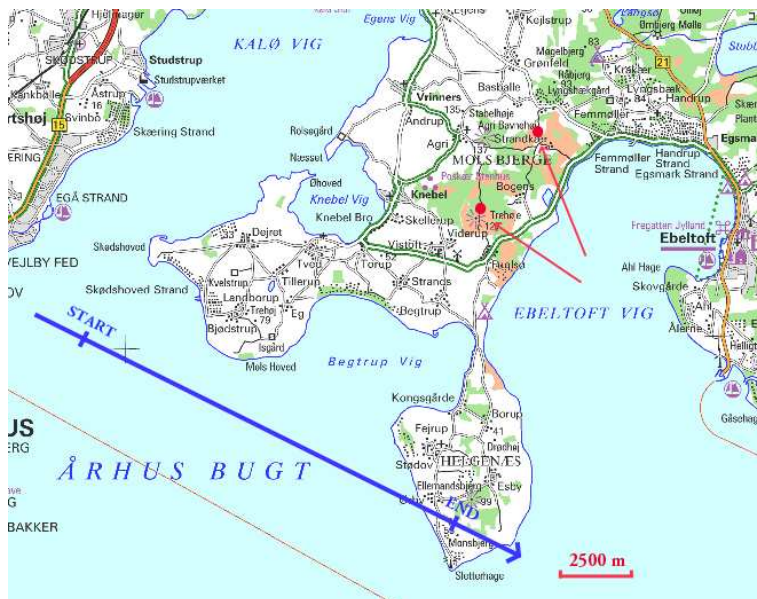


Figure 7.1: The geographical placement of Mols Bjerge. The blue arrow shows the flightline of the EMISAR where the acquisitions are made within the start and end points on 3 and 4 June 1997. The EMISAR is looking to the left and the red spot to the South indicates the test sites Trehøje and Benlighøj. The red spot to the North indicates Stenhøje. (Map material from the Danish Kort- og Matrikelstyrelsen (KMS) is reproduced according to agreement G18/1997 between NERI and KMS).

## 7.1 Description of test sites

Mols Bjerge is located at the peninsula in the southern part of Djursland in Jutland. It is a beautiful area where the hills are covered with heath, grassland and forest. Geologically Mols Bjerge is a terminal glacial moraine from the last glaciation Weichsel (Würm). The moraine is a mixture of sand, clay and pebbles [64], [67].

Figure 7.1 shows the geographical placement of Mols Bjerge as well as the flightline of the EMISAR and the three test sites. The test areas of study are located at Trehøje and Benlighøj, which are indicated by the southern red spot, and Stenhøje indicated by the northern red spot.

In Figure 7.2 two of the test sites are indicated on an ortho-photo from 1995.

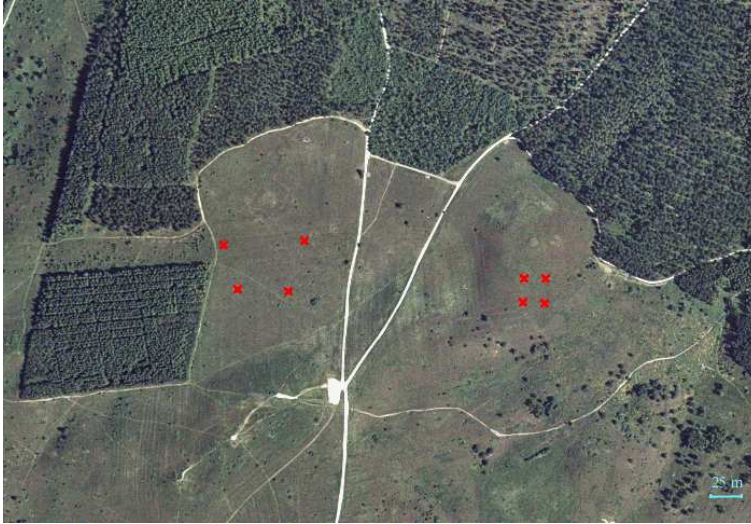


Figure 7.2: An aerial view of two of the test sites at Mols Bjerger displayed on an ortho-photo from 1995. The test area Trehøje is located within the four red crosses to the left. The four red crosses to the right represent the test site Benlighøj. (Ortho-photos are copyright Kampsax 1995).

The four red crosses to the left comprise the Trehøje test area whereas the four red crosses to the right represent the test site Benlighøj. Likewise, the displayed crosses in Figure 7.3 represent the test site at Stenhøje. The ortho-photos are from 1995 and originally geometrically rectified according to system 34 for Jutland. However for practical purposes, the coordinate system used in the following is Universal Transverse Mercator (UTM), zone 32, datum ED50.

The test areas are all classified as grasslands by Jacobsen (2000) [38]. The Trehøje test site illustrated in the photo in Figure 7.4 (a) is an old abandoned grassland, which was dominated by *Deschampsia flexuosa*. Stenhøje test site was characterized by the green and vigorous vegetation of *Festuca rubra* as displayed in the photo in Figure 7.4 (b). The photos in Figure 7.5 show the test area at Benlighøj, which was grazed and dominated by *Deschampsia flexuosa*.

The criteria for selecting the test sites for this study have been homogeneity in terms of soil moisture, above ground biomass and vegetation characteristics within each site. Between the sites differences exist in the plant species, the volumetric structure of vegetation and most likely in the biomass content. Although Mols Bjerger is a very hilly area the three selected test sites are flat and



Figure 7.3: An ortho-photo illustrating the test site Stenhøje at Mols Bjerge 1995. The test area is located within the red crosses. (Ortho-photos are copyright Kampsax 1995.)

orientated towards the EMISAR in such a way that the incidence angles  $\varphi$  for the EMISAR images within Trehøje, Benlighøj and Stenhøje are almost identical. At the test areas Trehøje and Benlighøj the local  $\varphi$  is  $39^\circ$  whereas the local  $\varphi$  at Stenhøje is  $41^\circ$ .

At the time the fieldwork was performed the weather was calm, sunny and hot and dry conditions had been prevailing for some weeks. In Figure 7.6 is shown the temperature and precipitation at Mols Bjerge from 1 May 1997 to 30 June 1997. Although the figure gives a hint of the weather conditions prior to the fieldwork on 4 June 1997 at Mols Bjerge it should be noted that the temperature and precipitation are averaged over 24 hours within an area of  $40 \times 40$  km.

## 7.2 Trehøje 1997

The setup for the fieldwork at Trehøje is outlined in Figure 7.7. Here the corners of the site are marked with crosses and the biomass samples were collected at the red circles. The area which is displayed in Figure 7.4 (a) was dominated by





(a)



(b)

Figure 7.4: (a) Abandoned grassland at the test site in Trehøje dominated by *Deschampsia flexuosa* and (b) *Festuca rubra* at the test site in Stenhøje. Photos were taken 4 June 1997 at Mols Bjerge.



(a)



(b)

Figure 7.5: (a) The test area in Benlighøj with grazed vegetation dominated by *Deschampsia flexuosa* and (b) close up of a typical scene within the test site with manure. Photos were taken 4 June 1997 at Mols Bjerger.

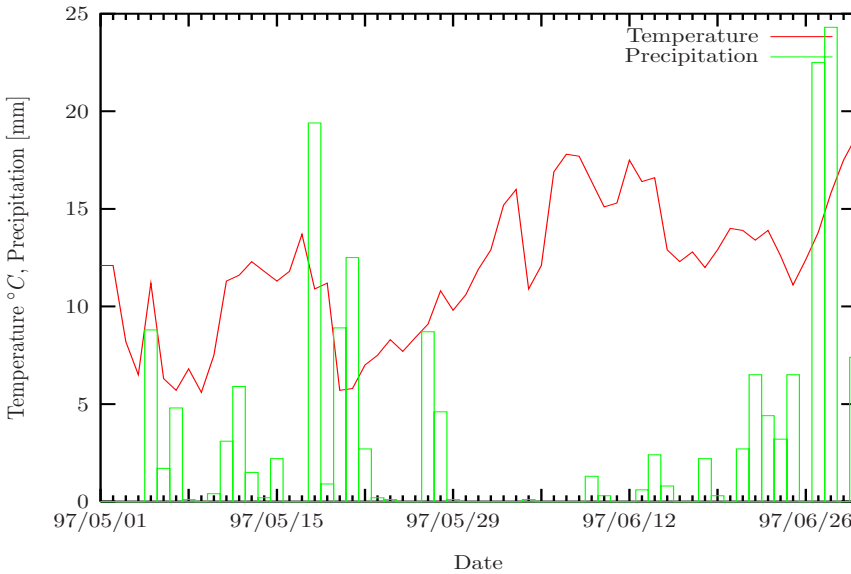


Figure 7.6: Temperature and precipitation at Mols Bjerge from 1 May 1997 to 30 June 1997. Fieldwork was performed 4 June 1997. The temperature and precipitation are averaged over 24 hours within an area of  $40 \times 40$  km. (Copyright Danish Institute of Agricultural Sciences).

*Deschampsia flexuosa* with a 100% degree of covering.

Considerable complexity is introduced by the dense vegetation, which makes it highly complicated to separate the soil and vegetation radar backscatter contributions using C- and L-band. Such a separation would require a very detailed description of the vegetation characteristics, which is not available. Neither TDR measurements nor soil samples were therefore collected within this test area.

### 7.2.1 Biomass samples

At Trehøje three biomass samples were collected at random within a sub-area of  $5 \text{ m} \times 5 \text{ m}$ . Based on a visual evaluation the vegetation within the sub-area is representative for the whole test area. Each sample is numbered in such a fashion that sample number  $i$  in Figure 7.7 corresponds to number  $\text{BT}_i$  in Table 7.1. The methodology in terms of collecting and analyzing the biomass is



Figure 7.7: The test area in Trehøje within Mols Bjerge displayed on an ortho-photo from 1995. The crosses marks the corners of the test site and the locations of the biomass samples 1–3 collected 4 June 1997 are shown with red circles. (Ortho-photos are copyright Kampsax 1995).

described in Section 3.1.1.

The tussocks of *Deschampsia flexuosa*, which were growing close together were characterized by a dense tangled vegetation containing both withered and fresh material. The average height of the tussocks was 25 cm and in places stems rise above the tussocks by 15 cm. The moraine was layered by 10 cm humus and on top came the *Deschampsia flexuosa*. The tussocks covered approximately 85% of this area, the other 15% was due to narrow paths and a few mulberry bushes.

Sample BT<sub>1</sub> was at an area of tussocks of *Deschampsia flexuosa* and the distribution of vegetation was 70% fresh *Deschampsia flexuosa*, 40% withered *Deschampsia flexuosa* and 60% moss. BT<sub>2</sub> was collected in a growth of *Carex arenaria* and contains 5% fresh *Deschampsia flexuosa*, 40% withered *Deschampsia flexuosa*, 20% fresh *Carex arenaria*, 60% withered *Carex arenaria*. Sample BT<sub>3</sub> was collected in the narrow space between two tussocks and its content was 5% fresh *Deschampsia flexuosa*, 100% withered *Deschampsia flexuosa*, 50% moss, and 5% *Galium saxatile*.

Referring to Table 7.1 the water in weight percent in the three samples is very

Nr.:	Fresh weight kg/m <sup>2</sup>	Dry weight kg/m <sup>2</sup>	Dry weight mean kg/m <sup>2</sup>	Dry weight std. kg/m <sup>2</sup>	Water weight %
BT <sub>1</sub>	7.96	4.31	–	–	45.80
BT <sub>2</sub>	2.96	1.65	–	–	44.30
BT <sub>3</sub>	3.26	1.58	2.51	0.90	51.50
BS <sub>4</sub>	1.59	0.74	–	–	53.80
BS <sub>5</sub>	0.92	0.44	–	–	52.00
BS <sub>6</sub>	1.59	0.49	–	–	69.10
BS <sub>7</sub>	0.98	0.37	0.51	0.081	62.50
BB <sub>8</sub>	1.26	0.59	–	–	53.50
BB <sub>9</sub>	0.98	0.50	–	–	49.10
BB <sub>10</sub>	0.61	0.39	–	–	35.60
BB <sub>11</sub>	1.31	0.58	–	–	55.90
BB <sub>12</sub>	3.34	1.05	0.62	0.11	68.60

Table 7.1: Biomass samples collected at Mols Bjerge 4 June 1997 at the test sites in Trehøje, Stenhøje and Benlighøj. The index refers to the numbers of the red circles in the Figures 7.7, 7.8 and 7.12.

much the same as expected due to the homogeneity in terms of vegetation. Sample BT<sub>1</sub> was collected at a tussock, hence the relatively high fresh and dry weight.

### 7.3 Stenhøje 1997

The fieldwork at Stenhøje is outlined in Figure 7.8 where the area under study is located at the beginning and end of the transects T1 and T2.

During the campaign TDR measurements were performed at the pink crosses at the two transects. These transects are crossing each other in order to disclose a possible anisotropy in the autocovariance function. The biomass samples were collected at the red circles in Figure 7.8. Here the red circles constitute the four corners in a square with its centre at the point where T1 and T2 cross each other. The soil samples were collected at a and b. The points at which the biomass and soil samples were collected were chosen prior to the fieldwork. The area as it appears in the photo in Figure 7.4 (b) was very homogeneous with a green and vigorous vegetation. The soil was a dry sandy loam with pebbles.

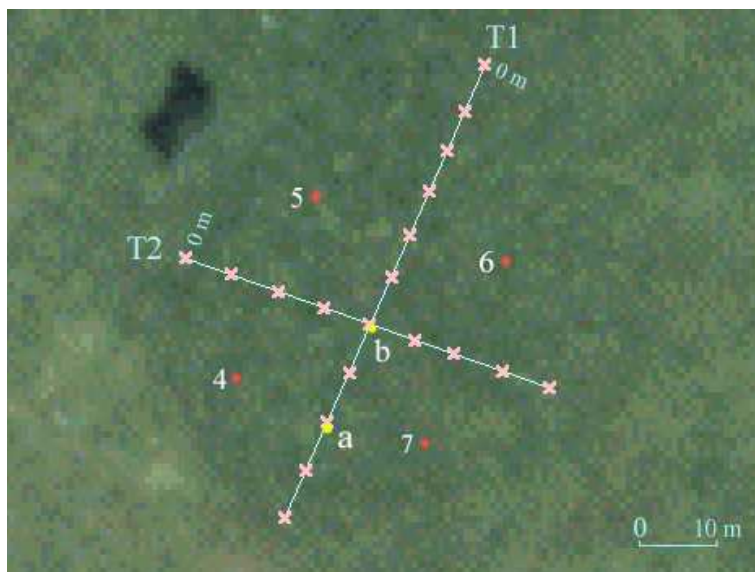


Figure 7.8: Fieldwork performed in Stenhøje at Mols Bjerge on 4 June 1997 shown on an ortho-photo. The blue lines represent the transects T1 and T2 used for TDR measurements. The locations for the TDR measurements are shown with pink crosses. Biomass samples 4–7 are collected at the red circles and soil samples a and b are collected at the yellow circles. (Ortho-photos are copyright Kampsax 1995).

### 7.3.1 Biomass samples

The vigorous vegetation was dominated by *Festuca rubra* and the estimated average height was 20 cm. The degree of cover was almost 100% and although there were local variations in the composition of the species the volumetrical and geometrical structure was very much constant. The biomass samples 4–7 were collected at random with one sample in each of the four quadrants in Figure 7.8. Sample  $BS_i$  in Table 7.1 refers to number  $i$  at the red circles in Figure 7.8. In Section 3.1.1 is described how the biomass samples were collected and analyzed.

The content of  $BS_4$  was 80% *Festuca rubra*, 10% *Poa pratensis*, < 5% *Elymus repens*, 20% *Achillea millefolium*, < 5% *Taraxacum ruderalia* agg. and 30% moss. The distribution of vegetation in  $BS_5$  was < 5% *Poa pratensis*, 60% *Festuca rubra*, 10% *Taraxacum ruderalia* agg., 10% *Convolvulus arvensis*, < 5% *Achillea millefolium*, < 5% *Elymus repens*, 60% moss and < 5% *Vicia hirsuta*. In sample  $BS_6$  the distribution was 10% *Taraxacum ruderalia* agg., 40% *Festuca*

Sample Nr.:	$\rho_f$ g/cm <sup>3</sup>	$S^2(\rho_f)$ g <sup>2</sup> /cm <sup>6</sup>	$\rho_d$ g/cm <sup>3</sup>	$\rho_s$ g/cm <sup>3</sup>	$\theta_p$	$\theta_w$ vol. %	$\theta_r$ vol. %	$\Delta m_d$ weight %
SS <sub>a</sub>	1.31	0.15	1.21	1.72	0.51	10.53	20.75	5.0
SS <sub>b</sub>	1.29	0.11	1.19	1.71	0.52	9.69	18.25	5.9
SB <sub>c</sub>	0.94	0.11	0.79	1.48	0.7	15.6	22.25	11.8
SB <sub>d</sub>	1.08	0.1	0.87	1.52	0.65	21.51	33.25	14.0

Table 7.2: Soil samples collected at the test sites in Stenhøje and Benlighøj 4 June 1997 at Mols Bjerge. The fresh, dry and the saturated bulk densities of the soil samples are referred to as  $\rho_f$ ,  $\rho_d$  and  $\rho_s$ . The porosity of the samples is  $\theta_p$ , the volumetric water content is  $\theta_w$  and the relative water content  $\theta_r$ . The organic content given in percent of the dried soil sample is  $\Delta m_d$ . The variance of the bulk density of the fresh soil samples is  $S^2(\rho_f)$ . The index refer to the sites of collection in the Figures 7.8 and 7.12 shown by the yellow circles a–d. At each site 4 soil samples were taken and their average is listed in the table.

*rubra*, 50% *Achillea millefolium*, 5% *Poa pratensis*, < 5% *Elymus repens* and < 5% *Hieracium pilosella*. In the last sample BS<sub>7</sub> the various species were distributed as follows: 40% moss, in particular *brachythecium sp.*, 80% *Festuca rubra*, 5% *Poa pratensis*, 5% *Medicago lupulina*, 20% *Achillea millefolium*, < 5% *Vicia lathyroides*, 5% *Plantago lanceolata*, < 5% *Elymus repens*, < 5% *Hypochoeris radicata*, < 5% *Rumex acetosella* and < 5% *Hieracium pilosella*.

The calculated characteristics in Table 7.1 show that the water content in the samples BS<sub>6</sub> and BS<sub>7</sub> was higher than in the samples BS<sub>4</sub> and BS<sub>5</sub>. Since there was no significant change in soil moisture within the area there is no simple explanation for that besides what may be caused by the natural sampling error and the specific water content in the various species.

### 7.3.2 Soil samples

The soil samples were collected at the yellow spots a and b at transect T1 in Figure 7.8, and at each location four samples were taken. For a description of the method of collecting and analyzing the samples refer to Section 3.1.2. Table 7.2 shows the averaged calculated characteristics, SS<sub>a</sub> and SS<sub>b</sub>, of the four samples.

The analyzed characteristics of the samples SS<sub>a</sub> and SS<sub>b</sub> in Table 7.2 seem very similar having a mean volumetric water content  $\theta_w$  of 10%. What is noticeable is the low  $\theta_w$  and the low content of organic matter.

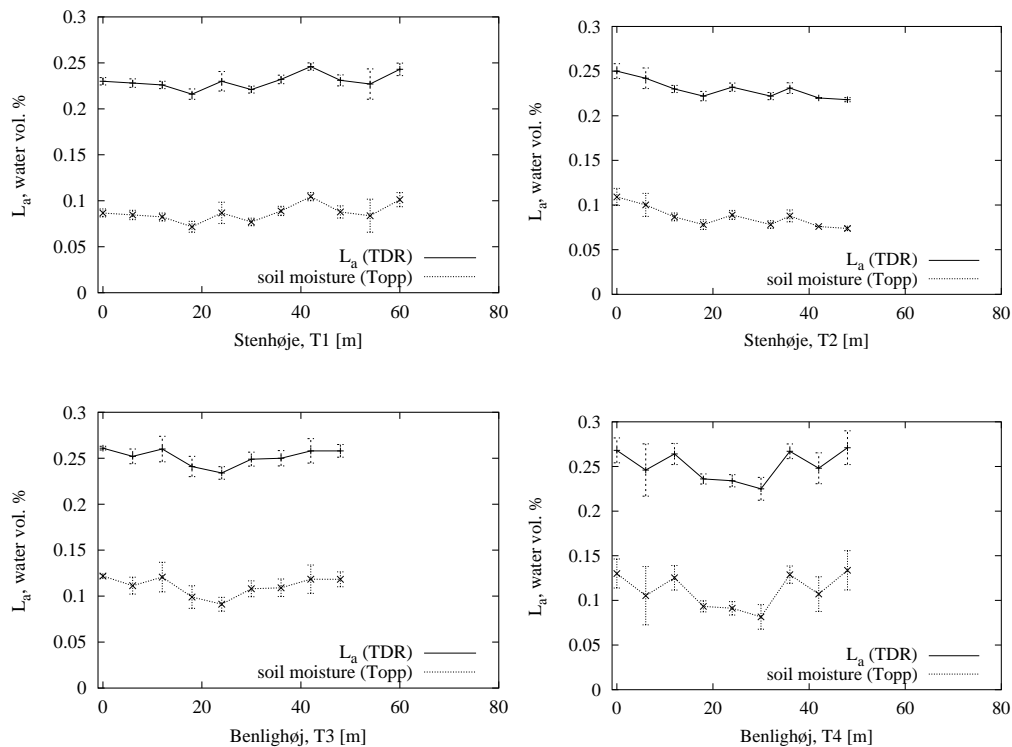


Figure 7.9: Plots showing the variations of the apparent probe length  $\bar{L}_a$  and the volumetric water content  $\theta_w$  along the transects T1–T4 at the test sites Stenhøje and Benlighøj 4 June 1997 at Mols Bjerge. The volumetric water content is estimated from a third-order polynomial relationship published by Topp *et al.* (1980) [80]. The errorbars indicate the standard deviation.

### 7.3.3 Time-Domain Reflectometry

At Stenhøje the spatial distribution of the apparent dielectric constant  $K_a$ , and thereby the volumetric soil moisture content, was evaluated using TDR measurements. For a brief introduction to the TDR methodology refer to Section 3.1.3.

The two transects T1 and T2 along which the TDR measurements were performed are illustrated in Figure 7.8. In order to analyze to what extent anisotropy exists in the TDR readings and in the autocorrelation, T1 and T2 are almost perpendicular to each other. The points of measurements are indicated with pink crosses at the transects and the spacing between the points was 6 m. At each location four measurements were made within an area of 80 cm  $\times$  80 cm.



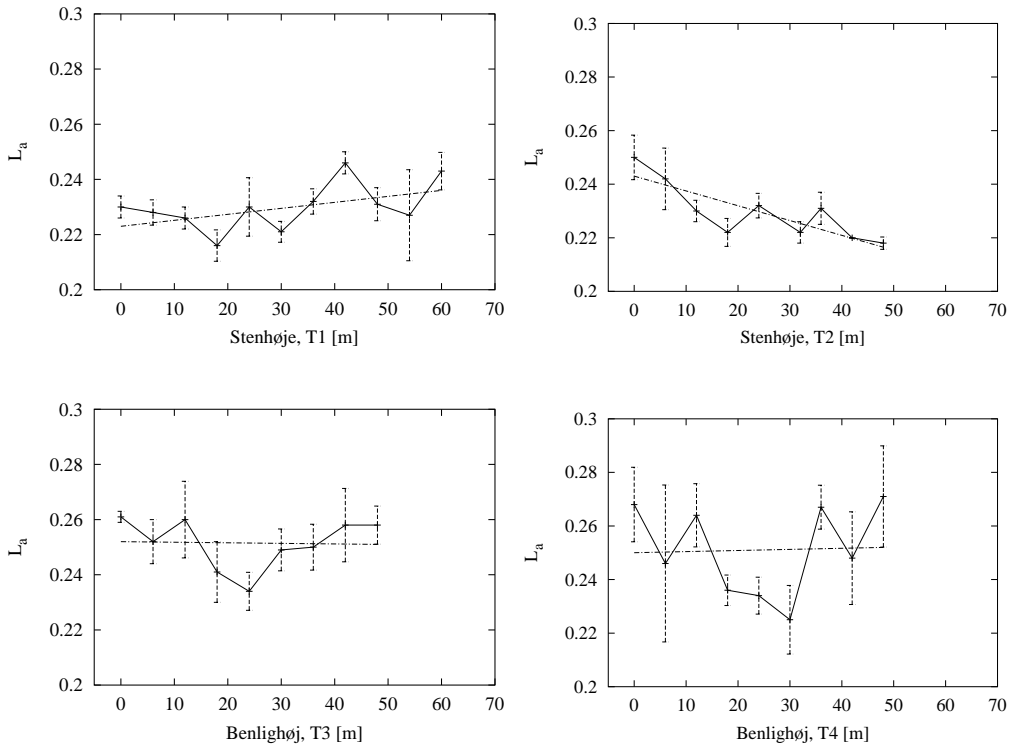


Figure 7.10: The variation in the apparent probe length  $L_a$  along the transects T1–T4 at the test sites Stenhøje and Benlighøj 4 June 1997 in Mols Bjerge. The straight line represents the best linear fit in a least squares sense.

Based on the apparent probe length  $\bar{L}_a$ , which is the average of the four TDR readings at each location, the apparent dielectric constant  $K_a$  is estimated using (3.2). Given  $K_a$  the volumetric water content  $\theta_w$  can be estimated from the third-order polynomial relationship (3.1) published by Topp *et al.* (1980) [80]. This calibration function is valid for four soils ranging from sandy loam to heavy clay soils and it therefore seems appropriate at Stenhøje.

A graphical presentation of the estimated  $\theta_w$  and  $\bar{L}_a$  along the transects T1–T2 at Stenhøje is shown in Figure 7.9. From the figures we note that the mean level of the estimated  $\theta_w$  along both transects using (3.1) was approximately 9%.

Of course, the TDR measurements along the transects T1 and T2 only provide knowledge at the specific points of measuring. In order to get information at any desired point at the transects interpolation between the points is needed. How-

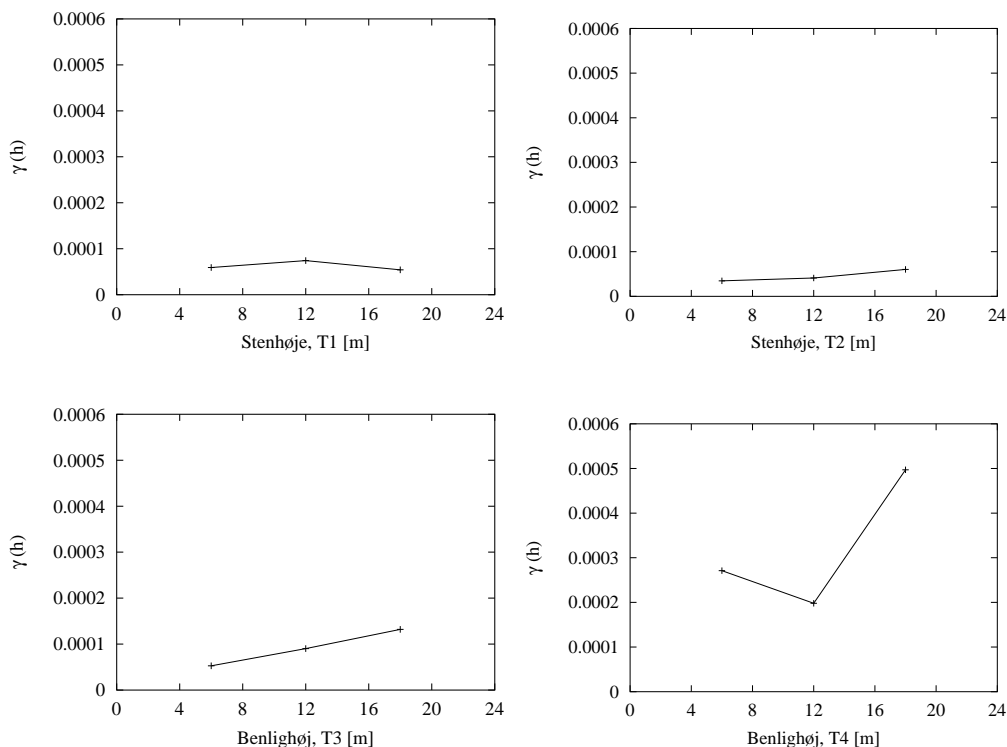


Figure 7.11: The experimental semi-variograms of the apparent probe length  $L_a$  along the transects T1–T4 at the test sites Stenhøje and Benlighøj 4 June 1997 in Mols Bjerge.

ever, using the kriging method for interpolating we have to require correlation between point pairs.

At first glance, there is a trend in  $\bar{L}_a$  along T1 and T2 in Figure 7.9. In order to calculate the autocorrelation this trend therefore has to be subtracted. In Figure 7.10 a straight line has been fitted to the readings  $\bar{L}_a$  using a linear least squares regression. According to the fitted lines there is a small trend along the transects, which shows an anisotropy in the TDR readings.

The linear trends are subtracted from  $\bar{L}_a$  and based on the results and (3.3) the experimental semi-variograms are estimated. These estimated semi-variograms are presented in Figure 7.11. Due to the small number of point pairs it is not possible to deduce anything about the nugget effect, sill or range of influence. However, the semi-variograms and the plots in Figure 7.10 indicate an auto-

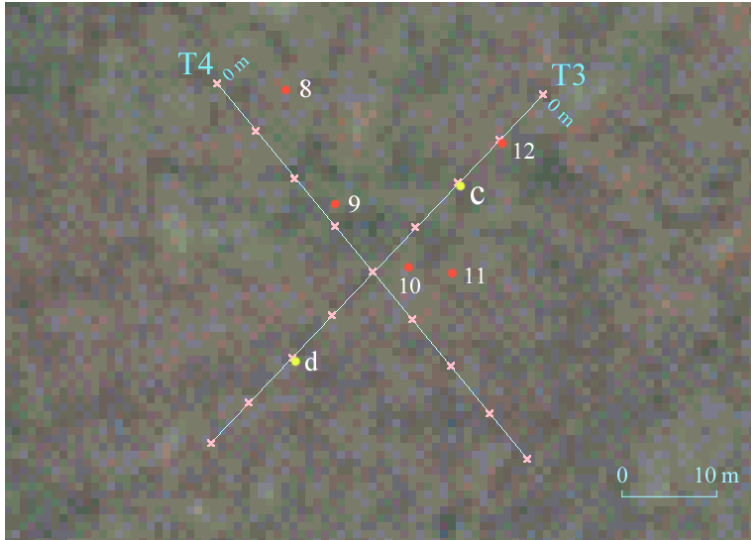


Figure 7.12: Fieldwork accomplished in Benlighøj on 4 June 1997 at Mols Bjerge displayed on an ortho-photo from 1995. The transects T3 and T4 used for TDR measurements are in blue colours and the sites of TDR measuring are shown with pink crosses. Biomass samples 8–12 are collected at the red circles and soil samples c and d are collected at the yellow circles. (Ortho-photos are copyright Kampsax 1995).

correlation.

## 7.4 Benlighøj 1997

The setup for the fieldwork at Benlighøj is sketched in Figure 7.12, where the test site is located within the start and endpoints of the transects T3 and T4. The TDR measurements were performed at the pink crosses at T3 and T4 and again the transects are crossing each other in order to disclose a possible anisotropy in the autocovariance function. The red circles in Figure 7.12 are chosen at random and mark the sampling points for the biomass. The locations of the sampling points for the soil samples were chosen prior the the fieldwork and are indicated by the yellow circles in the figure.

Benlighøj test site was grazed and showed evidence from cattle in terms of manure and paths where the cattle walk. The upper soil layer was a dry and

firm sandy loam with pebbles and manure. In Figure 7.5 the photos reflect that the area was grazed and consequently the vegetation was low.

### 7.4.1 Biomass samples

The dominant species was *Deschampsia flexuosa* with an average height of 5 cm. Also *Carex arenaria* was widely distributed with an average height of 20 cm. The overall degree of covering was approximately 80%.

In Figure 7.12 the red circles 8–12 indicate the sampling points for the biomass, which were chosen at random within sub-areas of different vegetation characteristics. Again the sample number  $i$  in Figure 7.12 corresponds to  $BB_i$  in Table 7.1. The methodology of collecting and analyzing the biomass is outlined in Section 3.1.1.

Sample  $BB_8$  was laid out in a growth of *Agrostis capillaris*. The content was 70% *Agrostis capillaris*, 20% *Deschampsia flexuosa*, 5% *Poa pratensis*, < 5% *Rumex acetosa* and < 5% *Campanula rotundifolia*. The samples  $BB_9$  was collected in a belt dominated by *Holcus mollis* and the distribution of vegetation in the samples was 60% *Holcus mollis*, < 5% *Deschampsia flexuosa* and 70% alm. cypres-moss. Concerning  $BB_{10}$  it was gathered in a thin growth of vegetation and the content was 20% *Deschampsia flexuosa*, 5% bægerværter, 60% alm. cypres-moss and < 5% *Rumex acetosella*. The content of  $BB_{11}$  was 90% *Deschampsia flexuosa*, 5% *Carex arenaria*, 90% alm. cypres-moss, < 5% *Poa pratensis* and it was collected in a relative dense vegetation. Finally  $BB_{12}$  was laid out in a sub-area which was dominated by *Holcus mollis* influenced by manure. Here the distribution was 90% *Holcus mollis* and 40% *Deschampsia flexuosa*.

It is obvious when examining Table 7.1 that the fresh weight and water in weight percent of the samples is very much influenced by the sampling locations.  $BB_{10}$  which was collected in a thin vegetation had, as expected, a low fresh weight. The corresponding low water in weight percent is ascribed to withered material. Likewise  $BB_{12}$  had a relatively high fresh weight and high amount of water in weight percent. In this case the bias is due to the manure in the sample.

### 7.4.2 Soil samples

In Figure 7.12 the yellow spots indicate the two locations c and d where soil samples were collected. The samples were gathered at transect T3 and at each

location four samples were collected. In Table 7.2 statistics of the four samples collected at c and d is referred to as  $SB_c$  and  $SB_d$ . A brief description concerning the methodology of collecting and analyzing the samples is given in Section 3.1.2.

According to Table 7.2 the bulk densities of sample  $SB_d$  are larger than the bulk densities of  $SB_c$ . This is due to the manure, which is more recent in  $SB_d$  than in  $SB_c$ . The mean  $\theta_w$  is 18% and what is noticeable is the relative high content of organic matter at the two locations c and d.

### 7.4.3 Time-Domain Reflectometry

The over-all distribution of the apparent dielectric constant  $K_a$  within the test site at Benlighøj was evaluated using TDR measurements. For a brief introduction to the TDR device and the fundamental theory refer to Section 3.1.3.

The TDR measurements were performed at the transects T3 and T4 in Figure 7.12. The spacing between the points at which the measurements were made was 6 m and at each point four measurements were performed within  $80\text{ cm} \times 80\text{ cm}$ . The apparent dielectric constant  $K_a$  is estimated using (3.2) and the apparent probe length  $\bar{L}_a$ , where  $\bar{L}_a$  is the average of the four TDR measurements made at each location.

In Figure 7.9 the variations of  $\theta_w$  and  $\bar{L}_a$  along T3 and T4 is illustrated. The volumetric water content  $\theta_w$  is here estimated using  $K_a$  and the third-order polynomial relationship (3.1) published by Topp *et al.* (1980) [80]. This relation is valid for four soils ranging from sandy loam to heavy clay soils. According to the figure the mean  $\theta_w$  along T3 and T4 was 11%.

In order to be able to predict values of  $K_a$  at every desired point along the transects using the kriging method for interpolation we again have to require that neighbouring points of TDR measurements are correlated. Based on  $\bar{L}_a$  the experimental semi-variograms are estimated using (3.3). These semi-variograms are presented in Figure 7.11. Unfortunately we again are forced to conclude that it is not possible to deduce anything about the nugget effect, sill and range of influence. The reason is the small number of point pairs. However, according to Figure 7.9 and the semi-variogram for T3 in Figure 7.11 the point pairs at T3 and T4 are correlated.

Apparently there is no trend in  $\bar{L}_a$  along T3 and T4 in Figure 7.9. Fitting a straight line using a linear least squares regression supports the assertion, as displayed in Figure 7.10. We hereby assume that  $L_a$ , and thereby  $K_a$ , is isotropic within the test site at Benlighøj.

## 7.5 Discussion

The three semi-natural grassland areas, which are the subject of the study, are located at Trehøje, Stenhøje and Benlighøj within Mols Bjerge. Criteria for selecting the test sites were homogeneity in terms of soil moisture, above ground biomass and vegetation characteristics. This implies that the dominant plant species and the volumetrical and geometrical appearance of the vegetation were homogeneously distributed within each of the test areas. The final criterion for selecting the test areas was that mutual differences between the sites exist concerning one or more of the properties described above.

Based on a visual evaluation of the three test areas 4 June 1997 Trehøje test site possessed the largest volume of above ground biomass, Stenhøje the second largest and Benlighøj the smallest. This is also reflected by the photos in the Figures 7.4 and 7.5 and again supported by the average height of the above ground biomass, which was 25 cm, 20 cm and 5 cm in the test sites at Trehøje, Stenhøje and Benlighøj.

Within the three test sites biomass samples were collected. Statistics from these *in situ* data are presented in Table 7.1 and here the calculated dry biomass at Trehøje, Stenhøje and Benlighøj are  $2.51 \text{ kg/m}^2 \pm 0.90 \text{ std.}$ ,  $0.51 \text{ kg/m}^2 \pm 0.081 \text{ std.}$  and  $0.62 \text{ kg/m}^2 \pm 0.11 \text{ std.}$  In order to test to what extent the difference in the volume of the above ground biomass between Trehøje and the test site at Benlighøj is expressed in the collected biomass samples the *t*-test for unequal standard deviations is applied. The calculated result is  $2(1 - F_{t(2)}(2.08)) < 0.2$  and the *null hypothesis*  $H_0$  that there is no difference between the biomass samples at Trehøje and the test site at Benlighøj is therefore only unlikely on the level of 20% [10]. Likewise, the difference in biomass between Trehøje and Stenhøje and the difference between Stenhøje and Benlighøj is not detectable. However, it should be noted that due to the very small number of samples the uncertainty in estimating the standard error is too large to decide whether or not differences based upon the collected biomass samples in Table 7.1 are significant. Nevertheless, the estimated biomass reflects the experiences from the field.

Based on the collected biomass samples a determination of the representative plant species within the test sites was carried out. The determination showed that within both test sites at Trehøje and Benlighøj the dominant species of vegetation were *Deschampsia flexuosa* and *Carex arenaria*. *Deschampsia flexuosa* and *Carex arenaria* were not found within the test site at Stenhøje where instead *Festuca rubra* was quite prominent.

Based on the soil samples in Table 7.2 the mean estimated volumetric water

content  $\theta_w$  at Stenhøje was 10%. In Section 7.3 it was demonstrated that using Topp's relationship and the TDR measurements the mean  $\theta_w$  was 9%. It is therefore concluded that Topp's relationship, which is valid for soils ranging from sandy loam to heavy clay soils, is well suited for the soil type at Stenhøje.

Again referring to Table 7.2 the mean  $\theta_w$  derived from the soil samples at Benlighøj was 18%. However, this is not consistent with the mean  $\theta_w$  of 11% derived from Topp's relationship and the TDR measurements in Section 7.4. Clearly Topp's relationship is not appropriate for the soil type in the test site at Benlighøj. The reason is that Topp's calibration function is not valid for soil types with a high content of organic matter. Here Benlighøj, contrary to Stenhøje, contains a significant amount of organic matter due to the manure. The fine-textured organic soil in the test site at Benlighøj binds the water molecules and therefore it is expected that the apparent dielectric constant  $K_a$ , and thereby the estimate  $\theta_w$  using Topp's relation, will be lower than for a sandy coarse-textured soil [39].

Although the actual soil moisture content in the test sites at Stenhøje and Benlighøj was different, the estimated  $\theta_w$  at the two test sites was quite similar using Topp's calibration function. This implies that  $K_a$  at Stenhøje and Benlighøj was almost the same.

In the Sections 7.3.3 and 7.4.3 evidence suggested that neighbouring points of TDR measurements were correlated along the transects at Stenhøje and Benlighøj. Because of the homogeneity of the physical properties at the test sites the corresponding auto-covariance functions are believed to be isotropic within the areas. At the transects at Stenhøje test site  $K_a$  was ranging from 4.67 to 6.25, which corresponds to a range in the estimated  $\theta_w$  from 7% to 11%. Along the transects at Benlighøj  $K_a$  was ranging from 5.06 to 7.34. Dubois (1995) and Ji (1996) showed that the standard deviation of soil moisture retrieval using polarimetric SAR is less than 4.5% under near bare field conditions [26], [37]. Since the radar backscattering coefficient is strongly affected by  $K_a$  it is therefore unlikely that a variation in soil moisture within and between Stenhøje and Benlighøj test sites 4 June 1997 could be detected using polarimetric EMISAR.





# EMISAR data versus Gjern

---

In Chapter 6 *in situ* data from Ladegaards Enge were presented and analyzed. The key issue in this chapter is to investigate to what extent the collected *in situ* data are correlated with the geometrically rectified one-look C-(5.3 Ghz) and L-(1.25 Ghz) band polarimetric EMISAR data. The *in situ* data were collected simultaneously with the EMISAR acquisitions 3 June 1997. The *in situ* data to be used in this investigation are the apparent dielectric constant  $K_a$  and the dominant species of vegetation covering the test site. In the Figures 6.22 and 6.3, maps of  $K_a$  and the dominant species of vegetation at Ladegaards Enge are presented.

In order to support this investigation three training areas are selected each assigned to the three sub-areas mentioned in Section 6.1. The criteria for selecting the training areas are relative homogeneity in terms of vegetation and soil moisture. The geographical locations of the three training areas are shown in Figure 8.1 and in the analyses that follow the three training sets will be identified by their colour codes. Sub-area I, which represents a marsh, was the wettest part of the test site and is given a blue colour. Sub-area II, which was intermediate in terms of soil moisture, is assigned a red colour and the driest part of the test site was sub-area III which is given a green colour. The various types of the dominant species of vegetation within the three sub-areas I, II and III are shown in the Figures 6.8 (b), 6.8 (a) and 6.7 (b).

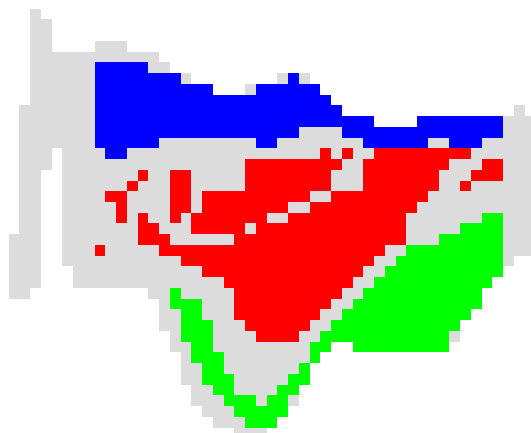


Figure 8.1: The training areas or classes which represent the test site at Ladegaards Enge. The blue training area is located in sub-area I, which was a marsh characterized with water above ground level. The red area is located in sub-area II, which was dominated by *Deschampsia caespitosa* and the green area is located in sub-area III where *Alopecurus pratensis* was prevailing. The grey background represents a mixture of various types of vegetation.

As we have seen the test area at Ladegaards Enge is very small. It covers in total only 10300 m<sup>2</sup> and the smallest patches of dominant species of vegetation in Figure 6.3 correspond to the size of a pixel. Due to the small test site it follows that substantial demands have to be put on the geometrically rectification of the polarimetric EMISAR data, see Section 3.3. This is a crucial task in the matching of the remotely sensed data with the available *in situ* data.

It is therefore relevant to know how accurately the geometry of the rectification matches the reference. For re-sampling the bilinear interpolation is applied and using (3.8) the measured geometric error  $\hat{\sigma}_o^2$  at a point is 2.3 [m<sup>2</sup>] in both the Northern and Eastern directions. This corresponds to a standard deviation of about 0.5 pixel, which is fairly good for our application. The affine transformation is therefore well suited for the rectification of the EMISAR data covering this small test area. After the re-sampling the number of pixels/observations is 1115 and one pixel corresponds to  $\sim 9.25$  m<sup>2</sup>. In Section 3.3 is presented the common methods for geometrical transformation and re-sampling and our strategy

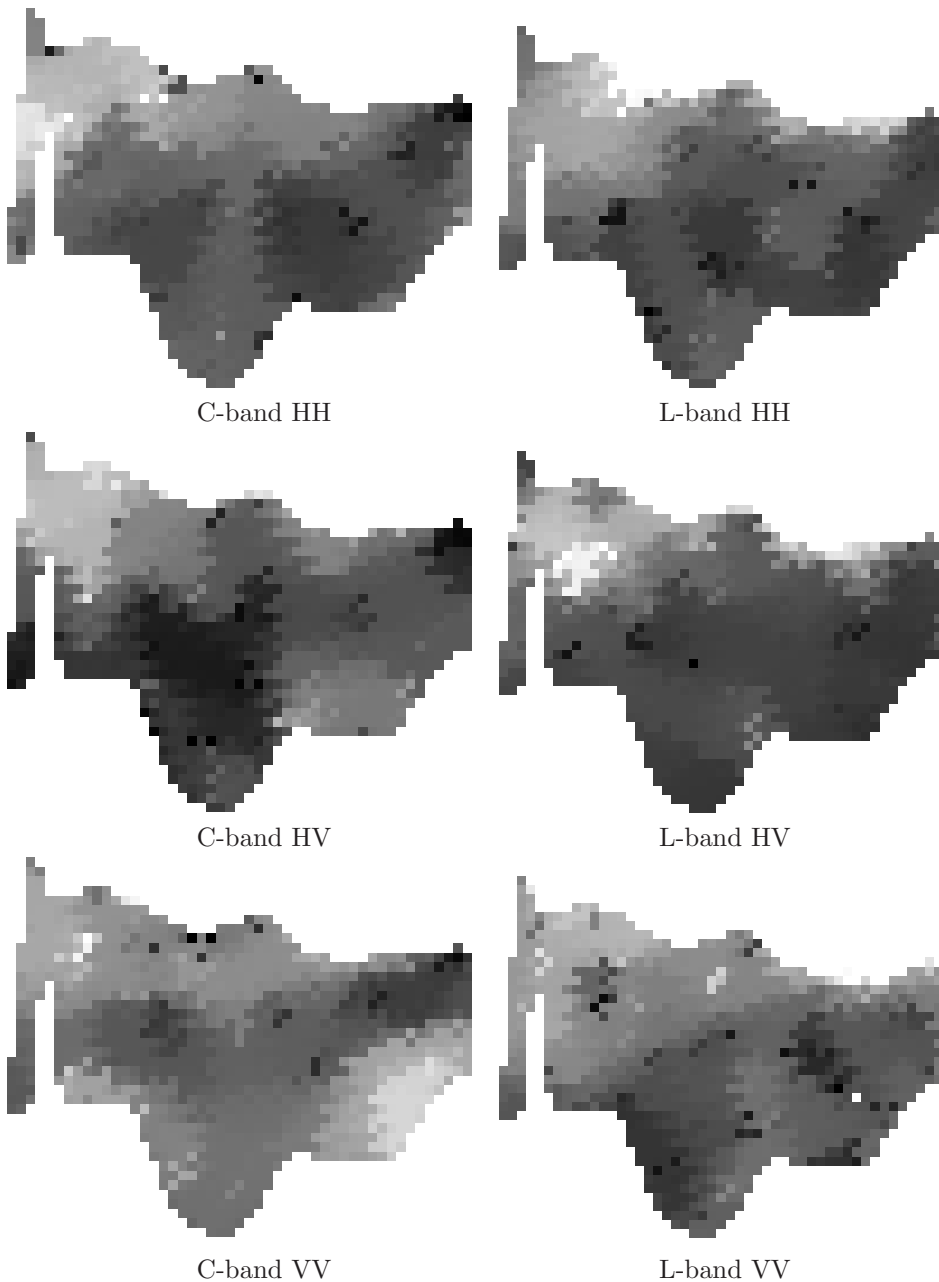


Figure 8.2: Restored polarized C- and L-band EMISAR amplitude data using the Gamma *pixel prior* in a simulated annealing algorithm. The data are geometrically rectified and cover the test site at Ladegaards Enge 3 June 1997. One pixel corresponds to  $\sim 9.25 \text{ m}^2$  and the images are stretched linearly between their mean  $\pm 3.5$  std.

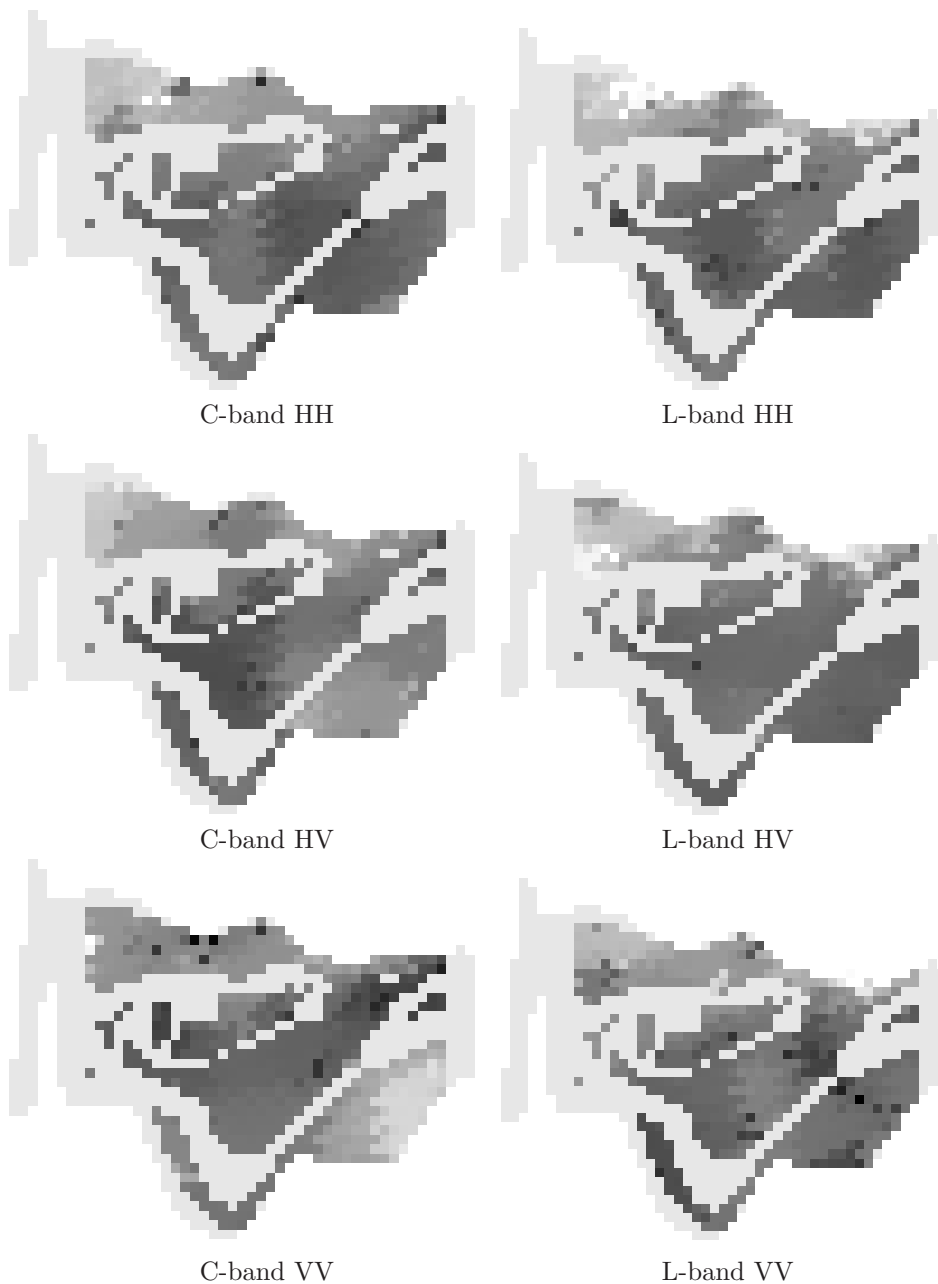


Figure 8.3: Restored polarized C- and L-band EMISAR amplitude data using the Gamma *pixel prior* in a simulated annealing algorithm. The data are geometrically rectified and cover the three training areas at Ladegaards Enge 3 June 1997, see Figure 8.1. One pixel corresponds to  $\sim 9.25 \text{ m}^2$  and the images are stretched linearly between their mean  $\pm 3.5$  std.

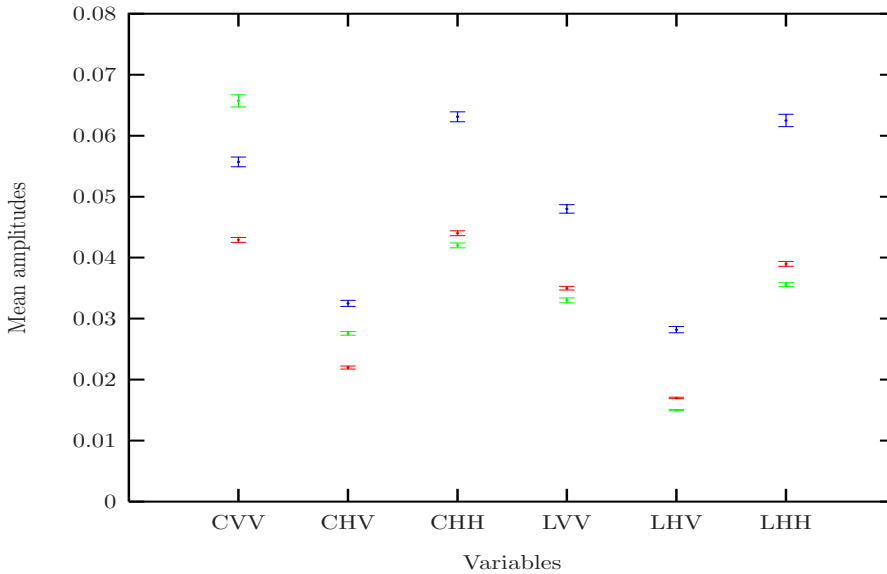


Figure 8.4: Mean amplitudes for the restored and geometrically rectified polarized C- and L-band EMISAR data covering the three training areas at Lade-gaards Enge 3 June 1997, see Figure 8.3. The blue colour represents sub-area I, red colour represents sub-area II and green represents sub-area III. The errorbars indicate the standard deviation of the mean amplitudes.

for sampling GCP is outlined.

When we recall that the smallest patches of dominant species of vegetation correspond to the size of a pixel substantial demands also have to be put on the quality of the restorations. In Section 5.7 it was demonstrated that the Gamma *pixel prior* implemented in a SA algorithm performs fairly well when it comes to reconstructing fine structures as well as preserving homogeneous areas and boundaries between adjacent regions. We therefore have applied the Gamma *pixel prior* and the SA algorithm in the restorations of CVV, CHV, CHH, LVV, LHV and LHH. The restored data have been geometrically rectified to the UTM system zone 32 ED(50) and the extracted data covering the test site at Lade-gaards Enge are presented in Figure 8.2. In Figure 8.3 the equivalent restored data are presented corresponding to the three training areas in Figure 8.1. A representation of the mean amplitudes of the restored EMISAR data is given in Figure 8.4.

In order to make further use of the polarimetric aspects of the EMISAR data

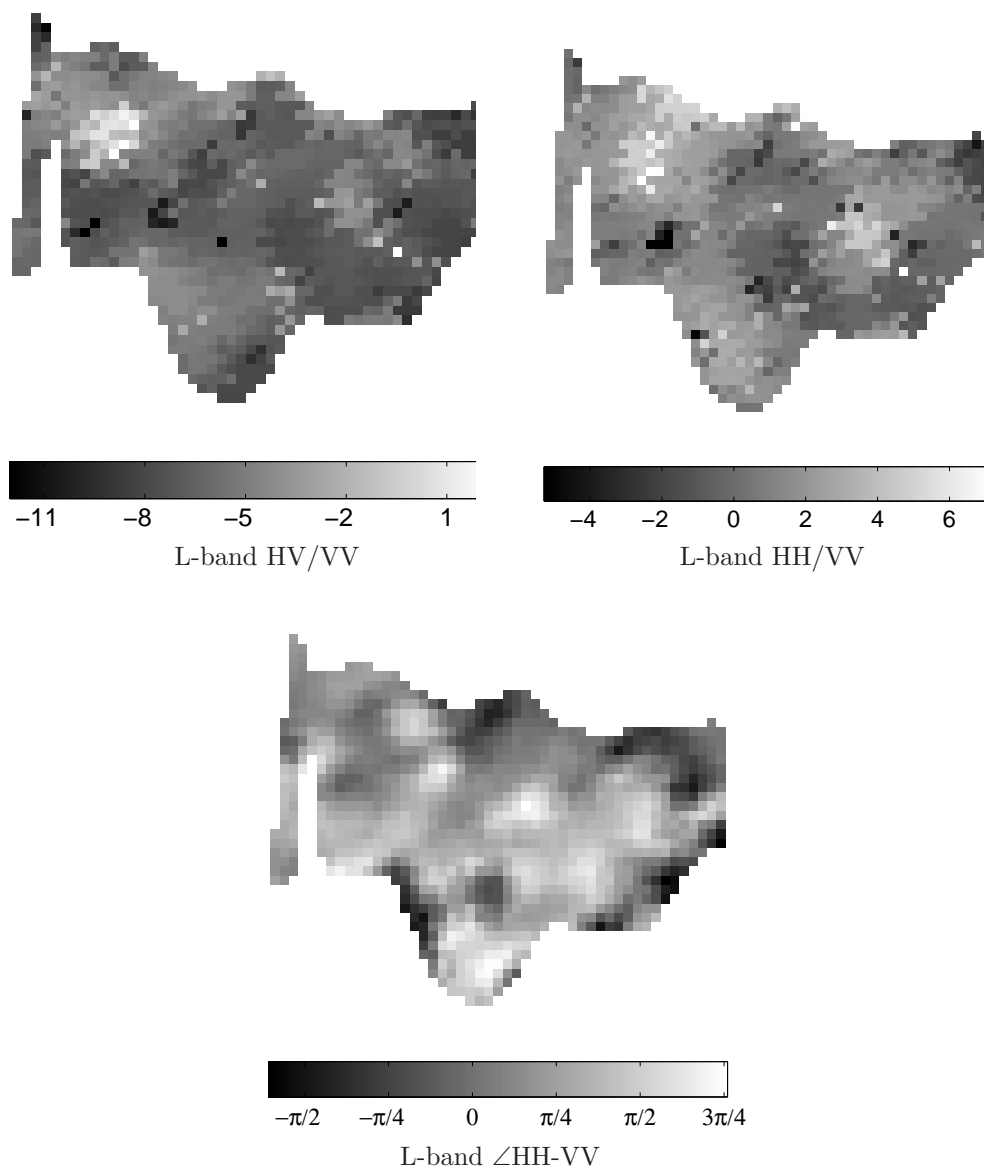


Figure 8.5: Restored geometrically rectified L-band ratios and phase differences in the test site at Ladegaards Enge 3 June 1997. HV/VV and HH/VV are indicated by the dB scales and  $\angle$ HH-VV is stretched linearly between -1.96 rad and 2.38 rad. One pixel corresponds to  $\sim 9.25 \text{ m}^2$ .

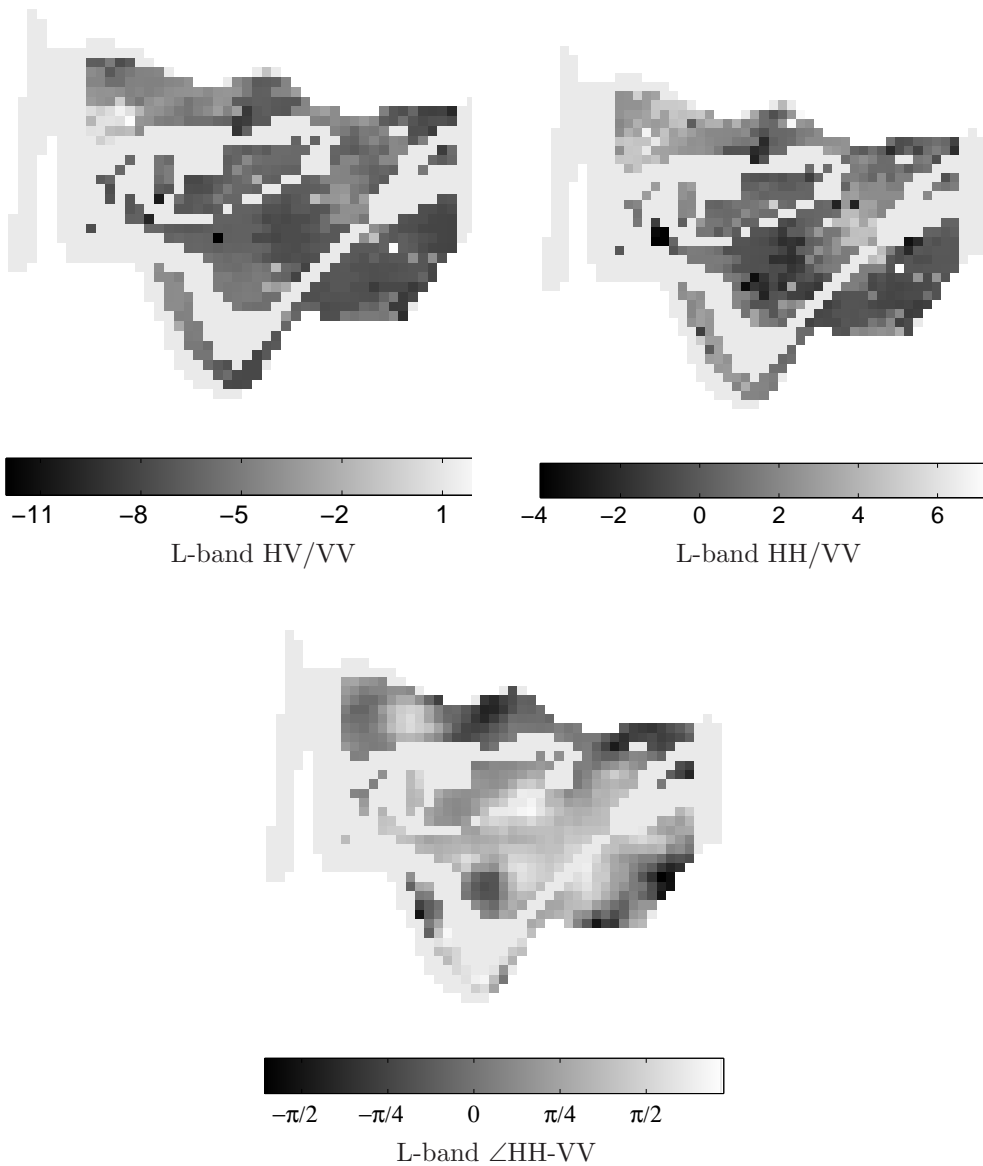


Figure 8.6: Restored geometrically rectified L-band ratios and phase differences in the three training areas at Ladegaards Enge 3 June 1997, see Figure 8.1. The grey background represents the rest of the test site. HV/VV and HH/VV are indicated by the dB scales and  $\angle$ HH-VV is stretched linearly between -1.96 rad and 2.38 rad. One pixel corresponds to  $\sim 9.25 \text{ m}^2$ .

also lowpass filtered  $\angle$ LHH-LVV and restored amplitude ratios LHV/LVV and LHH/LVV are included in the analyses, see Section 1.2.1. These geometrically rectified data are presented in Figures 8.5 and 8.6. All images are stretched linearly between their mean  $\pm 3.5$  std.

The multivariate variables used in our analyses now include CVV, CHV, CHH, LVV, LHV, LHH, LHV/LVV, LHH/LVV and  $\angle$ LHH-LVV. The analyses comprise two multivariate data sets, one set containing observations from the whole test site and one containing observations from the three training areas only. Each of the variables in the multivariate data sets is standardized to zero mean and variance one.

The following classical multivariate techniques are used in the preliminary analyses of the EMISAR data: In Section 8.1 Principal Components (PC) are used for detecting linear relationships and for measuring the 'interestingness', which is maximized in terms of the variance. The separation between the sub-areas is maximized using Canonical Discriminant Analysis (CDA) in Section 8.2. This is followed up by a discussion of what could be the reason for certain frequencies and polarizations of the EMISAR to interact with the physical properties of the sub-areas. In Section 8.3 Multiple Discriminant Analysis (MDA) is used to classify observations (pixels) from the whole test site into the three predefined classes based on observations from the three training areas. In Section 8.4 mapping of  $K_a$  from EMISAR data is carried out using linear Multiple Regression Analysis (MRA). In Section 8.5 the natural grouping of the observations is explored using Cluster Analysis (CA).

## 8.1 Principal components

In this section preliminary studies are made in order to disclose any possible structure and to determine the "real" dimensionality of the multivariate data set, see Section 3.5.1.

In Figure 8.7 are shown scatter-plots of the variables mentioned above after they have been transformed into the PC space. The observations are here covering the whole test site. Starting in the upper left corner going right the scatter-plots are: PC1/PC2, PC1/PC3,  $\dots$ , PC4/PC5. The colours used in the plots magenta-blue-cyan-green-yellow and red represent the number of hidden observations 0, 1, 2, 3, 4 and  $> 4$ .

The scatter-plot PC1/PC2 of the first and second principal components is the one that exhibits most structure. This is not surprising when we recall that the



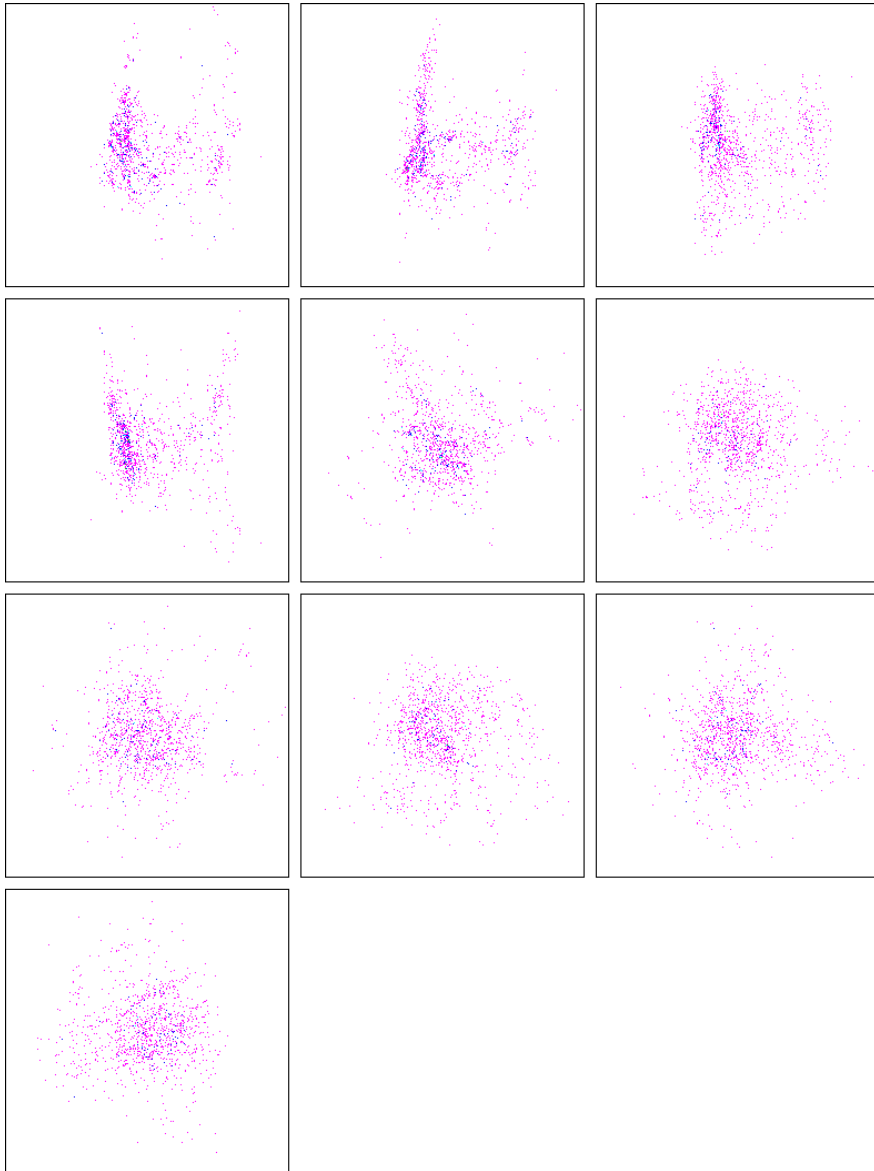


Figure 8.7: Scatter-plots of variables transformed into the principal component space. The variables are restored geometrically rectified C- and L-band polarized EMISAR amplitude data from the whole test site at Ladegaards Enge 3 June 1997, see text page 178. Starting in the upper left corner going right the scatter-plots are: PC1/PC2, PC1/PC3, ..., PC4/PC5. The colours magenta-blue-cyan-green-yellow and red represent the number of hidden observations 0, 1, 2, 3, 4 and  $> 4$ .

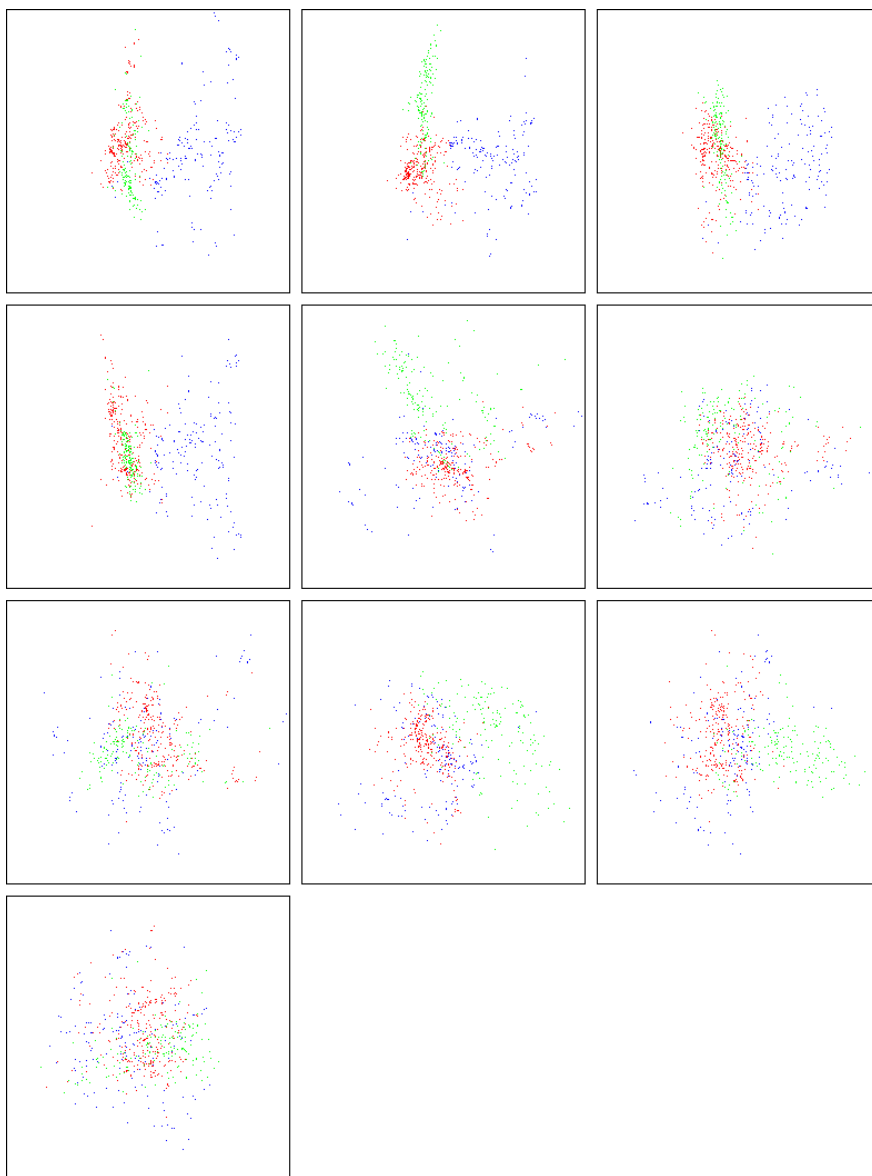


Figure 8.8: Scatter-plots of variables transformed into the principal component space. The variables are restored geometrically rectified C- and L-band polarized EMISAR amplitude data from Ladegaards Enge 3 June 1997, see text page 178. Starting in the upper left corner going right the scatter-plots are: PC1/PC2, PC1/PC3, . . . , PC4/PC5. The green dots represent sub-area III which was the dry area within the test site where *Alopecurus pratensis* was dominating. The red dots represent sub-area II which was the humid part of the test area where *Deschampsia caespitosa* was prevailing and the blue dots represent sub-area I which was a wet marsh.

	Eigenvalue	Difference	Proportion	Cumulative
1	4.2120	2.5694	0.4680	0.4680
2	1.6425	0.5653	0.1825	0.6505
3	1.0772	0.1275	0.1197	0.7702
4	0.9497	0.5067	0.1055	0.8757
5	0.4430	0.0447	0.0492	0.9249
6	0.3982	0.1606	0.0442	0.9692
7	0.2376	0.2030	0.0264	0.9956
8	0.0347	0.0295	0.0039	0.9994
9	0.0051		0.0006	1.0000

(a)

Variable	PC1	PC2	PC3	PC4	PC5	PC6
CVV	0.1746	-.1323	0.8227	0.2596	0.0034	-.0549
CHV	0.3945	-.1346	0.2418	0.1773	-.1437	0.5177
CHH	0.3902	-.1395	-.0233	0.1747	0.0569	-.8188
LVV	0.3201	-.5087	-.2951	-.0292	0.0355	0.1501
LHV	0.4471	0.0188	-.1422	-.1121	0.4824	0.1353
LHH	0.4407	-.0143	-.2782	0.0738	-.3796	0.0547
LHV/LVV	0.2834	0.5581	0.0870	-.1554	0.5063	0.0558
LHH/LVV	0.2517	0.5996	-.0499	0.0804	-.5322	-.0345
∠LHH-LVV	-.1464	0.1207	-.2636	0.9062	0.2419	0.1021

(b)

Table 8.1: Tables of variables transformed into the principal component space. The variables are geometrically rectified C- and L-band polarized EMISAR data from the whole test site at Ladegaards Enge 3 June 1997, see text page 178. In (a) eigenvalues are listed in descending order and in (b) the eigenvectors corresponding to the six highest eigenvalues are given in the basis vectors of the original variables.

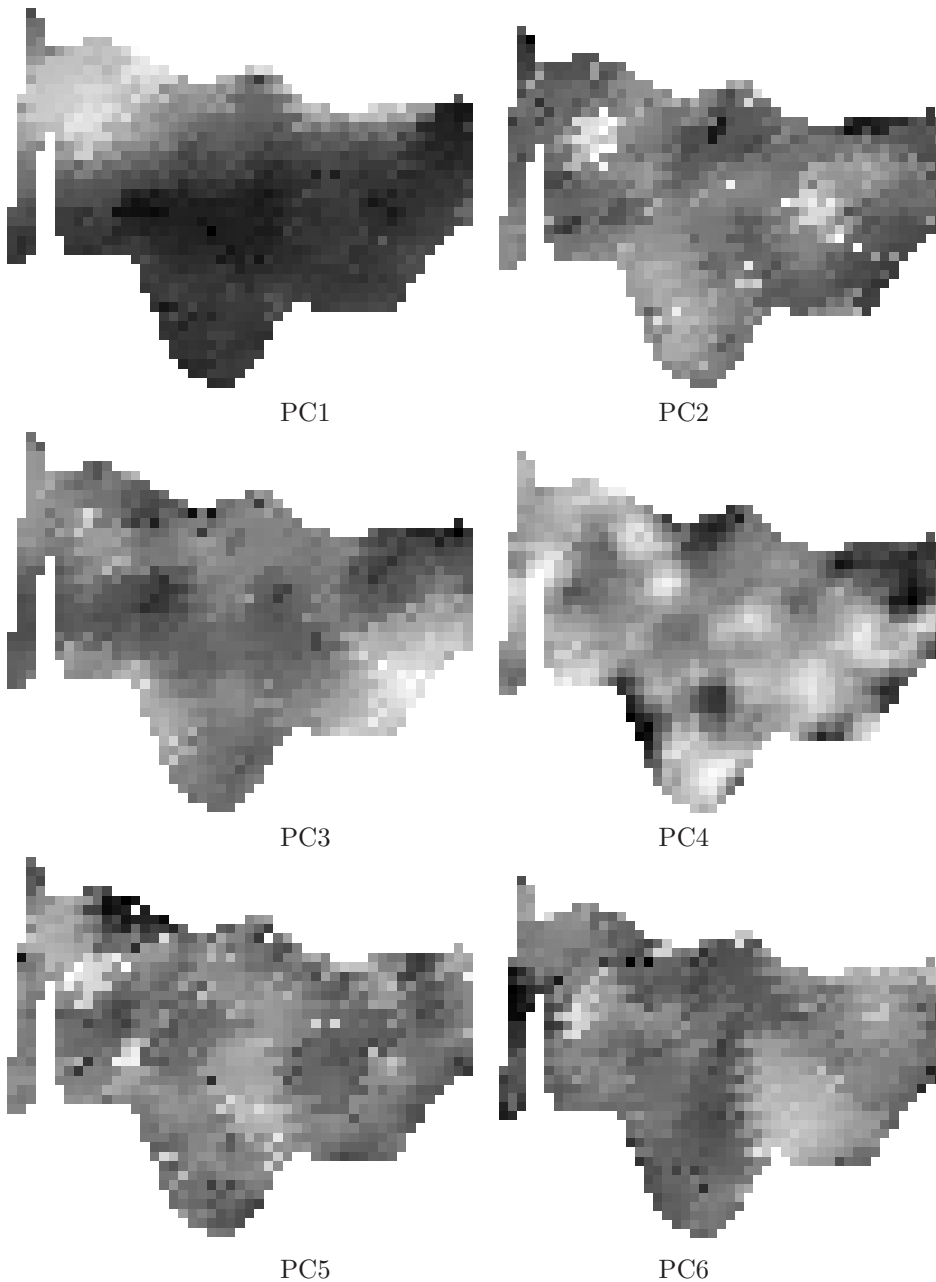


Figure 8.9: Geographical placement of the principal components corresponding to the six highest eigenvalues. The variables are geometrically rectified C- and L-band polarized EMISAR data from Ladegaards Enge 3 June 1997, see text page 178. One pixel corresponds to  $\sim 9.25 \text{ m}^2$  and the images are stretched linearly between their mean  $\pm 3.5$  std.

first PC are the linear transforms of the original variables with the highest variance. The scatter-plots of the remaining PC, in particular those that do not contain PC1, have less structure due to the smaller variance of the linear transforms.

Observations belonging to the sub-areas I, II and III only are assigned the colours blue, red and green and the variables listed on page 178 are in Figure 8.8 transformed into the PC space. The colours in the PC1/PC2 scatter-plot in Figure 8.8 are concentrated in three clusters and we assume that the three clusters represent the three sub-areas. Because the structure in the plots in Figure 8.7 and 8.8 is similar it is therefore likely that the previously mentioned structure in Figure 8.7 largely is explained by differences between the three sub-areas.

In Table 8.1 (a) we note that 46.8% of the variance is explained by PC1 and the PC1/PC2 scatter-plot in Figure 8.8 shows that PC1 is a good discriminator especially between the sub-areas I and the sub-areas II and III. Referring to Table 8.1 (b) and the first eigenvector we notice that the variables responsible for most of the variance are CHV, CHH, LVV, LHV and LHH. A drawback of PC is that it does not take into account how the observations are distributed within the test site. In Figure 8.9 the geographical distribution of PC1 within the test site at Ladegaards Enge is therefore shown. The image is stretched linearly between its mean  $\pm 3.5$  std and as expected the bright and dark areas correspond to sub-area I and the sub-areas II and III.

According to Table 8.1 (a) 18.3% of the variance is explained by PC2 and an examination of the PC1/PC2 scatter-plot in Figure 8.8 unveils that PC2 performs poorly in discriminating between the sub-areas II and III. However, PC3 is well suited for discriminating between the sub-areas II and III and here 12.0% of the variance is accounted for. The variable responsible for most of the variance is according to PC3 in Table 8.1 (b) CVV. The geographical distribution of PC3 is shown in Figure 8.9. The image is stretched linearly between its mean  $\pm 3.5$  std and some of the area corresponding to sub-area III is bright whereas the area corresponding to sub-area II is dark.

Besides detecting linear relationships PC can be used for reducing the redundancy in the data set. In Table 8.1 the eigenvalues and their corresponding eigenvectors are listed. Here we note that 65.1% of the variance is explained by PC1 and PC2 and 92.5% of the variance is accounted for by PC1,  $\dots$ , PC5 alone. Since the measure of 'interestingness' that is maximized is the variance, much of the information is concentrated in PC1 and PC2.

Unfortunately the variance also is the Achilles' heel of PC. That is to say PC has

difficulties in separating the signal from the noise. This is in particular a problem in the presence of outliers, which are expected in the restored polarimetric EMISAR data to be used, see text on page 112.

The polarized amplitudes VV, HV and HH of different frequencies e.g. CVV and LHH are statistically uncorrelated whereas the polarized amplitudes VV, HV and HH within each frequency e.g. CVV and CHH are statistically correlated. However, during the annealing process this correlation is lost and the restored amplitudes within each frequency are therefore statistically uncorrelated. As mentioned on page 111, the variance of the restored EMISAR data is larger in regions with large mean amplitude levels than in regions with small mean amplitude levels. This is to some extent supported by Figure 8.4, where e.g. the variances of CVV, CHH and LHH are larger for areas with high mean amplitude levels compared to areas with small mean amplitudes levels.

## 8.2 Synergy between *in situ* data and EMISAR data

In this section the interaction between the polarized wavebands of the EMISAR and the physical properties of the sub-areas is studied. This is carried out using Canonical Discriminant Analysis (CDA), which maximizes the separation between the sub-areas, see Section 3.5.2.

In Figure 8.10 are shown the two canonical variates CAN1 and CAN2 of the training data belonging to the sub-areas I, II and III as described in the introduction to this chapter. Based on the three training areas the canonical variates and their geographical distributions covering the whole test site are shown in Figure 8.11. Because there are three sub-areas or groups the discriminants span two dimensions. The variables are given on page 178.

As it appears from Figure 8.10 the first linear discriminant CAN1 expresses the difference between sub-area I and the sub-areas II and III. The corresponding squared canonical correlation in Table 8.2 (a) shows that 79.8% of the variance is accounted for by CAN1. The second linear discriminant CAN2 expresses primarily the difference between sub-area II and sub-area III. Here the squared canonical correlation in Table 8.2 (a) indicates that 56.1% of the variance is explained by CAN2. The observed over all  $R^2$  for testing of the *null hypothesis*  $H_0$  that all three sub-areas have equal means is 0.42, which is significant at the 0.0001 level. We thereby reject  $H_0$  and conclude that the three sub-areas have different means.

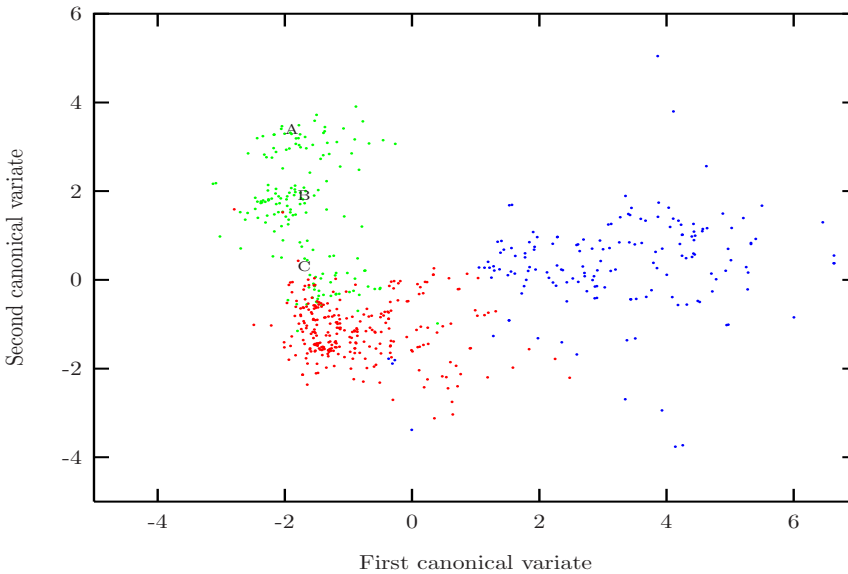


Figure 8.10: Linear discriminant plot for the three sub-areas within Ladegaards Enge 3 June 1997. The variables and their correlations are shown in Table 8.2 (b). The blue dots represent a wet marsh which corresponds to sub-area I. The red dots represent sub-area II which was a humid part of the test area where *Deschampsia caespitosa* was prevailing and the green dots represent the dry sub-area III where *Alopecurus pratensis* was dominating.

CAN1 in Table 8.2 (b) shows the total sample correlations between the first canonical variables and the original variables. Here we see that the difference between sub-area I and the sub-areas II, III to a large extent are due to the variables CHV, CHH, LVV, LHV and LHH. This is also supported by the corresponding mean amplitudes in Figure 8.4, which have high responses in sub-area I and low responses in the sub-areas II, III. The same variables are also significant in PC1 according to Table 8.1 (b). The geographical distribution of the first canonical variate in Figure 8.11 therefore shows similarities with PC1 in Figure 8.9. According to CAN1 in Table 8.2 (b) the amplitude ratios LHV/LVV, LHH/LVV and the phase difference  $\angle\text{LHH-LVV}$  contribute to a lesser extent to the separation of the sub-areas. The significance of the amplitude ratios is discussed in Section 8.4.

Sub-area I was a swampy area with standing water saturated with vegetation and pre-dominated by *Glyceria maxima* and *Carex elata* All., see photo in Figure 6.8 (b). The biomass comprised fresh and withered material. The vegetation

	Canonical Correlation	Adjusted Canonical Correlation	Approximate Standard Error	Squared Canonical Correlation
1	0.8935	0.8918	0.0082	0.7984
2	0.7492	0.7466	0.0178	0.5613

(a)

Variable	CAN1	CAN2
CVV	0.0204	0.9515
CHV	0.5687	0.5905
CHH	0.8407	0.0603
LVV	0.7812	0.0327
LHV	0.9120	0.0172
LHH	0.9046	0.0631
LHV/LVV	0.4380	-0.0031
LHH/LVV	0.4030	0.0554
$\angle$ LHH-LVV	-0.4602	-0.2528

(b)

Table 8.2: (a) The squared canonical correlations and (b) the total sample correlations between the canonical variables and the original variables. The sample represents the three sub-areas within Ladegaards Enge of varying vegetation and soil moisture. The variables are geometrically rectified C- and L-band polarized EMISAR data covering Ladegaards Enge 3 June 1997, see text page 178.

rose approximately 0.5 m above the water and the straws were randomly orientated. The straws of the withered material were to a large extent horizontal.

According to CAN1 in Table 8.2 (b) CHV, CHH, LVV, LHV and LHH are responsible for most of the discriminating power between sub-area I and the sub-areas II and III and the corresponding mean amplitudes in Figure 8.4 show that sub-area I had the highest backscattering coefficient. Due to the wet conditions, sub-area I was also the sub-area with the highest  $K_a$ , which probably explains most of discriminatory power of CAN1. Sub-area II again had a higher  $K_a$  than sub-area III, which to a lesser extent is reflected in the mean amplitudes for CHH, LVV, LHV and LHH in Figure 8.4.

However, differences in vegetation characteristics probably also explain why CHV, CHH, LVV, LHV and LHH discriminate between sub-area I and the sub-



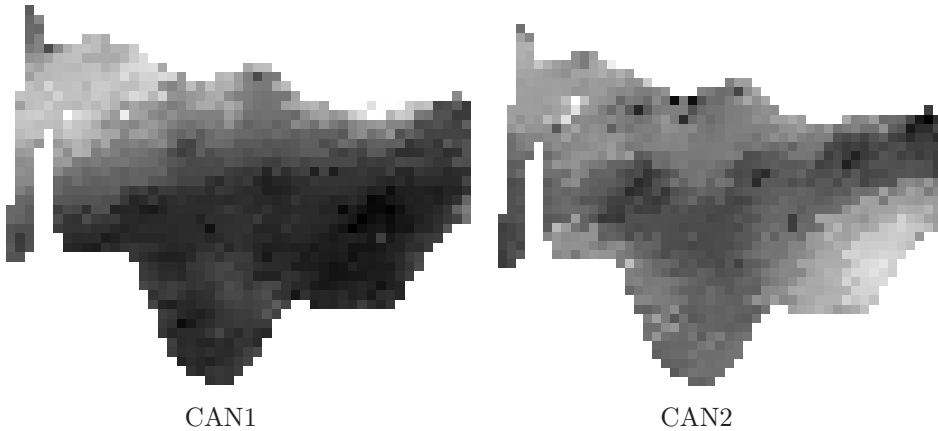


Figure 8.11: The geographical distribution of the first and second canonical variates in Figure 8.10. The canonical variates are based on the three training areas shown in the Figures 8.3 and 8.6. The variables are geometrically rectified C- and L-band polarized EMISAR data from Ladegaards Enge 3 June 1997, see text page 178. One pixel corresponds to  $\sim 9.25 \text{ m}^2$  and the images are stretched linearly between their mean  $\pm 3.5$  std.

areas II and III. Referring to Figure 8.4 and CAN1 in Table 8.2 (b) evidence suggests that CHH and LHH is better at discriminating between sub-area I and the sub-areas II and III than CHV and LHV. This could be explained by the horizontal orientated straws of length  $\sim 6 \text{ cm}$  and  $\sim 20 \text{ cm}$ , which were more frequent in sub-area I than in the sub-areas II and III.

CAN2 in Table 8.2 (b) shows the total sample correlations between the second canonical variables and the original variables. In this case the discriminatory power between the sub-areas II and III is concentrated in CVV and CHV. This is supported by the corresponding restored CHV and CVV images in Figure 8.3 and mean amplitudes in Figure 8.4. In particular there is a powerful response from the eastern part of sub-area III in the CVV image in Figure 8.3. According to Table 8.1 (b) the variables CVV and CHV are also significant in PC3 and the geographical distribution of the second canonical variate in Figure 8.11 therefore has an appearance similar to the PC3 image in Figure 8.9.

The vegetation in sub-area II was dominated by *Deschampsia caespitosa* and as the photo in Figure 6.8 (a) illustrates the straws from the fresh vegetation were mainly ranging from oblique to vertical. Below the fresh vegetation was withered material and here the prevailing direction was horizontal. From the surface of the soil the maximum length of the fresh straws was approximately

20 cm. The CAN2 sample correlation for CHV in Table 8.2 (b) is 0.59 and in the CHV image in Figure 8.3 there is a faint response from the eastern part of sub-area II. This suggests that oblique straws of length  $\sim 6$  cm were present in sub-area II. However, the CHV mean amplitudes in Figure 8.4 suggests that the oblique orientation of straws of length  $\sim 6$  cm were less frequent in sub-area II than in the sub-areas I and III.

Again referring to the C-band HV image in Figure 8.3 it is striking that besides the bright area, which corresponds to sub-area I, there is also a less bright area located within sub-area III near the river. This suggests that the C-band HV polarization, besides interacting with the swampy conditions in sub-area I, also interacted with certain conditions within sub-area III. This bright area located within sub-area III in the C-band HV image in Figure 8.3 is coincident with a small plant community of *Phalaris arundinacea*. It is therefore likely that the C-band HV polarization interacted with the leaves or seed-bearing parts of *Phalaris arundinacea*.

A very characteristic feature of the vegetation was the ears of *Alopecurus pratensis* in the eastern part of sub-area III. As it appears from the photo in Figure 6.7 (b) the ears or the seed-bearing part of the grass were quite prominent. These ears were approximately 6 cm long and vertically orientated. It is therefore perfectly imaginable that the C-band VV polarization with its wavelength of 5.6 cm interacted with these ears. This interaction might possibly explain the high response from CVV within sub-area III in Figure 8.3.

It is interesting that the green dots, which represent sub-area III in Figure 8.10, are grouped together in three clusters. These clusters probably reflect three communities of varying plant compositions. The clusters A and C both probably correspond to regions where the ears of *Alopecurus pratensis* were dominating or frequent. The clusters are due to the interaction between the ears and the C-band VV polarization and according to the corresponding correlation of 0.95 in CAN2 in Table 8.1 (b) the discriminating power is outstanding. This is also reflected by the mean CVV amplitudes in Figure 8.4 that indicates that the vertical orientation of straws of length  $\sim 6$  cm was more frequent in sub-area III than in the sub-areas I and II. Cluster A corresponds to the bright region in the eastern part of sub-area III in Figure 8.11 where the concentration of ears was high. Cluster C represents the less bright area in the western part of sub-area III near the river in Figure 8.11, where the ears were frequent. Cluster B probably is partly due to the previously mentioned C-band HV response from the small plant community of *Phalaris arundinacea* and partly due to a transition zone between sub-area III and II, where the concentration of ears of *Alopecurus pratensis* was smaller. This transition zone is faintly visible in the CVV image in Figure 8.3 surrounding the brightest part of sub-area III.

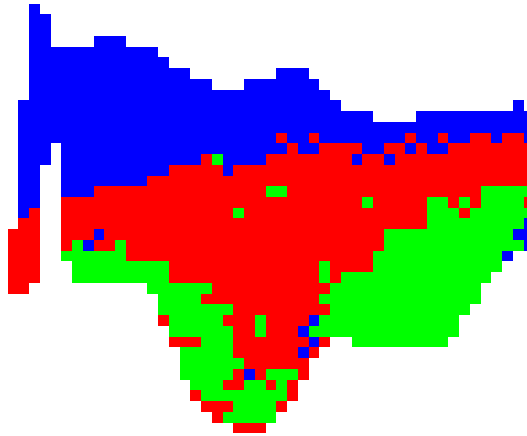


Figure 8.12: Supervised classification using Multiple Discriminant Analysis of EMISAR data covering the three test sites at Ladegaards Enge. The training areas are shown in Figure 8.1 where the colours red, green and blue correspond to sub-area I, II and III. The variables are geometrically rectified C- and L-band polarized EMISAR data covering Ladegaards Enge 3 June 1997, see text page 178. One square corresponds to  $\sim 9.5 \text{ m}^2$ .

In situations where the microwaves double-bounce from e.g. the soil surface and the vegetation a phase shift of  $\pi$  radians between HH and VV is introduced [81], [59]. The L-band HH-VV phase difference in the test site at Ladegaards Enge is shown in Figure 8.6. Here the mean  $\angle\text{LHH-LVV}$  for sub-area I was  $0.00 \text{ rad} \pm 0.05 \text{ std}$ ,  $0.86 \text{ rad} \pm 0.03 \text{ std}$  for sub-area II and  $0.64 \text{ rad} \pm 0.07 \text{ std}$  for sub-area III. The fact that the phase difference within sub-area II was larger than in sub-area I and III supports the *in situ* knowledge from the field. Here sub-area II was characterized by stems ranging from oblique to vertical with an approximate length of 20 cm. The stems in sub-area I were more or less randomly orientated and in sub-area III the prevailing orientation of the stems was vertical and their length was approximately 1 m. The long stems and leaves in sub-area III made multiple scattering for L-band more plausible than double-bounce scattering. The discriminating power of the L-band phase difference in terms of separating the three sub-areas is reflected by CAN1 and CAN2 in Table 8.2 (b). Here the corresponding correlations for  $\angle\text{LHH-LVV}$  are -0.46 and -0.25.

It is noticeable that the blue dots in Figure 8.10 representing sub-area I seem to have a large variance. As mentioned previously this is due to the high amplitude level of sub-area I, which results in a large variance.

From class	I	II	III	Total
.	206 (40.63)	194 (38.26)	107 (21.10)	507 (100.00)
I	163 (100.00)	0 (0.00)	0 (0.00)	163 (100.00)
II	8 (2.87)	266 (95.34)	5 (1.79)	279 (100.00)
III	1 (0.60)	16 (9.64)	149 (89.76)	166 (100.00)
Total	378 (33.90)	476 (42.69)	261 (23.41)	1115 (100.00)

(a)

From class	I	II	III	Total
.	206 (40.63)	194 (38.26)	107 (21.10)	507 (100.00)
I	161 (98.77)	2 (1.23)	0 (0.00)	163 (100.00)
II	11 (3.94)	262 (93.91)	6 (2.15)	279 (100.00)
III	2 (1.20)	19 (11.45)	145 (87.35)	166 (100.00)
Total	380 (34.08)	477 (42.78)	258 (23.14)	1115 (100.00)

(b)

Table 8.3: (a) Number of observations and percent classified into class and (b) number of observations and percent classified into class using *leave-one-out* cross-validation. The observations are classified using quadratic discriminant analysis. The classes I, II and III correspond to the three sub-areas within Ladegaards Enge and the training areas and classified observations are shown in the Figures 8.1 and 8.12. The variables are geometrically rectified C- and L-band polarized EMISAR data covering Ladegaards Enge 3 June 1997, see text page 178. The dot represents observations which are not belonging to any of the training areas.

## 8.3 Supervised classification of EMISAR data

Based on a number of features each observation in the test area is classified into one of the three classes defined by the three training areas. Supervised Bayes classification is carried out using Multiple Discriminant Analysis (MDA), see Section 3.6.1 for further description. The feature vector is the nine measured or derived variables given on page 178. Feature extraction is a dimension reducing technique that creates linear combinations of features which have good discriminatory power between classes [69]. Thereby the unwanted effect of the phenomenon termed the *curse of dimensionality* is reduced [9]. Methods of feature extraction could e.g. be principal components or canonical correlations analysis. However, in order to be able to compare the results obtained from the MDA directly with the results obtained in the Sections 8.1 and 8.2 we will again make use of all nine variables.

In Figure 8.12 is presented the result of the supervised classification using the training areas given in Figure 8.1. As we see the over all impression is convincing. The classes of the training areas are preserved during the classification and the grey unclassified areas in Figure 8.1 have been classified in accordance with the *a priori* knowledge from the field. An example is the blue area, representing the swampy region, dominating in the right part of the image in Figure 8.12. This is in perfect agreement with the experience from the test area that the swampy area was increasing downstream.

Table 8.3 (a) shows the confusion matrix which contains information about actual and predicted classifications. For example it appears that 95.3% of the pixels which really belong to sub-area II are effectively assigned to sub-area II and 2.9% are assigned to sub-area I. The dot represents observations which are not belonging to any of the training areas prior to the classification. We note that 100% of the observations belonging to sub-area I are assigned to sub-area I, which indicates that sub-area I is well separated from sub-area II and III.

The error rate of the total number of observations correctly assigned within the three training areas is according to Table 8.3 (a) 4.9%. This is surprisingly low and we therefore use the *leave-one-out* cross-validation to evaluate the predictive accuracy of the classification [69]. The confusion matrix of the cross-validation is shown in Table 8.3 (b) and here the error rate of the total number of observations correctly assigned within the three training areas is 6.6%. This suggests some degree of inhomogeneity in one or two of the covariance matrices of the three training areas. This could e.g. be due to sub-area III, which was inhomogeneous in terms of the plant species. The observed over all  $R^2$  for testing of the *null hypothesis*  $H_0$  that all three classified areas have equal means is 0.35, which is significant at the 0.0001 level. We thereby conclude that the three classified

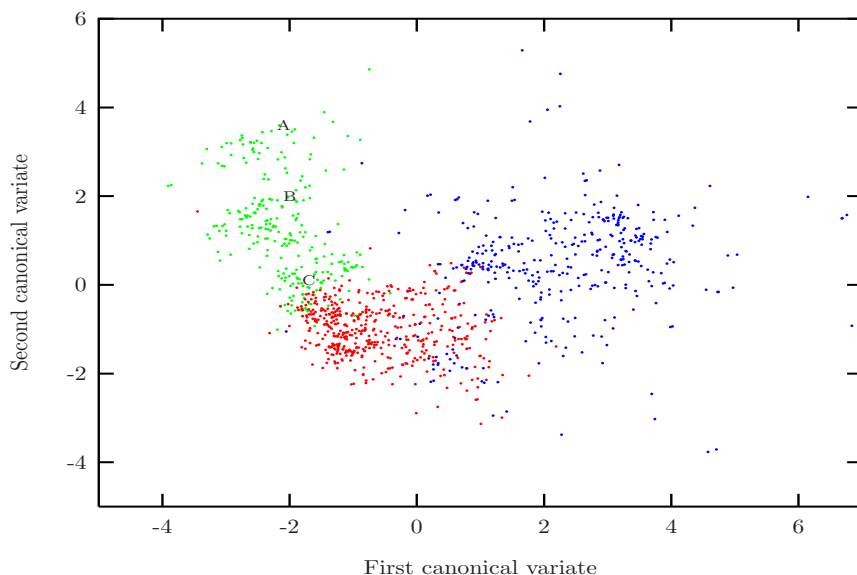


Figure 8.13: Linear discriminant plot for the classified result in Figure 8.12 of Ladegaards Enge 3 June 1997 using the training areas in Figure 8.1. The variables and their correlations are shown in Table 8.4 (b). The blue dots represent a wet marsh which corresponds to sub-area I. The red dots represent sub-area II which was a humid part of the test area where *Deschampsia caespitosa* was prevailing and the green dots represent the dry sub-area III where *Alopecurus pratensis* was dominating.

areas have different means. In Section 8.2  $R^2$  was 0.42, which shows that the separation is better using the three training areas only. This difference could be explained by the pixels outside the training areas, which belong to the transition zone between the classes. Consequently, some of these pixels are assigned a class membership based on a low *a posteriori* probability, which results in a decrease of  $R^2$ . This is also evident in the plot in Figure 8.13 of the two canonical variates CAN1 and CAN2 of the classified observations. Here the classes are more grown together than in Figure 8.10.

As in Section 8.2 the first linear discriminant CAN1 expresses the difference between sub-area I and the sub-areas II and III and the second linear discriminant CAN2 expresses the difference between sub-area II and sub-area III. Besides the differences in terms of separating classes the structures in Figure 8.13 and Figure 8.10 remain very similar. This similarity is also reflected in the total sample correlations between the two canonical variables CAN1 and CAN2 and the origi-

	Canonical Correlation	Adjusted Canonical Correlation	Approximate Standard Error	Squared Canonical Correlation
1	0.8604	0.8591	0.0078	0.7402
2	0.6796	0.6776	0.0161	0.4618

(a)

Variable	CAN1	CAN2
CVV	-0.0291	0.9483
CHV	0.5537	0.6034
CHH	0.7704	0.2136
LVV	0.8172	0.1381
LHV	0.8535	0.2082
LHH	0.8240	0.2022
LHV/LVV	0.3643	0.1555
LHH/LVV	0.2516	0.1483
$\angle$ LHH-LVV	-0.4059	-0.2544

(b)

Table 8.4: (a) The squared canonical correlations and (b) the total sample correlations between the canonical variables and the original variables. The sample represents the supervised classification of the test site in Figure 8.12 using the training areas in Figure 8.1. The variables are geometrically rectified C- and L-band polarized EMISAR data covering Ladegaards Enge 3 June 1997, see text page 178.

nal variables. A comparison between CAN1 and CAN2 in the Tables 8.4 (b) and 8.2 (b) shows that the variables that express most of the difference between the sub-areas very much are the same. Again we notice that the green dots, which represent sub-area III in Figure 8.13, are grouped together in three clusters. As explained in Section 8.2 these clusters are probably reflecting three communities of varying plant species and concentration of ears within sub-area III.

None of the classified observations are assigned to the reject class using the threshold 0.05. That is to say the largest *a posteriori* probability for class membership is larger than 0.05 for all observations. This supports that the test area can be subdivided into the sub-areas I, II and III represented by the classified blue, red and green areas in Figure 8.12. The overall performance of the classification is therefore good.

Parameter	Estimate	Standard		
		Error	$t$ Value	$Pr >  t $
Intercept	56.3494	0.3200	176.12	< .0001
CVV	-5.5856	0.4038	-13.83	< .0001
CHV	-3.3667	0.5331	-6.31	< .0001
CHH	6.7463	0.4926	13.70	< .0001
LVV	1.5121	1.1542	1.31	0.1904
LHV	6.7735	2.6213	2.58	0.0099
LHH	1.1543	2.4903	0.46	0.6431
LHV/LVV	0.5223	2.2062	0.24	0.8129
LHH/LVV	-0.2869	2.0009	-0.14	0.8860
$\angle$ LHH-LVV	2.0875	0.3418	6.11	< .0001

Table 8.5: Estimates for the intercept and the coefficients for the model using multiple regression analysis. The dependent variable is the  $K_a$  displayed in Figure 6.22. The independent and standardized variables are geometrically rectified C- and L-band polarized EMISAR data covering Ladegaards Enge 3 June 1997, see text page 178.

## 8.4 Mapping $K_a$ from EMISAR data

As mentioned in Section 3.1.3 the microwave data from the EMISAR are highly affected by the apparent dielectric constant  $K_a$  and thereby soil moisture. In this section we wish to study a possible linear relationship between the estimated  $K_a$  in Figure 6.22, derived from the TDR-readings, and the polarimetric EMISAR data. This is carried out using linear Multiple Regression Analysis (MRA), which is briefly described in Section 3.4. Here the dependent variable is the estimated  $K_a$  in Figure 6.22 and the independent variables are the variables given on page 178.

In Table 8.5 is given the model parameters, namely the intercept and the coefficients including all nine independent variables. The  $t$  test is used for testing the *null hypothesis*  $H_0$  that the parameters equal zero. Here we notice from Table 8.5 that the  $Pr > |t|$  values are not significant at the 0.05 level for all the parameters. A backward-elimination technique is therefore used to eliminate the variables one by one, that are likely to be zero, until all the remaining variables in the model are significant at the 0.05 level. The result is given in Table 8.6 and using (3.9) the estimate  $\hat{\sigma}^2$  of how well the model as a whole accounts for the variation in the dependent variables is 114.

The dependent variable  $K_a$  is predicted by a linear combination of the inde-



Parameter	Estimate	Standard		
		Error	$t$ Value	$Pr >  t $
Intercept	56.3494	0.3198	176.22	< .0001
CVV	-5.7133	0.3905	-14.63	< .0001
CHV	-3.1664	0.5066	-6.25	< .0001
CHH	6.9264	0.4666	14.84	< .0001
LVV	1.5062	0.4487	3.36	0.0008
LHV	7.7166	0.5316	14.52	< .0001
$\angle$ LHH-LVV	2.1097	0.3363	6.27	< .0001

Table 8.6: Estimates for the intercept and the coefficients for the model using multiple regression analysis. The table corresponds to Table 8.5 after a backward-elimination of all variables that do not produce a  $t$  statistic significant at the 0.05 level. The estimates are used in the regression equation for predicting the  $K_a$  values in the Figures 8.14 (a) and 8.16 at Ladegaards Enge 3 June 1997.

pendent variables in Table 8.6 and a geographical distribution of the predicted  $K_a$  is shown in Figure 8.14 (a). As mentioned above the dependent variable is the estimated  $K_a$  value in Figure 6.22. However, in order to make a pixel to pixel comparison possible the map in Figure 6.22 is re-sampled to the size of the geometrically rectified polarimetric EMISAR data. This re-sampled map is shown in Figure 8.14 (b). A comparison between the Figures 8.14 (a) and 8.14 (b) shows that the spatial distribution of the predicted  $K_a$  and the actual  $K_a$  is quite similar. At first glance this suggests that the model is well suited for predicting  $K_a$ .

The measure of how much of the variation in  $K_a$  can be accounted for by our independent variables is  $R^2$ . Using (3.10)  $R^2$  is 0.58, which indicates that a significant amount of the variation is explained by the model. Some reservation should be taken in the interpretation of  $R^2$  because outliers, which according to text on page 112 are expected in the data, can seriously affect the statistics.

The difference between the predicted  $K_a$  and the actual re-sampled  $K_a$ , which is called the residual, is illustrated in Figure 8.15. If our model had been good the residuals in Figure 8.15 would have been randomly distributed about the mean within the test site. However, there is some structure, showing that the residuals are correlated. The reason for that is that the predicted  $K_a$  is either over- or under estimated within small patches at the test site. This indicates that some 'unknown factor' other than the soil moisture is operating. Although the model as a whole is capable of predicting the spatial distribution of  $K_a$  it does not take this 'unknown factor' into account.

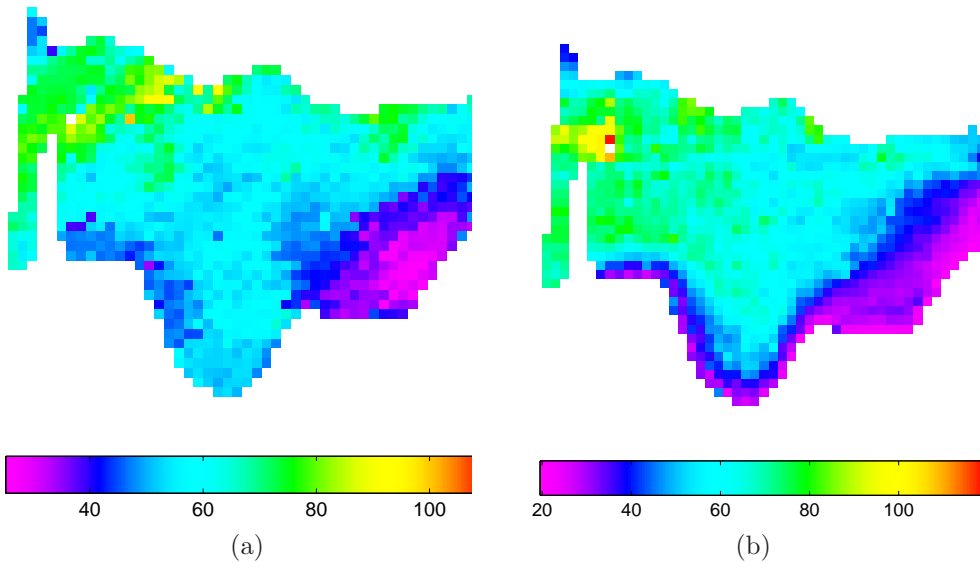


Figure 8.14: (a) Predicted  $K_a$  values at Ladegaards Enge 3 June 1997 using linear multiple regression. The dependent variable is the re-sampled  $K_a$  shown in (b). The independent variables are listed in Table 8.6. In (b) is shown the  $K_a$  values in Figure 6.22 re-sampled to the size of the geometrically rectified polarimetric EMISAR data. One pixel corresponds to  $\sim 9.25 \text{ m}^2$ .

In Figure 8.16 is shown a scatter-plot of the re-sampled actual  $K_a$  in Figure 8.14 (b) and the predicted  $K_a$  in Figure 8.14 (a). The straight black line is the line that best fits the points in a least squares sense. In the ideal case where  $R^2$  equals 1 the grey line would be the best fitted line. The two lines in Figure 8.16 cross each other at  $K_a(\text{actual}) = 56$  and the model over-estimates  $K_a$  for  $K_a(\text{actual}) < 56$  and under-estimates  $K_a$  for  $K_a(\text{actual}) > 56$ . The fact that the two lines are crossing each other shows that a trend exists in the residuals signifying that the dependent variable  $K_a$  and the residuals are correlated. However, this correlation is to be expected while  $\text{Cor}(Y_i, Y_i - X_i) = 1 - R^2$  where  $Y_i$  is the dependent variable and  $X_i$  the predicted result. The correlation between the residuals and  $K_a(\text{actual})$  is therefore  $1 - 0.58 = 0.42$ , which suggests that another model might be more appropriate.

We note from Table 8.6 that CHH and LHV contribute to the predicted  $K_a$ . This is in agreement with results in Section 8.2 that suggested that the C-band HH and L-band HV polarizations were affected by  $K_a$  in the sub-areas I and II. The yellow and red area in Figure 8.14 (b) with the highest  $K_a$  is coincident

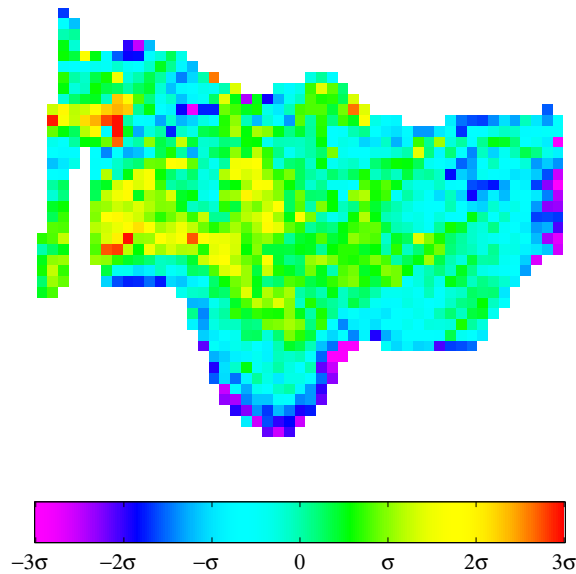


Figure 8.15: The residual between the actual re-sampled  $K_a$  values in Figure 8.14 (b) and the predicted  $K_a$  values in Figure 8.14 (a). The standard deviation  $\sigma$  is 10.7 and one pixel corresponds to  $\sim 9.25 \text{ m}^2$ .

with a small bright area at the same location in the LHV image in Figure 8.2. It is striking that this area again coincides with the small plant community of *Glyceria fluitans* (8) in Figure 6.3. This suggests that the model besides being affected by  $K_a$  is strongly affected by the vegetation at Ladegaards Enge.

The assertion above that the model is strongly affected by the vegetation is supported by Figure 8.16 where it is the green dots which significantly contribute to the bias between the black and the grey lines. In case only the red and blue dots had been included in the analysis the model fit would have been better. Here we recall that the green dots represent the relatively dry sub-area III dominated by the long vertical straws of *Alopecurus pratensis*. In Section 8.2 we made it probable that the C-band VV polarization interacted with the ears of *Alopecurus pratensis*, which is also reflected by the relatively small CVV coefficient in Table 8.6.

From the analyses above the previous mentioned 'unknown factor' is probably the vegetation cover at Ladegaards Enge, which played a central role in the model for predicting soil moisture using MRA. This is a major problem because

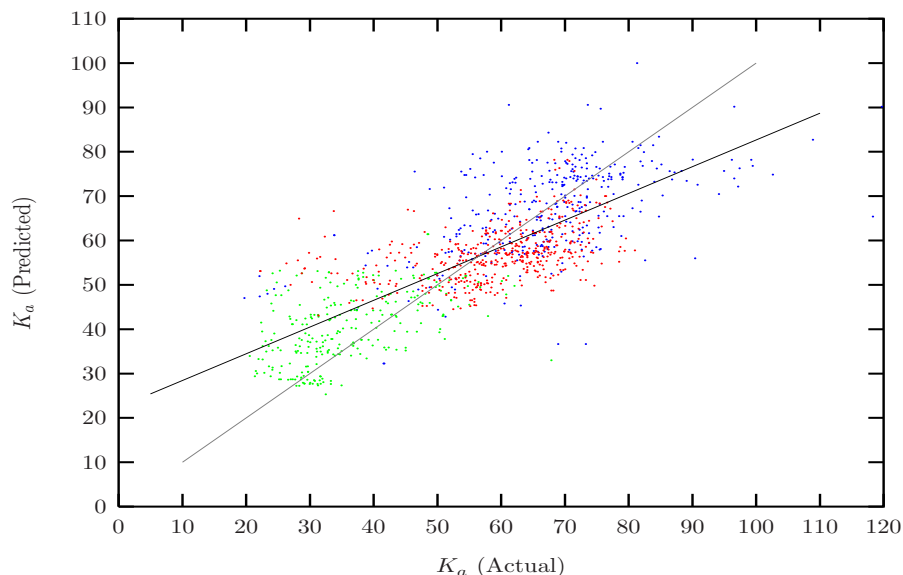


Figure 8.16: Scatter-plot of the re-sampled actual  $K_a$  in Figure 8.14 (b) and the predicted  $K_a$  in Figure 8.14 (a). The straight black line is the line that best fits the points in a least squares sense. The straight grey line shows the best fitted line in the case  $R^2 = 1$ . The dots are assigned colours according to their geographical distribution determined by the classification in Figure 8.12 (b) in Ladegaards Enge 3 June 1997.

the model has difficulties separating the return caused by the soil moisture from the return due to vegetation multiple scatter. This is also reflected in Figure 8.17 where the return from the restored C- and L-band polarized EMISAR data in Figure 8.2 is plotted against the estimated  $K_a$  in Figure 6.22. As we see there is a weak correlation between the amplitude and  $K_a$  for  $K_a > 50$ . However, for  $K_a < 50$  corresponding to the dry sub-area III no correlation exists. This was possibly due to the dense vegetation in sub-area III, which was less transparent to the C- and L-band. Especially for CVV we note the high amplitudes for  $K_a < 30$ . These high amplitudes were possibly due to the previously mentioned interaction between the ears of *Alopecurus pratensis* and the C-band VV polarization.

In order to assess how much the presence of vegetation cover affected the soil moisture estimates various models have been proposed. Dubois *et al.* (1995) [26] developed an empirical model for the retrieval of soil moisture and Ji *et al.* (1996) [37] applied that model under near bare field conditions using C- and

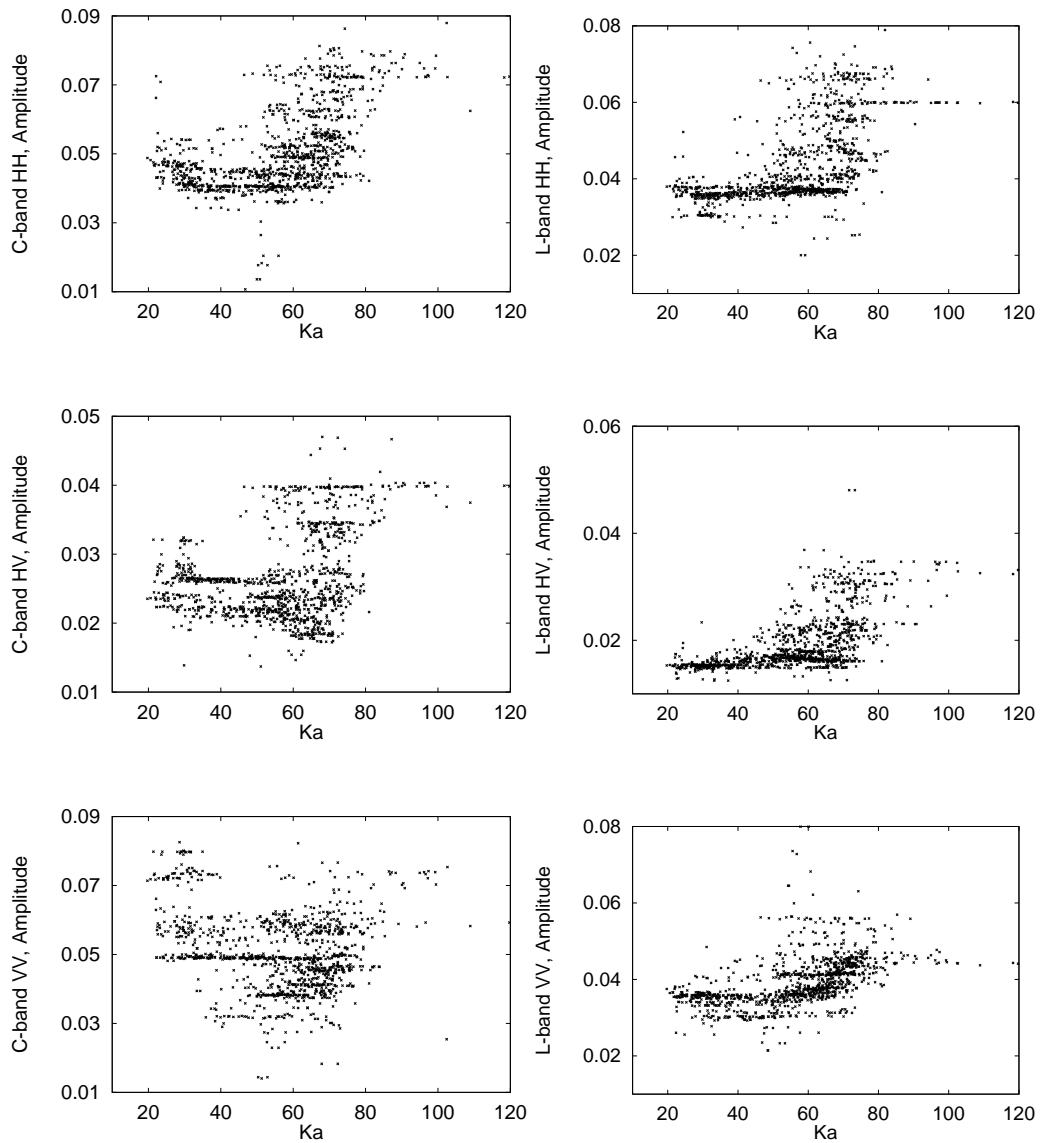


Figure 8.17: The restored and geometrically rectified polarimetric C- and L-band EMISAR data in Figure 8.2 plotted against the actual  $K_a$ . The  $K_a$  values are displayed in Figure 6.22 covering Ladegaards Enge 3 June 1997.

L-band polarized EMISAR data. A criterion for the model to provide accurate soil moisture estimates is that the L-band HV/VV ratio is less than  $-11$  dB.

With the exception of a few pixels this criterion was unfortunately not met at Ladegaards Enge where the L-band HV/VV ratio according to Figure 8.5 was mostly larger than  $-8$  dB. Another criterion for separating the contributions from the soil and vegetation suggests the dry biomass to be less than  $0.5$  kg/m<sup>2</sup> using the polarized L-band [35]. Again this criterion was not met according to Table 6.1. Here the dry biomass within Ladegaards Enge was greater than  $0.7$  kg/m<sup>2</sup>. In case the criteria above had been fulfilled the co-polarized L-band HH/VV ratio could be used for soil moisture retrieval [26]. However, as demonstrated the test site probably was too vegetated. This is also indicated in Table 8.5 where the contribution from the L-band HH/VV ratio is negligible. This suggests that a very detailed knowledge of e.g. the architecture of the vegetation and its biomass is required in order to improve the model and the prediction of  $K_a$ .

## 8.5 Unsupervised classification of EMISAR data

While the classes (clusters) were selected in advance in MDA we now seek the natural grouping of the observations in a predetermined number of clusters. The unsupervised classification of the observations is performed using Cluster Analysis (CA). For a brief introduction to cluster analysis refer to Section 3.6.2.

In Figure 8.18 (a) is shown the geographical distribution of three clusters using the nine measured and derived variables listed on page 178. It is hereby possible to compare the unsupervised result in Figure 8.18 (a) with the supervised result in Figure 8.12. In order to point out that the clusters in Figure 8.18 (a) are possibly due to other physical properties than the ones separating the three sub-areas in Section 8.2 and 8.3 the clusters are presented in grey levels. The darkest grey level represents cluster 1, the intermediate grey level cluster 2 and the brightest grey level cluster 3.

It is noticeable that the distribution of clusters in Figure 8.18 (a) to a large extent reflects the field experiences. Cluster 1 is located in the part of the test site that is less humid, corresponding to sub-area II and III and cluster 2 is located in the swampy sub-area I. Except for two single pixels, cluster 3 coincides with the small plant community of *Glyceria fluitans* (8) in Figure 6.3. Significant at the 0.0001 level the observed over all  $R^2$  for testing of the *null hypothesis*  $H_0$  that all three clusters have equal means is 0.44. This value is only slightly better than the  $R^2$  values 0.42 and 0.35 derived in the Sections 8.2

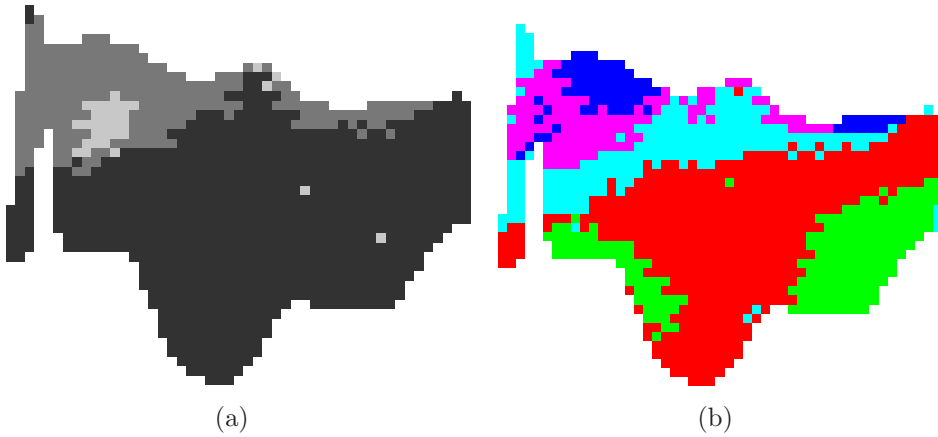


Figure 8.18: Unsupervised classification using cluster analysis of the geometrically rectified C- and L-band EMISAR data covering Ladegaards Enge 3 June 1997. In (a) all nine variables given on page 178 are used in the analysis. Here the darkest grey level represents cluster 1, the intermediate grey level cluster 2 and the brightest grey level cluster 3. In (b) the variables CVV, CHH, LVV and LHV and LHH are used in the clustering. The red colour represents cluster 1, cyan cluster 2, magenta cluster 3, blue cluster 4 and green cluster 5. One pixel corresponds to  $\sim 9.25 \text{ m}^2$ .

and 8.3. One explanation of the improved separation is that cluster analysis is well suited for outlier detection. One of the clusters could hold the outliers and according to Figure 8.18 (a) the single pixels in cluster 3 are probably outliers. Another explanation for the improved separation is that the observations in CA are assigned to the nearest centroid, which not necessarily is the case when the analysis is based on data from the training areas.

The canonical variates CAN1 and CAN2 of the clusters in Figure 8.18 (a) are illustrated in Figure 8.19 and their corresponding eigenvalues and the total sample correlation are listed in Table 8.7. As it appears from Figure 8.19 the first canonical variate CAN1 expresses the difference between cluster 1 and the clusters 2 and 3. According to Table 8.7 (a) the eigenvalue or squared canonical correlation shows that 81% of the variance is accounted for by the first linear discriminant. The second linear discriminant CAN2 discriminates between cluster 2 and 3 and from the corresponding eigenvalue we note that only 38% of the variance is explained.

An examination of the total sample correlations CAN1 between the first canon-

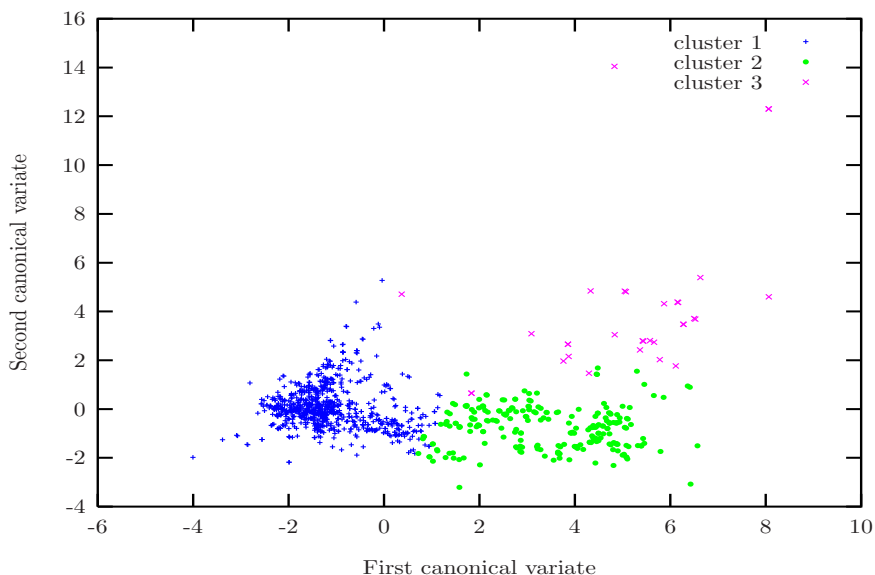


Figure 8.19: Linear discriminant plot of the three clusters in Figure 8.18 (a). The variables are geometrically rectified C- and L-band polarized EMISAR data covering Ladegaards Enge 3 June 1997, see text page 178. The variables and their canonical correlations are shown in Table 8.7.

ical variables and the original variables in Table 8.7 (b) shows that a major part of the differences between cluster 1 and the clusters 2 and 3 is explained by the variables CHV, CHH, LVV, LHV and LHH. The same variables played a major role in the discriminatory power of CAN1 in Table 8.2 (b). For further discussion refer to Section 8.2.

In an attempt to discover new classes five clusters instead of three are chosen in the clustering in Figure 8.18 (b). This will also reduce the disturbing effect of outliers. The variables now used are CVV, CHH, LVV, LHV and LHH because of their large discriminating power in CDA, MDA and MRA in the sections 8.2 8.3 and 8.4. Due to the selected variables the location of the clusters in Figure 8.18 (b) are expected to more or less reflect the location of the sub-areas in Figure 8.1. On the whole the colours of the clusters are therefore chosen to reflect the colours of the sub-areas they are located in. The red cluster 1 consequently corresponds to sub-area II, the cyan, magenta and blue clusters 2, 3 and 4 correspond to sub-area I and the green cluster 5 corresponds to sub-area III.

The observed over all  $R^2$  is 0.70, which is significant at the 0.0001 level. With



	Canonical Correlation	Adjusted Canonical Correlation	Approximate Standard Error	Squared Canonical Correlation
1	0.9001	0.8993	0.0057	0.8102
2	0.6148	0.6119	0.0186	0.3779

(a)

Variable	CAN1	CAN2
CVV	0.3237	-0.0759
CHV	0.7907	-0.1473
CHH	0.7768	-0.3562
LVV	0.6483	-0.6096
LHV	0.9396	0.0435
LHH	0.8910	-0.1957
LHV/LVV	0.6300	0.7428
LHH/LVV	0.5267	0.5452
$\angle$ LHH-LVV	-0.2658	0.0114

(b)

Table 8.7: (a) The squared canonical correlations and (b) the total sample correlations between the canonical variables and the original variables. The sample represents the grouping of the observations from Ladegaards Enge into the three clusters in Figure 8.18 (a) using cluster analysis. The variables are geometrically rectified C- and L-band polarized EMISAR data covering Ladegaards Enge 3 June 1997, see text page 178.

that  $H_0$  is rejected and it is concluded that the clusters have different means. Obviously, this  $R^2$  is larger than any of the previously calculated values but that does not mean that the classes thereby are better separated using five clusters. The reason for the larger value is that  $R^2$  increases with increasing number of classes.

The canonical variates CAN1 and CAN2 of the five clusters are shown in Figure 8.20. The first linear discriminant CAN1 expresses the differences between the clusters 1, 5 and cluster 2 and the clusters 3, 4. The corresponding squared canonical correlation in Table 8.8 (a) shows that 91% of the variance is accounted for by CAN1. The second linear discriminant CAN2 expresses the difference between cluster 5 and the clusters 1, 2 and 4. Here the corresponding eigenvalue in Table 8.8 (a) shows that 60% of the variance is explained by CAN2. Al-

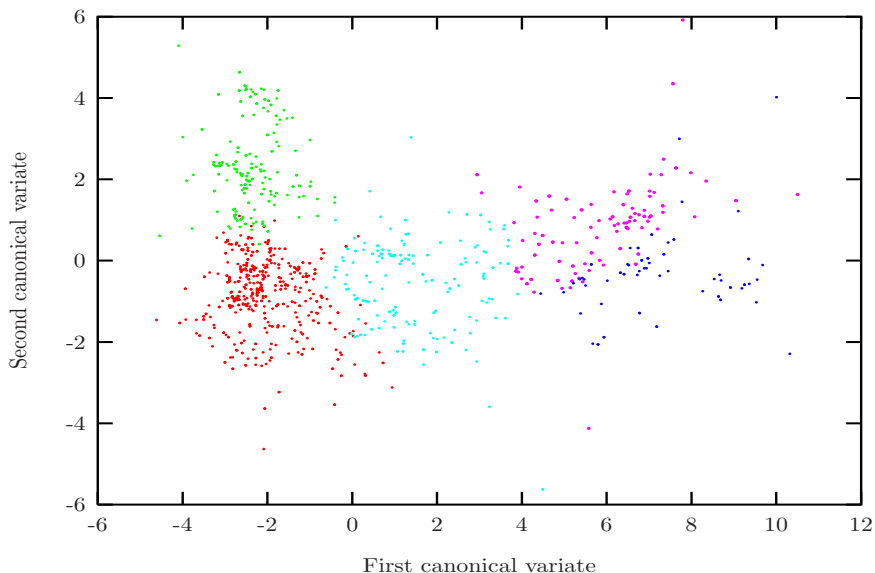


Figure 8.20: Linear discriminant plot of the five clusters in Figure 8.18 (b). The variables are CVV, CHH, LVV, LHV and LHH and their canonical correlations are shown in Table 8.8. The red cluster 1 is located in sub-area II. The cyan, magenta and blue clusters represent cluster 2, 3 and 4, which are located in sub-area I. The green cluster 5 corresponds to sub-area III. The variables are geometrically rectified C- and L-band polarized EMISAR data covering Lade-gaards Enge 3 June 1997, see text page 178.

though the discriminants span four dimensions due to the five clusters, CAN3 and CAN4 are neglected because according to their squared canonical correlations in Table 8.8 (a) they are of less significance.

The total sample correlations between the first canonical variables and the original variables in Table 8.8 (b) show that the discriminatory power of CAN1 most widely is due to CHH, LVV, LHV and LHH. We find that the same variables had a significant discriminatory power in CAN1 in the CDA in Section 8.2. From Table 8.8 (b) we note that the discriminatory power of CAN2 almost solely is concentrated in CVV. Not surprisingly CVV also played a central role in the discriminatory power of CAN2 in Section 8.2. Here it was argued that the high CVV in sub-area III to a large extent was due to the ears of *Alopecurus pratensis*.

As we see the distribution of clusters in Figure 8.18 (b) largely reflects the dis-

	Canonical Correlation	Adjusted Canonical Correlation	Approximate Standard Error	Squared Canonical Correlation
1	0.9556	0.9553	0.0026	0.9132
2	0.7735	0.7723	0.0120	0.5983
3	0.5709	0.5699	0.0202	0.3259
4	0.2046	0.2032	0.0287	0.0419

(a)

Variable	CAN1	CAN2	CAN3	CAN4
CVV	0.2810	0.9208	0.1715	-0.1992
CHH	0.8259	-0.0277	0.0632	-0.3879
LVV	0.7795	-0.1979	0.3464	-0.2008
LHV	0.9268	0.0025	-0.3463	0.0457
LHH	0.9257	-0.1144	0.1662	0.3073

(b)

Table 8.8: (a) The squared canonical correlations and (b) the total sample correlations between the canonical variables and the original variables. The sample represents the unsupervised classification of the test site at Ladegaards Enge in Figure 8.18 (b) using cluster analysis. The variables are geometrically rectified C- and L-band polarized EMISAR data covering Ladegaards Enge 3 June 1997, see text page 178.

tribution of vegetation communities in Figure 6.3. Furthermore it is noticeable that the green dots in cluster 5 in Figure 8.18 (b) seem to comprise three clusters as in Figure 8.10. As explained in Section 8.2 these clusters probably are due to various plant communities within sub-area III.

## 8.6 Discussion

In this chapter the relation between the *in situ* data collected in the small wetland environment at Ladegaards Enge and the polarized C- and L-band EMISAR data, see text on page 178, has been analyzed. The *in situ* data for the investigation are the apparent dielectric constant  $K_a$  and the dominant species of vegetation presented in Chapter 6 covering the test site 3 June 1997.

In the initial phase of the analyses Principal Components (PC) in Section 8.1 were used to explore the structure and redundancy in the multivariate data set. The scatter-plots in Figure 8.7 proved the existence of structure and in Figure 8.8 it was made probable that the structure to a large extent is ascribed by the three sub-areas in the test site of varying soil moisture and vegetation characteristics. In terms of the redundancy in the multivariate data it turned out that 92.5% of the variance is accounted for by the first five PC. This indicates that the “real” dimensionality of the multi-variate data set is closer to 5 than 9. The principal components PC4, . . . , PC9 account for 23.0% of the information carrying variance and their geographical distributions are shown in Figure 8.9. The structure in these remaining PC indicates that a significant amount of information is embedded in the polarimetric EMISAR data besides what can be explained by the collected *in situ* data.

The dividing of the test site into three sub-areas was additionally supported by the supervised classification using Multiple Discriminant Analysis (MDA) in Section 8.3. Here the error rate of the total number of observations correctly assigned within the three training areas was only 6.6% and none of the observations were assigned the reject class. In general the classified result in Figure 8.12 reflects the conditions at Ladegaards Enge 3 June 1997 remarkably well.

An unsupervised classification of the test site was in Section 8.5 performed using Cluster Analysis (CA). Using all nine variables and three clusters the classification in Figure 8.18 (a) to a large extent reflects the conditions in the test site at Ladegaards Enge. However, due to the high dimensionality of the multivariate data set and the relatively small number of observations some uncertainty in the clustering is expected [9]. In order to reduce this problem and the disturbing effect of outliers, the classified result in Figure 8.18 (b) was based on five clusters and only five variables. Here the reduced number of variables were selected due to their high discriminatory power in Section 8.2. Using these variables the correspondence between the clusters in Figure 8.18 (b) and the classes in Figure 8.12 is expected.

It is interesting that the blue swampy sub-area I in Figure 8.12 according to the CA in fact comprises three sub-areas. These three sub-areas correspond to the cyan, magenta and blue clusters 2, 3 and 4 in Figure 8.18 (b). This is in perfect accordance with the field experience, where the clusters 3 and 4 are located in an area with standing water and cluster 2 is located in a swampy area without standing water.

According to Section 8.2 evidence suggested that the polarized frequencies were affected by the soil moisture at Ladegaards Enge. This was valid for sub-area II and in particular for sub-area I. However, as shown in Section 8.4 the test site was too vegetated for reliable soil moisture estimates to be made using the

empirical model for soil moisture retrieval introduced by Dubois *et al.* (1995) [26]. Due to the complexity introduced by the vegetation the vegetation characteristics therefore have to be well explained in order to separate the return due to soil moisture from the return due to vegetation. However, as the predicted  $K_a$  in Figure 8.14 (a) shows, the vegetation multiple scattering seems to reflect the actual soil moisture quite well. The explanation for this is that the various plant communities require specific soil moisture conditions, which again are reflected in the plant species.

Because the three sub-areas had different soil moisture contents this implies that also the vegetation characteristics in the sub-areas were different. As shown in Section 8.2 strong evidence suggested that this difference in vegetation characteristics resulted in different backscattering coefficients from the sub-areas. Here the C-band HV and VV and the L-band VV, HV and HH polarizations discriminated between sub-area I and the sub-areas II and III. The C-band VV and HV polarizations discriminated between sub-area II and III. To a smaller extent the L-band HH-VV phase difference also discriminated between the three sub-areas. The phase difference within sub-area II was larger than in sub-area I, which is surprising because rush in a wet area normally provides excellent conditions for double-bounce scattering to occur. However, the straws or rush in sub-area I were randomly orientated, whereas in sub-area II the straws were ranging from oblique to vertical with an approximate length of 20 cm.



# EMISAR data versus Mols Bjerge

---

The *in situ* data collected at Mols Bjerge were presented and analyzed in Chapter 7. The objective of this chapter is to analyze the relation between these *in situ* data and the one-look C- and L- band polarimetric EMISAR data. The fieldwork within Mols Bjerge was performed 4 June 1997, which was coincident with the overflight by EMISAR making an acquisition at C-band (5.30 GHz). The day before, the EMISAR had made an acquisition at L-band (1.25 GHz).

Within Mols Bjerge the three test sites of interest are located at Trehøje, Benlighøj and Stenhøje. Each of these grassland areas was selected in terms of their homogeneity when it comes to vegetation cover and soil moisture conditions. However, the volumetric structure of the above ground biomass, the plant species and possibly the biomass in the three test areas were different. The *in situ* data to be used are primarily the volumetric structure of the above ground biomass content and the vegetation characteristics of the dominant plant species.

For an aerial view of the three test areas refer to the ortho-photos in Figures 7.2 and 7.3. The three test sites are in Figure 9.1 assigned the colours red, green and blue and in the succeeding analyses they represent Trehøje, Stenhøje and Benlighøj respectively. Trehøje test site covers 6854 m<sup>2</sup> and was an old aban-

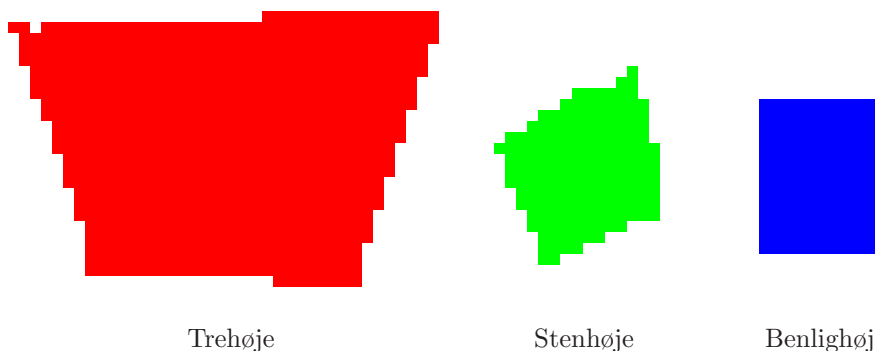


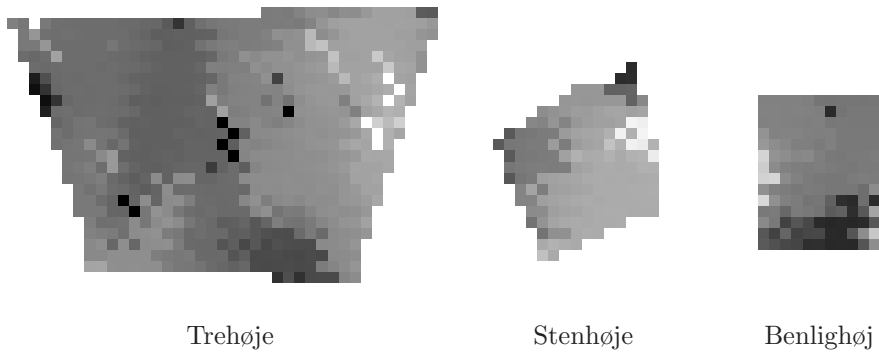
Figure 9.1: The colours of the training areas or classes, which represent the three test sites at Mols Bjerge.

doned grassland dominated by the dense and tangled vegetation of *Deschampsia flexuosa*. This area had the largest volume of above ground biomass and is illustrated in Figure 7.4 (a). The test area at Stenhøje covers 1545 m<sup>2</sup> and is shown in Figure 7.4 (b). Here the vegetation was green and vigorous and the dominant species of vegetation was *Festuca rubra*. Benlighøj test site is displayed in the Figures 7.5 (a)–(b) and covers 1425 m<sup>2</sup>. It was a grazed area with low vegetation and manure from cattle and the prevailing plant species was *Deschampsia flexuosa*.

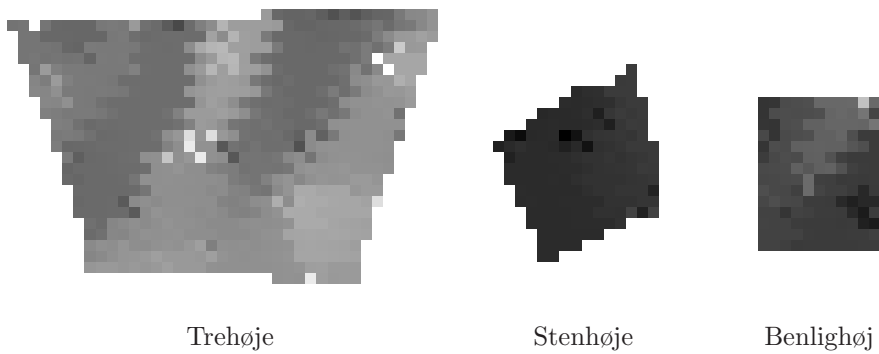
In order to match the EMISAR data with the collected *in situ* data the EMISAR data are geometrically rectified to the UTM system zone 32 ED(50). For re-sampling bilinear interpolation is applied. For a brief description of geometrical transformations and sampling strategies of GCP refer to Section 3.3. The nearby surroundings of the three test sites were quite similar to the conditions within the test areas. Using (3.8) the observed or measured geometric error  $\hat{\sigma}_o^2$  of the re-sampling is 2.3 m<sup>2</sup> in both the Northern and Eastern directions. The relatively large test areas taken into consideration  $\sigma_o^2$  is therefore negligible.

In Section 5.7 the Gamma *pixel prior* implemented in a SA algorithm was seen to be convincing in terms of restoring fine structures and preserving homogeneous regions. The three test sites at Mols Bjerge were all relatively homogeneous and the Gamma *pixel prior* and the SA algorithm are therefore used in the restorations of CVV, CHV, CHH, LVV, LHV and LVV. These restored and geometrically rectified EMISAR amplitude data corresponding to the three test areas are presented in Figures 9.2, 9.3 and 9.4. A graphical representation of the mean amplitudes of the restored EMISAR data is given in Figure 9.5.



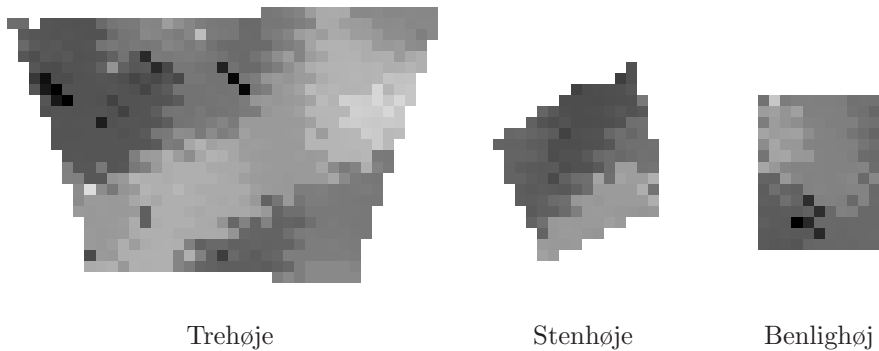


(a) C-band VV

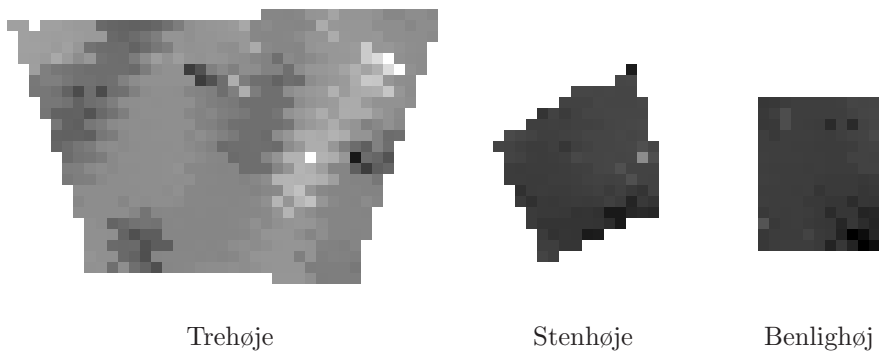


(b) L-band VV

Figure 9.2: Restored C- and L-band VV polarized EMISAR amplitude data using the Gamma *pixel prior* in a simulated annealing algorithm. The data are geometrically rectified and cover the three test sites at Mols Bjerger 3 and 4 June 1997. One square corresponds to  $\sim 9.25 \text{ m}^2$  and the three test areas are stretched linearly among their mean  $\pm 3.5$  std.

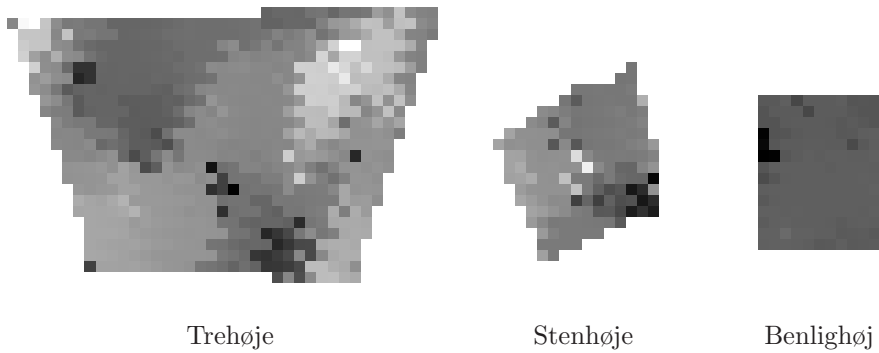


(a) C-band HV

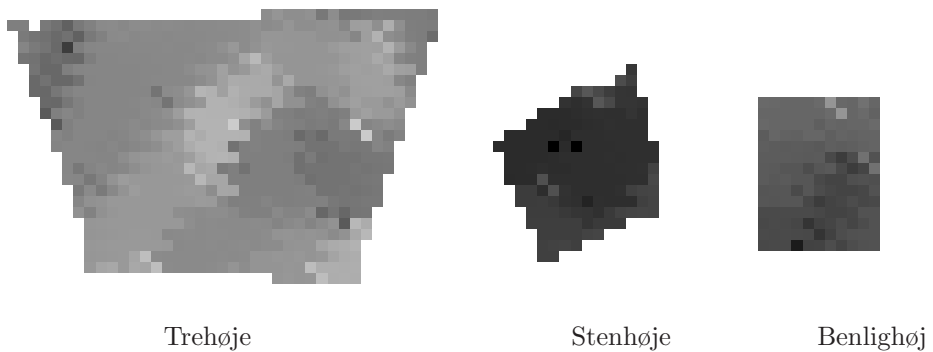


(b) L-band HV

Figure 9.3: Restored C- and L-band HV polarized EMISAR amplitude data using the Gamma *pixel prior* in a simulated annealing algorithm. The data are geometrically rectified and cover the three test sites at Mols Bjerger 3 and 4 June 1997. One square corresponds to  $\sim 9.25 \text{ m}^2$  and the three test areas are stretched linearly among their mean  $\pm 3.5$  std.



(a) C-band HH



(b) L-band HH

Figure 9.4: Restored C- and L-band HH polarized EMISAR amplitude data using the Gamma *pixel prior* in a simulated annealing algorithm. The data are geometrically rectified and cover the three test sites at Mols Bjerge 3 and 4 June 1997. One square corresponds to  $\sim 9.25 \text{ m}^2$  and the three test areas are stretched linearly among their mean  $\pm 3.5$  std.

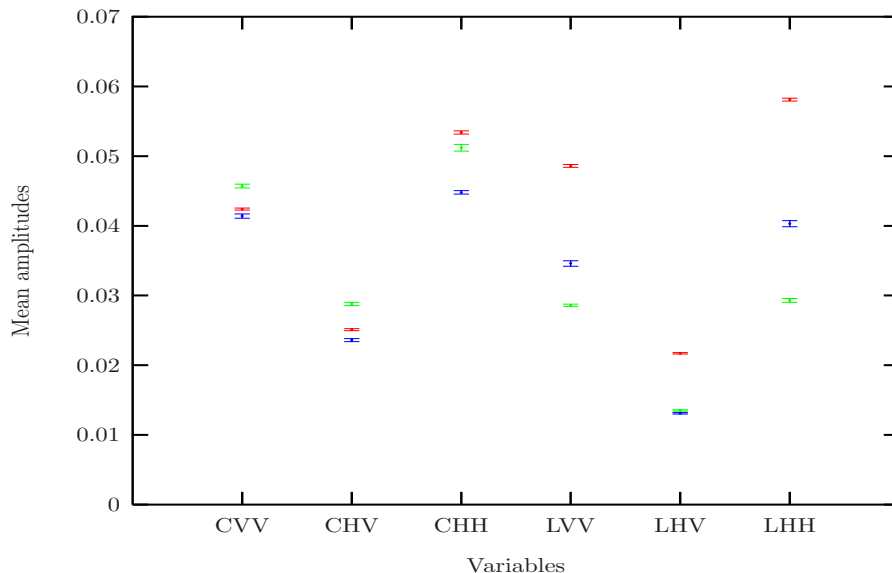


Figure 9.5: Mean amplitudes for the restored and geometrically rectified polarized C- and L-band EMISAR data covering the three test sites at Mols Bjerge 3 and 4 June 1997. The geographical distribution of the restored and geometrically rectified EMISAR data is shown in Figures 9.2, 9.3 and 9.4. The red colour represents Trehøje, the green colour represents Stenhøje and blue represents Benlighøj. The errorbars indicate the standard deviation of the mean amplitudes.

Besides the restored amplitudes important information is also carried by the amplitude ratios and phase differences, see Section 1.2.1. The analyses therefore include restored LHV/LVV and LHH/LVV ratios and lowpass filtered  $\angle$ LHH-LVV. These geometrically rectified data are presented in Figures 9.6 and 9.7, where the data are stretched linearly between the mean amplitude of the three test areas  $\pm 3.5$  std. After re-sampling one pixel corresponds to  $\sim 9.25$  m<sup>2</sup>.

In order to explore the relation between the *in situ* data and the geometrically rectified EMISAR data the following preliminary multivariate analyses are carried out: In Section 9.1 Principal Components (PC) are used to study the information bearing variances of the multi-dimensional EMISAR data. The synergy between the *in situ* data and the polarized EMISAR data is explored in Section 9.2 using Canonical Correlation Analysis (CDA). A supervised classification of the three test sites at Mols Bjerge is performed in Section 9.3 using Multiple Discriminant Analysis (MDA). The multivariate data set again comprises the

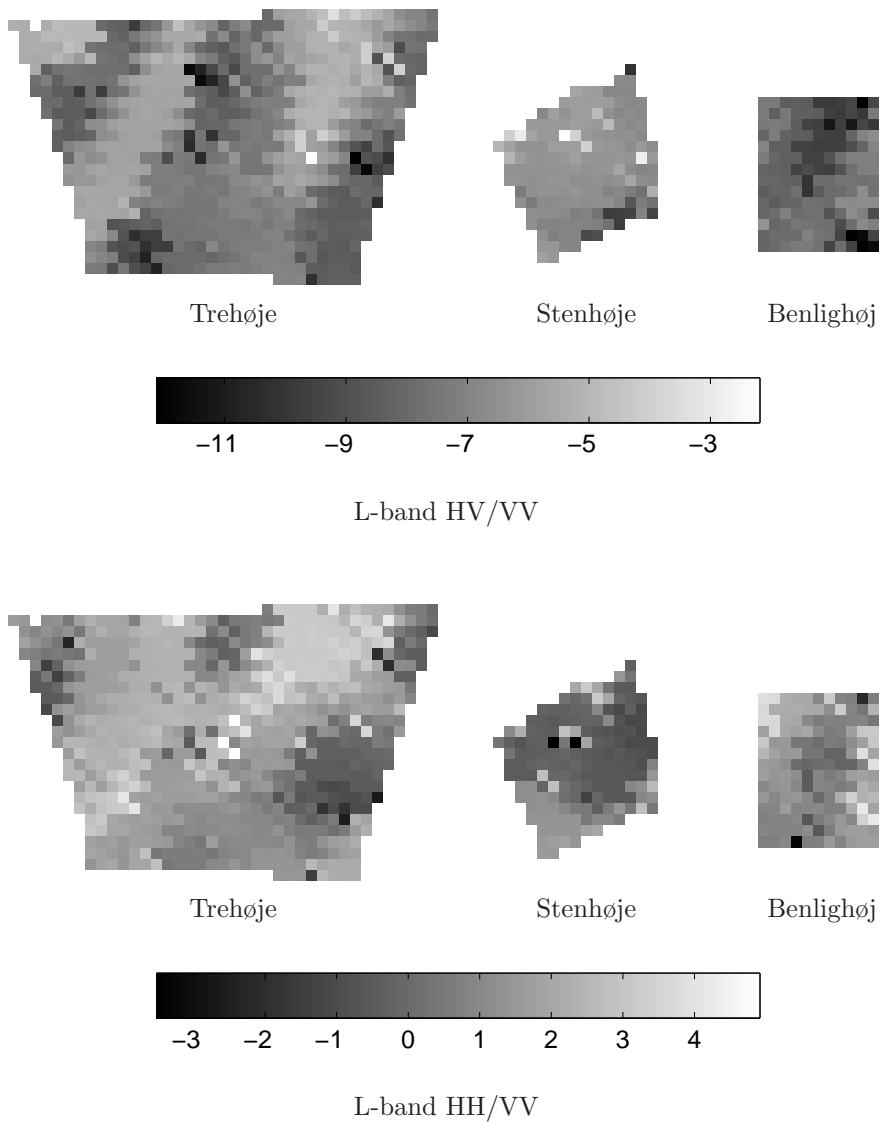


Figure 9.6: Restored and geometrically rectified L-band ratios within the three test sites at Mols Bjerge 3 June 1997. HV/VV and HH/VV are indicated by the dB scales and one pixel corresponds to  $\sim 9.25 \text{ m}^2$ .

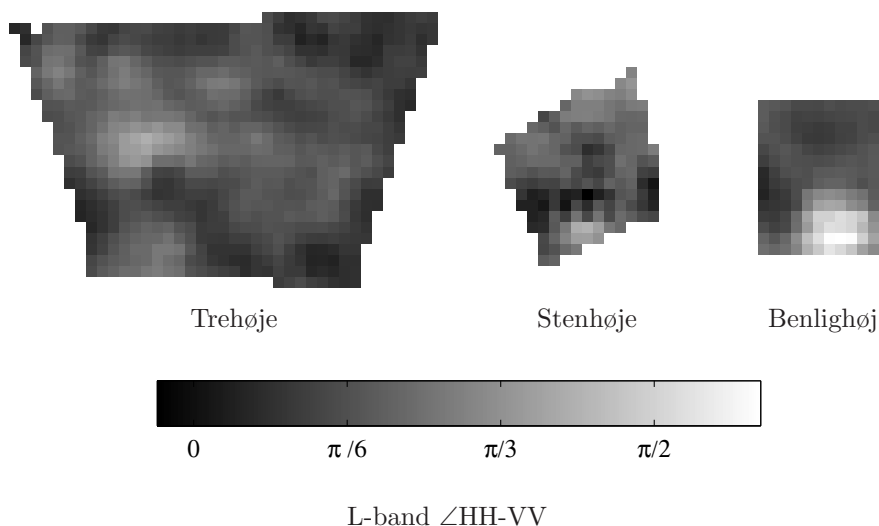


Figure 9.7: Geometrically rectified phase differences between L-band HH-VV data within the test sites at Trehøje, Benlighøj and Stenhøje at Mols Bjerge 3 June 1997.  $\angle\text{LHH-LVV}$  is stretched linearly between  $-0.11$  rad and  $1.93$  rad. One pixel corresponds to  $\sim 9.25$  m<sup>2</sup>.

variables CVV, CHV, CHH, LVV, LHV, LHH, LHV/LVV, LHH/LVV and  $\angle\text{LHH-LVV}$ . The variables are standardized to zero mean and variance one.

## 9.1 Principal components

Correlated multi-band data often possess a significant amount of redundancy. Principal Components (PC) is a multivariate technique used to remove this redundancy by simplifying the correlation structure in multivariate data. For a brief description of PC refer to Section 3.5.1.

The variables transformed into the PC space are listed on page 216 and in Figure 9.8 are shown scatter-plots of various combinations of PC. Starting in the upper left corner going right the scatter-plots are: PC1/PC2, PC1/PC3, ..., PC4/PC5. The colours used in the plots magenta-blue-cyan-green-yellow and red represent the number of hidden observations 0, 1, 2, 3, 4 and  $> 4$ .



Figure 9.8: Scatter-Plots of variables transformed into the principal component space. The variables are restored geometrically rectified C- and L-band polarized EMISAR amplitude data from the three test sites at Trehøje, Benlighøj and Stenhøje at Mols Bjerge 3 and 4 June 1997, see text page 216. Starting in the upper left corner going right the scatter-plots are: PC1/PC2, PC1/PC3, ..., PC4/PC5. The colours magenta-blue-cyan-green-yellow and red represent the number of hidden observations 0, 1, 2, 3, 4 and  $> 4$

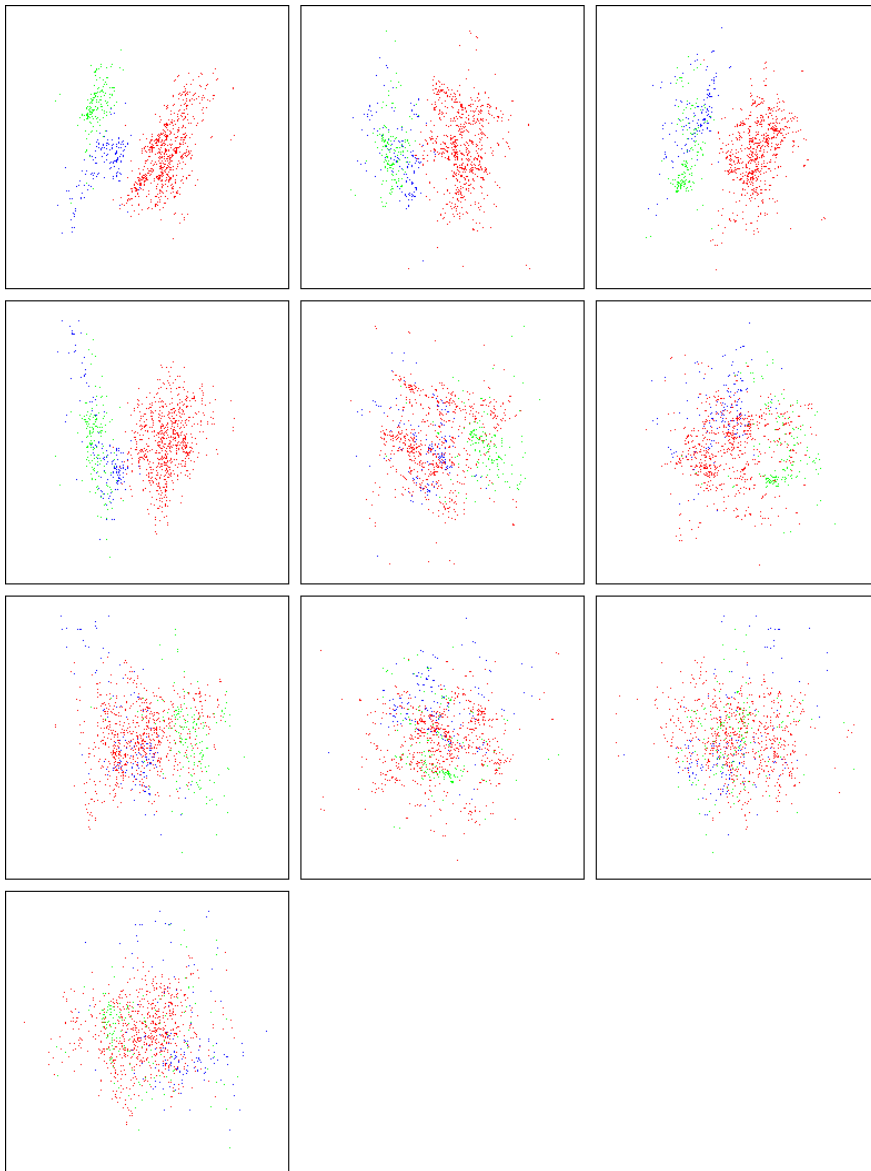


Figure 9.9: Scatter-Plots of variables transformed into the principal component space. The variables are restored geometrically rectified C- and L-band polarized EMISAR-data from the three test sites at Trehøje, Benlighøj and Stenhøje at Mols Bjerge 3 and 4 June 1997, see text page 216. Starting in the upper left corner going right the scatter-plots are: PC1/PC2, PC1/PC3, . . . , PC4/PC5. The red dots represent Trehøje, the green dots represent Stenhøje and the blue dots Benlighøj.



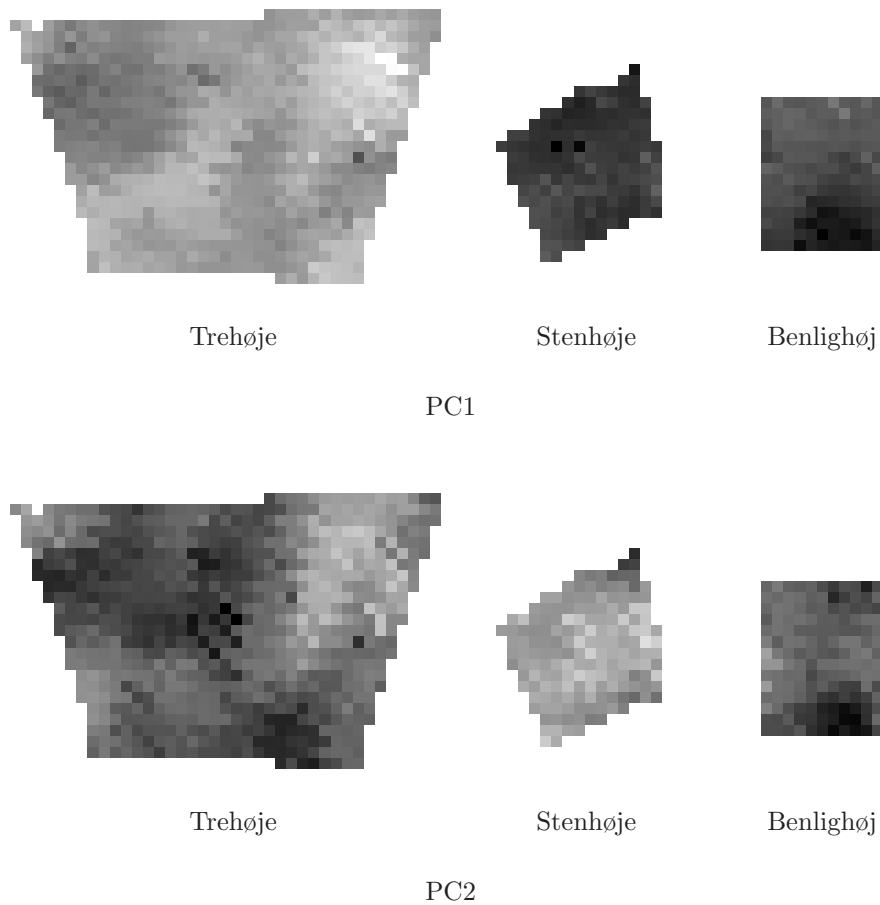


Figure 9.10: Geographical distribution of the principal components PC1 and PC2 within the three test sites at Mols Bjerge. The variables are restored geometrically rectified C- and L-band polarized EMISAR amplitude data from 3 and 4 June 1997, see text page 216. One pixel corresponds to  $\sim 9.25 \text{ m}^2$  and the three test areas are stretched linearly among their mean  $\pm 3.5$  std.

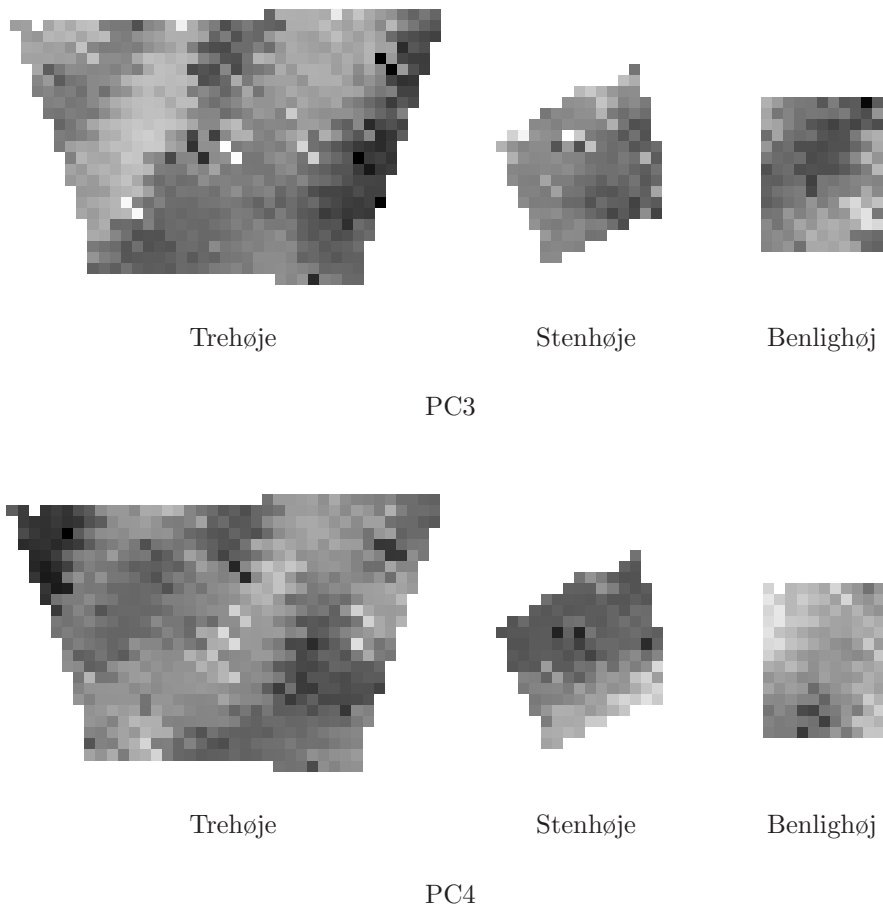


Figure 9.11: Geographical distribution of the principal components PC3 and PC4 within the three test sites at Mols Bjerge. The variables are restored geometrically rectified C- and L-band polarized EMISAR amplitude data from 3 and 4 June 1997, see text page 216. One pixel corresponds to  $\sim 9.25 \text{ m}^2$  and the three test areas are stretched linearly among their mean  $\pm 3.5$  std.

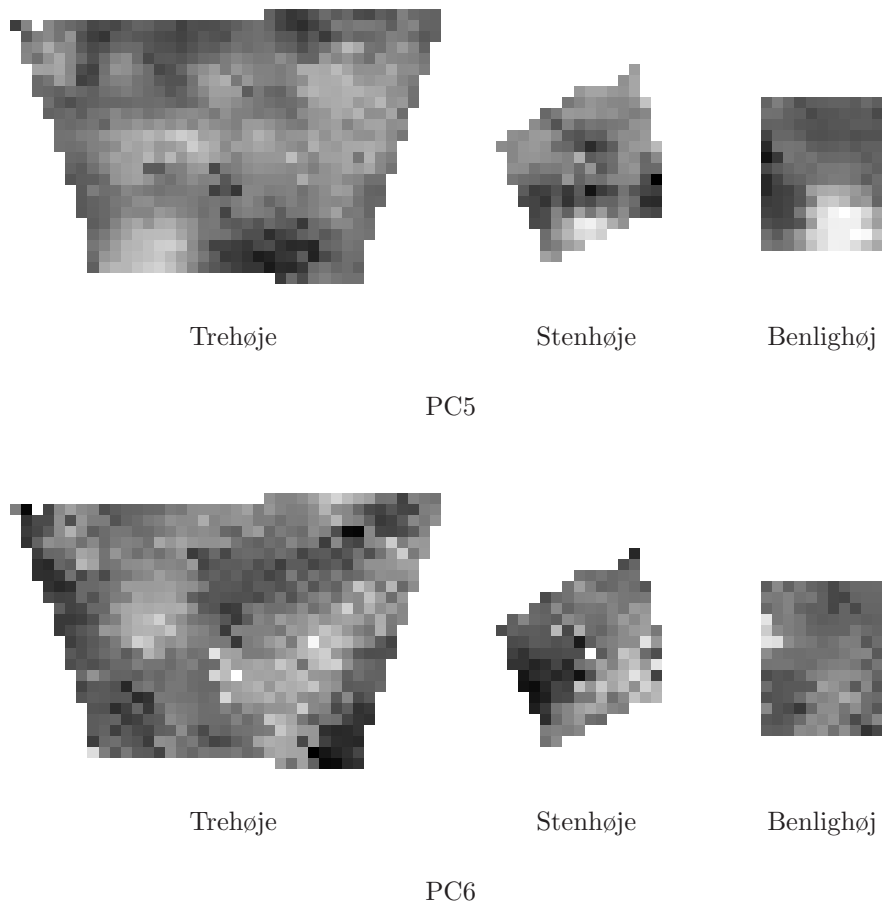


Figure 9.12: Geographical distribution of the principal components PC4 and PC5 within the three test sites at Mols Bjerge. The variables are restored geometrically rectified C- and L-band polarized EMISAR amplitude data from 3 and 4 June 1997, see text page 216. One pixel corresponds to  $\sim 9.25 \text{ m}^2$  and the three test areas are stretched linearly among their mean  $\pm 3.5$  std.

	Eigenvalue	Difference	Proportion	Cumulative
1	3.1686	1.5180	0.3521	0.3521
2	1.6507	0.2186	0.1834	0.5355
3	1.4321	0.4355	0.1591	0.6946
4	0.9966	0.2516	0.1107	0.8053
5	0.7449	0.2036	0.0828	0.8881
6	0.5414	0.0951	0.0602	0.9483
7	0.4462	0.4352	0.0496	0.9978
8	0.0111	0.0027	0.0012	0.9991
9	0.0084		0.0009	1.0000

(a)

Variable	PC1	PC2	PC3	PC4	PC5	PC6
CVV	0.0339	0.6028	-.3105	0.1348	0.0936	0.2360
CHV	0.3009	0.2460	-.2065	0.5366	0.2907	0.3054
CHH	0.3037	0.3585	0.0526	-.2514	0.4623	-.7018
LVV	0.4429	-.3057	-.3380	-.2139	0.0373	0.0949
LHV	0.4932	-.0292	0.1194	-.3699	-.0232	0.3481
LHH	0.4993	-.3043	0.0356	0.1467	0.0044	-.0364
LHV/LVV	0.1005	0.3976	0.6200	-.2865	-.0904	0.3328
LHH/LVV	0.2182	-.1003	0.5512	0.5841	-.0532	-.1803
$\angle$ LHH-LVV	-.2639	-.3043	0.2006	-.0588	0.8247	0.2895

(b)

Table 9.1: Eigenvalues and eigenvectors from the principal component analysis. The variables are geometrically rectified C- and L-band polarized EMISAR-data from the test sites at Trehøje, Benlighøj and Stenhøje 3 and 4 June 1997, see text page 216. In (a) the eigenvalues are listed in descending order and in (b) the eigenvectors corresponding to the six highest eigenvalues are given in the basis vectors of the original variables.

The linear transforms of the original variables with the largest variation are the first two linear transforms PC1 and PC2. It is therefore not surprising that the scatter-plot PC1/PC2 in Figure 9.8 is the plot that exhibits most structure. The remaining scatter-plots PC1/PC3, ..., PC4/PC5 possess less structure i.e. smaller variance.

As it appears from the PC1/PC2 scatter-plot in Figure 9.8 the observations seem to form three clusters in the PC space. For our purpose it is of particular interest to know how these clusters are geographically distributed throughout the three test areas at Mols Bjerge. A natural step is therefore to investigate if the three clusters in fact represent the three test sites. In order to pursue that objective observations from the test sites at Trehøje, Benlighøj and Stenhøje are assigned the colours red, green and blue and the variables on page 216 are again transformed into the PC space.

This is illustrated in Figure 9.9 and because the colours in the PC1/PC2 scatter-plot are located in the three clusters we assume that the three clusters represent the three test sites. The geographical distribution of the principal components PC1, ..., PC6 is illustrated in the Figures 9.10, 9.11 and 9.12. In Table 9.1 (a) we see that 35.2% of the variance is accounted for by PC1 and according to Figure 9.9 and the PC1/PC2 scatter-plot, PC1 is excellent in terms of separating Trehøje from Benlighøj and Stenhøje. Referring to Table 9.1 (b) and the first eigenvector we note that the variables responsible for most of the variance are the L-band polarizations VV, HV and HH. The distribution of PC1 within the three test sites is shown in Figure 9.10 and here it is obvious that the Trehøje test site stands out.

We see from Table 9.1 (a) that 18.3% of the information bearing variance is carried by PC2 and according to the PC1/PC2 scatter-plot in Figure 9.9 PC2 is satisfactory in discriminating between Stenhøje and Benlighøj. This is also reflected by PC2 in Figure 9.10. The variable responsible for most of the variance is according to the second eigenvector in Table 9.1 (b) the C-band VV polarization.

Certain reservations have to be made when PC are applied to SAR data. Although the information is equated to variance the same variance can also be the Achilles' heel of PC. This is e.g. a problem when outliers, which are present in the data to be used, can distort the eigenvalues, see text on page 112. It should be noted, that C- and L-band polarimetric SAR data are statistically uncorrelated whereas the polarized variables in C- and L-band respectively are statistically correlated. However, during the annealing process this correlation is lost and the restored amplitudes within each frequency are therefore statistically uncorrelated.

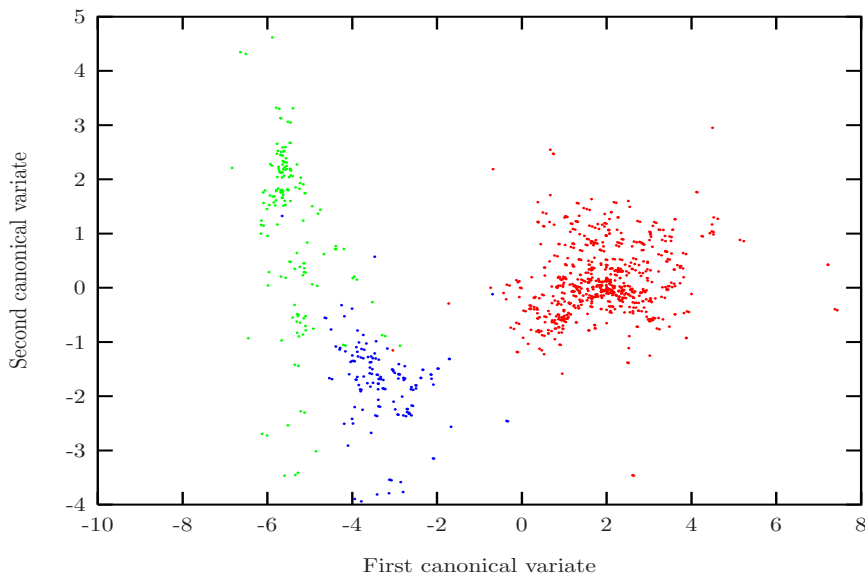


Figure 9.13: Linear discriminant plot for the three test areas at Trehøje, Benlighøj and Stenhøje. The eigenvalues and canonical correlations are shown in Table 9.2 (b). The variables are geometrically rectified C- and L-band polarized EMISAR-data from the test sites at Trehøje, Benlighøj and Stenhøje 3 and 4 June 1997, see text page 216. The red dots represent Trehøje, the green dots Stenhøje and the blue dots Benlighøj.

## 9.2 Synergy between *in situ* data and EMISAR data

In this section the relation between the polarimetric EMISAR data and the prevailing conditions in the test sites at Mols Bjerge is analyzed. In order to make a possible improvement of the separation in Section 9.1 we will in this section make use of Canonical Discriminant Analysis (CDA). For a brief introduction to CDA refer to Section 3.5.2.

The two canonical variates CAN1 and CAN2 of the observations belonging to the three test sites are displayed in Figure 9.13 and their geographical distributions are shown in Figure 9.14. We note that the discriminants span two dimensions due to the three test areas. The colour codes red, green and blue are representing Trehøje, Stenhøje and Benlighøj respectively and the variables and their correlations are listed in Table 9.2 (b).

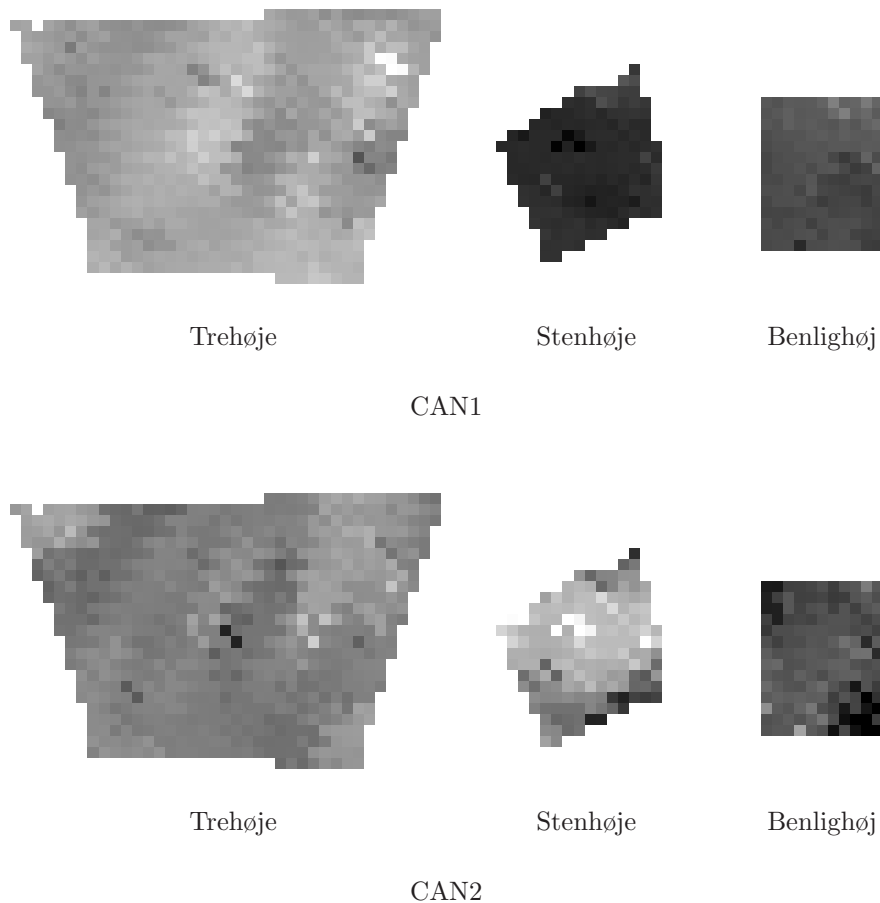


Figure 9.14: The geographical distribution of the first and second canonical variates in Figure 9.13. The variables are geometrically rectified C- and L-band polarized EMISAR-data covering Trehøje, Benlighøj and Stenhøje test sites 3 and 4 June 1997, see text page 216. One pixel corresponds to  $\sim 9.25 \text{ m}^2$  and the three test areas are stretched linearly among their mean  $\pm 3.5$  std.

The first linear discriminant CAN1 in Figure 9.13 discriminates between the three test areas. In particular the difference between Trehøje and the areas Stenhøje and Benlighøj is well expressed. The second linear discriminant CAN2 expresses the difference between Stenhøje and Benlighøj. Referring to Table 9.2 (a) the eigenvalues or squared canonical correlations indicate that 89.8% of the variance is accounted for by CAN1 and 45.2% by CAN2. The observed overall  $R^2$  is 0.33, which is significant at the 0.0001 level. This rejects the *null hypothesis*  $H_0$  that all three test sites have equal means.

The total sample correlations between the first canonical variables and the original variables are listed in CAN1 in Table 9.2 (b). As mentioned previously CAN1 is in particular superior in discriminating between Trehøje and the areas Stenhøje and Benlighøj and according to Table 9.2 (b) this discriminating power to a large extent is ascribed the variables LVV, LHV and LHH. This is in agreement with the corresponding restored mean amplitude levels in Figure 9.5. We recall that the variables LVV, LHV and LHH were also significant in PC1 in Table 9.1 (b) and the geographical distributions of CAN1 and PC1 in the Figures 9.14 and 9.10 are therefore quite similar.

The photo in Figure 7.4 (a) illustrates Trehøje test site, which was characterized by the tussocks of *Deschampsia flexuosa*. As it appears the vegetation was dense, tangled and dominated by randomly oriented stems. The average height of the tussocks was 25 cm and vertical stems of *Carex arenaria* rose approximately 15 cm above the tussocks. The biomass comprised both fresh and withered material of the approximate length  $\sim 20$  cm and we therefore could expect a response from the L-band polarizations. Referring to Figure 9.5 this was also the case. In Table 9.2 (b) the observed correlations for LVV, LHV and LHH are 0.88, 0.89 and 0.94 for CAN1. Here differences in the above ground biomass between Trehøje test site and the areas at Stenhøje and Benlighøj probably explain the discriminating power of the L-band. The dense vegetation at Trehøje was transparent to the L-band, which leads to multiple scattering and thereby higher backscattering coefficient. In particular horizontal stems of length  $\sim 20$  cm seem to have been more frequent in Trehøje test site than in the other two. According to CAN1 in Table 9.2 (b) the C-band polarizations had less discriminating power. This suggests that the difference between Trehøje test site and the areas at Stenhøje and Benlighøj was smaller, when it comes to stems of length  $\sim 6$  cm in the upper part of the vegetation.

Due to the volume scattering in the vegetation, SAR has shown to be well suited for biomass discrimination. The effect from the vegetation is relatively large for the cross-polarized channels and the cross-polarized ratio HV/VV has proved to be a good vegetation index [26]. Vegetation is more transparent to L-band than C-band and because the vegetation cover in the three test sites was relatively high the L-band HV/VV ratio is used. The L-band HV/VV ratio is illustrated in



	Canonical Correlation	Adjusted Canonical Correlation	Approximate Standard Error	Squared Canonical Correlation
1	0.9478	0.9474	0.0031	0.8983
2	0.6721	0.6697	0.0168	0.4517

(a)

Variable	CAN1	CAN2
CVV	-0.2138	0.4066
CHV	0.2710	-0.0217
CHH	0.3115	0.4862
LVV	0.8849	-0.0029
LHV	0.8922	0.3008
LHH	0.9440	-0.0926
LHV/LVV	0.0513	0.5599
LHH/LVV	0.3508	-0.2583
∠LHH-LVV	-0.2198	-0.2406

(b)

Table 9.2: (a) The squared canonical correlations and (b) the total sample correlations between the canonical variables and the original variables. The sample represents the test sites at Trehøje, Benlighøj and Stenhøje at Mols. The variables are geometrically rectified C- and L-band polarized EMISAR data covering Mols Bjerger 3 and 4 June 1997, see text page 216.

Figure 9.6 and here the mean ratio for Trehøje is  $-7.03 \text{ dB} \pm 0.05 \text{ std}$ ,  $-6.51 \text{ dB} \pm 0.08 \text{ std}$  for Stenhøje and  $-8.4 \text{ dB} \pm 0.1 \text{ std}$  for Benlighøj. According to these L-band HV/VV ratios, Stenhøje had the highest biomass content and Benlighøj the lowest. This, however, is not quite consistent with the field experiences and the considerations above where the volume of the above ground biomass at Trehøje was larger than at Stenhøje. The explanation probably is the orientation of the stems, which affected the cross-polarized ratio. At Stenhøje the stems were more likely to be oblique than at Trehøje.

As mentioned above both Stenhøje and Benlighøj can be separated by CAN1 and CAN2. A comparison between the total sample correlations in Table 9.2 (b) and the mean amplitudes in Figure 9.5 shows that the discriminatory power between Stenhøje and Benlighøj expressed by CAN1 to a large extent is due to LVV and LHH. Likewise a comparison between Table 9.2 (b) and Figure 9.5 discloses

that a major part of the discriminatory power between Stenhøje and Benlighøj expressed by CAN2 is ascribed to the variables CVV, CHH and LHV/LVV.

Concerning the L-band VV polarization in Figure 9.5 it is evident that the mean amplitude level for Benlighøj was higher than for Stenhøje. This probably was due to the long stems of *Carex arenaria*, which were frequent at Benlighøj but not found at Stenhøje. The stems of *Carex arenaria* illustrated in Figure 7.5 (b) were vertically oriented and rose approximately 20 cm above the ground. This is coincident with the wavelength of L-band and it is therefore likely that the L-band VV polarization interacted with the stems of *Carex arenaria*. Also the L-band HH polarization had, according to Figure 9.5, great significance in terms of separating Stenhøje from Benlighøj and again the mean amplitude level for Benlighøj is higher than for Stenhøje. This phenomenon most likely was caused by the withered material from *Deschampsia flexuosa* and *Carex arenaria* at Benlighøj, which was mostly horizontal oriented as displayed in the photo in Figure 7.5 (b).

Another explanation for the amplitude level of the test site at Benlighøj to be higher than at Stenhøje for LVV and LHH could be that the actual soil moisture content was higher at Benlighøj than at Stenhøje, see Table 7.2. This is due to the microwave frequencies of the EMISAR, which are strongly sensitive to the dielectric constant  $K_a$  and thereby the soil moisture [35]. However, this explanation is not consistent with the discussion in Section 7.5. Here it was argued that although the actual soil moisture content within the test sites at Stenhøje and Benlighøj was different,  $K_a$  was very much the same due to the different soil constituents.

According to Figure 9.5 and the C-band polarizations CVV, CHV and CHH we note that the mean amplitude level for Stenhøje is higher than for Benlighøj. The reason probably is the ears of *Festuca rubra*, which were present at Stenhøje but almost absent at Benlighøj. The Stenhøje test site is illustrated in the photo in Figure 7.4 (b) and here the stems and ears of *Festuca rubra* were quite prominent. The ears were randomly oriented and had a length of approximately 5 cm and they were therefore likely to interact with the wavelength of C-band polarizations.

A conspicuous feature of Figure 9.13 is that the green dots representing Stenhøje seem to be well separated along CAN2 forming at least three clusters. In accordance with the field experiences this could be explained by the concentration of ears of *Festuca rubra*, which was varying within Stenhøje test site.

The discriminating power of LHV/LVV in CAN2 in Table 9.2 (b) and the LHV/LVV image in Figure 9.6 suggests that the biomass content in Stenhøje test site was larger than at Benlighøj. This is consistent with the experiences

from the field where the volume of the above ground biomass at Stenhøje was larger than at Benlighøj.

In order to assess how much the presence of vegetation cover affects the backscatter contribution from the soil moisture various models have been proposed. Dubois *et al.* (1995) [26] developed a criterion that requires that the L-band HV/VV ratio is less than  $-11$  dB for the model to provide accurate soil moisture estimates. Unfortunately this criterion was not met within any of the three test sites where the mean L-band HV/VV ratio was larger than  $-8.4$  dB. Another criterion for separating the backscatter contributions from the soil and vegetation suggests the dry biomass to be less than  $0.5$  kg/m<sup>2</sup> [35] using the polarized L-band. That criterion was also not met according to Table 7.1 with the reservation that the biomass estimates are uncertain. This is also indicated by the L-band HH/VV ratios, which are displayed in Figure 9.6. The co-polarized ratio decreases with increasing  $K_a$  and is therefore well suited for retrieving soil moisture if the vegetation is sparse [26]. The mean HH/VV ratio for Trehøje is  $1.56$  dB  $\pm 0.04$  std,  $0.17$  dB  $\pm 0.1$  std for Stenhøje and  $1.34$  dB  $\pm 0.09$  std for Benlighøj. We note that the ratios are close to one which indicates that the test areas were heavily vegetated.

In the case of double-bounce scattering from the soil surface and the vegetation a phase shift of  $\pi$  radians between HH and VV occurs [81]. In Figure 9.7 is illustrated the L-band HH-VV phase differences in the three test sites at Mols Bjerge. The estimated phase statistics in terms of the mean radians and standard deviation were  $0.53$  rad  $\pm 0.01$  std for Trehøje,  $0.61$  rad  $\pm 0.02$  std for Stenhøje and  $1.93$  rad  $\pm 0.03$  std for Benlighøj. It is noticeable that the phase difference was larger in the test area at Benlighøj than in the areas at Trehøje and Stenhøje. This probably was due to the long vertical stems of *Carex arenaria* and the relatively bare soil surface at Benlighøj. The discriminatory power of  $\angle$ LHH-LVV between Benlighøj and Stenhøje is faintly reflected by CAN2 in Table 9.2 (b) where the observed correlation is  $-0.24$ .

### 9.3 Supervised classification of EMISAR data

In this section a supervised Bayes classification of the three test sites at Mols Bjerge is carried out using Multiple Discriminant Analysis (MDA). For a brief introduction to MDA refer to Section 3.6.1. The training areas or classes are the three test sites Trehøje, Stenhøje and Benlighøj shown in Figure 9.1. These classes each represent different characteristics in terms of the above ground biomass and plant species. The feature vector consists of the variables listed on page 216. Using all nine variables the classified result is then comparable with

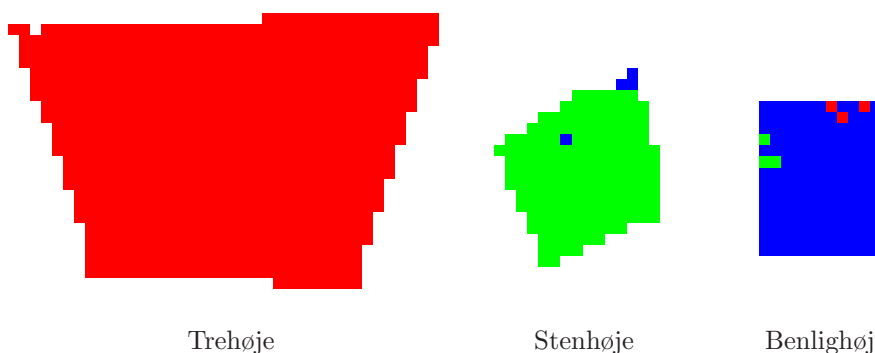


Figure 9.15: Supervised classification using Multiple Discriminant Analysis of EMISAR data covering the three test sites at Mols Bjerge. The training areas are shown in Figure 9.1 where the colours red, green and blue correspond to the areas at Trehøje, Stenhøje and Benlighøj. The variables are geometrically rectified C- and L-band polarized EMISAR data covering Mols Bjerge 3 and 4 June 1997, see text page 216. One square corresponds to  $\sim 9.5 \text{ m}^2$ .

the results obtained in the Sections 9.1 and 9.2. Based on the features each observation within the test areas is classified into one of the three classes.

The classified result is presented in Figure 9.15 and according to the training areas in Figure 9.1 the classification is good. This is also reflected by the confusion matrix in Table 9.3 (a), which contains information about actual and predicted classifications. Here we note that all observations which originally belong to the Trehøje test site are assigned to the Trehøje test site. The error rate of the total number of observations correctly assigned within the three training areas is, according to Table 9.3 (a), less than 1.0%. However, this result is to be expected. Obviously, when the discriminant functions that best discriminate between the three test sites, are based on the same three test sites which are used to evaluate how accurate the prediction is, we are likely to get good classifications.

In order to assess the accuracy of this *post hoc* prediction we therefore use the *leave-one-out* cross-validation [69]. According to the confusion matrix of the cross-validation in Table 9.3 (b) the error rate of the total number of correctly assigned observations within the three test sites is still 1.0%, which suggests homogeneity of the covariance matrix within each of the three test areas. The observed over all  $R^2$  for testing of the *null hypothesis*  $H_0$  that all three classified

From class	T	S	B	Total
T	741 (100.00)	0 (0.00)	0 (0.00)	741 (100.00)
S	0 (0.00)	161 (96.41)	6 (3.59)	167 (100.00)
B	3 (1.95)	2 (1.30)	149 (96.75)	154 (100.00)
Total	744 (70.06)	163 (15.35)	155 (14.60)	1062 (100.00)

(a)

From class	T	S	B	Total
T	741 (100.00)	0 (0.00)	0 (0.00)	741 (100.00)
S	0 (0.00)	161 (96.41)	6 (3.59)	167 (100.00)
B	3 (1.95)	2 (1.30)	149 (96.75)	154 (100.00)
Total	744 (70.06)	163 (15.35)	155 (14.60)	1062 (100.00)

(b)

Table 9.3: (a) Number of observations and percent classified into class and (b) number of observations and percent classified into class using *leave-one-out* cross-validation. The observations are classified using Multiple Discriminant Analysis. The classes T, S and B correspond to the three test areas Trehøje, Benlighøj and Stenhøje at Mols Bjerge. The training areas and classified observations are shown in the Figures 9.1 and 9.15. The variables are geometrically rectified C- and L-band polarized EMISAR data covering Mols Bjerge 3 and 4 June 1997, see text page 216.

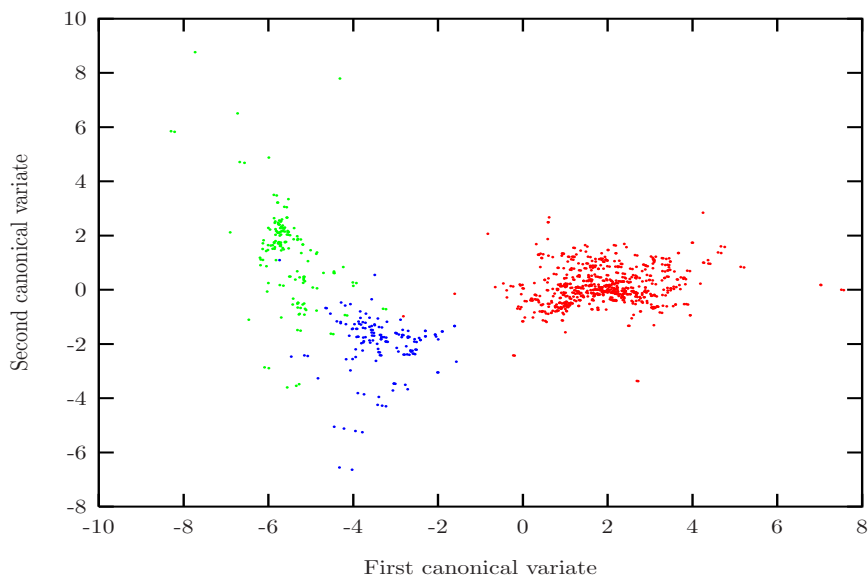


Figure 9.16: Linear discriminant plot for the classified result in Figure 9.15 of the three test sites at Mols Bjerge. The canonical correlations are shown in Table 9.4 (b). The colours red, green and blue correspond to the areas Trehøje, Stenhøje and Benlighøj. The variables are geometrically rectified C- and L-band polarized EMISAR data covering Mols Bjerge 3 and 4 June 1997, see text page 216.

areas have equal means is 0.33, which is significant at the 0.0001 level. It is therefore safe to assume that the three classified areas have different means. The classified areas in Figure 9.15 are almost identical with the training sites and it is therefore not surprising that both  $R^2$  in Section 9.2 and in this section are identical.

As mentioned above the classified areas in Figure 9.15 are very similar to the training areas, and we therefore would expect the statistics from the CDA to be like the corresponding analysis in Section 9.2. The canonical variates CAN1 and CAN2 of the classified observations are shown in Figure 9.16. Like in Section 9.2 the three test sites are separated by the first linear discriminant CAN1. Especially the separation between the test site at Trehøje and the test areas Stenhøje and Benlighøj is good. The second linear discriminant CAN2 expresses the difference between Stenhøje and Benlighøj. This separation is also good i.e. only few pixels are misclassified.

	Canonical Correlation	Adjusted Canonical Correlation	Approximate Standard Error	Squared Canonical Correlation
1	0.9482	0.9478	0.0031	0.8991
2	0.6865	0.6842	0.0162	0.4713

(a)

Variable	CAN1	CAN2
CVV	-0.2184	0.4108
CHV	0.2696	-0.0134
CHH	0.3024	0.4947
LVV	0.8889	0.0101
LHV	0.8850	0.3025
LHH	0.9469	-0.0737
LHV/LVV	0.0359	0.5530
LHH/LVV	0.3514	-0.2372
$\angle$ LHH-LVV	-0.2208	-0.2461

(b)

Table 9.4: (a) The squared canonical correlations and (b) the total sample correlations between the canonical variables and the original variables. The sample represents the supervised classification of the test sites at Trehøje, Stenhøje and Benlighøj in the Figures 9.15 and 9.16. The training areas are displayed in Figure 9.1 and the variables are geometrically rectified C- and L-band polarized EMISAR data covering Mols Bjerger 3 and 4 June 1997, see text page 216.

The corresponding two eigenvalues or squared canonical correlations given in Table 9.4 are 0.90 and 0.47. In Table 9.2 they were 0.90 and 0.45. In fact a comparison between CAN1 and CAN2 and their correlations in Table 9.4 and Table 9.2 unveils, as expected, that the statistics and the variables that express most of the difference between the three test sites are very much the same. For a discussion concerning the variables and their correlations the reader is therefore referred to Section 9.2.

## 9.4 Unsupervised classification of EMISAR data

In this section the natural grouping or association of the observations from the three test sites at Mols Bjerge is explored. This is carried out using the unsupervised classification technique Cluster Analyses (CA). In CA nothing or little is known about the number of clusters (classes) and their structure beforehand. For a short description of this technique refer to Section 3.6.2.

At first it seems natural to study to what extent the clustering algorithm chooses to group the observations into three clusters using all nine variables. The distribution of the clusters is shown in Figure 9.17 (a) and the variables are the C- and L-band polarized EMISAR data listed on page 216. The clusters might reflect other physical properties of the test sites than the ones separating the test sites in the Sections 9.2 and 9.3. This is emphasized by displaying the clusters in Figure 9.17 (a) in grey levels. Here the darkest grey level represents cluster 1, the intermediate grey level cluster 2 and the brightest grey level cluster 3.

It is noteworthy that Stenhøje and Benlighøj in Figure 9.17 (a) are assigned to cluster 3, whereas Trehøje appears more inhomogeneous containing both cluster 1 and 2. In order to test the *null hypothesis*  $H_0$  that the three clusters have equal means the over all  $R^2$  is calculated. Significant on the 0.0001 level  $R^2$  is 0.38. This rejects  $H_0$  and we hereby conclude that the clusters are different. This value is larger than  $R^2$  derived in the Sections 9.2 and 9.3 indicating that the clusters are better separated than the classes derived from the training areas. The separation is improved because the observations in CA are assigned to the nearest centroid. This is far from always the case when the classification is based on data from training samples.

In Figure 9.18 the canonical variates CAN1 and CAN2 of the clusters in Figure 9.17 (a) are illustrated. The corresponding eigenvalues and total sample correlations are listed in Table 9.5. The first canonical variate CAN1 is convincing in separating cluster 3 from the clusters 1 and 2 and according to Table 9.5 (a) 88.9% of the variance is accounted for. The second linear discriminant CAN2 accounts for 51.2% of the variance and here cluster 1 is to a lesser extent separated from cluster 2.

The total sample correlations between the first canonical variables and the original variables in Table 9.5 (b) show that the discriminatory power of CAN1 most widely is due to the variables LVV, LHV and LHH. These variables were also responsible for the major part of the discriminatory power of CAN1 in Table 9.2 (b). In Section 9.2 was accounted for what possibly could be the reason for LVV, LHV and LHH to discriminate between the test site at Trehøje and the test areas at Stenhøje and Benlighøj



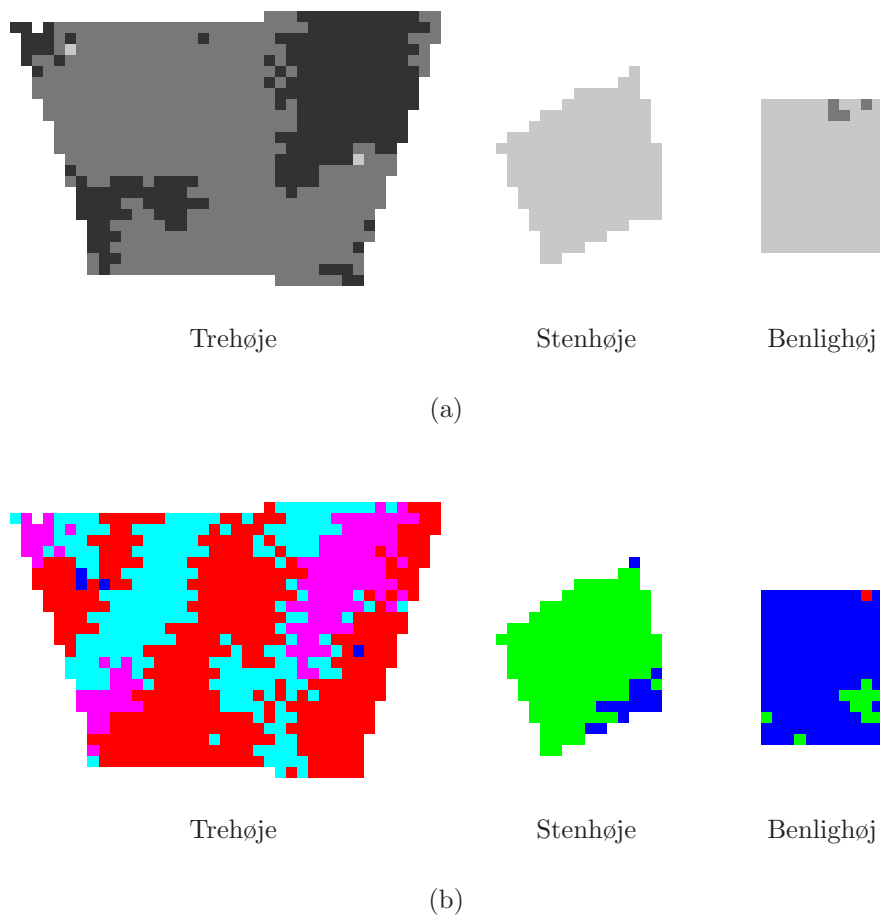


Figure 9.17: Unsupervised classification of polarimetric EMISAR data using Cluster Analysis. The data are geometrically rectified C- and L-band polarized EMISAR data covering the three test sites at Mols Bjerger 3 and 4 June 1997. In (a) all of the variables presented on page 216 are used in the clustering. Here the darkest grey level represents cluster 1, the intermediate grey level cluster 2 and the brightest grey level cluster 3. In (b) the variables CHH, LVV, LHV, LHH and LHV/LVV are used in the clustering. Here the blue colour represents cluster 1, green cluster 2, red cluster 3, cyan cluster 4 and magenta cluster 5. One pixel corresponds to  $\sim 9.5 \text{ m}^2$ .

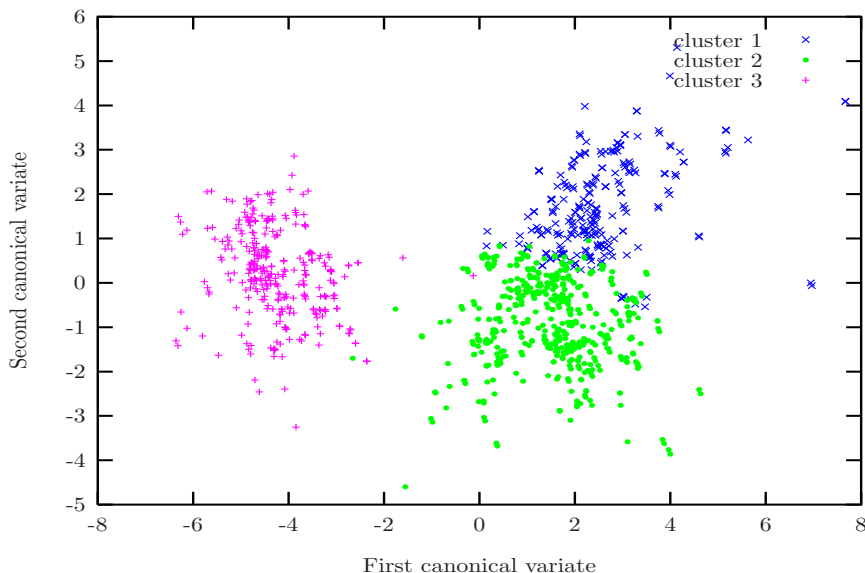


Figure 9.18: Linear discriminant plot for the classified result in Figure 9.17 (a) of the three test sites Trehøje, Stenhøje and Benlighøj. The variables are geometrically rectified C- and L-band polarized EMISAR data covering Mols Bjerge 3 and 4 June 1997, see text page 216. The canonical correlations are shown in Table 9.5 (b).

As mentioned above CAN2 discriminates between cluster 1 and cluster 2. We note that the distribution of the clusters in Figure 9.17 (a) is not reflecting any difference between the test sites Stenhøje and Benlighøj. Observations from these sites are located in cluster 3. According to Table 9.5 (b) the discriminatory power of CAN2 is concentrated in the variables CVV, CHV, CHH and LHV/LVV. Since the observations in the clusters 1 and 2 are located in the Trehøje test area these variables apparently discriminate between two sub-environments within Trehøje test area. *In situ* data to confirm the existence of these sub-environments are not available.

In order to reduce the disturbing effect of outliers and enable the detection of potential new classes, a new set of variables is selected and the number of clusters is extended from three to five. The selected variables are CHH, LVV, LHV, LHH and LHV/LVV because they have proven to be of major significance in both CDA and MDA in the Sections 9.2 and 9.3. The classification using this new set is presented in Figure 9.17 (b). Due to the selected variables the location of the clusters are expected to be more or less coincident with the training

	Canonical Correlation	Adjusted Canonical Correlation	Approximate Standard Error	Squared Canonical Correlation
1	0.9427	0.9422	0.0034	0.8886
2	0.7158	0.7138	0.0150	0.5123

(a)

Variable	CAN1	CAN2
CVV	-0.0976	0.5864
CHV	0.3274	0.5677
CHH	0.4396	0.5754
LVV	0.8514	-0.2915
LHV	0.9372	0.1176
LHH	0.9184	-0.1367
LHV/LVV	0.1756	0.5241
LHH/LVV	0.3417	0.1841
$\angle$ LHH-LVV	-0.2896	-0.2806

(b)

Table 9.5: (a) The squared canonical correlations and (b) the total sample correlations between the canonical variables and the original variables. The sample represents the unsupervised classification of the test sites at Trehøje, Stenhøje and Benlighøj in the Figures 9.17 (a) and 9.18. The variables are geometrically rectified C- and L-band polarized EMISAR data covering Mols Bjerger 3 and 4 June 1997, see text page 216.

sites. That is the blue colour represents cluster 1 corresponding to Benlighøj, green represents cluster 2 corresponding to Stenhøje and red, cyan and magenta colours represent the clusters 3, 4 and 5 corresponding to Trehøje.

In order to test  $H_0$  that the five clusters have equal means the over all  $R^2$  is calculated. Significant at the 0.0001 level the calculated  $R^2$  is 0.73, which rejects  $H_0$ . We therefore conclude that the clusters have different means. It is noticeable that the value of 0.73 is larger than any of the previously calculated  $R^2$  values. However,  $R^2$  is a measure of how well the clusters are separated and consequently  $R^2$  increases with increasing number of clusters. It is therefore expected that the  $R^2$  value of 0.73 is larger than the others because this value represents five classes whereas previously calculated values represent only three.

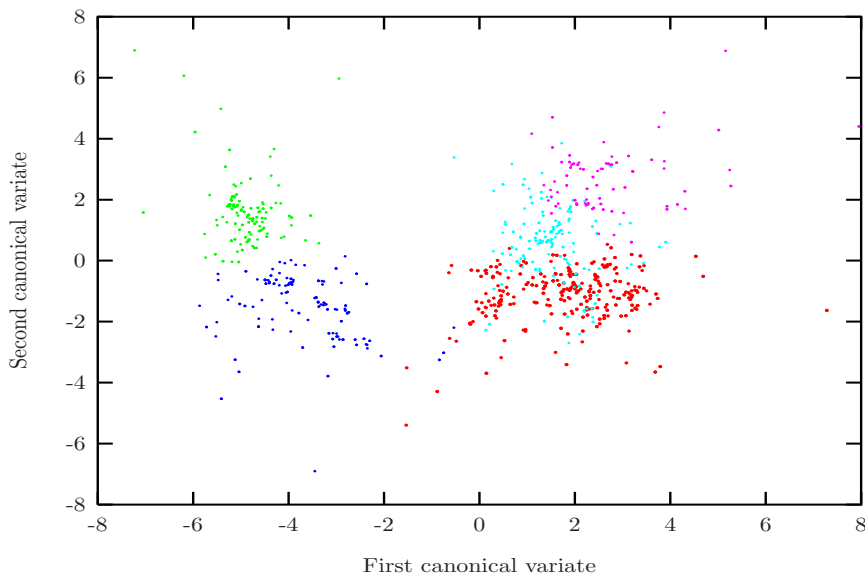


Figure 9.19: Linear discriminant plot for the classified result in Figure 9.17 (b) of the three test sites Trehøje, Stenhøje and Benlighøj. The blue colour represents cluster 1, green cluster 2, red cluster 3, cyan cluster 4 and magenta cluster 5. The variables used in the clustering are CHH, LVV, LHV, LHH and LHV/LVV, which are geometrically rectified C- and L-band polarized EMISAR data covering Mols Bjerge 3 and 4 June 1997, see text page 216. The corresponding canonical correlations are shown in Table 9.6 (b).

Using CDA the linear discriminants span four dimensions due to the five clusters. However, because the squared canonical correlations for CAN3 and CAN4 in Table 9.6 (a) are relatively small, they are neglected. The canonical variates CAN1 and CAN2 are displayed in Figure 9.19. The first linear discriminant CAN1 is primarily well suited for separating the clusters 1 and 2 from the clusters 3, 4 and 5. The corresponding squared canonical correlation in Table 9.6 (a) shows that 89.2% of the variance is accounted for by CAN1. The second linear discriminant CAN2 expresses the difference between clusters 2, 4 and 5 and the clusters 1 and 3. Here the corresponding squared canonical correlation in Table 9.6 (a) shows that 67.2% of the variance is explained by CAN2.

According to CAN1 in Table 9.6 (b) the total sample correlations between the first canonical variables and the original variables are to a large extent explained by LVV, LHV and LHH. As demonstrated previously these variables also played a significant role in the discriminatory power of CAN1 in Section 9.2. Concern-

	Canonical Correlation	Adjusted Canonical Correlation	Approximate Standard Error	Squared Canonical Correlation
1	0.9444	0.9441	0.0033	0.8920
2	0.8203	0.8193	0.0100	0.6728
3	0.6696	0.6687	0.0169	0.4483
4	0.4711	.	0.0239	0.2219

(a)

Variable	CAN1	CAN2	CAN3	CAN4
CHH	0.4094	0.5288	0.6757	-0.3048
LVV	0.8728	-0.3698	0.2050	0.1384
LHV	0.9242	0.2819	-0.0903	0.1170
LHH	0.9308	-0.2067	-0.0467	-0.0519
LHV/LVV	0.1171	0.9344	-0.2915	0.1643

(b)

Table 9.6: (a) The squared canonical correlations and (b) the total sample correlations between the canonical variables and the original variables. The sample represents the unsupervised classification of the three test sites Trehøje, Stenhøje and Benlighøj at Mols Bjerger in the Figures 9.17 (b) and 9.19. The variables are geometrically rectified C- and L-band polarized EMISAR data covering Mols Bjerger 3 and 4 June 1997, see text page 216.

ing CAN2 the total sample correlations between the second canonical variables and the original variables are also listed in Table 9.6 (b). Here the discriminatory power of CAN2 is concentrated in CHH and LHV/LVV. We find that the same variables had significant discriminatory power in CAN2 in Section 9.2. For a discussion concerning the discriminatory power of CAN1 and CAN2 in relation to the physical properties of the three test sites refer to Section 9.2.

## 9.5 Discussion

Using multivariate techniques EMISAR data have in this chapter been analyzed in terms of their correlation with the *in situ* data. The EMISAR data were geometrically rectified one-look C- and L-band polarized EMISAR data from 3 and 4 June 1997, see text page 216. The *in situ* data were collected 4 June

1997 in three grassland areas located at Trehøje, Stenhøje and Benlighøj at Mols Bjerger, see Chapter 7. Here the volumetric structure of the above ground biomass and the dominant plant species were of particular interest.

In order to explore the presence of structure and compress the information in the multivariate data, the variables were in Section 9.1 transformed into the Principal Components (PC) space. The scatter-plots in Figure 9.9 proved the existence of structure and that a majority of the structure was due to differences between the three sub-areas. Here 53.6% of the information-bearing variance was concentrated in PC1 and PC2. However, the geographical distribution of the next four PC, that is PC3, . . . , PC6, in Figures 9.11 and 9.12 showed also structure. This suggests that additional information was embedded in the polarimetric EMISAR data besides what was explainable by the *in situ* data available. We also note that the first five principal components PC1, . . . , PC5 explain 88.8% of the variance. This level of redundancy shows that it is worthwhile compressing the information in the first few PC.

Also the supervised classification using MDA in Section 9.3 discriminated between the three test areas. Here the training areas were represented by the three test areas themselves. Using the threshold of 0.05, none of the classified observations were assigned to the reject class. In addition the cross-validated error rate of correctly assigned observations was only 1.0%. With the reservation that the prediction was *post hoc*, the overall performance of the classification was therefore good.

An unsupervised classification of the test sites was in Section 9.4 performed using Cluster Analysis (CA). Using all nine variables and only three clusters the classified result in Figure 9.17 (a) discriminated between Trehøje test site and the areas at Stenhøje and Benlighøj. However, the classification was unable to distinguish between Stenhøje and Benlighøj. In order to suppress the unwanted effect of outliers and reduce the *curse of dimensionality*, the number of clusters was increased to five and the number of variables reduced to the five [9]. Here the five variables with the highest discriminatory power in Table 9.2 were selected. As expected the clusters in Figure 9.17 (b) therefore separate the three test sites. From the cluster analysis we note that the test area at Trehøje in Figure 9.17 (b) comprises the red cluster 3, the cyan cluster 4 and the magenta cluster 5. This suggests an inhomogeneity in Trehøje test site, which it is not possible to account for by the *in situ* data available.

In Section 9.2 it was shown that the L-band VV, HV and HH polarizations discriminated between Trehøje and the test areas at Stenhøje and Benlighøj. This was most likely due to the large volume of above ground biomass at Trehøje, which is illustrated in Figure 7.4 (a). The volume of the above ground biomass in the test areas at Stenhøje and Benlighøj was smaller as indicated in the

Figures 7.4 (b) and 7.5 (a)–(b). As demonstrated in Section 7.5 the number of biomass samples was unfortunately too small to confirm this difference.

Due to volume scattering in the vegetation the cross-polarized amplitude ratio HV/VV is often used as an indicator of biomass. However, according to the L-band HV/VV ratios in Section 9.2 the biomass contents in Stenhøje test site was higher than at Trehøje. Apparently this is inconsistent with suggestion stated above, that Trehøje test site had the largest biomass content. The explanation probably is differences in the geometrical structure of the dominant plant species within the two test sites. Here the oblique straws were more frequent at Stenhøje than at Trehøje, which affected the cross-polarized ratio. The co-polarized amplitude ratio HH/VV is sensitive to the dielectric constant and is therefore used for retrieving soil moisture. However, as shown in Section 9.2 the test areas were too vegetated for reliable soil moisture estimates to be made using the criterion of Dubois *et al.* (1995) [26]. A detailed knowledge of the vegetation characteristics in the test sites would therefore be necessary for the backscatter contribution due to soil moisture to be separated from the vegetation backscatter.

The plant species in the test sites at Stenhøje and Benlighøj were different. Stenhøje was dominated by *Festuca rubra* and at Benlighøj *Deschampsia flexuosa* and *Carex arenaria* were dominating. The L-band VV and the C-band VV, HV and HH polarizations were affected by the difference in vegetation characteristics and discriminated between the test sites at Stenhøje and Benlighøj. Faint evidence suggested a larger phase difference between L-band HH and VV in Benlighøj test area than in the test sites at Trehøje and Stenhøje. This probably was due to double-bounce scattering between the straws of *Carex arenaria* and the relatively bare soil surface at Benlighøj.





# Conclusion

---

## 10.1 Summary

In order to facilitate the extraction of biotope relevant information the main part of this thesis has been concerning restoration of SAR data. Due to the small size of the semi-natural ecosystems under study, it has been of paramount importance for this investigation that the proposed restoration methods are capable of restoring fine structures as well as preserving homogeneous areas. The restorations are carried out in a signal adaptive mode using MRF in a Bayesian framework. Various *a priori* models have been implemented in both the local optimizer Iterated Conditional Modes (ICM) and the global optimization technique Simulated Annealing (SA).

In Oliver and Quegan (1998) and Stewart *et al.* (2000) ratios of SAR data are used as a quality measure of various reconstructions and segmentations [59], [78]. In this work a new technique for algorithm optimization, which relies on ratios of SAR data and their histograms, has been proposed. A quantitative evaluation of the restorations based on statistics of the ratio images and their histograms is presented together with comparative analyses of restorations using ICM and SA.

The Gaussian *a priori* model, the exponential *a priori* model and the LaPlace

*a priori* model have been implemented in the ICM algorithm. Among these three *a priori* models the exponential prior proved to be the most convincing in terms of preserving discontinuities and mean amplitude levels in SAR data. Unfortunately, the exponential prior was not satisfactory in terms of preserving sharp transitions between regions. We have therefore developed two new *a priori* models, namely, the Gamma *pixel prior* and the Gamma *mean prior*, which aim at solving this problem using a specially designed energy function. Implemented in the ICM algorithm the Gamma *pixel prior* showed to be a little better than the Gamma *mean prior* when it comes to preserving discontinuities and mean amplitude levels.

As our study has demonstrated, the restored SAR data using the presented *a priori* models and the ICM algorithm possessed some unwanted clutter. This is due to the ICM algorithm, which performs gradient descent and therefore easily gets trapped in local energy minima. This property of ICM unfortunately makes ICM unsuitable for preserving details and homogeneous areas in SAR data.

In order to avoid the artefacts created by ICM the Gamma *pixel prior* has been implemented in a SA algorithm. The preservation of details and homogeneous areas was further enhanced by introducing a Multi-Temperature Annealing (MTA) schedule, where the temperature is adapted to the statistics of the local energy represented by the clique potentials. As the results show, our proposed annealing algorithm is fast and satisfactory in terms of preserving small details, edges, homogeneous areas and mean amplitude levels.

In the presented *a priori* models pair-site cliques with different weights in a 2nd order neighbourhood configuration have been used. For comparison, also interactions involving pair-site cliques with equal weights in a 2nd order neighbourhood configuration are implemented in the Gamma *pixel prior*. Our results show that a small but significant amount of additional contextual information can be extracted using pair-site cliques with different weights instead of using pair-site cliques with equal weights.

Another aspect of this thesis was to explore to what extent the geophysical and biophysical properties characterizing the semi-natural environments are detectable in polarimetric SAR data. Because the preservation of fine structures and homogeneous areas was crucial for this investigation, the Gamma *pixel prior* implemented in the SA algorithm was used for restoration.

Our analyses show that the VV, HV and the HH polarizations for both C- and L-band possessed power in discriminating between the different plant communities. Also the L-band HV/VV and HH/VV ratios and the L-band phase difference between HH and VV contributed to the discrimination, but to a lesser extent. The cross-polarized ratio HV/VV is known to be a good vegetation index and

is therefore used as an indicator of biomass. However, as the analyses from the grasslands at Mols Bjerge show, differences in the geometrical structure of the dominant plant species are more likely to affect the cross-polarized ratio than differences in biomass. The results also show that the empirical model for soil moisture retrieval introduced by Dubois *et al.* (1995) was unsuitable for reliable soil moisture estimates to be made in the test areas [26]. This was due to the dense vegetation and the co-polarized L-band HH/VV ratio was therefore more likely to reflect vegetation backscatter than backscatter due to soil moisture. The L-band phase difference between HH and VV has in this work proven to be a useful indicator of plant communities in wetlands and grasslands where vertical oriented straws are frequent.

Using multivariate techniques we have demonstrated that a strong relation exists between the biophysical properties in the wetland at Gjern and the three grasslands at Mols Bjerge and the polarized EMISAR data. In other words, polarimetric SAR can provide important vegetation structural information about wetlands and grasslands.

The analyses presented in this thesis show that a vast amount of information is embedded in polarized SAR data even at very small scales and that SA using the Gamma *pixel prior* and the MTA schedule is convincing in terms of retrieving it. The analyses also show that the results using the Gamma *pixel prior* through a SA algorithm are generally applicable. This is demonstrated in Appendix B where the algorithm is applied on EMISAR data covering a large scene from the Gjern area. Here human artefacts such as houses and roads and cover types such as forests and towns to a large extent are preserved. The reservation concerns thin line features, point scatterers and very small object corresponding to the size of a few pixels which are likely to be smoothed out by the Gamma *pixel prior*.

## 10.2 Discussion

The new optimization principle has in the work presented proved to possess some very advantageous properties. Firstly, it is completely data-driven and no prior knowledge about the image scene is required. Secondly, using appropriate *a priori* models, it is possible *via* synthetic SAR data to tune the algorithms in such a fashion that discontinuities and mean levels of amplitudes are preserved. This is of course of great importance in situations where the preservation of the radiometric content or the preservation of boundaries between adjacent regions is of concern.

Although the Gamma *pixel prior* implemented in the SA algorithm has proved to be successful in terms of restoring details and homogeneous areas in polarized SAR data, it still possesses some flaws in terms of e.g. creating artefacts and badly restored edges. Further research in the development of more sophisticated energy functions and *a priori* models is therefore required for these problems to be reduced. The presented algorithms are applied to SAR amplitude data only. In order to take full advantage of the information embedded in the polarized SAR data the algorithms need to be extended for restoration of the complex covariance matrix.

We have restated some of the results obtained by Ozesmi and Bauer (2002), Price *et al.* (2002) and Kouskoulas *et al.* (1999) that show that polarimetric SAR is well suited for characterizing vegetation characteristics [61], [66], [44]. However, our research has extended the knowledge further by showing that C- and L-band polarimetric SAR also provides a prospective platform for characterizing the biophysical properties of wetlands and grasslands and at very small scales.

This opens up possibilities in detailed mapping of plant communities in semi-natural grasslands and wetlands using multifrequency polarized SAR data. One possibility is the application of Discriminant Analysis (DA) and representative training areas to explore the distribution of specific plant communities and sub-environments. Another possibility is the use of Principal Components (PC) and Cluster Analysis (CA) to obtain a general view of a region and possibly disclose unknown biotopes.

The fusion of polarimetric SAR data with data from other sources provides the most promise for improving wetland and grassland classification. Here another source could e.g. be spectral data, which in Jacobsen *et al.* (2000) have proven to be excellent for identification of plant communities in semi-natural grasslands at Mols Bjerge [38].

# Synthetic SAR images

---

In Chapter 5 ICM and SA algorithms were evaluated on synthetic SAR- and EMISAR amplitude data. Here the performance of the algorithms was analyzed using statistics derived from ratio images and their histograms.

This appendix is organized as follows: Figure A.1 shows the original five grey-levels image and 5.1 (b) shows the image with synthetic SAR speckle. The corresponding ratio image with histogram is displayed in Figure A.2. Restorations using SA and the Gamma *pixel prior* involving eight pair-site interactions with equal weights  $w_c = w$  are shown in Figure A.3. In the figure the restorations comprise both synthetic one grey-level and five grey-levels SAR data. The corresponding ratio images with histograms are shown in the Figures A.4 and A.5. The filtering of the synthetic one grey-level and five grey-levels SAR data using the 40% quantile filter is illustrated in Figure A.6. The corresponding ratio images with histograms are shown in the Figures A.7 and A.8. In Figure A.9 are shown a segmentation of the synthetic one grey-level and five grey-levels SAR data using SA and the *segann* algorithm. The corresponding ratio images with histograms are shown in the Figures A.10 and A.11

The data constitute a  $150 \times 150$  array and if nothing else is mentioned the algorithms involve the eight pair-site interactions with the weights of the cliques given in Figure 4.2. Parameters from the fine tuning of the SA and ICM algorithms are listed in the Tables A.1 and A.2 together with statistics derived from

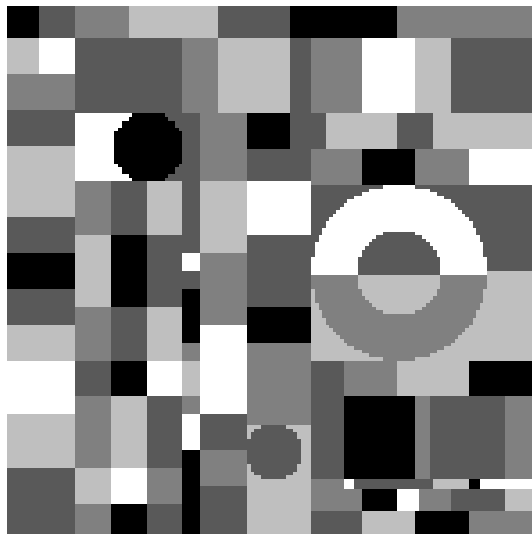


Figure A.1: The original synthetic five grey-levels image.

the ratio images.

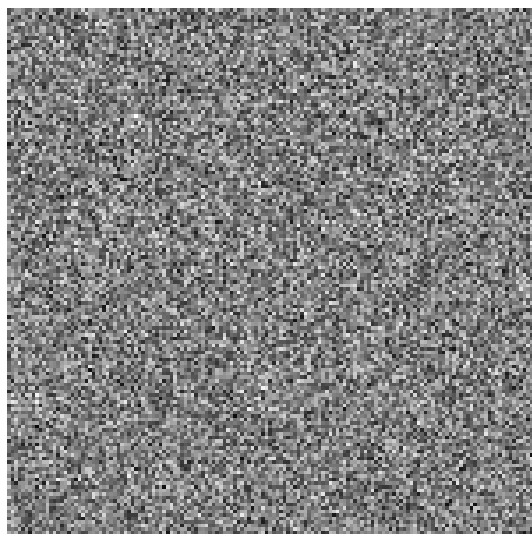
The homogeneous synthetic one grey-level SAR data are presented in Figure 5.1. The mean value is 0.05, which corresponds to the mean of the EMISAR data in Figure 5.2. The speckle is independent, identically-distributed without any traces of structure except for the natural clutter. The synthetic five grey-levels SAR data are shown in Figure 5.1 (b). The five grey levels are uniformly distributed within the range of 0.02 and 0.12, which corresponds to the range of interest in the EMISAR data in Figure 5.2. The smallest objects measure  $3 \times 3$  pixels.

The basic properties of SAR speckle, upon which the generation of the synthetic SAR amplitude data is founded, is outlined in Section 2.5. Using the expressions (2.5) and (2.6) the synthetic Rayleigh distributed speckle with mean  $\mu$  is easily generated. The variance  $\sigma^2$  is given by

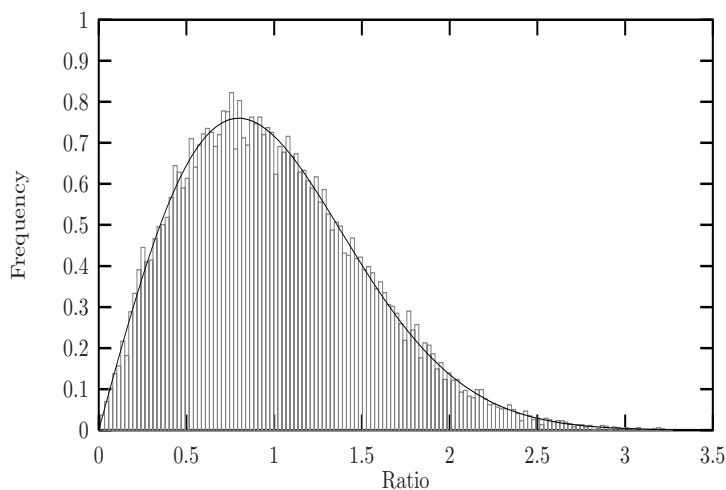
$$\sigma^2 = \frac{2\mu^2}{\pi}, \quad (\text{A.1})$$

and subsequently  $\sigma^2$  is used in the pseudo-random generator `gnoise` to produce the identically distributed independent zero-mean Gaussian noise of  $X$  and  $Y$ .

The timings are obtained on a PC with a 350 MHz Intel Pentium II processor over a 150 by 150 pixel image. The execution speed for the SA algorithm is 46.9 kpixels/s, which is equivalent to an execution time per iteration of 0.48 s. The ICM algorithms require an execution speed of 56.2 pixels/s, which corresponds to the 1000 grey-levels or classes used in the ICM algorithms. The execution time per iteration is thereby 400 s.



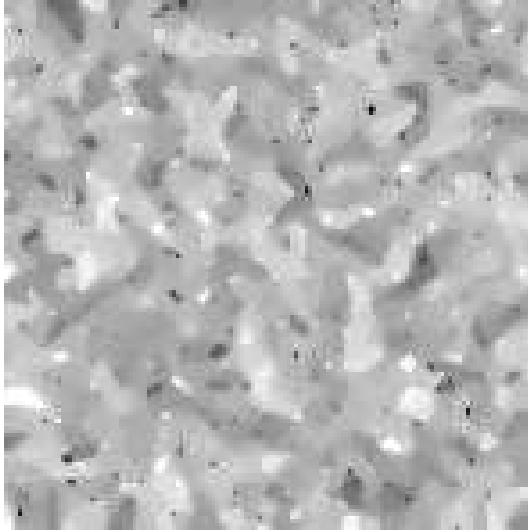
(a)



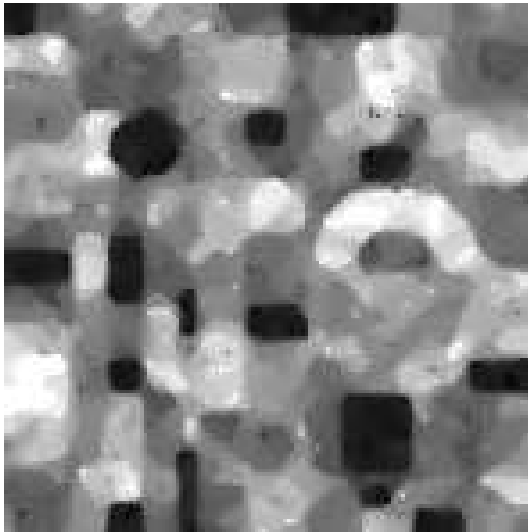
(b)

Figure A.2: (a) The ratio between the synthetic five grey-levels SAR data in Figure 5.1 (b) and the original image in Figure A.1 and (b) a comparison of the histogram of the ratio image and the theoretical Rayleigh distribution. The estimated values  $\bar{z}$  and  $S^2(z)$  are 1.0021 and 0.2744, see Section 5.2. The chi-square test statistics  $\chi^2(84)$  is 72.1. The value corresponding to the 0.05 significance level for the  $\chi^2(84)$  distribution is 106.39. The hypothesis that the observed ratio frequencies match the Rayleigh distribution is therefore accepted.



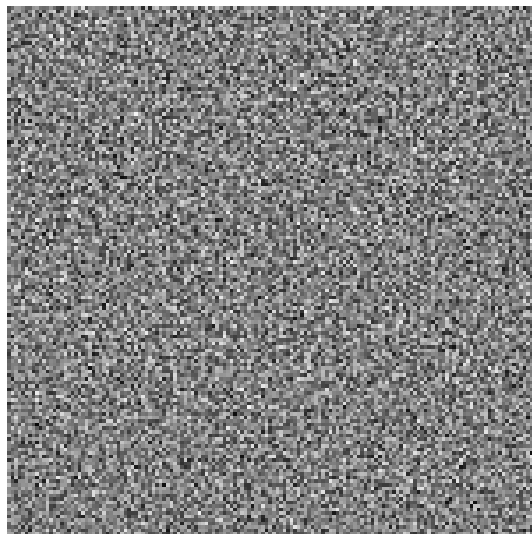


(a)

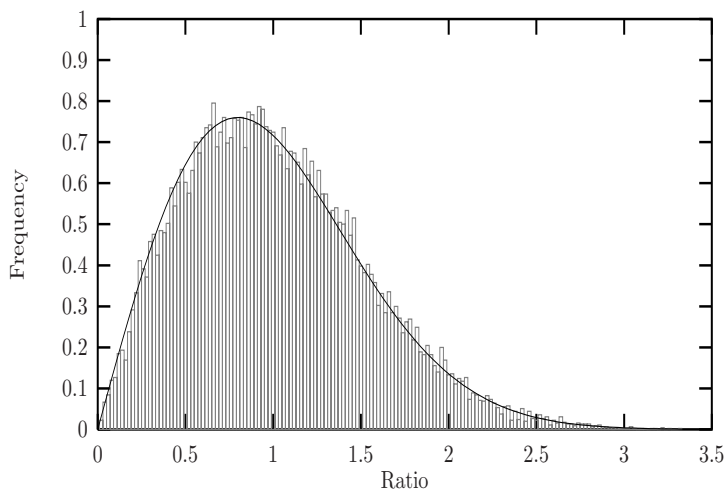


(b)

Figure A.3: (a) The restored synthetic one grey-level SAR data in Figure 5.1 (a) and (b) the restored five grey-levels SAR data in Figure 5.1 (b) using the Gamma *pixel prior* in a SA algorithm with eight pair-site interactions with equal weights. The length of the Markov chain is one and the cooling schedule used is logarithmic. The data are stretched linearly between their mean  $\pm 3$  std.

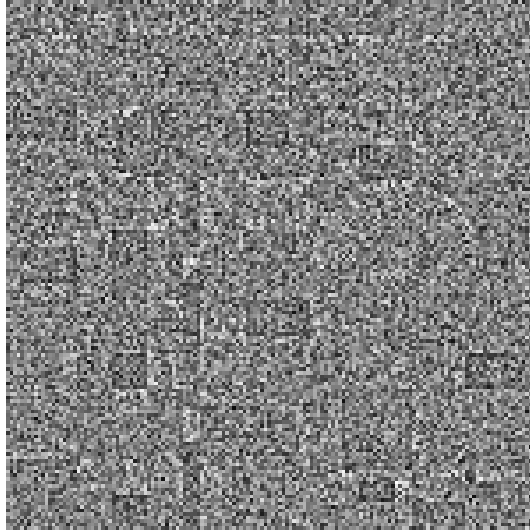


(a)

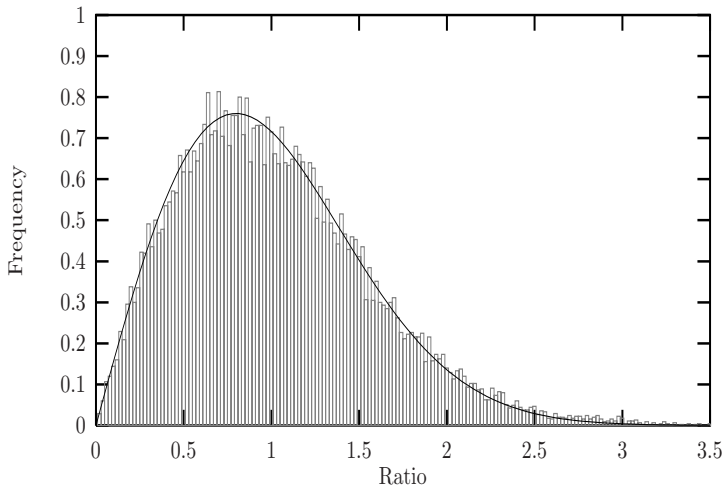


(b)

Figure A.4: (a) The ratio between the homogeneous synthetic one grey-level SAR data in Figure 5.1 (a) and the restored data in Figure A.3 (a) using the Gamma *pixel prior* and SA. The SA algorithm involves eight pair-site interactions with equal weights. In (b) is the histogram of the ratio image shown together with the theoretical Rayleigh distribution.

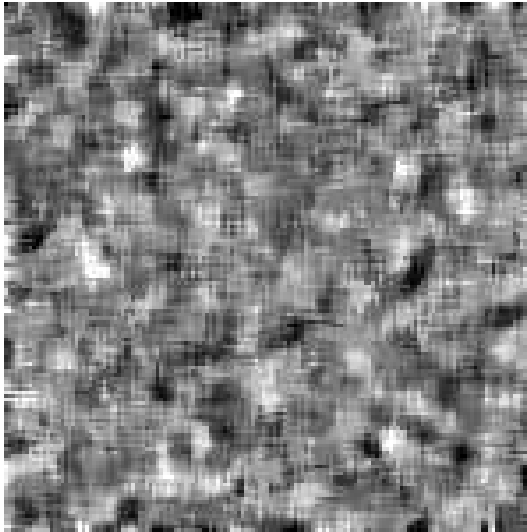


(a)

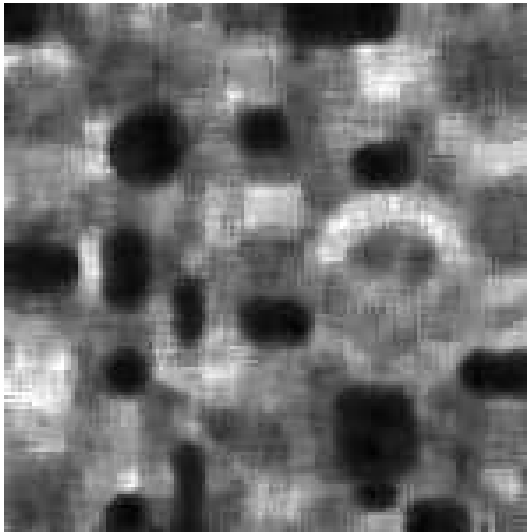


(b)

Figure A.5: (a) The ratio between the synthetic five grey-level SAR data in Figure 5.1 (b) and the restored data in Figure A.3 (b) using the Gamma *pixel prior* and SA. The SA algorithm involves eight pair-site interactions with equal weights. In (b) is the histogram of the ratio image shown together with the theoretical Rayleigh distribution.

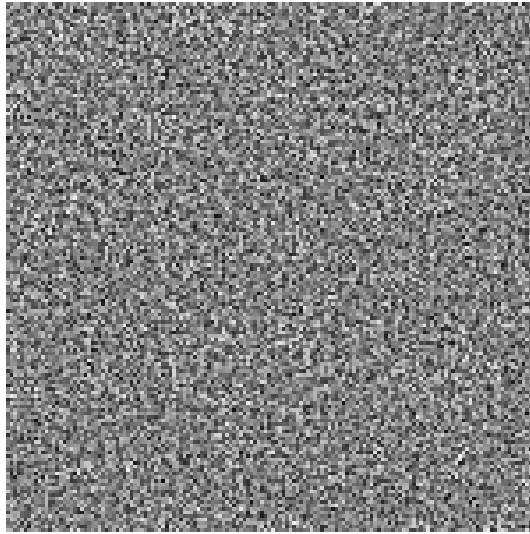


(a)

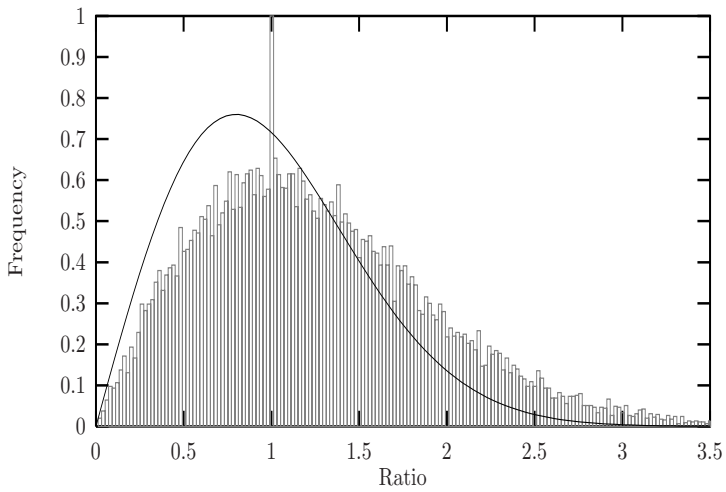


(b)

Figure A.6: (a) The restored homogeneous synthetic one grey-level SAR data in Figure 5.1 (a) and (b) the restored five grey-levels SAR data in Figure 5.1 (b) using the 40% quantile filter with window size 7. The data are stretched linearly between their mean  $\pm 3$  std.

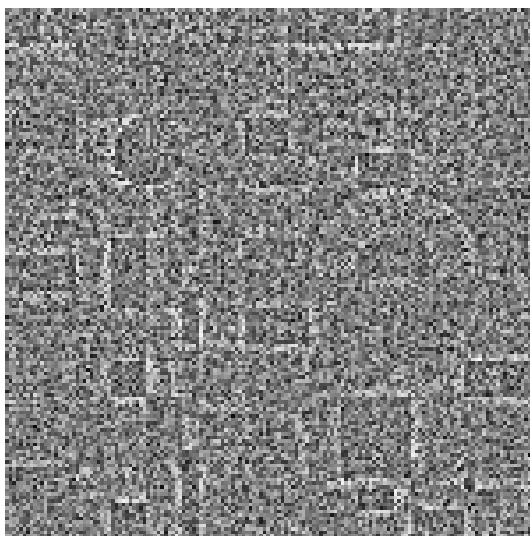


(a)

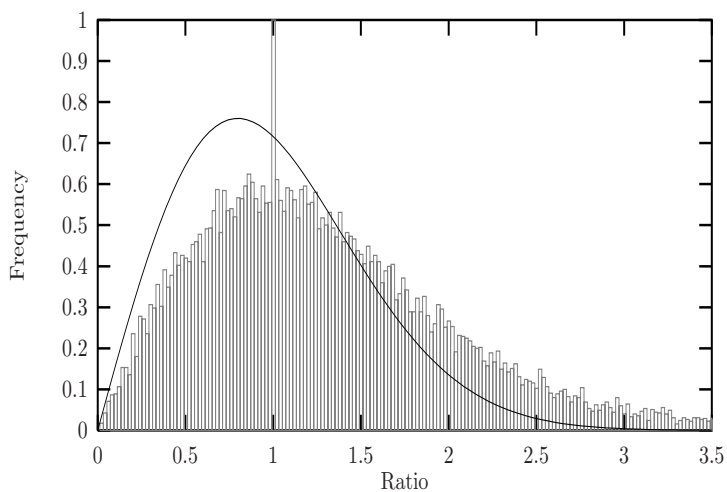


(b)

Figure A.7: (a) The ratio between the homogeneous synthetic one grey-level SAR data in Figure 5.1 (a) and the restored data in Figure A.6 (a) using the 40% quantile filter with window size 7. In (b) is the histogram of the ratio image shown together with the theoretical Rayleigh distribution.

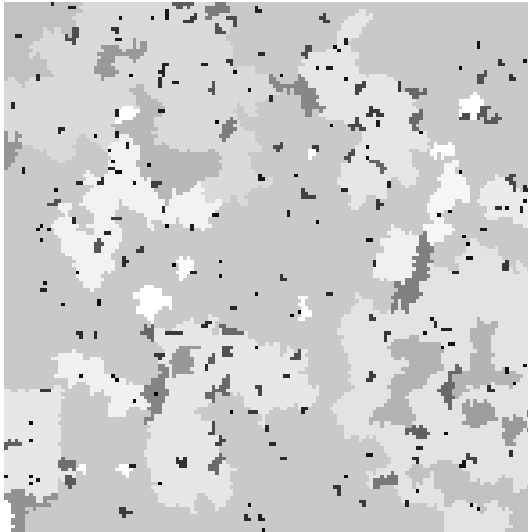


(a)

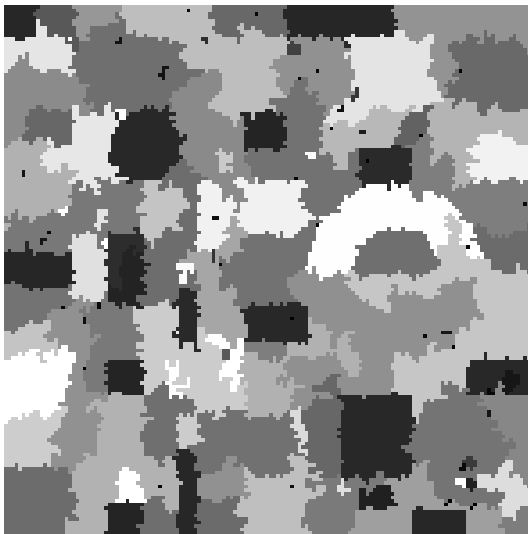


(b)

Figure A.8: (a) The ratio between the synthetic five grey-level SAR data in Figure 5.1 (b) and the restored data in Figure A.6 (b) using the 40% quantile filter with window size 7. In (b) is the histogram of the ratio image shown together with the theoretical Rayleigh distribution.

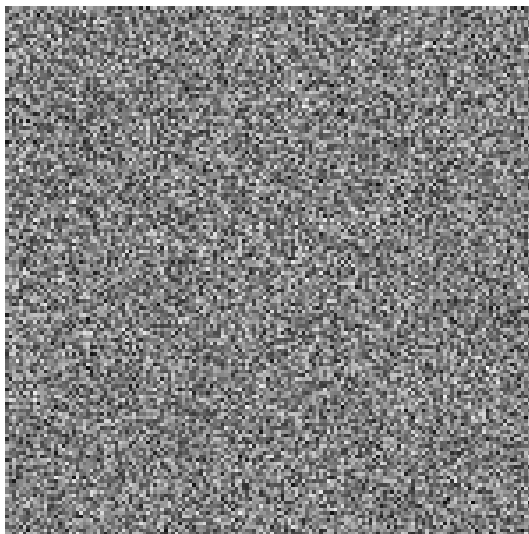


(a)

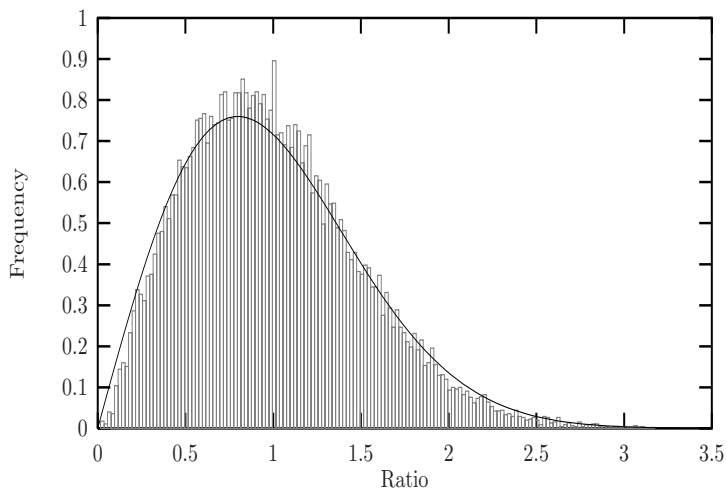


(b)

Figure A.9: (a) The segmented homogeneous synthetic one grey-level SAR data in Figure 5.1 (a) and (b) the segmented five grey-levels SAR data in Figure 5.1 (b) using the *segann* SA algorithm from Sheffield. The shape penalty is set to 5 and the probability for merging regions is  $3e-4$ . The data are stretched linearly between their mean  $\pm 3$  std.



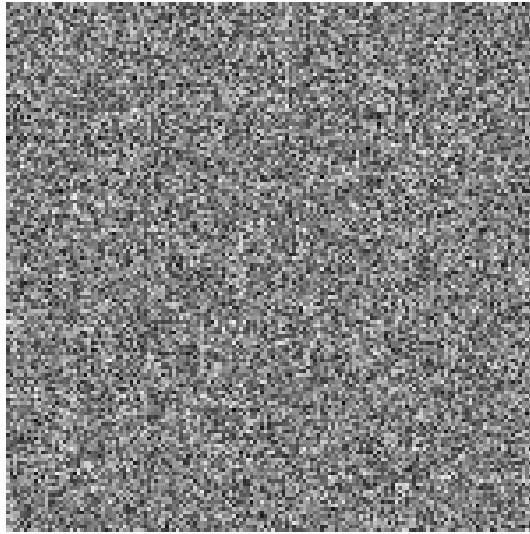
(a)



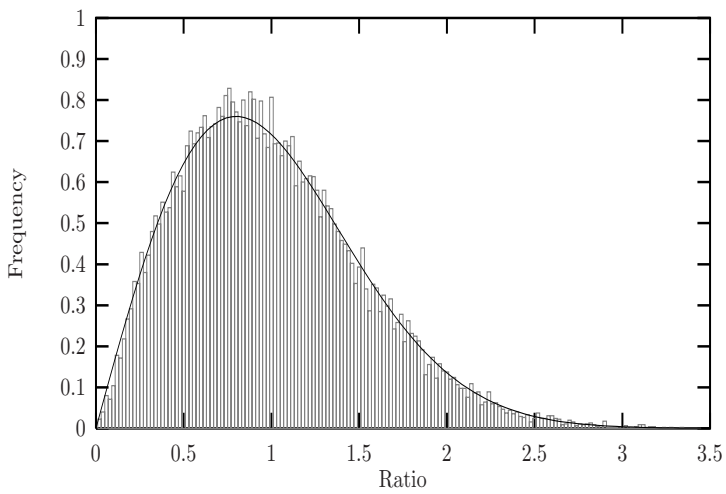
(b)

Figure A.10: (a) The ratio between the homogeneous synthetic one grey-level SAR data in Figure 5.1 (a) and the segmented data in Figure A.9 (a) using the *segann* SA algorithm from Sheffield. In (b) is the histogram of the ratio image shown together with the theoretical Rayleigh distribution.





(a)



(b)

Figure A.11: (a) The ratio between the synthetic five grey-level SAR data in Figure 5.1 (b) and the segmented data in Figure A.9 (b) using the *segann* SA algorithm from Sheffield. In (b) is the histogram of the ratio image shown together with the theoretical Rayleigh distribution.

<i>Iterated Conditional Modes, T = 1</i>					
parameters	Gauss	Exponential	LaPlace	Gamma, mean	Gamma, pixel
$k$				7	5
$\alpha$	2	2	2	2	2
$\beta$	3	5	3	0.5	0.5
$n$	9	9	9	9	9
$\bar{z}$	1.1083	0.9957	1.0554	1.0554	1.0440
$S^2(z)$	0.3307	0.2571	0.2920	0.2901	0.2813
$f$	75	78	77	74	76
$\chi^2(f)$	1216	97	545	797	573
$p\{x \leq \chi^2(f)\}$	> 0.999	< 0.95	> 0.999	> 0.999	> 0.999

(a)

<i>Iterated Conditional Modes, T = 1</i>					
parameters	Gauss	Exponential	LaPlace	Gamma, mean	Gamma, pixel
$k$				7	5
$\alpha$	2	2	2	2	2
$\beta$	3	5	3	0.5	0.5
$n$	9	9	9	9	9
$\bar{z}$	1.0905	0.9757	1.0587	1.0598	1.0450
$S^2(z)$	0.4061	0.2892	0.3122	0.311	0.2970
$f$	77	81	68	54	55
$\chi^2(f)$	5496	214	1206	1404	748
$p\{x \leq \chi^2(f)\}$	> 0.999	> 0.999	> 0.999	> 0.999	> 0.999

(b)

Table A.1: Parameters from the fine tuning of the ICM algorithms and statistics derived from the corresponding ratio images. In (a) are shown results based on synthetic homogeneous one grey-level SAR data and in (b) the results are applied to synthetic five grey-levels SAR data. The quantity  $k$  is a control parameter that governs the peak of the Gamma distribution,  $\alpha$  is a shape parameter,  $\beta$  is a weighting factor and  $n$  is number iterations, see Section 5.6. The values  $\bar{z}$  and  $S^2(z)$  are the mean and variance of the ratio image. The ‘‘Goodness of Fit’’ test statistics between the observed frequencies and the theoretical Rayleigh distribution is  $\chi^2(f)$ , where  $f$  is degrees of freedom.

<i>One grey-level image</i>				
parameters	SA pixel prior equal $w_c$	SA pixel prior different $w_c$	SA Segann	40% quantile filter
$k$	3.75	3.75		
$T_0$	0.65	0.65		
$\chi_0$	0.30	0.30		
$\bar{z}$	1.014	1.010	0.999	1.25
$S^2(z)$	0.271	0.267	0.2425	0.44
$f$	77	78	79	79
$\chi^2(f)$	84	91	283	12687
$p\{x \leq \chi^2(f)\}$	< 0.95	< 0.95	> 0.999	> 0.999

(a)

<i>Five grey-levels image</i>				
parameters	SA pixel prior equal $w_c$	SA pixel prior different $w_c$	SA Segann	40% quantile filter
$k$	3.75	3.75		
$T_0$	0.65	0.65		
$\chi_0$	0.30	0.30		
$\bar{z}$	1.025	1.023	0.999	1.32
$S^2(z)$	0.312	0.310	0.2698	0.63
$f$	62	53	78	67
$\chi^2(f)$	232	156	103	> 40000
$p\{x \leq \chi^2(f)\}$	> 0.999	> 0.999	< 0.95	> 0.999

(b)

Table A.2: Parameters from the fine tuning of various algorithms and statistics derived from the corresponding ratio images. In (a) are shown results based on synthetic homogeneous one grey-level SAR data and in (b) the results are applied to synthetic five grey-levels SAR data. In the *pixel prior* using the SA algorithm the Markov chain is homogeneous and the cooling schedule used is logarithmic. The quantity  $k$  governs the peak of the Gamma distribution,  $T_0$  is the starting temperature and  $\chi_0$  is the acceptance ratio, see Section 5.7. The values  $\bar{z}$  and  $S^2(z)$  represent the mean and variance of the ratio image. The match between the observed frequency data and the theoretical Rayleigh distribution is measured by the means of the  $\chi^2(f)$  “Goodness of Fit” test, where  $f$  is degrees of freedom.



## APPENDIX B

# Large EMISAR scene

---

The results presented in this thesis using the Gamma *pixel prior* through a SA algorithm have been based on very limited datasets. In order to investigate to what extent the results are more generally applicable the SA algorithm is applied on a wider scene containing more human artefacts and a larger range of cover types. The human artefacts include e.g. houses, roads and point scatterers and the cover types include textured regions such as towns and forests.

The wider scene used is the slant-range C-band VV-polarized EMISAR amplitude data in Figure B.1, see Section 1.2. The EMISAR is looking down from the top. The size of the image in the azimuth direction is  $\sim 7.4$  km and the ground range of the image in the range direction is  $\sim 9.5$  km. The area covered by the EMISAR data is hereby approximately  $70 \text{ km}^2$ . The data, which constitute a  $2450 \times 2450$  array, were acquired 3 June 1997 and cover the river valley of Gjern and its surroundings in Jutland. From the left the river Gudenå flows into the small lake Sminge Sø and continues from there to the upper part of the image. From the right Sminge Sø has inflow from the stream Gjern Å, which cuts through the Gjern Stream Valley situated in the middle of the image. The surroundings of Gjern Stream Valley are hilly and covered with forest. In the bottom left corner of the image the town Voel is situated. The town Gjern is situated in the middle of the image just right of the Gjern Stream Valley and in the upper right corner the town Fårvang is recognizable. Within and between the towns roads are detectable. In the country small farms are visible

and between the various agriculture fields hedges, small forests and trees can be located. The small test area at Ladegaards Enge can be recognized 1 cm to the right of Sminge Sø.

Figure B.2 illustrates the restoration of the slant-range C-band VV-polarized EMISAR amplitude data in Figure B.1 using (5.8). The ratio between the C-band VV-polarized EMISAR data in Figure B.1 and the restored data in Figure B.2 is presented in Figure B.3. The ratio image in Figure B.4 (a) shows a small region extracted from Figure B.3. The region covers a  $150 \times 150$  array of relatively homogeneous agricultural fields located in the upper middle part of the image in Figure B.1. The ratio data in Figures B.5 (a) also constitute an  $150 \times 150$  array extracted from Figure B.3, but this time covering the upper part of the forest surrounding the Gjern Stream Valley in Figure B.1. The ratio image in Figure B.6 (a) covers the town Fårvang and again the ratio data constitute an  $150 \times 150$  array extracted from Figure B.3.

The C-band EMISAR data in Figure B.1 contain various line features such as rivers, streams, hedges and roads. The river Gudenå is very distinct in Figure B.1 and so is the restored equivalent in Figure B.2. Here all the coils of the river are preserved and the boundaries appear sharp. The stream Gjern Å is too small to be clearly identified in the Gjern Stream Valley in Figure B.1. However, the few places in Figure B.1, where there is small evidence of the stream, are preserved in Figure B.2. The major part of the hedges, which are surrounding the agricultural fields and pastures in Figure B.1, is preserved in Figure B.2. This also includes most of the roads between the towns.

In Section 5.7 it was demonstrated that although (5.8) is well suited for restoring discontinuities such as edges and sharp transitions, the reconstruction is not perfect as indicated by the structure in Figure 5.32(a). This is also indicated in the ratio image in Figure B.3 where the structure reflects the discontinuities at e.g. rivers, hedges and roads. Although the consequences of the smoothing effect using (5.8) are small and negligible for large areas, the smoothing has sever consequences for very small areas of the size of  $3 \times 3$  pixels or less. This is evident for the very narrow roads and single-row hedges in Figure B.1, which are either only partly restored or over-smoothed in Figure B.2. Note, that the line features are equally well restored using the proposed annealing algorithm whether they have relatively small amplitudes levels like e.g. the river Gudenå and the roads, or they have relatively high amplitudes levels like e.g. the hedges.

The ratio data in Figure B.4 (a) possess very little structure. This indicates that the agricultural fields, which they represent, are relatively homogeneous. The statistics of the ratio image in Figure B.4 (a) are  $\bar{z} = 1.026$ ,  $S^2(z) = 0.352$  and  $\chi^2(63)$  is estimated to 1200.  $H_0$  is hereby rejected, which is supported by the histogram in Figure B.4 (b) where the observed frequencies do not match

the theoretical Rayleigh distribution.

As demonstrated in Section 5.7 (5.8) is capable of restoring homogeneous areas in SAR amplitude data. However, this is not in agreement with the bias in the histogram in Figure B.4 (b). Given that the data are not radiometrically distorted the reason probably is, that the agricultural fields are not truly homogeneous. Instead they probably contain large amplitude point scatterer or small patches of different vegetation and soil moisture characteristics of the size of a resolution cell i.e. a pixel. In the EMISAR data the pixels covering these individual patches are recognized as outliers that are independent of their neighbours. These outliers are also defined as a MRF although with an empty neighbourhood. As a consequence the ratio data in Figure B.4 (a) are not identically distributed and therefore neither Rayleigh distributed everywhere. Since the proposed annealing algorithm is designed to restore Rayleigh distributed SAR data this probably explains the bias between the observed frequencies and the theoretical Rayleigh distribution in Figure B.4 (b). Nevertheless, a visual comparison between the EMISAR data in Figure B.1 and the reconstructed result in Figure B.2 shows, that relatively homogeneous regions such as Sminge Sø and the agricultural fields are well restored. This also includes the small variations in brightness located within these areas.

Texture plays a dominant role in the discrimination of different forest types. Within the scene in Figure B.1 the various forest types can be seen as the bright areas surrounding the Gjern River Valley. These forest texture types include secondary forest and cultivated forest. The secondary forest, which is covering the hilly surroundings of the river valley, is a mixture of natural and planted deciduous and coniferous forest. The cultivated forest is primarily located on the fringes and is possibly coniferous. The small gaps in the forest, which stand out as darker, often rectangular areas, originate from selective logging activities. The forest is more transparent to the L-band than to the C-band. Since the EMISAR data in Figure B.1 are C-band VV polarized, we will therefore expect the major part of the backscatter from the forest to be due to multiple scattering in the forest canopy and not double-bounce scattering from e.g. the ground and trunks. Due to the multiple scattering a significant part of the microwaves is reflected back towards the radar. This explains the relative bright appearance of the forest.

The ratio data in Figure B.5 (a) cover an area with forest and the statistics of the data are  $\bar{z} = 1.05$ ,  $S^2(z) = 0.47$  and  $\chi^2(72) > 17000$ . This again rejects the  $H_0$  hypothesis, which is also reflected in the poor match between the theoretical Rayleigh distribution and the observed frequencies in Figure B.5 (b). A comparison between the statistics and histograms of the ratio data in Figure B.4 (a), (b) and Figure B.5 (a), (b) shows, that the histogram of the ratio data in Figure B.5 (b) has the largest bias between the theoretical Rayleigh distribu-

tion and the observed frequencies. This again is reflected in the structure in Figure B.5 (a), which is slightly more pronounced than in Figure B.4 (a).

Based upon the analyses above it is concluded, that the agricultural fields are better preserved than the forest. This has two main reasons. Firstly, in Figure B.1 the EMISAR data covering the forest contain more outliers than the EMISAR data covering agricultural fields. This is mainly due to large amplitude point scatterer or gaps between the trees and gaps within the canopy of the size of a pixel. As mentioned above these outliers are independent of their neighbours and as the number of outliers increases, the SAR amplitude data are less likely to be Rayleigh distributed everywhere. Because the number of outliers is smaller in the agricultural fields than in the forest and because the annealing algorithm is only designed to restore Rayleigh distributed data, it follows that the agricultural fields in Figure B.2 are better preserved than the forest.

Secondly, the EMISAR data covering the forest possess more discontinuities than the EMISAR data covering the agricultural fields. This is mainly due to the different tree species and gaps between the trees. Since discontinuities are not completely restored by the annealing algorithm, the larger number of discontinuities in the forest has the effect that the agricultural fields in Figure B.2 are better preserved than the forest. However, despite the fact that the forest is not perfectly restored in a statistical sense, a comparison of the forest texture in Figure B.1 and the restored equivalent in Figure B.2 shows, that most of the structure and details are preserved.

Texture plays also an important role in the classification of towns. In Figure B.1 the three towns Voel, Gjern and Fårvang are easily identified by their characteristic coarse texture. This coarse texture is due to the high concentration of man-made features such as houses, buildings, streets and roads. The characteristic bright response these features gives rise to in the towns in Figure B.1 is caused by the so-called double-bounce scattering. This phenomenon occurs when the micro-waves are able to first bounce off e.g. a street and then again bounce off a building and directly towards the radar.

Ratio data covering the town Fårvang are displayed in Figure B.6 (a). Given the statistics  $\bar{z} = 1.12$ ,  $S^2(z) = 1.05$  and  $\chi^2(72) > 10^{12}$  of the ratio image, the  $H_0$  hypothesis is rejected. This is strongly supported by the structure in Figure B.6 (a) and by the bias between the observed frequencies and the theoretical Rayleigh distribution in Figure B.6 (b). Comparing the statistics and histograms of the ratio data in the Figures B.4 (a), B.5 (a) and B.6 (a) it is obvious, that the ratio data in Figure B.6 (a) possesses the largest bias between the observed frequencies and the theoretical Rayleigh distribution. This implies that the town Fårvang is not as well restored as the agricultural fields and the



forests using (5.8) and the annealing schedule.

This worse restoration is partly due to a larger number of outliers and partly due to a larger number of discontinuities in the region covering the town Fårvang than in the regions that cover the agricultural fields and the forest in Figure B.1. The outliers are due to large amplitude point scatterer or objects of the size of a pixel e.g. houses, roads, streets and vehicles. As previously mentioned these outliers are independent of their neighbours which implies, that they are not properly restored by the proposed annealing algorithm. Furthermore, neither the large number of discontinuities is properly restored through the annealing, which additionally deteriorates the restoration. The reservations made above concerning the restoration of Fårvang are clear in Figure B.2, where the smallest details of the town in Figure B.1 are smoothed out.

In summary, it is demonstrated that the results presented in this thesis using the Gamma *pixel prior* through a SA algorithm are generally applicable. The various human artefacts and texture types in Figure B.1 are on the whole reproduced in Figure B.2. The reservation concerns thin line features, point scatterers and very small object corresponding to the size of a few pixel. They have a tendency of being smoothed out by the Gamma *pixel prior* and the annealing schedule.

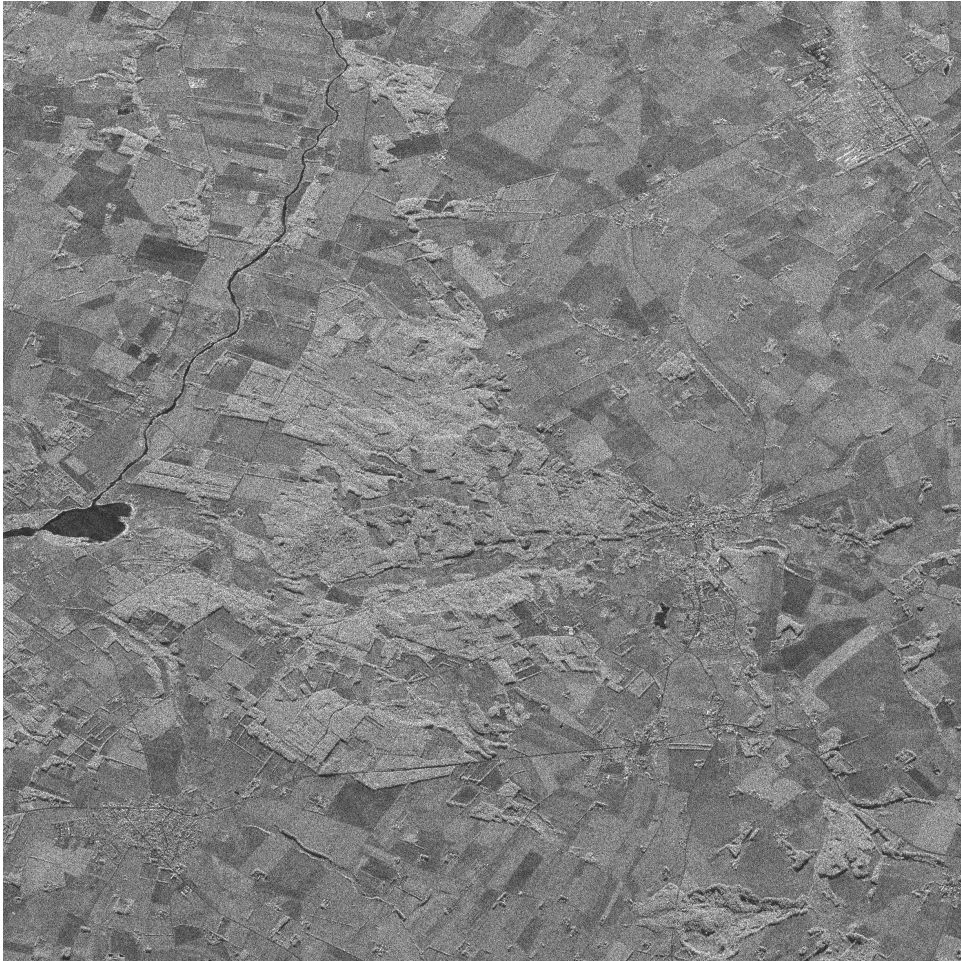


Figure B.1: The C-band VV-polarized EMISAR amplitude data covering the river valley of Gjern and its surroundings 3 June 1997

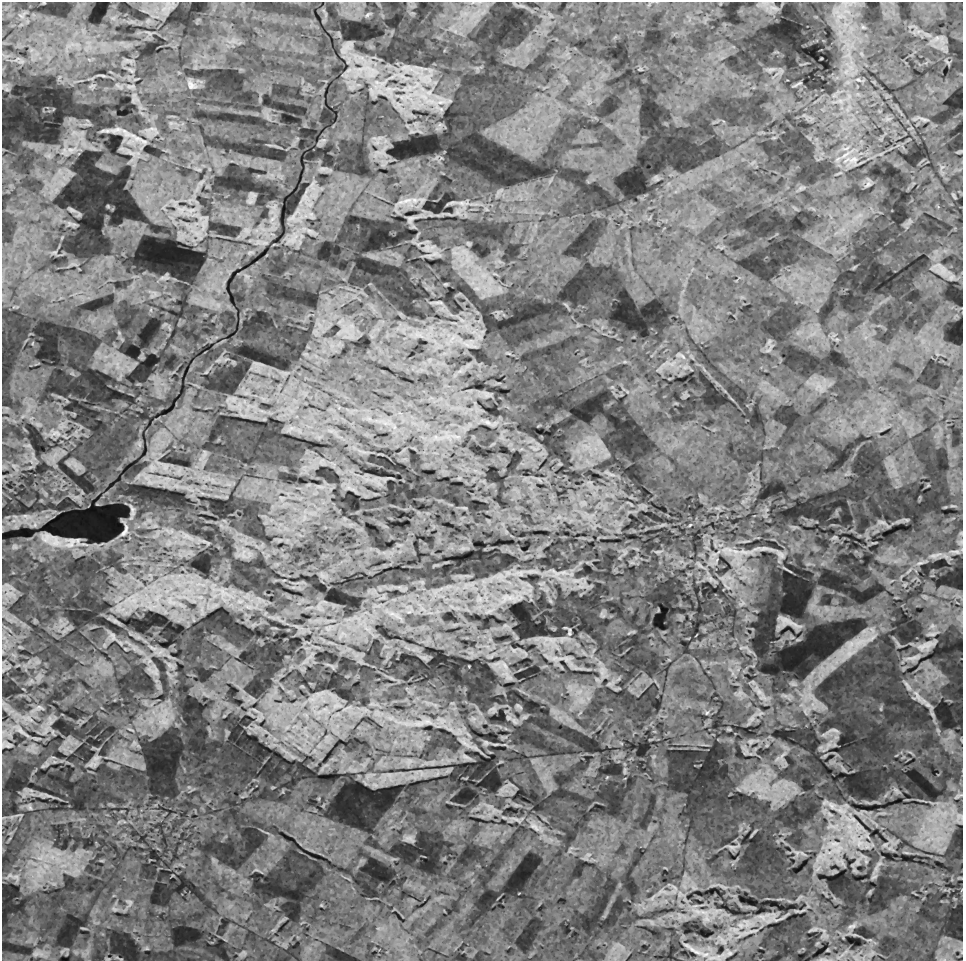


Figure B.2: The restored C-band VV-polarized EMISAR amplitude data in Figure B.1 using the Gamma *pixel prior* and SA. The cooling schedule is logarithmic with an inhomogeneous Markov chain

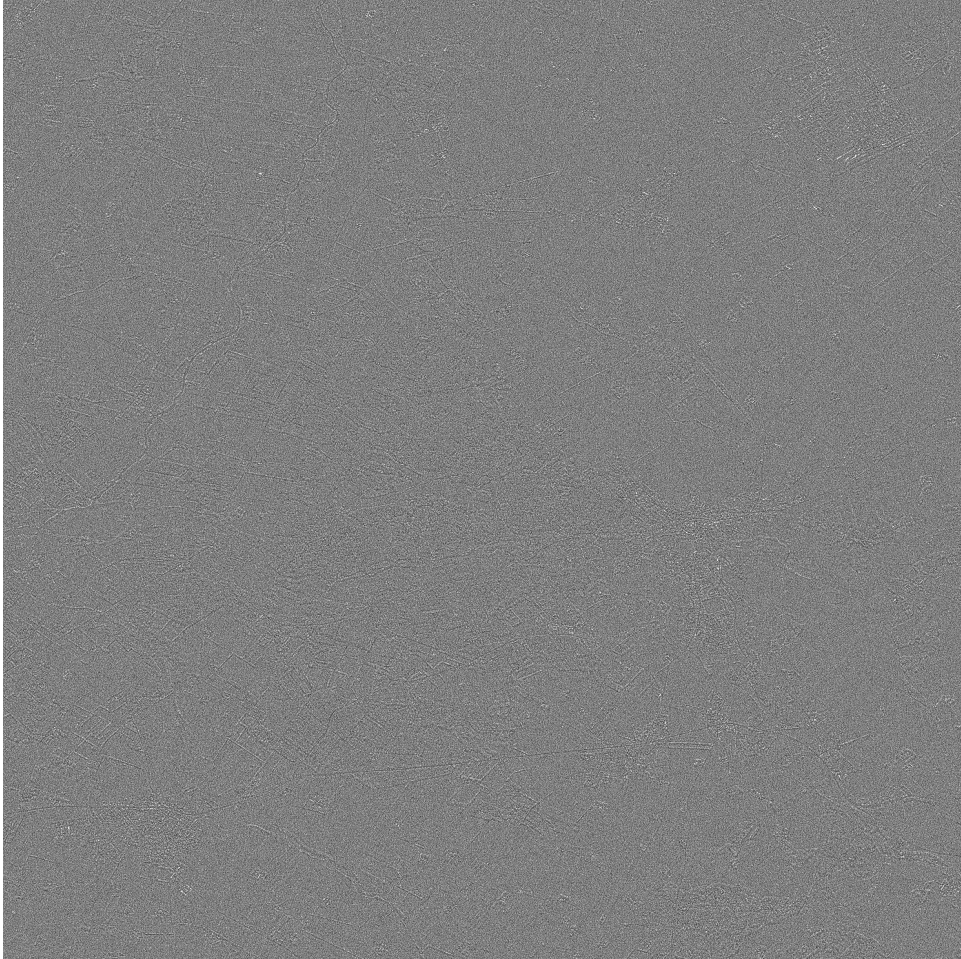
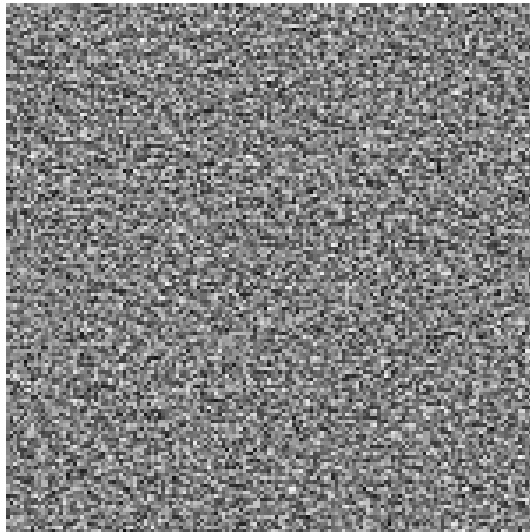
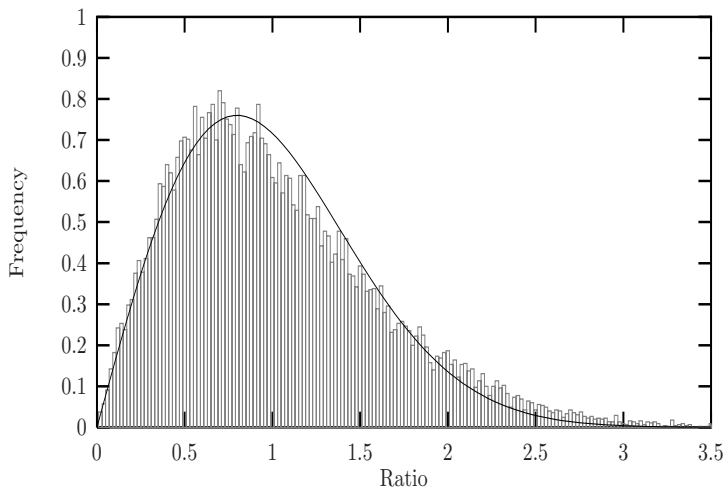


Figure B.3: The ratio between the C-band VV-polarized EMISAR amplitude data in Figure B.1 and the restored data in Figure B.2 using the Gamma *pixel prior* and SA.

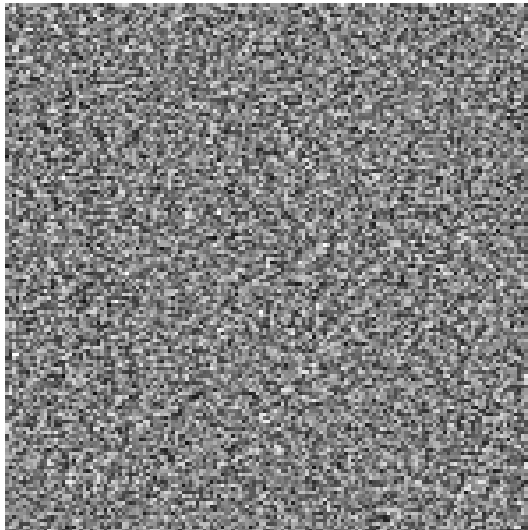


(a)

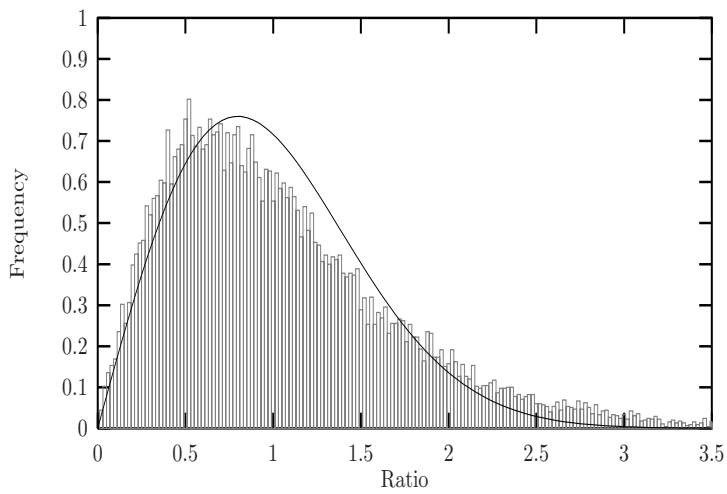


(b)

Figure B.4: (a) Region in the ratio image in Figure B.3, that covers agricultural fields. In (b) is the histogram of the ratio image shown together with the theoretical Rayleigh distribution.

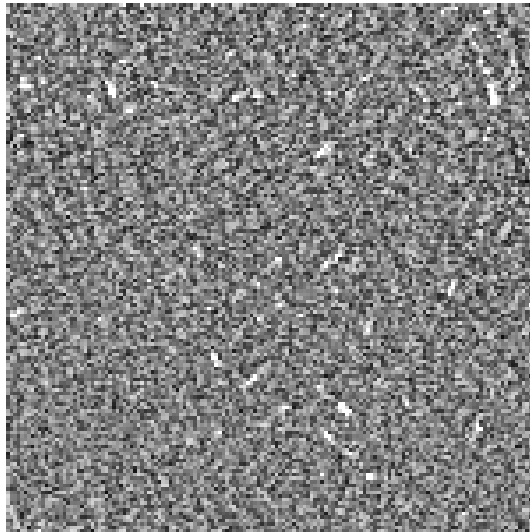


(a)

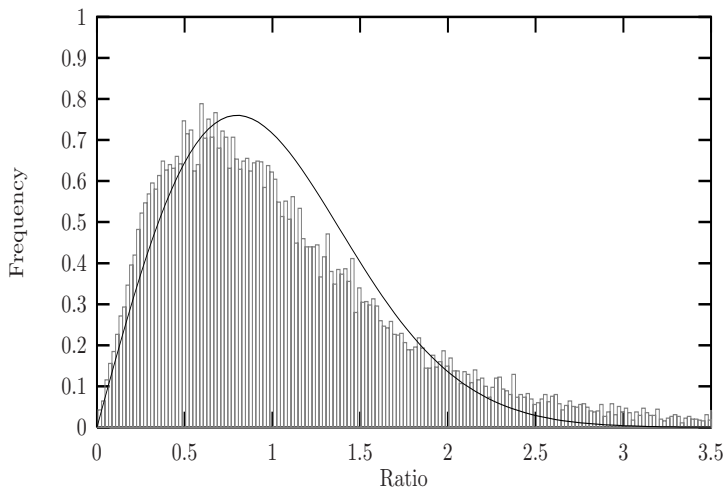


(b)

Figure B.5: (a) Region in the ratio image in Figure B.3, that covers a forest. In (b) is the histogram of the ratio image shown together with the theoretical Rayleigh distribution.



(a)



(b)

Figure B.6: (a) Region in the ratio image in Figure B.3, that covers the town Fårvang. In (b) is the histogram of the ratio image shown together with the theoretical Rayleigh distribution.





## Vegetation list

---

Vegetation from biomass samples collected within the test sites at Gjern and Mols Bjerge. Both the Danish and Latin names of the species are listed:

Almindelig Røllike	<i>Achillea millefolium</i>
Almindelig Hvene	<i>Agrostis capillaris</i>
Eng-Rævehale	<i>Alopecurus pratensis</i>
Liden Klokke	<i>Campanula rotundifolia</i>
Eng-Karse	<i>Cardamine pratensis ssp. pratensis</i>
Nikkende Star	<i>Carex acuta</i>
Sand-Star	<i>Carex arenaria</i>
Stiv Star	<i>Carex elata ssp. elata</i>
Ager-Snerle	<i>Convolvulus arvensis</i>
Mose-Bunke	<i>Deschampsia cespitosa</i>
Bølget Bunke	<i>Deschampsia flexuosa</i>
Almindelig Kvik	<i>Elymus repens</i>
Rød Svingel	<i>Festuca rubra</i>
Almindelig Mjødurt	<i>Filipendula ulmaria</i>
Lyng-Snerre	<i>Galium saxatile</i>
Manna-Sødgræs	<i>Glyceria fluitans</i>
Høj Sødgræs	<i>Glyceria maxima</i>
Håret Høgeurt	<i>Hieracium pilosella</i>

---

Fløjlgræs	<i>Holcus lanatus</i>
Krybende Hestegræs	<i>Holcus mollis</i>
Almindelig Kongepen	<i>Hypochoeris radicata</i>
Lyse-Siv	<i>Juncus effusus</i>
Humle-Sneglebælg	<i>Medicago lupulina</i>
Rørgræs	<i>Phalaris arundinacea</i>
Lancet-Vejbred	<i>Plantago lanceolata</i>
Almindelig Eng-Rapgræs	<i>Poa pratensis</i>
Almindelig Rapgræs	<i>Poa trivialis</i>
Kragefod	<i>Potentilla palustris</i>
Lav Ranunkel	<i>Ranunculus repens</i>
Almindelig Syre	<i>Rumex acetosa</i>
Almindelig Rødknæ	<i>Rumex acetosella</i>
Vand-Skræppe	<i>Rumex hydrolapathum</i>
Fandens Mælkebøtte	<i>Taraxacum ruderalia</i> agg.
Smalbladet Dunhammer	<i>Typha angustifolia</i>
Tofrøet Vikke	<i>Vicia hirsuta</i>
Vår-Vikke	<i>Vicia lathyroides</i>

## APPENDIX D

# Vegetation data Gjern 1997

---

The vegetation at Ladegaards Enge June 1997 was mapped according to a coordinate system with its origin at the centre of the test area and its axes going south–north and east–west, see Figure [D.1](#).

The botanical evaluation was carried out by botanist J. Petersen along 13 transects all in the south–north direction with 10 metres spacing. Furthermore the vegetation was evaluated along the 6 transects illustrated in Figure [6.4](#). Along each transect the distribution of the various plant species was evaluated on a scale from 1–4. The most dominant species were assigned the score 4 and the least dominant species received the score 1. For the most dominant species the distribution was estimated together with the average height of the vegetation.

Based on this botanical evaluation the distribution of the dominant plant species at Ladegaards Enge June 1997 is shown in the Figures [6.3](#) and [D.1](#).

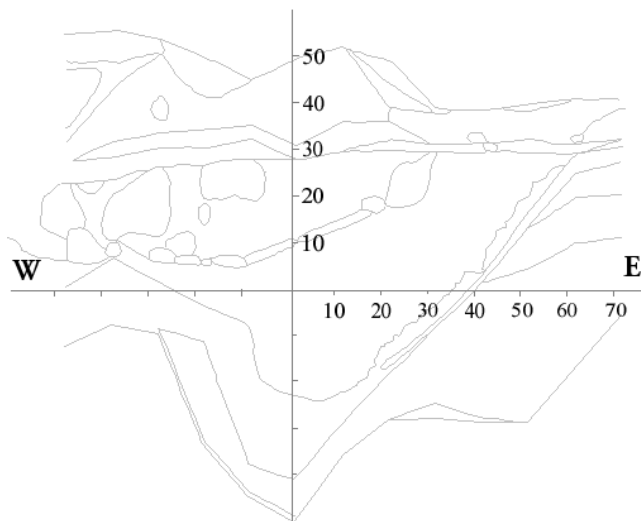


Figure D.1: Outline of the coordinate system used in the mapping of the vegetation at Ladegaards Enge June 1997. The distribution of the dominant plant species is sketched.

# Programs

---

A significant part of this work has been the development of computer programs implementing the different optimization algorithms presented in Chapter 5. The programs were developed in the C programming language on a PC with a 350 MHz Intel Pentium II processor running Linux. The serial programs have been adapted to the HIPS-2 image processing software. For pseudo-random number generation is used the linear congruential algorithm (rand) with 32-bit integer arithmetic [65].

The following list contains the main software developed.

- Algorithms based on MRF and ICM:
  - icm\_gauss:** Performs a restoration of Rayleigh distributed SAR data using the Gaussian *a priori* model involving the 8 pair-site cliques with different weights in a second order neighbourhood configuration.
  - icm\_exp:** Performs a restoration of Rayleigh distributed SAR data using the exponential *a priori* model involving the 8 pair-site cliques with different weights in a second order neighbourhood configuration.
  - icm\_LaPlace:** Performs a restoration of Rayleigh distributed SAR data

using the LaPlace *a priori* model involving the 8 pair-site cliques with different weights in a second order neighbourhood configuration.

**icm\_Gamma\_mean:** Performs a restoration of Rayleigh distributed SAR data using the Gamma *a priori* model involving the 8 pair-site cliques with different weights in a second order neighbourhood configuration. The estimate of the local energy level is defined as the mean of the pixels involved in the neighbourhood configuration.

**icm\_Gamma\_cpix:** Performs a restoration of Rayleigh distributed SAR data using the Gamma *a priori* model involving the 8 pair-site cliques with different weights in a second order neighbourhood configuration. The estimate of the local energy level is defined as the centre pixel itself.

- Algorithms based on MRF and SA:

**sa\_cpix:** Performs a restoration of Rayleigh distributed SAR data using the Gamma *a priori* model and the Metropolis algorithm. The 8 pair-site cliques with different weights in a second order neighbourhood configuration are involved and the estimate of the local energy level is defined as the centre pixel itself.

**sa\_cpix9:** Performs a restoration of Rayleigh distributed SAR data using the Gamma *a priori* model and the Metropolis algorithm. Here the 8 pair-site cliques with equal weights in a second order neighbourhood configuration are involved and the estimate of the local energy level is defined as the centre pixel itself.

# References

---

- [1] Anderberg, M. R. *Cluster Analysis for Application*. Academic Press, New Yor, 1973.
- [2] Andersen, E. H. *Hydrology of A Floodplain*. Ph.D. thesis, Danish National Environmental Research Institute (NERI), 2001.
- [3] Anderson, T. W. *An Introduction to Multivariate Statistical Analysis*. 3rd. ed., John Wiley & Sons, New York, 2003.
- [4] Andrews, H. C. *Digital Image Restoration*. N. J.: Prentice-Hall, Englewood Cliffs, 1977.
- [5] Baggesen, K. H., Nielsen, A. A., Larsen, R. A scheme for initial exploratory data analysis of multivariate image data. *Proceedings of 12th Scandinavian Conference on Image Analysis (SCIA)* , pp. 717–724, 2001.
- [6] Besag, J. E. Spatial interaction and the statistical analysis of lattice systems. *J. Royal Stat.Soc.Ser., Ser. B*, **36**, pp. 192–236, 1974.
- [7] Besag, J. E. On the statistical analysis of dirty pictures. *J. Royal Stat.Soc.Ser., Ser. B*, **48**, pp. 259–302, 1986.
- [8] Besag, J. E. Towards Bayesian image analysis. *Journal of Applied Statistics*, **16**(3), pp. 395–407, 1989.
- [9] Bishop, C. M. *Neural Networks for Pattern Recognition*. Oxford University Press, Oxford, 1995.
- [10] Blæsild, P. *Forelæsnings Noter*. Afdeling for teoretisk statistik, Århus Universitet, 1989.

- [11] Carstensen, J. M. *Description and Simulation of Visual Texture*. Ph.D. thesis, IMSOR, Technical University of Denmark, 1992.
- [12] Carstensen, J. M. *Digital Image Processing*. IMM, Technical University of Denmark, 2000.
- [13] Cerny, V. Thermodynamical approach to the traveling salesman problem: an efficient simulation algorithm. *Journal of Optimization Theory and Applications*, **45**, pp. 41–51, 1985.
- [14] Chellappa, R., Jain, A. *Markov Random Fields: Theory and Application*. Academic Press Inc., San Diego, 1993.
- [15] Chow, C. K. A recognition method using neighbor dependence. *IEEE Trans. on Electronic Computer*, **11**, pp. 683–690, 1962.
- [16] Christensen, S., Rasmussen, K.R., Møller, K. *Modeling regional groundwater flow to streams*. Department of Earth Sciences, Aarhus University, 1996.
- [17] Conradsen, K. *En Introduktion til Statistik*, volume 2B. IMSOR, Lyngby, Danmarks Tekniske Universitet, 1984.
- [18] Conradsen, K. *En Introduktion til Statistik*, volume 1A. IMM, Lyngby, Danmarks Tekniske Universitet, 1995.
- [19] Conradsen, K. and Ersbøll, B. K. Data dependent orthogonal transformations of multichannel image data. *Technical Report, IMSOR, Technical University of Denmark*, 1991.
- [20] Conradsen, K., Nielsen, A. A., Schou, J., Skriver, H. A test statistic in the complex Wishart distribution and its application to change detection in polarimetric SAR data. *IEEE Trans. Geosci. Remote Sensing*, **41**(1), pp. 4–19, 2003.
- [21] Datcu, M., Seidel, K. and Walessa, M. Spatial information retrieval from remote-sensing images—Part I: Information theoretical perspective. *IEEE Trans. on geoscience and remote sensing*, **36**(5), pp. 1431–1445, 1998.
- [22] Davis, J.L. & A.P. Annan. Electromagnetic detection of soil moisture. *Progress report 1. Can. J. Remote Sensing*, **3**, pp. 76–86, 1977.
- [23] Deutsch, C.V., Journel, A.G. *GSLIB Geostatistical Software Library and User's Guide*. 2nd. ed., Oxford University Press, 1998.
- [24] Dong, Y., Milne, A. K., Forster, B. C. A review of sar speckle filters: Texture restoration and preservation. *IEEE International Geoscience and Remote Sensing Symposium*, **2**, pp. 633–635, 2000.



- [25] Dubes, R. C., Jain, A. K. Random field models in image analysis. *Journal of Applied Statistics*, **16**(2), pp. 131–164, 1989.
- [26] Dubois, P. C., Zyl, van Jakob, Engman, T. Measuring soil moisture with imaging radars. *IEEE Trans. Geosci. Remote Sensing*, **33**(4), pp. 915–926, 1995.
- [27] Elachi, C. *Introduction to the Physics and Techniques of Remote Sensing*. John Wiley & Sons, New York, 1987.
- [28] Ellenberg, H., et al. Zeigerwerte von Pflanzen in Mitteleuropa Scripta Geobotanica. *Göttingen*, 2. Aufl., **18**, 1992.
- [29] Geman, S. and Geman, D. Stochastic relaxation, Gibbs distribution and the Bayesian restoration of images. *IEEE Trans. Pattern Anal. Machine Intell.*, **6**, pp. 721–741, 1984.
- [30] Groom, G., Mikkelsen, H., Skriver, H., Hansen, B., Thomsen, A., Nielsen, A. A. Activities and early results from DANMAC: The Danish multisensor airborne campaign . *Third International Airborne Remote Sensing Conference and Exhibition, Copenhagen, Proceedings* , **2**, pp. 617–624, 1997.
- [31] Hajek, B. Cooling schedules for optimal annealing. *Mathematics of Operations Research*, **13**, pp. 321–329, 1988.
- [32] Haralick, R. M. Statistical and structural approaches to texture. *Proceedings of IEEE*, **67**(5), pp. 786–804, 1979.
- [33] Hartelius, K. *Analysis of Irregularly Distributed Points*. Ph.D. thesis, Institute of Mathematical Modelling, Technical University of Denmark, 1996.
- [34] Hassner, M. and J. Sklansky. The use of Markov random fields as models of texture. *Comput. Graphics Image Process.*, **12**, pp. 357–370, 1980.
- [35] Henderson, F., Lewis, A. Principles & Applications of Imaging Radars. *Manual of remote sensing*, **2**, pp. 407–414, 1998.
- [36] Isaaks, E. H. & Srivastava, R. M. *An Introduction to Applied Geostatistics*. Oxford University Press, New York, 1989.
- [37] J. Ji, Keur, P., Thomsen, A. & Skriver, H. Soil moisture retrieval using the Danish L- & C-band polarimetric SAR. *The Proceedings of IGARSS*, 1996.
- [38] Jacobsen, A., Nielsen, A.A., Ejrnæs, R., Groom, G.B. Spectral identification of plant communities for mapping of semi-natural grasslands. *Canadian Journal of Remote Sensing*, **26**(5), pp. 370–383, 2000.

- [39] Jacobsen, O. H., Schönning, P. Comparison of TDR calibration functions for soil water determination. *Proceedings of the Symposium: Time-Domain Reflectometry Applications in Soil Science, SP report*, **3**(11), pp. 25–33, June, 1995.
- [40] Jaynes, E. Information theory and statistical mechanics. *Physical review*, **106**, pp. 620–630, 1957.
- [41] Journel, A. G., Huijbregts, C. J. *Mining Geostatistics*. Academic Press, London, 1978.
- [42] Kindermann, R., Snell, J. L. *Contemporary Mathematics: Markov Random Fields and their Applications*. American Mathematical Society, Providence, Rhode Island, 1980.
- [43] Kirkpatrick, S., Gelatt Jr., C. D. and Vecchi, M. P. Optimization by simulated annealing. *Science*, **220**, pp. 671–680, 1983.
- [44] Kouskoulas, Y., Pierce, L., Ulaby, F. T., Dobson, M. C. Classification of short vegetation using multifrequency SAR. *IEEE International Geoscience and Remote Sensing Symposium*, **2**, pp. 735–737, 1999.
- [45] Lakshmanan, S. and Derin, H. Simultaneous parameter estimation and segmentation of Gibbs random fields using simulated annealing. *IEEE Transactions on Pattern Analysis and Machine Intelligence*, **11**(8), pp. 799–813, 1989.
- [46] Li, S. Z. *Markov Random Field Modeling in Computer Vision*. Springer-Verlag Tokyo, Hong Kong, 1995.
- [47] MacQueen, J.B. Some methods for classification and analysis of multivariate observations. *Proceedings of the Fifth Berkeley Symposium on Mathematical Statistics and Probability*, pp. 281–297, 1967.
- [48] Marr, D. *A Computational Investigation Into the Human Representation and Processing of Visual Information*. W. H. Freeman, San Francisco, 1982.
- [49] McCloy, K. (Editor), Groom, G., Hansen, B., Nielsen, A. A., Skriver, H., and Thomsen, A. DANMAC, DANish Multisensor Airborne Campaign, Final Report 1996–1998. Technical report, Foulum, 1999.
- [50] Metropolis, N., Rosenbluth, A. W., Rosenbluth, M. N., Teller, A. H. and Teller, E. Equations of state calculations by fast computing machines. *Journal of Chemical Physics*, **21**, pp. 1087–1091, 1953.
- [51] Morrison, K., Bennett, J. C., Brown, S. C. M., Cookmartin, G., McDonald, A. J., Quegan, S., Dampney, P. Very high resolution polarimetric L, S, C and X-band 3D SAR imagery of the scattering characteristics of wheat

- canopies. *Geoscience and Remote Sensing Symposium*, , **6**, pp. 2531–2533, 2000.
- [52] Niblack, W. *An Introduction to Digital Image Processing*. Strandberg Publishing Compagny, Birkerød, Denmark, 1985.
- [53] Nielsen, A. *Plantefordelende Faktorer i 2 Vådområder på et Ånært Areal*. Specialrapport, Biologisk Institut, Afdeling for Botanisk Økologi, Aarhus Universitet,, 1999.
- [54] Nielsen, A. A. *Analysis of Regularly and Irregularly Sampled Spatial, Multivariate, and Multi-temporal Data*. Ph.D. thesis, Institute of Mathematical Modelling, Technical University of Denmark,, 1994.
- [55] Nielsen, A. A. *Geostatistik og analyse af spatielle data*. Geografiske Informationssystemer–Kursusnoter, IMM, Danmarks Tekniske Universitet, 1999.
- [56] Nissen, H. H., Møldrup, P. Theoretical background for the TDR methodology. *Proceedings of the Symposium: Time-Domain Reflectometry Applications in Soil Science, SP report*, **3**(11), pp. 9–23, June, 1995.
- [57] Oh, Y., Sarabandi, K. and Ulaby, F.T. An empirical model and inversion technique for radar scattering from bare soil surfaces. *IEEE Trans. Geosci. Remote Sensing*, **30**(2), pp. 370–381, March, 1992.
- [58] Oliver, C., Cook, R., McConnell, I. and Stewart, D. *Segmentation and simulated annealing*. , Preprint, October, 1996.
- [59] Oliver C. J., Quegan, S. *Understanding Synthetic Aperture Radar Images*. Artech House, Inc., London, 1998.
- [60] Otten, R., and van Ginneken, L. *The Annealing Algorithm*. Kluwer Academic, 1989.
- [61] Ozesmi, S. L., Bauer, M. E. Satellite remote sensing of wetlands. *Wetlands Ecology and Management*, **10**(5), pp. 381–402, 2002.
- [62] Park, J., Kurz L. J. Image enhancement using the modified ICM method. *IEEE Trans. on image processing*, **5**(5), pp. 765–771, May, 1996.
- [63] Pearson, K. On lines and planes of the closest fit to systems of points in space. *Philosophical Magazine*, **2**, pp. 559–572, 1901.
- [64] Press, F., Siever, R. *Earth*. 3rd. ed., W. H. Freeman and company, San Francisco, 1982.

- [65] Press, W. H., Teukolsky, S. A., Vetterling, W. T., Flannery, B. P. . *Numerical Recipes in C: The Art of Scientific Computing*. 2nd. ed., Cambridge University Press, Cambridge, 1992.
- [66] Price, K. P., Guo, X., Stiles, J. M. Comparison of Landsat TM and ERS-2 SAR data for discriminating among grassland types and treatments in eastern Kansas. *Computers and Electronics in Agriculture*, **37**(1–3), pp. 157–171, 2002.
- [67] Rasmussen, H. Weinberg. *Landskabsplan for Molsområdet*. Fredningsplanudvalget for Århus Amt, Phønix-Trykkeriet A/S, Århus, pp. 19–42, 1978.
- [68] Rees, W. G., Satchell, M. J. F. The effect of median filtering on synthetic aperture radar images. *International Journal of Remote Sensing*, **18**(13), pp. 2887–2893, 1997.
- [69] Ripley, B. D. *Pattern Recognition and Neural Network*. University Press, Cambridge, 1996.
- [70] Roughgarden, J., Running, S. W., Matson, P. A. What does remote sensing do for ecology? *Ecological Society of America*, **72**(6), pp. 1918–1922, 1991.
- [71] Rueckert, D. *Segmentation and Tracking in Cardiovascular MR Images using Geometrically Deformable Models and Templates*. Ph.D. thesis, Imperial college of science, Technology and Medicine, University of London, London, 1997.
- [72] SAS Institute Inc. *SAS/STAT User's Guide, Version 6, Fourth Edition, Volume 1*, Cary, NC: SAS Institute Inc. 1989.
- [73] SAS Institute Inc. *SAS/STAT User's Guide, Version 6, Fourth Edition, Volume 2*, Cary, NC: SAS Institute Inc. 1989.
- [74] Schou, J., Skriver, H. Restoration of polarimetric SAR images using simulated annealing. *IEEE Transactions on Geoscience and Remote Sensing*, **39**(9), pp. 2005–2016, 2001.
- [75] Skriver, H. *Extraction of Sea Ice Parameters from Synthetic Aperature Radar Images*. Ph.D. thesis, Electromagnetics Institute, Technical University of Denmark, 1989.
- [76] Søndergaard, M., Riemann, B. *Ferskvandsbiologiske Analysemetoder*. Akademisk Forlag, København, 1979.
- [77] Sonka, M., Hlavac, V., Boyle, R. *Image Processing, Analysis and Machine Vision*. 2nd. ed., Chapman & Hall Computing, 1999.

- [78] Stewart, D., Blacknell, D., Blake, A., Cook, R., Oliver, C. Optimal approach to SAR image segmentation and classification. *Radar, Sonar and Navigation, IEE Proceedings*, **147**(3), pp. 134–142, 2000.
- [79] Thomsen, A. Manual and automated TDR measurements. *Proceedings of the Symposium: Time-Domain Reflectometry Applications in Soil Science, SP report*, **3**(11), pp. 39–43, June, 1995.
- [80] Topp, G.C., Davis, J.L. & Annan, A.P. Electromagnetic determination of soil water content: Measurements in coaxial transmission lines. *Water Resour. Res.*, **16**, pp. 574–582, 1980.
- [81] Ulaby, F.T, Elachi. *Radar Polarimetry for Geoscience Applications*. Artech House, Inc., Norwood, MA, 1990.
- [82] Ulaby, F.T, Moore, R.K., Fung, A.K. *Microwave Remote Sensing, Active and Passive*. Artech House, Inc., Dedham, MA, Vol. I–III, 1986.
- [83] Van Laarhoven, P. J. M. and Aarts, E. H. L. *Simulated Annealing: Theory and Applications*. Reidel, 1987.
- [84] Vandermeulen, R., Verbeek, R., Berben, L., Delaere, D., Suetens, P. and Marchal, G. Continuous voxel classification by stochastic relaxation: Theory and application to MR imaging and MR angiography. *Image and Vision Computing*, **12**(9), pp. 559–572, 1994.
- [85] Watson, R. T., Zinyowera, M. C., Moss, R. H. The regional impacts of climate change. An assessment of vulnerability. *Published for the Intergovernmental Panel on Climate Change*, 1997.
- [86] White, R. G. A simulated annealing algorithm for SAR and MTI image cross-section estimation. *Proceeding of the SPIE—The International Society for Optical Engineering*, **2316**, pp. 137–145, 1994.
- [87] Windfeld, K. *Application of Computer Intensive Data Analysis Methods to the Analysis of Digital Images and Spatial Data*. Ph.D. thesis, IMSOR, Technical University of Denmark, 1992.
- [88] Xu, X., Li, D., Sun, H. Multiscale SAR image segmentation using a double Markov random field model. *IEEE Signal Processing and Its Applications, Proceedings*, **1**, pp. 349–352, 2003.
- [89] Zhang, Z., Prinnet, V., Ma, S. A new method for SAR speckle reduction. *IEEE International Geoscience and Remote Sensing Symposium*, **6**, pp. 3450–3452, 2002.